THE UNIVERSITY *of* EDINBURGH

High-Pressure Computational and Experimental Studies of Energetic Materials

Steven Hunter

A thesis submitted in fulfilment of the requirements for the degree of Doctor of Philosophy to the School of Chemistry, the University of Edinburgh.

July 2013

Abstract

On account of the high temperatures and pressures experienced by energetic materials during deflagration and detonation, it is important to know not only the physical properties of these materials at ambient temperatures and pressures, but also to understand how their structure and properties are affected by extreme conditions. Combined computational and experimental investigations of the effects of high pressures on the structure and properties of several energetic materials are described herein.

A comparison of the performances of different pseudopotentials and density functional theory (DFT) dispersion correction schemes in calculating crystal geometries and vibrational frequencies of crystalline ammonium perchlorate at high pressure is described. The results highlight the fact that care must be taken when choosing pseudopotentials for high-pressure studies. A comprehensive comparison of calculated vibrational modes (including symmetry) with experiment has been performed, with the frequencies of all internal modes predicted to lie within 5% of experimental values. This study established that no significant improvements in the calculation of crystal geometries of ammonium perchlorate are obtained by employing DFT-D corrections.

The enthalpy of fusion (ΔH_{fus}) of the highly metastable β-form of RDX (cyclotrimethylenetrinitramine) was determined to be 12.63 ± 0.28 kJ mol^{-1}. DFT-D calculations of the lattice energies of the α- and β-forms of RDX are described. Furthermore, the response of the lattice parameters and unit-cell volumes to pressure for the α-, γ- and ε-forms of RDX calculated using DFT-D are in very good agreement with experimental data. Phonon calculations provide good agreement with vibrational frequencies obtained from Raman spectroscopy, and a predicted inelastic neutron scattering (INS) spectrum of α-RDX shows excellent agreement with experimental INS data recorded as part of this study. The results of the high-pressure phonon calculations have been used to show that the heat capacities of the α-, γ- and ε- forms of RDX are only weakly affected by pressure.

DFT-D calculations have been utilised to describe accurately the structure and properties of both β-HMX (Cyclotetramethylenetetranitramine) and α-FOX-7 (1,1-Diamino-2,2-dinitroethylene) as a function of pressure. This work presents data for the experimental hydrostatic compression of both deuterated β-HMX and α-FOX-7 performed using neutron powder diffraction at the ISIS Neutron and Muon facility, in addition to experimental determinations of the INS spectra of both β-HMX and α-FOX-7. The DFT-D hydrostatic compression studies for both materials reproduce the experimental compression trends. Furthermore, the calculated vibrational properties as a function of pressure were in very good agreement with available experimental data. The results of the phonon calculations were then used to predict the effect of pressure on the heat capacities of β-HMX and α-FOX-7. These predictions suggest a very weak pressure dependence of heat capacities (approximately -1 $J\ K^{-1}\ mol^{-1}\ GPa^{-1}$) for these materials.

This work demonstrates that the DFT-D model performs extremely well over a range of conditions, and is able to describe accurately intramolecular and intermolecular interactions, and thus the structure and properties of organic molecular nitramine crystals. The computational model was therefore used to predict the high-pressure hydrostatic compression behaviour of a related nitramine, CL-20 (2,4,6,8,10,12-Hexanitro-2,4,6,8,10,12-hexaazaisowurtzitane), the results of which highlighted possible discrepancies in the experimental high-pressure X-ray diffraction data recorded for ε-CL-20. This prompted a high-pressure neutron powder diffraction study, which showed good agreement with the computational results, thereby highlighting radiation damage in the X-ray experiments.

Lay Summary of Thesis

On account of the high temperatures and pressures experienced by energetic materials (explosives, propellants and pyrotechnics) during deflagration (subsonic burning) and detonation (supersonic burning), it is important to know not only the physical properties of these materials at ambient temperatures and pressures, but also to understand how their structure and properties are affected by extreme conditions. Combined computational and experimental investigations of the effects of high-pressure on the structure and properties of several energetic materials are described herein.

A comparison of the performances of different computational methods (a standard 'conventional' method, and two new corrected methods) in calculating the crystal structure (a description of how the molecules in a solid material are arranged) and vibrational properties of crystalline ammonium perchlorate (a propellant – it is used in the booster rockets of NASA space shuttles) at high pressure is described. A comprehensive comparison of calculated vibrational frequencies with experiment has been performed, with the frequency of all internal modes predicted to lie within 5 % of experimental values. This study established that no significant improvements in the calculation of crystal geometries of ammonium perchlorate are obtained by the corrected methods.

The enthalpy of fusion (ΔH_{fus}, the heat released when something melts) of the highly metastable (energetically unfavourable) β-polymorph (polymorphs are the same chemical but with different arrangements of the molecules in the crystal structure, the Greek letters are just names to differentiate between different polymorphs) of RDX (an explosive – it is the explosive part of the plastic explosive C4). DFT-D (corrected-computational chemistry) calculations of the lattice energies (energy difference between the energy of the molecules in a crystal, and the energy of the same molecules in a gas) of the α- and β-polymorphs of RDX are described. Furthermore, the response of the lattice parameters and unit-cell volumes (size and shape of the crystal structure) to pressure for the α-, γ- and ε-polymorphs of RDX calculated using DFT-D are in very good agreement with experimental data. Calculated vibrational frequencies provide good agreement to previous experiment.

The results of the high pressure vibrational frequency calculations have been used to show that the heat capacities (a measurable physical property that shows the amount of heat required to change the temperature of a material by a given amount) of the α-, γ- and ε- forms of RDX are only weakly affected by pressure.

DFT-D calculations have been utilised to describe accurately the structure and properties of both β-HMX and α-FOX-7 (both other explosives which are similar to RDX – the explosive in C4) as a function of pressure. This work presents data for the experimental hydrostatic (equal in all directions) compression of both β-HMX and α-FOX-7 crystalline materials performed using neutron powder diffraction (experimental technique to determine the crystal structure), in addition to experimental determinations of the vibrational properties of both β-HMX and α-FOX-7. The DFT-D calculated hydrostatic compression trends for both materials reproduce the experimental compression trends. Furthermore, the vibrational properties as a function of pressure were calculated in very good agreement with available experimental data. The results of the vibrational frequency calculations were then used to predict the effect of pressure on the heat capacities of β-HMX and α-FOX-7. These predictions suggest a very weak pressure dependence of heat capacities for these materials.

This work demonstrates that the DFT-D model performs extremely well over a range of conditions, and is able to describe accurately the structure and properties of nitramine (the class of compounds that RDX, HMX and FOX-7 belong to) crystals. The computational model was therefore used to predict the high-pressure hydrostatic compression behaviour of a related nitramine, CL-20, the results of which highlighted possible discrepancies in the experimental high-pressure X-ray diffraction (experimental technique to determine the crystal structure) data recorded for ε-CL-20. This prompted a high-pressure neutron powder diffraction study, which showed good agreement with the computational results, thereby highlighting radiation damage in the X-ray experiments.

Declaration

I declare that this thesis was written by me and that the work detailed herein is my own, or I have contributed substantially to such work, except where proper reference is made to the work of another author.

Steven Hunter

Acknowledgements

There are numerous people I would like to thank for their advice and contributions throughout my PhD. First and foremost, I am forever grateful to my supervisors, Prof. Colin R. Pulham and Dr. Carole A. Morrison who together make an excellent team. Without their combined knowledge and encouragement I would not have been able to complete the research required to produce this thesis. Furthermore, I am indebted to Dr. Patricia Richardson for all her help, guiding me through my teething problems with computational chemistry. Thank you as well to all members of the Pulham group past and present, and to the members of CSEC for making the time during my PhD so enjoyable.

Many thanks to Drs. John Tomkinson, Anibal J. (Timmy) Ramirez-Cuesta and particularly Dr. Stewart F, Parker (TOSCA, ISIS) for their help and advice performing and analysing INS experiments, and additionally Dr. Philip J. Camp (The School of Chemistry, UoE) for several helpful conversations.

I would like to thank Dr. Peter J. Gould for his insights into the energetics community and ultimately for initiating (!) this research project. I thank the Scottish Funding Council (SPIRIT) and QinetiQ (in support of MOD research) for contribution towards a studentship; the ESPRC and The School of Chemistry, UoE, for the provision of high-performance computing time and the STFC Rutherford Appleton Laboratory for access to neutron facilities.

Finally, I am grateful for the love and support of my family and friends.

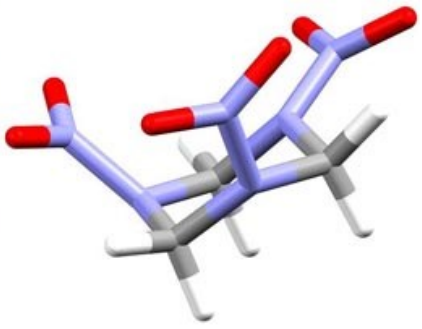

Cheers,

Steve Hunter

Contents

Glossary of Acronyms

AP	Ammonium perchlorate
BFGS	Broyden, Fletcher, Goldfarb and Shannon minimisation
B-M	Birch-Murnaghan
CA	Ceperley and Alder functional
CASTEP	Cambridge Serial Total Energy Package
CL-20	2,4,6,8,10,12-Hexanitro-2,4,6,8,10,12-hexaazaisowurtzitane
DAC	Diamond anvil cell
DDT	Deflagration-to-detonation transition
DFT	Density functional theory
DFT-D	Dispersion-corrected DFT
DSC	Differential scanning calorimetry
E_{cut}	Plane wave kinetic energy cut-off
EoS	Equation(s) of state
FOX-7	1,1-Diamino-2,2-dinitroethylene
GGA	Generalised gradient approximation
GIM	Group interaction modelling
GSAS	General Structure Analysis System
G06	Dispersion-correction proposed by Grimme (2006)
HF	Hartree-Fock
HMX	Cyclotetramethylenetetranitramine
INS	Inelastic neutron scattering
IR	Infrared
K-S	Kohn-Sham
LDA	Local density approximation
M-P	Monkhorst-Pack
NDC	No dispersion correction
OTF	On-the-fly
PBE	Perdew, Burke and Ernzerhof functional
PTM	Pressure-transmitting medium
PW91	Perdew & Wang (1991) functional
-PZ	Perdew and Zunger parameterisation of a functional

RDX	Cyclotrimethylenetrinitramine
RMS	Root-mean square
SCF	Self-consistent field
SPE	Single-point energy
STFC	Science and Technology Facilities Council
TS	Dispersion-correction proposed by Tkatchenko & Scheffler
vdW	van der Waals
00PBE	Set of ultrasoft pseudopotentials developed for use with PBE

Chapter 1

Introduction

1 Experimental Techniques

1.1 Energetic Materials

Since their first discovery, energetic materials (explosives, propellants and pyrotechnics) have fascinated mankind. Their devastating power has been utilised in a variety of applications, such as mining for metal ores,[1] excavation in construction projects,[2] space exploration[3] and most notably in military applications,[4] which have been instrumental in the development of modern society. Due to the intrinsic nature of energetic materials, their development has not been without unfortunate setbacks, such as casualties and fatalities, and accidental destruction of research facilities.[4] Nevertheless, the benefits of developing and controlling the destructive capabilities of energetic materials was and still is, so important, that the effort to develop, and more importantly understand energetic materials has never ceased.

1.1.1 Definition

Energetic materials are defined as materials with high enthalpies of formation that can release heat and, generally, gaseous products upon stimulus by heat, impact, shock, spark, *etc*.[4] A chemical explosion arises when an exothermic transformation occurs over an extremely short space of time, typically < 0.01 s. Due to the extreme speed of the reaction, the product gases do not have time to expand instantaneously, but remain inside the vessel that held the explosive charge. At this point, the volume of the blast chamber remains constant (and small) and the temperature generated by the gaseous reaction products is very high (commonly of the order of several thousand Kelvin) and thus the pressure resulting from the confinement of these extremely hot combustion products can reach several thousand atmospheres. This is sufficient to produce a shock-wave capable of breaking the walls of the chamber and causing damage to the surroundings.[4]

1.1.2 Classification

Energetic materials are generally classified into three categories: explosives, propellants and pyrotechnics. Pyrotechnics (such as flares or fireworks) undergo ‘slow’ combustion, at visibly observable rates, giving rise to coloured smoke, noise

and/or brightly-coloured light. Propellants, such as ammonium perchlorate (NH_4ClO_4, discussed in greater detail in Chapter 4), undergo rapid and predictable combustion, but do not detonate, although burning may be violent and accompanied by sparks or flames and a hissing/crackling sound. This is termed *deflagration* and is described later in this Chapter, Section 1.2.1. The resultant production of large volumes of hot gas can then be utilised for the propulsion of projectiles (such as bullets or even spacecraft) or in gas generators to drive turbines.

Explosives are further sub-divided into primary and secondary explosives. Primary explosives undergo a very rapid transformation from burning to detonation (termed the deflagration-to-detonation transition, which is described in more detail in Section 1.2) and are generally sensitive materials that require relatively mild stimulus (such as heat or shock) for initiation. The detonation event gives rise to a short, strong shock-wave, and therefore primary explosives are mainly used as initiators to detonate the less sensitive secondary explosives. Despite a wide array of compounds displaying explosive detonation upon mild stimulus, due to the rigorous constraints required of initiators, only a very few have successfully been integrated into practical and usable detonators. Some examples of primary explosives include materials such as, lead azide [$Pb(N_3)_2$] and mercury fulminate [$Hg(CNO)_2$].

Secondary explosives (also referred to as high explosives) are much less sensitive than primary explosives. They cannot readily be detonated by heat or mild shock and instead require initiation by the intense shock-wave produced by a primary explosive. However, once detonated, secondary explosives create a much more powerful and sustained shock-wave. In contrast to primary explosives, numerous high explosive compounds have been developed for practical use.

The most widely used secondary explosive of the nineteenth century was picric acid (Figure 1.1a), but due to its high sensitivity to initiation, coupled with the fact that the casting process to make the explosive was hazardous and the propensity for it to react to form very sensitive metal picrates, attention was focused on identifying less sensitive replacements that were easier to produce. At the turn of the twentieth century a replacement for picric acid was developed, possibly the most famous explosive, trinitrotoluene, TNT (Figure 1.1b). With the benefits of the use of

explosives in warfare highlighted, after World War I, research programmes were initiated with the aim of synthesising and developing more powerful explosives, the results of which were primarily RDX (Figure 1.1c) and HMX (Figure 1.1d). These two explosives are still the most widely used explosives used today in current munitions.

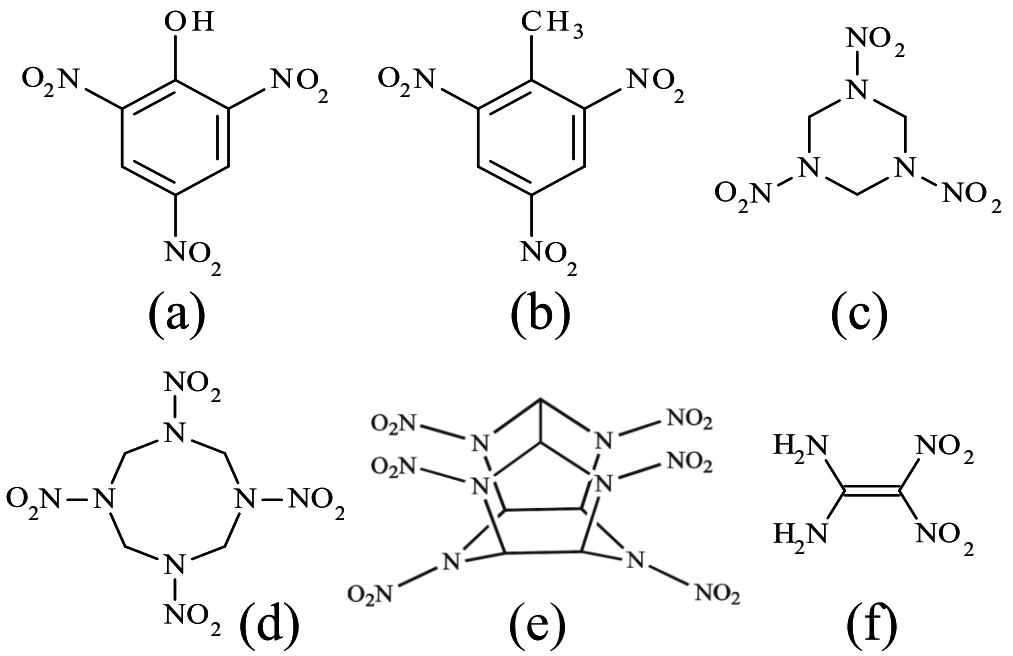

Figure 1.1 Molecular structures of secondary explosives. (a) picric acid, (b) TNT, (c) RDX, (d) HMX, (e) CL-20 and (f) FOX-7.

There are two main motivations that have driven recent developments in the synthesis of new energetic materials; (i) improving explosive power, and (ii) reducing the sensitivity to accidental initiation.

To improve the explosive power, materials synthesis has been more adventurous, with the design of polycyclic compounds, such as CL-20 (Figure 1.1e) and octanitrocubane. The explosive performance of CL-20 has been shown to exceed that of HMX.[5] This has been attributed to the high-energy density and inherent strain within the molecule (due to the caged structure). However, although these caged structures enhance the explosive performance, they are also sensitive to accidental initiation.

Examples of recently developed materials that display reduced sensitivity which are therefore less likely to be accidentally initiated are nitro-1,2,4-triazole-3-one (NTO), a heterocyclic compound with high energy and low sensitivity and FOX-7 (1,1-diamino-2,2-dinitroethene, Figure 1.1f) which displays a detonation velocity comparable to RDX but with dramatically reduced sensitivity (attributed to the high-degree of conjugation and hydrogen bonding within its crystal structure).[6] More comprehensive insights into the recent developments in the synthesis of energetic materials can be found in the reviews by Agrawal,[7] Pagoria *et al.*[8] and Badgujar *et al.*[9]

1.1.3 Properties

As alluded to in the previous section, a major goal in the development of energetic formulations, is the development of insensitive munitions, in order to improve safety. The aim is to design tailored energetic materials that have both specific functionality and a high threshold for accidental combustion or detonation. Properties of interest include: sensitivity to detonation, detonation velocity, physical properties (such as thermal stability, density, vibrational properties and crystal morphology *i.e.* polymorphism, which is described further in Section 1.4), and also the mechanical properties of the materials. In order to develop and fully understand these tailored energetic materials, one must not only know the properties of the components at standard temperatures and pressures, but to also know how these properties change under operational conditions (high temperatures and pressures). In consequence, it is imperative to understand the factors that affect the *deflagration-to-detonation transition* (DDT) of the energetic formulations.

1.2 Deflagration-to-Detonation Transition (DDT)

1.2.1 Deflagration

Once initiation has occurred, the behaviour of a reacting explosive depends on how fast the reaction front propagates through the material, the rate of deflagration. Deflagration is what is commonly known as burning or combustion. Deflagration propagates the reaction to adjacent areas in a material by thermal

conductivity, which can be by either conduction or convection. In conductive burning, material directly adjacent to an already burning region is heated by conduction to the point where it can also react. In convective burning, hot, high pressure gases carry heat away from burning regions, in the process heating previously unreacted material to the necessary temperature for reaction to occur. The limiting speed at which the burning front can propagate in a deflagrating reaction is the speed of sound in that material. Given the right conditions, it is possible for a reaction front to move faster than the sound speed, but this occurs by a different mechanism and is known as detonation.

1.2.2 Detonation

In a detonation, the reaction no longer propagates through thermal conductivity. Instead, it propagates by means of a supersonic shockwave through the material. The hot gaseous products from this reaction release enough energy to drive the shock front and so the detonation propagates through the material.

1.2.3 Factors Affecting the DDT

To understand the factors that influence the DDT, one must understand the factors that affect the rate of deflagration (or burning rate). The greatest influence on the burning rate is the external pressure, and this is the reason that confinement of explosives greatly increases the possible damage that they can do. When burning starts in a confined space, the hot gases evolved cause a rapid pressure increase, creating an overpressure between the reacted and unreacted material, which will in turn affect the properties of the material. As the pressure continues to increase rapidly, the burning rate also increases. Thus, in order to be able to effectively model the rate of deflagration, one must know how the properties of the energetic material are affected by high pressures. The way in which the heat generated by the reaction is partitioned within the system will directly affect the rate of deflagration, hence the effect of pressure on the heat capacities of energetic materials is of particular importance. Experimentally determining heat capacities under ambient conditions is relatively simple. On the other hand, measurement of heat capacities at elevated pressures is extremely difficult. An alternative is to use computational

methods to simulate the high-pressure structure and vibrational properties of energetic materials, and in turn predict the effect of pressure on the heat capacities.

1.3 Computational Chemistry – Density Functional Theory

1.3.1 History and Development

A description of the theoretical background to Density Functional Theory (DFT) is detailed later in this thesis (in Section 2.4). The fundamental aspects of the development of DFT are described here.

The evolution of the modern-day computational chemistry technique, DFT, began in 1926, with the creation of Thomas-Fermi theory.[10,11] Shortly after the introduction of the Schrödinger equation,[12] this theory was one of the earliest tractable schemes for solving the many-electron problem. Rather than the central variable being the electronic wavefunction, $\Psi(\boldsymbol{r}_1,\boldsymbol{r}_2,..\boldsymbol{r}_N)$ (as in the Schrödinger equation) the Thomas-Fermi model was an approximate method for finding the electronic structure using just the ground-state electron density, $\rho(\boldsymbol{r})$. However, due to the simplicity of the model, it suffers from many deficiencies, most prominently the model does not predict bonding interactions and also the electron-electron interaction is treated classically (Coulomb interaction), and thus the method does not take into account quantum effects, such as the exchange interaction.

In 1951, Slater developed the Xα scheme,[13] which combined the idea of the Thomas-Fermi model (describing electronic structure using just $\rho(\boldsymbol{r})$) with the orbital method proposed by Hartree,[14] to show how exchange effects could be treated (approximately) without much extra complication compared to the Hartree method. Later, Hohenberg and Kohn demonstrated the remarkable fact that there is a universal functional of the electron density, $\hat{E}[\rho(\boldsymbol{r})]$, which, if its form were known, could be used to obtain the exact ground state density and energy.[15] The modern version of density functional theory in use today is Kohn-Sham DFT (KS-DFT), which defines self-consistent equations that must be solved for a set of orbitals whose density, $\rho(\boldsymbol{r})$, is defined to be exactly that of the real system.

In KS-DFT the fully interacting system of *N*-electrons is mapped onto a fictitious auxiliary system of *N*-non-interacting "electrons" moving within an effective external (Kohn-Sham) potential, $V_{KS}(\boldsymbol{r})$, thereby coupling the electrons. The $V_{KS}(\boldsymbol{r})$ is comprised of three parts; an external potential, a classical Hartree (or Coulomb) potential and an exchange-correlation (XC) potential. The former two can be represented by equations and can be solved. However, this is not the case for the XC potential and so the XC contribution must be approximated, and the results obtained are only as good as the approximation used. This gives rise to the multitude of functionals available for use in DFT calculations; these functionals each propose different approaches to approximating the XC contribution. There are three main types of XC functionals, local density approximation (LDA) functionals, generalised gradient approximation (GGA) functionals and hybrid functionals, an explanation of each of these types and examples of popular functionals can be found in Section 2.4.3.

DFT has been an incredible success story; its low computational cost combined with useful accuracy, has made DFT a standard technique in most branches of chemistry and materials science. The importance of the development of DFT to the field of chemical research has been immense, underscored by the 1998 Nobel prize in Chemistry being jointly awarded to Walter Kohn ("*for his development of the density-functional theory*"),[16] and to John A. Pople ("*for his development of computational methods in quantum chemistry*").[17] Many current synthetic experimental investigations routinely include isolated molecule calculations, performed with a standard basis set and standard functional. Recent improvements in both computer hardware and computational electronic structure solution codes over the past decade have made it possible to perform systematic comparisons not only on isolated molecules, but also in the solid state. The breadth of applications that DFT finds uses is exemplified by Figure 1.2, which details the number of papers given by SciFinder Web when DFT is searched as a topic.[18] It shows that since the award of the Nobel prize, research incorporating the use of DFT has gone from strength to strength, in 2013 the number of papers will exceed 10,000.

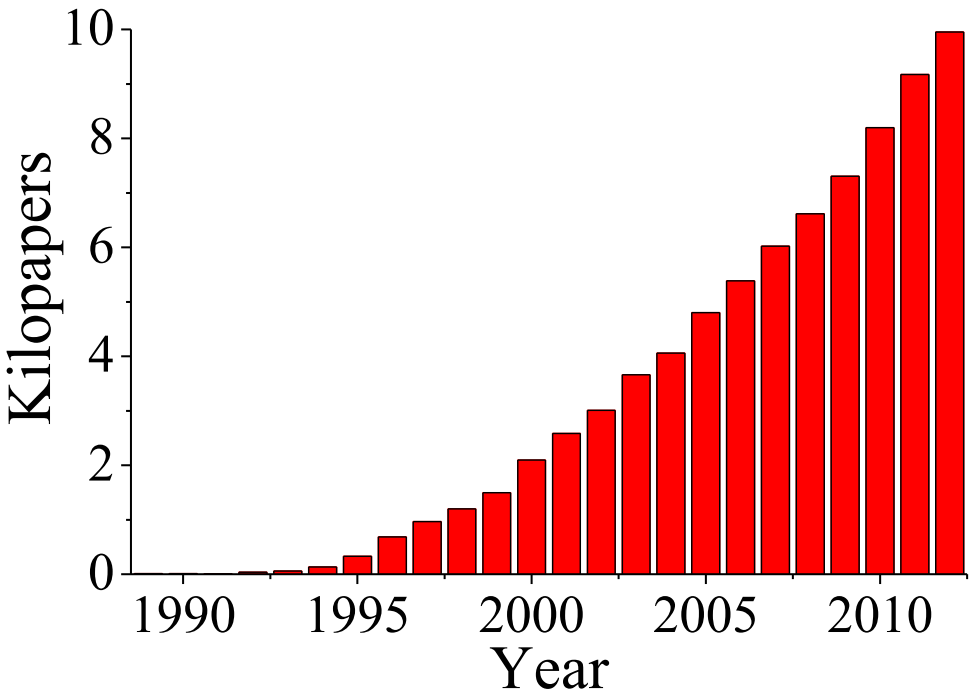

Figure 1.2 Numbers of papers (by year) when DFT is searched as a research topic in SciFinder.[18]

Despite its success, DFT in its current form (conventional DFT) has many limitations, including, but not limited to: too many different functionals; failures for strongly correlated systems; very slow for liquids (due to the large number of atoms required to simulate liquids); and failure to describe dispersion interactions. This final point is particularly important for the energetic materials of interest to this study (such as HMX, RDX, FOX-7 and CL-20) as the major component of the intermolecular interactions in these systems are van der Waals (vdW) and dispersion interactions.

1.3.2 Progress

As the use of DFT is a very active research field (Figure 1.2), and is utilised in such a broad range of applications, there have been numerous developments and thus one could not hope to comprehensively cover all of these developments. Consequently, only the developments most relevant to the research presented herein are given here; namely the major developments concerning the description of weak interactions (vdW and dispersion interactions).

A succinct way to describe the multitude of DFT-based dispersion corrections that have been developed, is to classify them into groups depending on the level of approximation each method makes in obtaining the long-range dispersion interactions. A very effective way of doing this was proposed in the excellent review by Klimeš and Michaelides; the "Stairway to Heaven".[19] A likeness to the proposed "Stairway to Heaven" is presented in Figure 1.3. Upon climbing each step of the stairway the level of approximation in the dispersion correction scheme is reduced and the overall accuracy is expected to increase, although the computational expense also increases for each step. The review article[19] gives an in-depth explanation of the corrections contained within each step. Here an overview of the most relevant schemes to this work (Steps 1 and 2) are given.

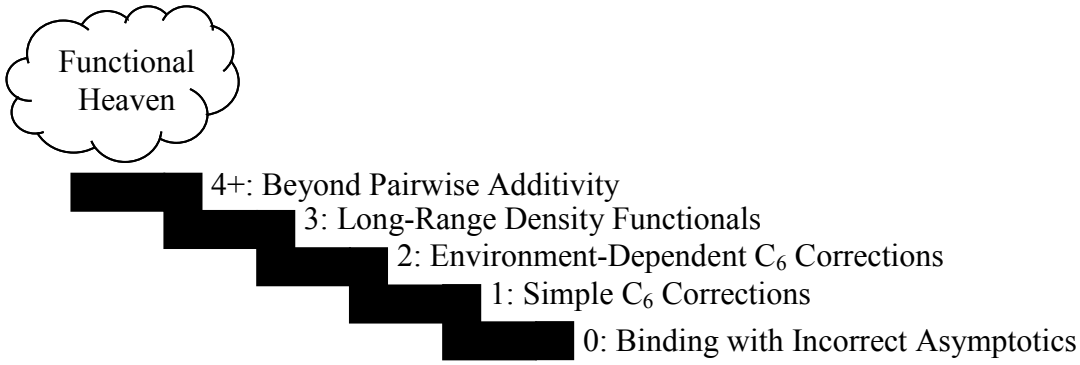

Figure 1.3 "Stairway to heaven" used to classify and group different DFT-based dispersion correction schemes.

Step 1: Simple C_6 Corrections

In these dispersion corrections the required asymptotic behaviour is achieved by the addition of an energy term which accounts for the long-range attraction. The total energy is then given by Equation 1.1:

$$E_{tot} = E_{KS-DFT} + E_{dispersion}$$

Equation 1.1

where $E_{KS\text{-}DFT}$ is the DFT energy computed with a given XC functional and the dispersion interaction contribution, $E_{dispersion}$ is given by Equation 1.2:

$$E_{dispersion} = \sum_{i \neq j} \frac{C_6^{ij}}{R_{ij}^6} f_{dmp}\left(R_{ij}\right)$$

Equation 1.2

where the dispersion coefficients, C_6^{ij} depend on the elemental pairs *i* and *j*. The dispersion contribution is assumed to be pair-wise additive within these approaches, and so the total dispersion contribution is therefore calculated as a sum over all pairs of atoms *i* and *j*. The dispersion-correction schemes on this step of the stairway use C_6 coefficients that are tabulated, isotropic and constant. Because of the simplicity and low computational cost of pairwise C_6/R^6 schemes of this type, they are widely used, but these schemes have at least 4 clear shortcomings which limit the accuracy one can achieve with these types of models (these are described in detail in Ref. 19).

Dispersion-corrections of this type are generally termed DFT-D, and perhaps the most successful DFT-D dispersion correction is the one published in 2006 by Grimme,[20] referred to in the wider literature as DFT-D2. This dispersion correction is utilised later in this thesis (termed G06, the internal CASTEP-code notation) and a theoretical derivation of the scheme is given in Section 2.4.9. Other parameterisations of the simple C_6 correction are also available, some of which are detailed in References 21-25.[21,22,23,24,25]

Step 2: Environment-Dependent C_6 Corrections

The next step on the stairway is very similar to the previous step, but instead of constant predetermined C_6 coefficients, dispersion-correction schemes on step 2 employ C_6 coefficients that vary with the environment of the atom. Some examples of these methods include the DFT-D3 scheme of Grimme,[26] the approach of Tkatchenko and Scheffler (which is briefly described later in section 2.4.9, termed TS in the CASTEP-code),[27] and the Becke-Johnson model (or sometimes referred to as the exchange-hole dipole moment, XDM).[28,29]

1.4 Polymorphism

The compounds studied in this thesis exhibit the phenomenon of polymorphism, *i.e.* the ability of a substance to exist in more than one crystalline state.[30] These different crystalline states (referred to as different polymorphs or forms) comprise the same molecules, but have different relative arrangements of the molecules in the solid state, i.e. different crystal structures. Polymorphism can greatly affect a range of properties such as melting/sublimation temperature, crystal

morphology, vibrational properties, heat capacity, conductivity, solubility, and density.[30,31]

An everyday example of polymorphism* is elemental carbon. Carbon can exist in numerous crystalline forms: the most common of which are diamond and graphite. The differences in their crystal structures create dramatic differences in their physical, electrical and chemical properties. Diamond is the hardest naturally occurring material known to man, it is electrically insulating, optically transparent and chemically inert. In contrast, graphite is black, very soft, electrically conducting and chemically reactive.

HMX (shown in Figure 1.1d) is an excellent illustrative example of the role played by polymorphism in energetic materials. Four crystalline phases have been structurally characterised, each of which can be crystallised from solution at ambient pressure, depending on the crystallisation rate and temperature.[32] They are denoted as the α,[33] β,[34,35] γ,[36] and δ forms,[37] the γ-form is not a true polymorph of HMX, it has been shown to be a hydrate.[33,36,37] Investigations have shown that the sensitivities to impact follow the order δ > γ > α > β.[38,39,40] The high risk of accidental detonation of the δ-, γ-, and α-forms means that only β-HMX is permitted in munitions used by the British armed forces.

Due to the marked differences in properties that polymorphism can manifest, much research on the effects of polymorphism in the field of materials chemistry has been undertaken, resulting in numerous reviews, a selection of which can be found in References 41-43.[41,42,43]

1.5 High Pressure

The field of high-pressure research has been of significant scientific interest for over a century. In 1905, P. W. Bridgman developed a pressure cell for compressing solids, which led to significant increases in the pressures attainable in controlled (static) high-pressure experiments. Initially pressures up to 0.7 GPa (~7000 atmospheres), could be achieved, but by the 1930s samples could be

* Technically as carbon is an element, the correct terminology is allotropy, however polymorphism and allotropy have exactly the same meaning.

routinely compressed to pressures of ~2 GPa.[44] Bridgman's tireless efforts never ceased and further technical innovation and development led to the introduction of opposed-anvil devices that had the capability of reaching pressures between 5 and 10 GPa.[45,46] With the development of this opposed anvil device, the pressures attainable represented a regime which had not previously been accessible. In these new accessible pressure regimes, well known substances started to behave in unexpected ways. A striking example is provided by water which upon compression crystallises into its ice-VI polymorph at ~1 GPa at room temperature, upon further compression the ice undergoes a further phase transition to ice-VII, this form of ice does not melt until 100 °C (at a pressure of 2.4 GPa).[47] For his pioneering work in the field of high-pressure research, in 1946 Bridgman received the Nobel prize in Physics.[48,49]

The most important breakthrough since Bridgman's work has been the invention of the diamond-anvil cell (DAC),[50] which is described in more detail in Section 3.1. This device not only facilitated the generation of higher pressures (pressures > 100 GPa can be reached in a DAC), but because diamonds are transparent to a wide range of electromagnetic radiation, allows visual observation, *in situ* diffraction (crystallography), and spectroscopic analysis of samples contained within the cell.

The types of apparatus described above are used to perform controlled static compression studies (such as those performed during the course of this work). With current pressure-cell technology, the highest pressures attainable are limited to a few Mbar (~300 GPa). An alternative method used in high-pressure studies is dynamic compression, where samples are compressed by means of a shock-wave through the material. Using these dynamic methods pressures in the terapascal regime (1000 GPa) have been reported recently.[51,52] However, these experiments are by no means routine and due to the nature of the experiments the pressure experienced by the material is only transient, and thus investigation of the change in structure and properties induced by the pressure is extremely challenging. A more comprehensive summary of the advances in high-pressure technology can be found in Katrusiak's excellent review.[53]

In high-pressure research, there is often use of more than one unit of pressure. The unit of gigapascals (GPa) will be employed in this work. The relationship between the three most common units are as follows:

1 GPa = 9869.2 atm = 10 kbar

1.6 Group Interaction Modelling

This work was partly funded by QinetiQ, and one of the objectives was to provide relevant data that can be used as input variables for Group Interaction Modelling (GIM).[54] GIM was originally developed as a technique for predicting the thermo-mechanical properties of polymers from fundamental parameters and chemical structure, QinetiQ uses an adaptation of this technique to predict the thermo-mechanical properties of energetic materials.

The general approach to determining mechanical and physical properties using the GIM is derived from the energy-volume potential well for their electronic interactions. The generality of the GIM method for polymers is based upon a mean-field approximation. This derives from a certain insensitivity of derived properties to minor changes in the potential well.

So we have for a particular material, values for the cohesive energy (lattice energy), E_{coh}, and the van de Waals' volume, V_w. The fundamental potential well takes the Lennard-Jones form as shown in Equation 1.3:

$$E = -E_{coh}\left[\left(\frac{V_0}{V}\right)^6 - 2\left(\frac{V_0}{V}\right)^3\right]$$

Equation 1.3

where $V_0 = 1.26V_w$. The negative sign in front of E_{coh} is to signify that the energy parameters are generally quoted as positive numbers. The repulsive and attractive long-range powers are 6-3 for the polymer materials rather than 12-6 as in the Lennard-Jones potential as a polymer can be considered as a 2-dimensional system of compliant van der Waals interactions perpendicular to a rigid chain. Thus, to a good approximation the volume is proportional to r^2 rather than r^3.

To get the potential well at any particular temperature we then need the thermal energy, H_T, and the configuration energy, H_c. The configurational energy for polymers is the fully amorphous $H_c = 0.107E_{coh}$ and for crystalline energetic materials such as RDX the fully crystalline $H_c = 0.04E_{coh}$ is used.[†] The thermal energy is the integral of the heat capacity contributions up to a given temperature. The total energy at temperature is then given by Equation 1.4.

$$E_T = -E_{coh} + H_c + H_T$$

Equation 1.4

The fundamental well also gives the thermal expansion coefficient which is used to calculate the equilibrium volume at a particular temperature, V_T. So, at temperature the potential well takes the Lennard-Jones form as shown in Equation 1.5.

$$E = -E_T\left[\left(\frac{V_T}{V}\right)^6 - 2\left(\frac{V_T}{V}\right)^3\right]$$

Equation 1.5

If one then wants to bring mechanical work into the procedure one has to integrate up the relevant arm of the potential well at the temperature at which the work is being done. If the mechanical work, $H_m = \int pdV$, and V_T has been corrected for volumetric strain due to imposed pressure a new local potential well can be calculated using the result of Equation 1.6 in Equation 1.5.

$$E_T = -E_{coh} + H_c + H_T + H_m$$

Equation 1.6

It is clear from this description that a key input parameter required to perform the GIM is the cohesive energy (lattice energy). Although the GIM method can predict heat capacities as a function of temperature, further improvement of the model can be obtained with knowledge of the effect of high pressures on the heat capacities. Furthermore information regarding the effect of mechanical work, *i.e.* the response of the structure to high pressures, would also be beneficial.

[†] The scaling parameters for the configuration energies are derived from empirical analysis of the thermal properties of a very large dataset of polymers. A complete explanation can be found in Section 1.2.6 of Reference 54.

1.7 General Aims and Outline of Research

In an effort to understand the factors that affect the deflagration-to-detonation transition (DDT) in energetic materials, combined high-pressure computational and experimental studies of several energetic materials have been performed. The aims of this work are as follows:

- to obtain complete ambient pressure vibrational information for a range of energetic materials by means of inelastic neutron scattering spectroscopy
- to investigate the suitability of the DFT-D functionals to predict accurately the high-pressure structure and vibrational properties of energetic materials
- to utilise the results of computational calculations and statistical thermodynamics to predict the effect of pressure on the heat capacities of energetic materials
- to provide relevant data that can used as input variables for Group Interactive Modelling (GIM)

Chapter 4 describes a comparison of different DFT dispersion corrections in calculating the high-pressure behaviour of crystalline ammonium perchlorate. A combined experimental and DFT-D study of various polymorphs of RDX is presented in Chapter 5. Chapter 6 explores the computationally calculated high-pressure behaviour of HMX and FOX-7. Chapter 7 illustrates that the DFT-D model can predict the compression behaviour of CL-20 and in turn be used to guide experimental endeavours. General conclusions and suggestions for future work can be found in Chapter 8.

1.8 References

1 Munroe, C. E.; Hall, C. in *Explosives in Metal Mining and Quarry Operations*, Wexford College Press, Palm Springs, **2003**.

2 Cooper, P. W. in *Explosives Engineering*, Wiley-VCH, New York, **1996**.

3 http://www.nasa.gov/returntoflight/system/system_SRB.html
4 Akhavan, J. in *The Chemistry of Explosives 3rd edition*, The Royal Society of Chemistry, Cambridge, **2011**.
5 Simpson, R. L.; Urtiew, P. A.; Ornellas, D. L.; Moody, G. L.; Scribner, K. J.; Hoffman, D. M. *Propell. Explos. Pyrotech.* **1997**, *22*, 249.
6 Bemm, U.; Ostmark, H. *Acta Cryst. C* **1998**, *54*, 1997.
7 Agrawal, J. P. *Prog. Energy Combust. Sci.* **1998**, *24*, 1.
8 Pagoria, P. F.; Lee, G. S.; Mitchell, A. R.; Schmidt, R. D. *Thermochim. Acta* **2002**, *384*, 187.
9 Badgujar, D. M.; Talawar, M. B.; Asthana, S. N.; Mahulikar, P. P. *J. Hazard Mater.* **2008**, *151*, 289.
10 Thomas, L. H. *Math. Proc. Cambridge Philos. Soc.* **1927**, *23*, 542.
11 Fermi, E. *Z. Phys. A: Hadrons Nucl.* **1928**, *48*, 73.
12 Schrödinger, E. *Phys. Rev.* **1926**, *28*, 1049.
13 Slater, J. C. *Phys. Rev.* **1951**, *81*, 385.
14 Hartree, D. R. *Proc. Cambridge Philos. Soc.* **1928**, *24*, 89.
15 Hohenberg, P.; Kohn, W. *Phys. Rev. B* **1964**, *136*, 864.
16 Kohn, W. *Rev. Mod. Phys.* **1999**, *71*, 1253.
17 Pople, J. A. *Rev. Mod. Phys.* **1999**, *71*, 1267.
18 *SciFinder Web*; Chemical Abstracts Service: Columbus, OH; DFT; CAPLUS; https://scifinder.cas.org (accessed April 26, 2013).
19 Klimeš, J.; Michaelides, A. *J. Chem. Phys.* **2012**, *137*, 120901.
20 Grimme, S. *J. Comput. Chem*. **2006**, *27*, 1787.
21 Zimmerli, U.; Parrinello, M.; Koumoutsakos, P. *J. Chem. Phys.* **2004**, *120*, 2693.
22 Neumann, M.; Perrin, M. *J. Phys. Chem. B* **2005**, *109*, 15531.
23 Ortmann, F.; Bechstedt, F.; Schmidt, W. G. *Phys. Rev. B* **2006**, *73*, 205101.
24 Jurečka, P.; Černý, J.; Hobza, P.; Salahub, D. R. *J. Comput. Chem.* **2007**, *28*, 555.
25 Bludský, O.; Rubeš, M.; Soldán, P.; Nachtigal, P. *J. Chem. Phys.* **2008**, *128*, 114102.
26 Grimme, S.; Antony, J.; Ehrlich, S.; Krieg, H. *J. Chem. Phys.* **2010**, *132*, 154104.
27 Tkatchenko, A.; Scheffler, M. *Phys. Rev. Lett*. **2009**, *102*, 073005.
28 Becke, A. D. *J. Chem. Phys.* **2005**, *122*, 064101.; Becke, A. D.; Johnson, E. R. *J. Chem. Phys.* **2005**, *122*, 154104.; Johnson, E. R.; Becke, A. D. *J. Chem. Phys.* **2005**, *123*, 024101.; Becke, A. D.; Johnson, E. R. *J. Chem. Phys.* **2005**, *122*, 154104.; Johnson, E. R.; Becke, A. D. *J. Chem. Phys.* **2005**, *123*, 154101.
29 Becke, A. D.; Johnson, E. R. *J. Chem. Phys.* **2007**, *127*, 154108.
30 Bernstein, J. in *Polymorphism in Molecular Crystals*, IUCr Monographs on Crystallograpy, Clarendon Press, Oxford, **2002**.
31 Giron, D. *Pharm. Sci. Technol. Today* **1998**, *1*, 191.
32 Cady, H. H.; Smith L. C. in *Studies on the Polymorphs of HMX*, LAMS-2652 TID-4500, **1961**.
33 Cady, H. H.; Larson, A. C.; Kromer, D. T. *Acta Cryst.*, **1963**, *16*, 617.

34 Eiland, P. F.; Pepinsky, R. *Z. Krystallogr.,* **1955**, *106*, 273.; Kohno, Y.; Maekawa, K.; Azuma, N.; Tsuchioka, T.; Hashizume, T.; Imamura, A. *Kogyo Kayaku*, **1992**, *53*, 227.
35 Choi, C. S.; Boutin, H. P. *Acta Cryst. B*, **1970**, *26*, 1235.
36 Main, P.; Cobbledick, R. E.; Small, R. W. H. *Acta Cryst. C*, **1985**, *41*, 1351.
37 Cobbledick, R. E.; Small, R. W. H. *Acta Cryst. B*, **1974**, *30*, 1918.
38 Palmer, S. J. P.; Field, J. E. *Proc. R. Soc. London Ser. A* **1982**, *383*, 399.
39 Herrmann, M.; Engel, W.; Eisenreich, N. *Propell. Explos. Pyrothech.* **1992**, *17*, 190.
40 Asay, B.; Henson, B. Smilowitz, L. Dickson, P. *J. Energ. Mater.* **2003**, *21*, 223.
41 Stahly, G. P. *Cryst. Growth Des.* **2007**, *7*, 1007.
42 Grepioni, F. *New J. Chem.* **2008**, *32*, 1657.
43 Bond, A. D. *Curr. Opin. Solid State Mater. Sci.* **2009**, *13*, 91.
44 Bridgman, P. W. in *The Physics of High Pressure*, Bell and Sons, London, **1931**.
45 Bridgman, P. W. *Proc. R. Soc.London Ser. A* **1950**, *203*, 1.
46 Bridgman, P. W. *Proc. Am. Acad. Arts Sci.* **1952**, *81*, 167.
47 Bridgman, P. W. *J. Chem. Phys.* **1937**, *5*, 964.
48 Bridgman, P. W. in *Nobel Lectures : Physics 1942 – 1962*, World Scientific, Singapore, **1998**.
49 http://www.nobelprize.org/nobel_prizes/physics/laureates/1946/
50 Merrill, L.; Bassett, W. A. *Rev. Sci. Instrum.* **1974**, 45, 290-294.
51 Nagao, H.; Nakamura, K. G.; Kondo, K.; Ozaki, N.; Takamatsu, K.; Ono, T.; Shiota, T.; Ichinose, D.; Tanaka, K. A.; Wakabayashi, K.; Okada, K.; Yoshida, M.; Nakai, M.; Nagai, K.; Shigemori, K.; Sakaiya, T.; Otani, K. *Phys. Plasmas* **2006**, *13*, 052705.
52 Eggert, J. H.; Hicks, D. G.; Celliers, P. M.; Bradley, D. K.; McWilliams, R. S.; Jeanloz, R.; Miller, J. E.; Boehly, T. R.; Collins, G. W. *Nat. Phys.* **2010**, *6*, 40.
53 Katrusiak, A. *Acta Cryst.* **2008**, *A64*, 135.
54 Porter, D. in *Group Interaction Modelling of Polymer Properties*, Marcel Dekker, New York, **1995**.

Chapter 2

Computational Chemistry

2 Computational Chemistry

2.1 The Schrödinger Equation

Quantum mechanical calculations are based on calculating a description of the electrons in a sample. To properly describe the behaviour of electrons, one must consider their wave-particle duality and the fact that an electron must follow the Heisenberg uncertainty principle. Thus the most complete description of an electron is a function that determines the probability of an electron being at a particular position. This is known as its wavefunction, from this, Schrödinger was able to derive an equation that allows the calculation of the energy of a system (E) from its wavefunction ($\Psi(\boldsymbol{r}_1,\boldsymbol{r}_2,..\boldsymbol{r}_N)$), using a formalism known as the Schrödinger equation, as shown in Equation 2.1:[1,2,3,4]

$$\hat{H}\Psi(\mathbf{r}_1,\mathbf{r}_2,..\mathbf{r}_N|\mathbf{R}_1,\mathbf{R}_2,..\mathbf{R}_N) = E\Psi(\mathbf{r}_1,\mathbf{r}_2,..\mathbf{r}_N|\mathbf{R}_1,\mathbf{R}_2,..\mathbf{R}_N)$$

Equation 2.1

The Hamiltonian operator, $\hat{H}$, operates on the wavefunction, returning the energy of the system multiplied by the wavefunction. It consists of the kinetic and potential energy terms of the system, namely:

(i) kinetic energy of the nuclei

(ii) kinetic energy of the electrons

(iii) potential energy of the nuclear-nuclear (coulombic) repulsion

(iv) potential energy of the electronic-electronic (coulombic) repulsion

(v) potential energy of the nuclear-electronic (coulombic) attraction

The full Hamiltonian operator can be expressed as given in Equation 2.2:

$$\hat{H} = -\sum_A \frac{\hbar^2}{2m}\nabla_A^2 - \sum_i \frac{\hbar^2}{2m_e}\nabla_i^2 + \sum_{A<B}\frac{e^2 Z_A Z_B}{4\pi\varepsilon_0 r_{AB}} + \sum_{i<j}\frac{e^2}{4\pi\varepsilon_0 r_{ij}} - \sum_{A,i}\frac{e^2 Z_A}{4\pi\varepsilon_0 r_{iA}}$$

Equation 2.2

where i and j represent different electrons, A and B different nuclei, $\hbar$ is Planck's constant divided by 2π, m_n is the mass of a nucleus, ∇ is the Laplacian operator, m_e is the mass of an electron, e is the charge of an electron, Z is the charge of a particle, ε_0 is the permittivity of free space, r_{AB} is the distance between particles A and B. As it is impossible to solve the Schrödinger equation, (except for very simple systems such as H_2^+) due to inter-electron terms, approximations need to be made, thus allowing approximate solutions to the Schrödinger equation to be obtained.[1,5]

2.2 The Born-Oppenheimer Approximation

The most important approximation is the Born-Oppenheimer approximation. Known as the 'short-cut' in quantum mechanics, it assumes that as the nuclei are much heavier than the electrons, the electrons travel much faster than the nuclei, so the electrons 'see' the nuclei as stationary. Thus it is possible to treat the nuclear and electronic degrees of freedom separately, thereby separating the nuclear and electronic wavefunctions.

It follows that the $-\sum_A \frac{\hbar^2}{2m_n}\nabla_A^2$ term becomes negligible since $-\sum_A \frac{\hbar^2}{2m_n}\nabla_A^2$ is smaller than $-\sum_i \frac{\hbar^2}{2m_e}\nabla_i^2$ by a factor of $\frac{m_n}{m_e}$. Also the $\sum_{A<B} \frac{e^2 Z_A Z_B}{4\pi\varepsilon_0 r_{AB}}$ term is constant and can be easily calculated using Coulomb's law. Thus the Born-Oppenheimer approximation simplifies the Hamiltonian operator as shown in Equation 2.3:

$$\hat{H} = -\sum_i \frac{\hbar^2}{2m_e}\nabla_i^2 + \sum_{i<j} \frac{e^2}{4\pi\varepsilon_0 r_{ij}} - \sum_{A,i} \frac{e^2 Z_A}{4\pi\varepsilon_0 r_{iA}}$$

Equation 2.3

this greatly simplifies the Schrödinger equation, which now only contains electronic terms.[6] However, there is still one major difficulty that prevents this electronic Schrödinger equation from being exactly solved – the electron-electron potential energy term. This term (the second component the Hamiltonian operator in Equation 2.3) can only be solved exactly for one electron systems due to the effects of two electron behaviours: exchange and correlation. Correlation arises from the fact that electrons repel each other according to Coulomb's law (with repulsion energy

$\frac{e^2}{4\pi\varepsilon_0 r_{ij}}$), thus the motion of one electron affects the motions of all others in the system. Exchange arises from the change in energy of the system when the spatial coordinates of two electrons are interchanged. Thus, computational chemistry calculations aim to approximate these exchange-correlation functionals of the Hamiltonian so that the electronic Schrödinger (Equation 2.4) equation can be (approximately) solved.

$$\hat{H}\Psi(\mathbf{r}_1,\mathbf{r}_2,..\mathbf{r}_N) = E\Psi(\mathbf{r}_1,\mathbf{r}_2,..\mathbf{r}_N)$$

Equation 2.4

2.3 Hartree-Fock Theory

The simplest *ab initio* method is the Hartree-Fock (HF) scheme. As well as the Born-Oppenheimer approximation, the main assumption made in HF theory is that electron correlation is completely ignored. This is implemented by allowing each electron to move in a uniform electric field created by all of the other electrons present in the sample, thus the specific correlation of electronic-electronic repulsion is not taken into account, and instead its average effect is used. On the other hand, electron exchange is treated exactly in HF theory by imposing the condition of an anti-symmetric wavefunction.

The starting point for HF calculations is a set of approximate one electron wavefunctions – *i.e.* the orbitals. For molecular calculations the approximate one electron wavefunctions are formed from a linear combination of atomic orbitals (LCAO).[7,8] These orbitals are described by the basis set used (see Section 2.4.4).

The ground state wavefunction and energy may be found by searching all possible wavefunctions for one that minimises the total energy. In HF theory the ansatz is a Hessian matrix known as the Slater determinant, shown in Equation 2.5;[9]

$$\Psi(\mathbf{r}_1,\mathbf{r}_2,..\mathbf{r}_N)=\frac{1}{\sqrt{N!}}\begin{vmatrix}\chi_1(\mathbf{r}_1) & \chi_2(\mathbf{r}_1)..\chi_N(\mathbf{r}_1)\\ \chi_1(\mathbf{r}_2) & \chi_2(\mathbf{r}_2)..\chi_N(\mathbf{r}_2)\\ : & : & :\\ \chi_1(\mathbf{r}_N) & \chi_2(\mathbf{r}_N)..\chi_N(\mathbf{r}_N)\end{vmatrix}$$

Equation 2.5

where $\chi_m(\boldsymbol{r}_N)$ is the m[th] spin-orbital (atomic orbital) that encompasses both position in Cartesian space and spin, i.e. $(\mathbf{r}_N)=\left(x,y,z,\uparrow or\downarrow\right)$, of the N[th] electron in the system. This determinant trivially satisfies both the need for asymmetry in the exact solution of the wavefunction, and the Pauli Exclusion Principle. For example, the Slater determinant for a two electron system can be formulated as given in Equation 2.6:

$$\Psi(\mathbf{r}_1,\mathbf{r}_2)=\frac{1}{\sqrt{2}}\left(\chi_1(\mathbf{r}_1)\chi_2(\mathbf{r}_2)-\chi_2(\mathbf{r}_2)\chi_1(\mathbf{r}_1)\right)$$

Equation 2.6

thus, if two electrons with the same spin are in the same place (i.e. $\boldsymbol{r}_1=\boldsymbol{r}_2$) the wavefunction (hence the probability of finding both electrons in the same place) becomes zero.

Overall HF theory simplifies the very complicated *N*-electron system into *N* one-electron Schrödinger equations, which are then solved to give one overall solution. As stated previously the ansatz in HF calculations is the Slater determinant, the equations are then solved in an iterative process using a self-consistent field (SCF). The calculated orbitals are gradually improved until the difference in the calculated system energy meets convergence criterion. Even though HF calculations completely ignore electron correlation, the theory can still perform extremely well, typically calculating overall system energies to within 10% of the most accurate computational strategies, *i.e.* coupled cluster methods. Nevertheless, disregarding correlation significantly affects the calculation of properties of the system, thus post-HF methods (e.g. Møller-Plesset Perturbation theory and coupled cluster methods) as well as other theories (such as DFT, see Section 2.4) have been developed to try to account for both exchange and correlation behaviour.

2.4 Density Functional Theory

In contrast to the HF method, density functional theory (DFT) takes another approach to obtain the electronic structure. Rather than deriving the E directly from calculating Ψ, DFT calculates the energy directly from the electron density, ρ. Obviously an immediate advantage of DFT over HF methods is that the electron density is an experimentally observable quantity, whereas the wavefunction is not.[‡,10]

2.4.1 Hohenberg-Kohn Theorems

One can consider the nuclear-electron term of the Hamiltonian operator in Equation 2.3 as the electrons interacting with an external potential, $\hat{V}_{ext}$ (created by the nuclei in the system) that can be defined by Equation 2.7 :

$$\hat{V}_{ext} = -\sum_{A,i} \frac{e^2 Z_A}{4\pi\varepsilon_0 r_{iA}}$$

Equation 2.7

thus the remainder of the Hamiltonian in Equation 2.3 can be collated into the electronic Hamiltonian, $\hat{F}$, given by Equation 2.8:

$$\hat{F} = -\sum_i \frac{\hbar^2}{2m_e}\nabla_i^2 + \sum_{i<j} \frac{e^2}{4\pi\varepsilon_0 r_{ij}}$$

Equation 2.8

DFT is made possible by implementing the two Hohenberg-Kohn theorems:[11]

Hohenberg-Kohn 1

The electron density determines the external potential; hence it uniquely determines the Hamiltonian operator, and thus the energy of the system. The electron density depends on only 3 spatial coordinates, thus this theorem lays the groundwork to reduce the many-body problem of N electrons with $3N$ spatial coordinates to a problem with just 3 spatial coordinates, by use of functionals of the electron density.

‡ An excellent review focusing on the fundamental general aspects of DFT (for a general audience) can be found in Ref. 10.

Thus the functional $\hat{F}[\rho(\boldsymbol{r})]$, where $\rho(\boldsymbol{r})$ is the electron density of the system can be defined in bra-ket notation by Equation 2.9.

$$\hat{F}[\rho(\boldsymbol{r})] = \left\langle \Psi \middle| \hat{F} \middle| \Psi \right\rangle$$

Equation 2.9

This functional is a universal functional in the sense that it has the same dependence on the electron density for any system, regardless of the external potential concerned. However, the exact electron density dependence of this functional is unknown. Thus the energy functional can be defined for a given (arbitrary) external potential, $V(\boldsymbol{r})$, by Equation 2.10.

$$\hat{E}[\rho(\boldsymbol{r})] = \hat{F}[\rho(\boldsymbol{r})] + \int V(\boldsymbol{r})\rho(\boldsymbol{r}).\mathrm{d}\boldsymbol{r}$$

Equation 2.10

Or Equation 2.10 can be represented in terms of the ground state many-body wavefunction as Equation 2.11.

$$\hat{E}[\rho(\mathrm{r})] = \left\langle \Psi \middle| \hat{H} \middle| \Psi \right\rangle$$

Equation 2.11

Hohenberg-Kohn 2

The functional that delivers the ground state energy of the system, delivers the lowest energy if and only if the input density is the true ground state density.

These theorems demonstrate the remarkable fact that there is a universal functional, $\hat{E}[\rho(\boldsymbol{r})]$ which if we knew its form, could be used to obtain the exact ground state density and energy.

2.4.2 Kohn-Sham Equations

Although these two Hohenberg-Kohn theorems prove the existence of a universal functional, they do not give any idea as to the nature of the functional, or how to actually calculate the ground state electron density. The result is that once

again we are back to the realm of using approximations to simplify a complex problem, but now, unlike (post) Hartree-Fock based methods, we have no systematic route to improve upon those approximations.

Within the formalism of DFT, the equations equivalent to the one-electron Schrödinger equations are known as the Kohn-Sham equations. Here the fully interacting system of *N*-electrons is mapped onto a fictitious auxiliary system of *N*-non-interacting "electrons" moving within an effective external (Kohn-Sham) potential, $V_{KS}(\boldsymbol{r})$, thereby coupling the electrons. The single-particle Kohn-Sham orbitals are then constrained to yield the same ground state electron density as that of the fully-interacting system, so the Hohenberg-Kohn theorems are still valid. Hence, the constraint imposed on the system (fixed particle number) is given in Equation 2.12.

$$\int \delta\rho(\boldsymbol{r})\,\mathrm{d}\boldsymbol{r} = 0$$

Equation 2.12

Variation of the energy functional in Equation 2.10 with respect to electron density subject to the constraint imposed in Equation 2.12 leads to the fundamental statement of DFT, known as the DFT variational theorem:

$$\delta\left\{F[\rho(\boldsymbol{r})] + \int V(\boldsymbol{r})\rho(\boldsymbol{r}).\mathrm{d}\boldsymbol{r} - \mu\int\left(\rho(\boldsymbol{r}).\mathrm{d}\boldsymbol{r} - N\right)\right\} = 0$$

Equation 2.13

where the Lagrange multiplier associated with the constraint condition, μ, is given by Equation 2.14.

$$\mu = \frac{\delta\hat{F}[\rho(\boldsymbol{r})]}{\delta\rho(\boldsymbol{r})} + V_{ext}(\boldsymbol{r})$$

Equation 2.14

Kohn and Sham then separated $\hat{F}[\rho(\boldsymbol{r})]$ into three parts:

$$\hat{F}[\rho(\boldsymbol{r})] = \hat{T}_s[\rho(\boldsymbol{r})] + \hat{E}_H[\rho(\boldsymbol{r})] + \hat{E}_{xc}[\rho(\boldsymbol{r})]$$

Equation 2.15

where $\hat{T}_s[\rho(\boldsymbol{r})]$ is the kinetic energy of a non-interacting gas (of density $\rho(\boldsymbol{r})$), $\hat{E}_H[\rho(\boldsymbol{r})]$ is the classical electrostatic (Hartree or Coulombic) energy, and $\hat{E}_{xc}[\rho(\boldsymbol{r})]$ is an implicit definition of the exchange-correlation energy of the system. Using the separation in Equation 2.15 the Lagrange multiplier becomes:

$$\mu = \frac{\delta \hat{T}[\rho(\boldsymbol{r})]}{\delta \rho(\boldsymbol{r})} + V_{KS}(\boldsymbol{r})$$

Equation 2.16

in which the Kohn-Sham potential is given by Equation 2.17.

$$V_{KS}(\boldsymbol{r}) = V_{ext}(\boldsymbol{r}) + V_H(\boldsymbol{r}) + V_{xc}(\boldsymbol{r})$$

Equation 2.17

The Hartree potential ($V_H(\boldsymbol{r})$) is given by Equation 2.18 and the exchange-correlation potential ($V_{xc}(\boldsymbol{r})$) by Equation 2.19.

$$V_H(\boldsymbol{r}) = \frac{\delta \hat{E}_H[\rho(\boldsymbol{r})]}{\delta \rho(\boldsymbol{r})} = \frac{\delta}{\delta \rho(\boldsymbol{r})} \frac{1}{2} \int\int \frac{\rho(\boldsymbol{r})\rho(\boldsymbol{r})'}{\left|\boldsymbol{r} - \boldsymbol{r}'\right|} \mathrm{d}\boldsymbol{r}\, \mathrm{d}\boldsymbol{r}' = \int \frac{\rho(\boldsymbol{r})'}{\left|\boldsymbol{r} - \boldsymbol{r}'\right|} \mathrm{d}\boldsymbol{r}'$$

Equation 2.18

$$V_{xc}(\boldsymbol{r}) = \frac{\delta \hat{E}_{xc}[\rho(\boldsymbol{r})]}{\delta \rho(\boldsymbol{r})}$$

Equation 2.19

The Lagrange multiplier in Equation 2.16 is precisely the same equation which would be obtained for a non-interacting system of particles moving in an external potential $V_{KS}(\boldsymbol{r})$. The ground state electron density is found by solving the one-electron Schrödinger equations in a self-consistent way:

$$\left[-\frac{1}{2}\nabla^2 + V_{KS}(\boldsymbol{r}) \right] \varphi_i(\boldsymbol{r}) = \varepsilon_i \varphi_i(\boldsymbol{r})$$

Equation 2.20

where ε_i corresponds to the energy eigenvalues of the single particle states, φ_i is the single particle wavefunction for particle *i* and the charge density is constructed from the Kohn-Sham orbitals as shown in Equation 2.21.

$$\rho(\boldsymbol{r}) = \sum_{i=1}^{N} \varphi_i(\boldsymbol{r})^* \varphi_i(\boldsymbol{r})$$

Equation 2.21

The total many-electron wavefunction is then constructed from the Slater determinant of the Kohn-Sham orbitals. Thus, the Kohn-Sham formulation transforms the *N*-body problem into *N* single-body problems, coupled via the Kohn-Sham potential $V_{KS}(\boldsymbol{r})$.

The only remaining problem is the fact that the Kohn-Sham potential has three parts as described in Equation 2.17; $V_{ext}(\boldsymbol{r})$ and $V_H(\boldsymbol{r})$ can be exactly calculated, however, the form of $V_{xc}(\boldsymbol{r})$ or rather $\hat{E}_{xc}[\rho(\boldsymbol{r})]$ is not known exactly. Thus in DFT, approximations of this exchange-correlation functional are made, giving rise to the series of functionals available for use in DFT (some key functionals are described in Section 2.4.3). Contrary to HF theory, in these functionals correlation is not ignored but the functionals try to approximate both exchange and correlation effects. These DFT functionals cannot be systematically improved until convergence in molecular properties is met, thus functionals are generally chosen by reputation, and one must search the literature to see what results have been obtained for different functionals studying systems similar to the system of interest.

2.4.3 DFT Functionals

Based on the early work of Thomas and Fermi,[12,13] the simplest functional is the Local Density Approximation (LDA). It assumes that the density can be treated locally as a uniform electron gas; the exchange-correlation energy at each point in the system is the same as that of a homogenous electron gas of the same density.[14] Thus the functional generally provides good results for systems where the electron density is fairly constant, such as solid-state metals. Even though this is a very simple approximation, the LDA has proved to be a remarkably successful one. Although the LDA generally underestimates the exchange energy and overestimates the correlation energy, the success of LDA is largely due to the fact that these errors tend to cancel.

The LDA uses the exchange-correlation energy for the uniform electron gas at every point in the system regardless of the homogeneity of the real charge density. For non-uniform charge densities the exchange-correlation energy can deviate significantly from the uniform result. This deviation can be expressed in terms of the gradient and higher spatial derivatives of the total charge density. The Generalised Gradient Approximation (GGA) uses the gradient of the charge density (as well as the actual charge density) to correct for this deviation. For use with molecular systems where the electron density is a rapidly changing property, such as those being studied in this work, a variety of different GGA functionals have been developed, employing different approximations. The most widely used GGA functionals are PBE (Perdew, Burke, and Ernzerhof[15,16]), PW91 (Perdew and Wang[17,18]) and BLYP (Becke 88 exchange functional,[19] and correlation functional of Lee, Yang, and Parr[20,21]).

Hybrid functionals are a further extension of the HF and DFT theories. These functionals are used for larger systems, where post-HF methods would take a very long time to compute, and hence are too expensive. The hybrid functionals make more approximations and some parameters include empirical data from experiments. These greater numbers of approximations increase the overall error, but reduce the computational time, thus larger basis sets may be used for the same computational cost with respect to pure HF method to obtain a more accurate result. Hybrid functionals are developed to suit a specific purpose, and so they are derived for a specific class of molecules. Functionals that work well for one class of molecules may not work for a different class. A common hybrid functional is B3LYP; it is obtained by adding gradient corrections to the LDA method - specifically the three parameter exchange correction of Becke,[§] and the aforementioned correlation function of Lee, Yang and Parr.[20]

2.4.4 Basis Sets

As well as the functional, a basis set is also needed to perform a calculation. The basis set is a set of functions, a linear combination of these functions are

[§] The three parameter exchange correction of Becke contains contributions from the LDA,[14] the Becke 88 GGA functional,[19] and Hartree-Fock exchange.[7]

combined providing a representation of the wavefunctions. The larger the basis set used, the more accurately the wavefunctions can be described. Thus as the finite basis set is expanded towards an infinite set of functions, the error of the approximation is minimised and the solution will converge towards the 'real' solution to the Schrödinger equation. However, as the basis set is increased, the computation power needed increases and so the time taken for calculation increases. Therefore a trade-off exists between the accuracy and computational cost.

There are two main types of basis set; localised and delocalised. If the model to be studied is periodic (*i.e.* a solid) then delocalised basis sets tend to be used. Localised basis sets are better applied for gas phase (single-molecule) models. As only crystalline materials are studied in this work (and hence utilising delocalised basis sets), localised basis sets will not be described here.

2.4.5 Bloch's Theorem

In a delocalised basis set, the electrons are considered nearly free particles, thus are not confined to the region of space around atomic nuclei. Hence the behaviour of the electrons can be considered sinusoidal and the wavefunction can be represented as a linear combination of plane-waves, expressed by Bloch's theorem, which states that the energy eigenfunction for a system of particles placed in a periodic potential may be written as the product of a plane wave envelope function and a periodic wavefunction, $u_j(\boldsymbol{r})$, that has the same periodicity of the potential, (*i.e.* $u_j(\boldsymbol{r}+\boldsymbol{l})=u_j(\boldsymbol{r})$ where $\boldsymbol{l}$ is the length of the unit cell). The one electron wavefunctions can now be represented by Equation 2.22:

$$\varphi_{j,\mathbf{k}}(\mathbf{r}) = u_{j,\mathbf{k}}(\mathbf{r})e^{i\mathbf{k}\cdot\mathbf{r}}$$

Equation 2.22

In Equation 2.22 *i* is the band index, and $\boldsymbol{k}$ is a wave vector within the first Brillouin zone of the reciprocal lattice. Since $u_j(\mathbf{r})$ is a periodic function, it can be expressed in terms of the Fourier series given in Equation 2.23.[22]

$$u_{j,\mathbf{k}}(\mathbf{r}) = \sum_{\mathrm{G}} c_{j,\mathbf{G}} e^{i\mathbf{G}\cdot\mathbf{r}}$$

Equation 2.23

Where $\boldsymbol{G}$ represents the reciprocal lattice vectors and $c_{j,\boldsymbol{G}}$ are plane wave expansion coefficients. Therefore the electron wavefunctions may be written as a linear combination of plane waves, as given in Equation 2.24:

$$u_{j,\boldsymbol{k}}(\boldsymbol{r}) = \sum_{\boldsymbol{G}} c_{j,\boldsymbol{k}+\boldsymbol{G}} e^{i(\boldsymbol{k}+\boldsymbol{G})\cdot\boldsymbol{r}}$$

Equation 2.24

Thus in a DFT calculation, the coefficients are optimised throughout the calculation (in a SCF cycle) until coefficients are found that minimise the energy and thus the electronic ground state is reached.

Plane waves are a simple way of representing electronic wavefunctions, hence are fast to compute (due to the implementation of pseudopotentials – which is described further in the next section). In principle, the plane wave series represented in Equation 2.24 is infinite, however so that this series can be handled computationally, the kinetic energy of the plane wave coefficients are truncated (thus achieving a finite basis set) by means of a plane wave kinetic energy cut-off, E_{cut}, given in Equation 2.25.

$$E_{cut} = \frac{\hbar^2}{2m}|\boldsymbol{k} + \boldsymbol{G}|^2$$

Equation 2.25

Thus plane waves offer as complete a basis set as is necessary in a continuous fashion, simply by injecting more plane-waves into the 'box' by increasing E_{cut}. The E_{cut} needed for each different system to be studied is established by means of convergence testing (progressively increasing the E_{cut} until the convergence criterion is reached on three successive calculations). A diagram illustrating how a higher number of plane waves generates a more accurate representation of the actual electron density can be seen in Figure 2.1.

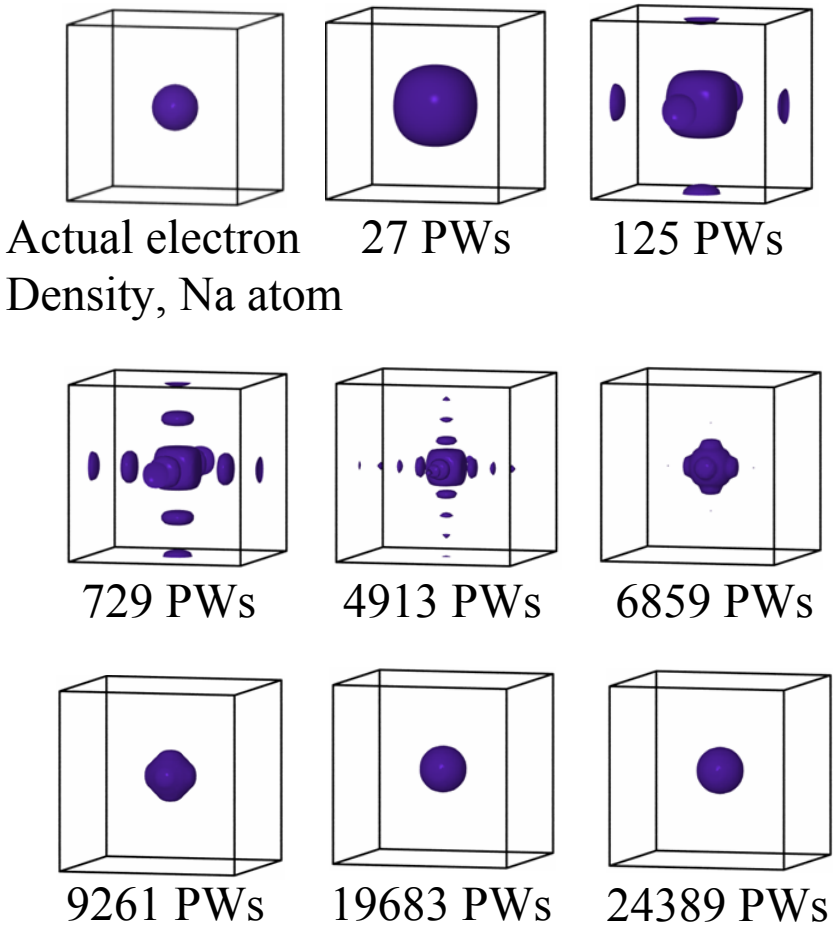

Figure 2.1 Figure illustrating how higher numbers of plane waves (PWs) build up towards a better definition of the electron density of a sodium atom in a box.[23]

2.4.6 Pseudopotentials

As a plane wave basis set is delocalised, it treats all areas of space equally, and thus is independent of the type of crystal. This last point represents a possible problem; as the plane-waves describe the entire 'box' (both atomic positions and 'free' space), a great number of plane waves are needed to correctly describe the total electron density of an atom. However, an innovative simplification has been developed to reduce the number of plane-waves needed. This simplification is the implementation of pseudopotentials. These replace the complicated effects of the motion of the core, non-valence electrons (which negligibly contribute to the physical properties of molecules, and require high wavenumber plane waves to describe accurately their electron density) with a smooth effective potential which still accurately represents the valence region (see Figure 2.2). Thus the total number

of plane-waves needed to represent the wavefunction is significantly reduced (by several orders-of-magnitude compared to the numbers of plane-waves required for all-electron methods), with no discernible reduction in computational accuracy.[24]

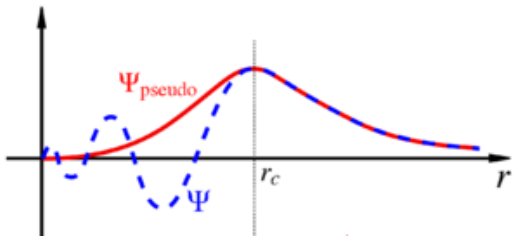

Figure 2.2 Schematic representation of the pseudopotential concept. Ψ all electron wavefunction, Ψ_{pseudo} pseudopotential representation of wavefunction. r_c represents the cut-off radius, after which the all electron and pseudopotential wavefunctions become identical.[25]

2.4.7 Periodic Boundary Conditions

Periodic boundary conditions are used to simulate a large system (an infinite crystal lattice) by modelling a small part that is far from its edge (a single crystallographic unit cell). Periodic boundary conditions replicate the simulation cell to infinity in all directions, by rigid translation in all three Cartesian directions. If an atom in the simulation cell has position $\boldsymbol{r}_i$ the imposed periodic boundary conditions produce mirror images of the atom at positions defined by Equation 2.26:

$$\boldsymbol{r}_{i,image} = \boldsymbol{r}_i = \mathrm{l}a + \mathrm{m}b + \mathrm{n}c$$

Equation 2.26

Where a, b and c are the lattice vectors of the unit cell, and l, m and n are any integer values from +∞ to -∞. Thus, each particle in the simulation cell is interacting not only with other particles in the computational box, but also with their images in the adjacent boxes. Hence, although it looks as though computations are only being carried out on a single unit cell, the structure and properties being calculated are actually for the bulk infinite crystal lattice.

2.4.8 K-Points

Following on from Bloch's theorem, given that each electron occupies a state of definite $\boldsymbol{k}$, the infinite number of electrons within the solid gives rise to an infinite number of k-points. At each k-point, only a finite number of the available

energy levels will be occupied. Thus one only needs to consider a finite number of electrons at an infinite number of k-points. This may seem to be replacing one infinity (number of electrons) with another one (number of k-points) to little discernible advantage. However, one does not need to consider all of these k-points; rather, since the electron wavefunctions will be almost identical for values of $\boldsymbol{k}$ that are sufficiently close, one can represent the wavefunctions over a region of reciprocal space by considering the wavefunction at a single k-point. It is therefore sufficient to consider the electronic states at a finite number of k-points in order to determine the ground state electron density of the solid. The net effect of Bloch's theorem therefore has been to change the problem of an infinite number of electrons to one of considering only the number of electrons in the unit cell at a finite number of k-points chosen so as to appropriately sample the Brillouin zone. An example of where these k-points are can be seen in Figure 2.3.

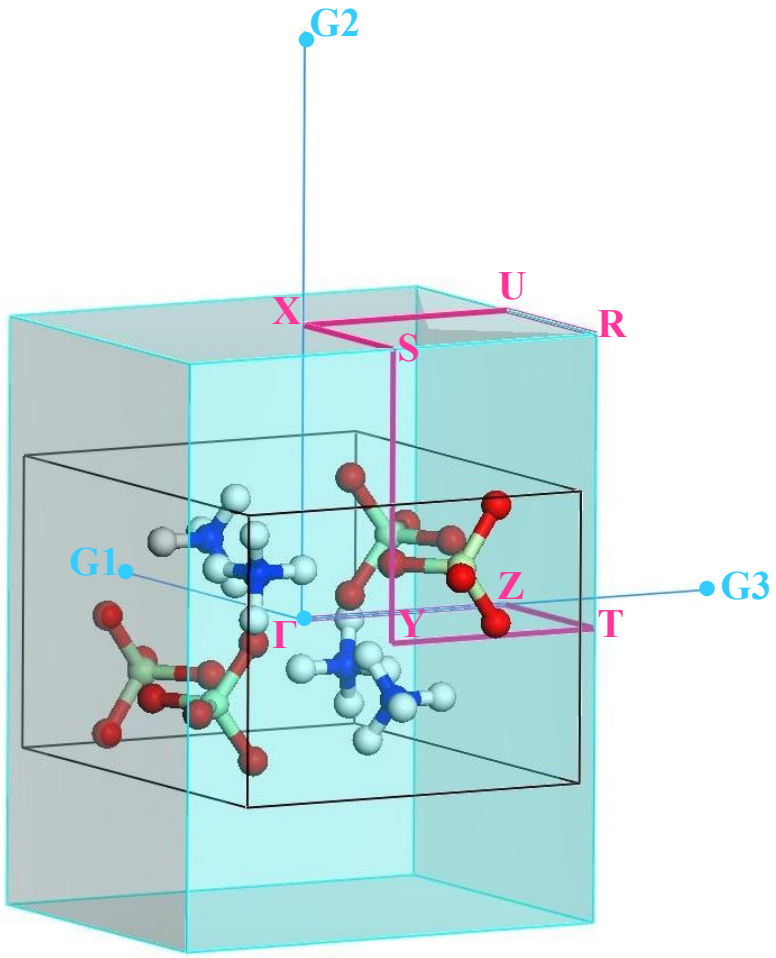

Figure 2.3 Example real-space unit cell (black) and Brillouin zone (light blue) for ammonium perchlorate. The pink line shows the Brillouin zone path with the high-symmetry k-points (Γ, Z, T, Y S, X, U and R) labelled. Points G1, G2 and G3 are the gamma points in the next successive Brillouin zones in all 3-dimensions (joined to the Γ point by the reciprocal lattice vectors).

K-point sampling of the Brillouin zone is obtained by using a Monkhorst-Pack (M-P) grid, which is an unbiased method of choosing a set of k-points.[26] An M-P grid is a rectangular grid of points with fractional coordinate dimensions M_x x M_y x M_z spaced evenly throughout the Brillouin zone. The larger the dimensions of the grid, the finer and more accurate will be the sampling.

2.4.9 DFT-D Dispersion Corrections

Perhaps the best-known deficiency of the GGA-DFT methods is that they cannot describe long-range electron correlations that are responsible for dispersion interactions.[27] This is due to the local nature of density-functionals, which renders

them incapable of treating the long-range electron correlations necessary to capture the all-important dispersive interactions between discrete molecules in the condensed phase. Development of augmented DFT methods capable of describing these dispersion interactions represents an active area of current interest. In recent years, several different types of methods have been proposed. These range from modifications of the exchange-correlation functionals to describe non-local dispersion interactions,[28,29] to dispersion-corrected atom-centered potentials (DCACPs),[30,31] and dispersion-corrected DFT (DFT-D) methods.[32,33,34,35]

In this work two of the dispersion-corrected DFT (DFT-D) methods developed have been utilised, the 2006 semi-empirical method proposed by Stefan Grimme[32] and a parameter-free non-empirical method developed by Tkatchenko & Scheffler[33]. In the CASTEP code exploited throughout this work these dispersion corrections are termed G06[32] and TS[33].

$$E_{DFT-D} = E_{KS-DFT} + E_{dispersion}$$

Equation 2.27

The G06 dispersion correction method developed by Grimme[32] includes a dispersion correction that is explicitly parameterised by introducing damped atom-pairwise corrections of the form C_6/R^6. The total dispersion-corrected energy of the system is given by Equation 2.27, where $E_{KS\text{-}DFT}$ is the usual Kohn-Sham energy of DFT as obtained from the chosen density functional. In the G06 functional, $E_{dispersion}$ is an empirical dispersion correction given by Equation 2.28.

$$E_{dispersion} = -s_6 \sum_{i=1}^{N_{at}-1} \sum_{j=i+1}^{N_{at}} \frac{C_6^{ij}}{R_{ij}^6} f_{dmp}\left(R_{ij}\right)$$

Equation 2.28

where s_6 is a global scaling factor that only depends on the density functional that is used (factor is 0.75 for the PBE functional used throughout this work), N_{at} is the number of atoms in the system, C_6^{ij} denotes the dispersion coefficient for atom pair ij and R_{ij} is the distance between atoms i and j. The damping function f_{damp} must be used to avoid near-singularities for small R, and is given by Equation 2.29.

$$f_{damp}(R_{ij}) = \frac{1}{1 + e^{-d(R_{ij}/s_r R_r - 1)}}$$

Equation 2.29

where R_r is the sum of atomic van der Waals (vdW) radii, d is a variable that determines the steepness of the damping function and s_r is a scaling factor. For the G06 dispersion correction these are fixed at d = 20 and s_r = 1.10. The values of R_r used were derived from the radius of the 0.01 au (atomic unit) electron density contour from ROHF/TZV(2d, 2p) (restricted open shell Hartree-Fock using a valence triple-zeta basis set with two sets of polarisation functions) computations of the atoms in the ground state.

The dispersion coefficients in Equation 2.28, C_6^{ij}, are parameterised by a geometric mean of the corresponding atomic coefficients as shown in Equation 2.30:

$$C_6^{ij} = \sqrt{C_6^i C_6^j}$$

Equation 2.30

Grimme proposed a simple computational scheme for calculation of the atomic C_6 coefficients that is derived from the London formula for dispersion.[36] The atomic coefficient for a given atom, k, is given by Equation 2.31:

$$C_6^k = 0.05 N I_p^k \alpha^k$$

Equation 2.31

where N has values of 2, 10, 18, 36 and 54 for rows 1-5 of the periodic table. I_p^k is the first atomic ionisation potential, and α^k the static dipole polarisability of atom k. These atomic ionisation potentials and static dipole polarisabilities were calculated by DFT using the PBE0 functional. The 0.05 proportionality constant in Equation 2.31 was optimised to adjust the calculated atomic ionisation potentials and static dipole polarisabilities to reproduce the experimentally determined[37] C_6 values for H, C-Ne and simultaneously, binding energies and bond distances of the rare-gas dimers of Ne-Xe.

The TS dispersion correction method was developed by Tkatchenko & Scheffler.[33] In contrast to G06 this dispersion correction is a parameter-free non-empirical method. However, the overall form of the dispersion correction is very

similar to that of Grimme; the TS dispersion energy is given by simply replacing the s_6 term in Equation 2.28 by a constant factor of 1/2. Again the damping function is given by Equation 2.29, however the scaling factor, s_r used by Tkatchenko & Scheffler[33] is functional-dependant ($s_r = 0.94$ for the PBE functional).

For the TS dispersion correction the atomic van der Waals radii were calculated in a fashion similar to the scheme used for the G06 dispersion correction, the major difference between the two dispersion-corrected functionals is the approach used to determine the dispersion coefficients. Contrary to the semi-empirical approach implemented for the G06 functional the authors of the TS functional employed a rigorous theoretical derivation (in which considers atomic hybridisation and makes use of the Hirshfeld surfaces of the molecules) to calculate the dispersion coefficients. A full derivation of how the TS coefficients were determined can be found in Reference 33.

2.4.10 Practical Application

In this work the computational aims were to use DFT methods to computationally calculate the structure and properties of various energetic materials at ambient and applied hydrostatic pressures. Prior to the calculation of structures and properties, the optimal computational parameters for each specific system were determined using the following approach:

- Define starting structure – this is the experimentally determined crystal structure. The simulation cell is the unit cell of the crystal structure with periodic boundary conditions imposed.
- Define functional and pseudopotentials to be used.
- Perform convergence testing – this involves performing a series of single point energy (SPE) calculations, first at fixed E_{cut}, to optimise the number of k–points used, followed by fixing this optimal number of k–points and perform another series of SPE calculations to optimise the E_{cut}. The energy is minimised when the change in energy between successive iterations in the SCF meets the predefined convergence tolerance.

These optimal computational parameters are then used as input for all subsequent calculations.

2.4.10.1 Lattice Energy Calculations

The lattice energies of certain energetic materials have been calculated using the following methodology:

(1) The lattice parameters of the experimental crystal starting structure were isotropically increased and decreased, ensuring that the intramolecular distances *i.e.* bond lengths and angles of the molecules in the crystal were left unchanged while the intermolecular distances were increased / decreased with changing unit cell size.

(2) SPE calculations were performed on a range of cell sizes

(3) Potential wells were constructed by plotting the calculated energy difference (E_0-E) of the smaller/larger volume crystal structures against V/V_0, where V_0 and E_0 are the energy and unit-cell volume of the experimental crystal structure, respectively (as shown in Figure 2.4).

(4) The resulting potential wells were fitted with Lennard-Jones type potentials of the form shown in Equation 2.32:

$$y = 4A\left(\left(\frac{B}{x}\right)^{C} - \left(\frac{B}{x}\right)^{D}\right) + E$$

Equation 2.32

where, *A*-*E* are free variables.

Thus, the lattice energy E_L (here defined to be negative) can be calculated from the difference in energy between the base of the well and the calculated variable *E* (*i.e.* the point at which the potential well levels off) divided by the number of molecules in the unit cell. In this study, zero point energy contributions have been neglected. A schematic diagram of the potential wells, along with the corresponding information that can be taken from it, is shown in Figure 2.4.

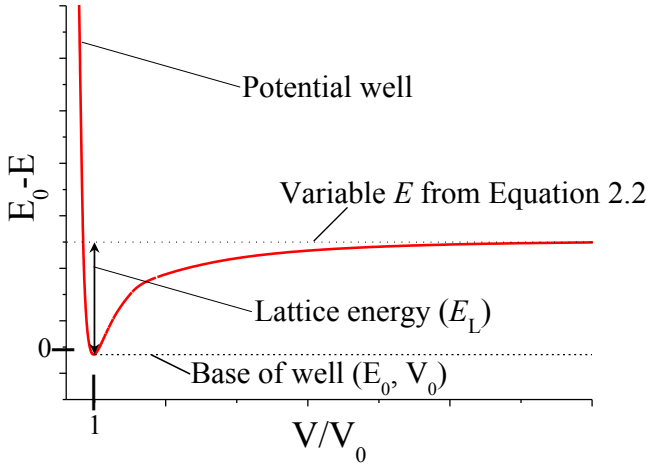

Figure 2.4 Schematic diagram of potential well used to fit Equation 2.32 to give lattice energies.

2.4.10.2 Geometry Optimisations

2.4.10.2.1 Minimisation Method

For a geometry optimisation, as the name suggests the starting structure is optimised to find a computational minima in energy. The Broyden, Fletcher, Goldfarb and Shannon (BFGS) minimisation method was used to perform the geometry optimisations.[38] In this method, the starting Hessian contains both internal (atom positions) and cell (lattice parameters) degrees of freedom, thus both atom positions and cell shape/size can be optimised simultaneously. Additionally an external stress tensor is computed into the Hessian, which allows the application of an external pressure.

The geometry proceeds through a recursive loop, the initial structural 'guess' is fed in through the Hessian, which the proceeds through a SCF cycle, the structure is then updated. This updated structure is then compared to the previous structure to see if the predefined convergence tolerances (change in energy, change in forces, change in atomic position and change in stress) are met. When all convergence tolerances are met, a stationary point on the potential energy surface has been found and the geometry optimisation is complete.

2.4.10.2.2 Hellmann-Feynman Theorem

The changes in energy and atomic positions are obtained by solution of the Kohn-Sham equations, however this is not the case for the forces and stresses. To obtain the forces and stresses within the system, the Hellmann-Feynman theorem is implemented.[39,40,41]

The Hellmann-Feynman theorem (shown in Equation 2.33) relates the derivative of the total energy with respect to a parameter, λ, to the expectation value of the Hamiltonian to that same parameter.

$$\frac{\partial \hat{E}}{\partial \lambda} = \langle \Psi_\lambda | \frac{\partial \hat{H}}{\partial \lambda} | \Psi_\lambda \rangle$$

Equation 2.33

By utilising Equation 2.33, the electrostatic force theorem can be derived from the Hamiltonian given in Equation 2.34 (which is simply the Hamiltonian given in Equation 2.2 with the first term omitted as it is negligibly small, written in a different notation).

$$\hat{H} = -\sum_i \frac{1}{2}\nabla_i^2 + \sum_{A<B} \frac{Z_A Z_B}{|\mathbf{R}_A - \mathbf{R}_B|} + \sum_{i<j} \frac{1}{|\mathbf{r}_i - \mathbf{r}_j|} - \sum_{A,i} \frac{Z_A}{|\mathbf{r}_i - \mathbf{R}_A|}$$

Equation 2.34

The Hamiltonian depends parametrically upon the atomic positions, $\mathbf{R}_A$, so the force on nucleus A is:

$$F_A = -\frac{\partial \hat{E}}{\partial \mathbf{R}_A} = \langle \Psi | -\frac{\partial \hat{H}}{\partial \mathbf{R}_A} | \Psi \rangle = \int \mathrm{d}^3\mathbf{r}\rho(\mathbf{r}) \frac{Z_A(\mathbf{r} - \mathbf{R}_A)}{|\mathbf{r} - \mathbf{R}_A|} + \sum_{A<B} \frac{Z_A Z_B (\mathbf{R}_A - \mathbf{R}_B)}{|\mathbf{R}_A - \mathbf{R}_B|}$$

Equation 2.35

Equation 2.35 is known as the electrostatic force theorem, which is used to find the equilibrium (optimised) geometry of the computational model by varying all of the R_A until the energy is a minimum and $-\frac{\partial \hat{E}}{\partial \mathbf{R}_A} = 0$ (all the forces are zero, in practice however, the optimised geometry is reached when the change in forces falls below the convergence criterion).

Similarly, the stresses within the computational model by relating the stress tensor, $\sigma_{\alpha\beta}$, to the strain tensor, $\varepsilon_{\alpha\beta}$, via the Hellmann-Feynman theorem as shown in Equation 2.36.

$$\sigma_{\alpha\beta} = \langle \Psi | - \frac{\partial \hat{H}}{\partial \varepsilon_{\alpha\beta}} | \Psi \rangle$$

Equation 2.36

2.4.10.3 Phonon Calculations

Following successful geometry optimisations, finite displacement phonon calculations were performed to calculate the vibrational properties of the optimised structures.[42] In a finite displacement calculation, each atom is displaced by a small amount, then a SCF calculation is performed to evaluate the forces on the perturbed configuration. Both positive and negative displacements are performed in each direction so that corresponding force constants can be calculated using central differences. The vibrational frequencies can be straightforwardly calculated from these force constants by invoking the harmonic approximation. The number of vibrational frequencies calculated is thus $3N$, where N is the number of atoms in the unit cell. However there are three centre-of-mass translations (with $\omega = 0$) along the x, y and z directions, thus in total $3N$-3 genuine vibrational modes are calculated.

2.5 Statistical Thermodynamics

2.5.1 Equipartition Theorem

The ultimate aim of this study is to determine the effect of pressure on the heat capacities of energetic materials. Thus the results of the phonon calculations were utilised to predict the heat capacities using statistical thermodynamics.[43] The equipartition theorem states that in thermal equilibrium the energy of a system is distributed (partitioned) equally throughout all of its degrees of freedom. Furthermore, the equipartition theorem makes quantitative predictions, specifically; every quadratic degree of freedom will (on average) possess an energy of $1/2k_BT$.

2.5.2 Partition Function

The partition function plays a vital role in thermodynamic calculations (in this work, namely the internal energies and ultimately the heat capacities).[5,44] The partition function, Q, given by Equation 2.37, determines how the particles within the system distribute themselves over accessible quantum states, and it is essentially just a sum of the Boltzmann law over all states:

$$Q_{tot} = \sum_{i=1}^{\infty} e^{-\frac{\varepsilon_i}{k_B T}}$$

Equation 2.37

where ε_i is the energy for quantum state i, k_B is Boltzmann's constant and T is the temperature. By exploiting this partition function, descriptions for internal energy and consequently heat capacity are enumerated in Equation 2.38 and Equation 2.39.

$$U = \mathrm{R}\,T^2 \left(\frac{\partial \ln Q}{\partial T} \right)_{N,V}$$

Equation 2.38

$$C_V = \left(\frac{\partial U}{\partial T} \right)_{N,V}$$

Equation 2.39

where R is the ideal gas constant, the subscripts N and V denote constant volume, and constant number of particles respectively.

Assuming that the different components of the energy of the system are separable (essentially independent of each other), the total partition function can be factorised into individual components (translational, electronic, rotational and vibrational), as shown in Equation 2.40.

$$Q_{tot} = q_{trans} q_{elec} q_{rot} q_{vib}$$

Equation 2.40

Thus to calculate the internal energy and hence heat capacity, the individual partition functions must be defined.

- Translational partition function

$$q_{trans} = \left(\frac{2\pi m \mathrm{k_B} T}{\mathrm{h}^2} \right)^{\frac{3}{2}} V$$

Equation 2.41

In Equation 2.41 m is the mass of the particle, h is Planck's constant and V is the volume of the system. Thus:

$$\left(\frac{\partial \ln q_{trans}}{\partial T} \right)_V = \frac{3}{2T}$$

Equation 2.42

Consequently, Equation 2.43 presents the translational contributions to the internal energies and heat capacities:

$$U_{trans} = \mathrm{R}T^2 \left(\frac{3}{2T} \right) = \frac{3}{2}\mathrm{R}T \Rightarrow C_{V,trans} = \frac{\mathrm{d}}{\mathrm{d}T}\frac{3}{2}\mathrm{R}T = \frac{3}{2}\mathrm{R}$$

Equation 2.43

This is simply proof of the equipartition function. Each of the three rotational (quadratic) degrees of freedom (with kinetic energy = $1/2m\boldsymbol{v}^2$) contribute $1/2\mathrm{k_B}T$ to the system energy, hence total energy of $3/2\mathrm{k_B}T$, which per mole is $3/2\mathrm{R}T$.

- Electronic partition function

$$q_{elec} = g_0 e^{\frac{-\varepsilon_0}{\mathrm{k_B}T}} + g_1 e^{\frac{-\varepsilon_1}{\mathrm{k_B}T}} + \ldots$$

Equation 2.44

Where g_n is the degeneracy of energy level n. In molecules, the electronic excited states are very much higher in energy than the electronic ground state, hence $\varepsilon_1 >> \mathrm{k_B}T$, therefore it (and all higher energy levels) is inaccessible. It is commonplace within thermodynamics to set the ground state electronic energy as 0 ($\varepsilon_0 = 0$), thus:

$$q_{elec} = g_0 \Rightarrow \left(\frac{\partial \ln q_e}{\partial T} \right)_V = 0 \Rightarrow U_{elec}, C_{V,elec} = 0$$

Equation 2.45

- Rotational partition function

$$q_{rot} = \frac{\pi^{\frac{1}{2}}}{\sigma_{rot}} \left(\frac{T^{\frac{3}{2}}}{\left(\Theta_{rot,x}\Theta_{rot,y}\Theta_{rot,z}\right)^{\frac{1}{2}}} \right)$$

Equation 2.46

Where σ_{rot} is the symmetry number and $\omega_{rot(x,\,y,\,z)}$ are the rotational temperatures for each rotational degree of freedom. Analogous to the translational contribution, the rotational contribution has three degrees of freedom (with kinetic energy = $1/2I\omega^2$) that contribute $1/2\mathrm{k_B}T$ to the system energy, and hence $3/2\mathrm{R}T$ to the total partition function as displayed in Equation 2.48.

$$\left(\frac{\partial \ln q_{rot}}{\partial T} \right)_V = \frac{3}{2} T$$

Equation 2.47

$$U_{rot} = \mathrm{R}T^2 \left(\frac{3}{2T} \right) = \frac{3}{2}\mathrm{R}T \Rightarrow C_{V,rot} = \frac{\mathrm{d}}{\mathrm{d}T}\frac{3}{2}\mathrm{R}T = \frac{3}{2}\mathrm{R}$$

Equation 2.48

- Vibrational partition function

First, for simplification, we define the 'thermodynamic beta', β, as given by Equation 2.49:

$$\beta = \frac{1}{\mathrm{k_B}T}$$

Equation 2.49

Equation 2.50 then gives the vibrational contribution to the partition function.

$$q_{vib,\kappa} = \sum_{n=0}^{\infty} e^{-\beta \mathrm{h}\omega_{vib,\kappa}\left(n+\frac{1}{2}\right)} = e^{-\frac{1}{2}\beta \mathrm{h}\omega_{vib,\kappa}} \frac{1}{1-e^{-\beta \mathrm{h}\omega_{vib,\kappa}}}$$

Equation 2.50

where $\omega_{vib,\kappa}$ is the vibrational frequency of mode, κ. The vibrational contribution to the internal energy can then be determined by differentiating with respect to the

thermodynamic beta in place of temperature, as illustrated in Equation 2.51, the internal energy is then given by Equation 2.52.

$$U_{vib} = \frac{\partial \ln q_{vib}}{\partial T} \equiv -\frac{\partial \ln q_{vib}}{\partial \beta} = -\frac{\partial}{\partial \beta}\sum_{\kappa=1}^{3N} \ln\left[\frac{e^{-\frac{1}{2}\beta \mathrm{h}\omega_{vib,\kappa}}}{1-e^{-\beta \mathrm{h}\omega_{vib,\kappa}}}\right]$$

Equation 2.51

$$\Rightarrow U_{vib} = \sum_{\kappa=1}^{3N}\left[\frac{1}{2}\mathrm{h}\omega_{vib,\kappa} + \frac{\mathrm{h}\omega_{vib,\kappa}}{e^{\beta \mathrm{h}\omega_{vib,\kappa}}-1}\right]$$

Equation 2.52

Consequently, given the vibrational contribution to the internal energy, the contribution to heat capacity is given by Equation 2.54.

$$C_{V,vib} = \frac{\partial U}{\partial T} = \frac{\partial \beta}{\partial T}\frac{\partial U}{\partial \beta} = -\frac{1}{\mathrm{k_B} T^2}\frac{\partial U}{\partial \beta}$$

Equation 2.53

$$\Rightarrow C_{V,vib} = \mathrm{k_B}\sum_{\kappa=1}^{3N}\frac{\left(\beta \mathrm{h}\omega_{vib,\kappa}\right)^2 e^{\beta \mathrm{h}\omega_{vib,\kappa}}}{\left(e^{\beta \mathrm{h}\omega_{vib,\kappa}}-1\right)^2}$$

Equation 2.54

In the solid state the dispersion of phonons throughout k-space also needs to be considered, thus the total vibrational contribution to the heat capacity in the solid state is given by Equation 2.55.

$$C_{V,vib,solid} = \mathrm{k_B}\int_0^{\mathbf{k}}\sum_{\kappa=1}^{3N}\frac{\left(\beta \mathrm{h}\omega_{vib,\kappa,\mathbf{k}}\right)^2 e^{\beta \mathrm{h}\omega_{vib,\kappa,\mathbf{k}}}}{\left(e^{\beta \mathrm{h}\omega_{vib,\kappa,\mathbf{k}}}-1\right)^2}\mathrm{d}\mathbf{k}$$

Equation 2.55

The 'vibrational' temperature of each vibrational mode can then be expressed by Equation 2.56. Substitution into Equation 2.54 and multiplication by Avogadro's number (to convert to molar heat capacity) results in the vibrational contribution to heat capacity as given by Equation 2.57.

$$\Theta_{vib,\kappa} = \frac{h\omega_{vib,\kappa}}{\mathrm{k_B}}$$

Equation 2.56

$$\Rightarrow C_{V,vib} = \mathrm{R}\sum_{\kappa=1}^{3N} \frac{\left(\frac{\Theta_{vib,\kappa}}{T}\right)^2 e^{\frac{\Theta_{vib,\kappa}}{T}}}{\left(e^{\frac{\Theta_{vib,\kappa}}{T}} - 1\right)^2}$$

Equation 2.57

Similarly, Equation 2.55 becomes:

$$\Rightarrow C_{V,vib,solid} = \mathrm{R}\int_0^{\mathbf{k}} \sum_{\kappa=1}^{3N} \frac{\left(\frac{\Theta_{vib,\kappa,\mathbf{k}}}{T}\right)^2 e^{\frac{\Theta_{vib,\kappa,\mathbf{k}}}{T}}}{\left(e^{\frac{\Theta_{vib,\kappa,\mathbf{k}}}{T}} - 1\right)^2} \mathrm{d}\mathbf{k}$$

Equation 2.58

Unlike the translational and rotational contributions to the partition function, the vibrational contribution does not necessarily follow the equipartition theorem. With regard to the vibrational component, both the kinetic energy and the potential energy of the harmonic oscillator must be considered (kinetic energy = $1/2m\boldsymbol{v}^2$ and potential energy = $1/2kx^2$). Although these are both quadratic degrees of freedom, the vibrational energy levels are highly quantised, with energy level spacing larger than at least an order of magnitude than those in rotational modes. Consequently, at room temperature, most molecules are in their ground vibrational state and higher energy levels are not thermally accessible. Thus the equipartition theorem only holds for the vibrational contribution (for molecular materials) at very high temperatures. As $T \to \infty, \beta \to 0$, thus $\frac{\partial \ln q_{vib}}{\partial T}$ tends to unity and the internal energy is thus $1/2\mathrm{k_B}T$ per degree of freedom, satisfying the equipartition theorem. Accordingly, as there are both kinetic and potential energy contributions, the molar heat capacity of a solid as $T \to \infty$ = 3R. This value of 3R for the specific heat capacity of a crystal is known as the Dulong-Petit Law.

- Total heat capacity

The total heat capacity is the sum of the component contributions, thus, as can be seen from Equation 2.59, the only variable in the calculation of heat capacities

is the vibrational contribution. A complete (3*N*-3) list of vibrational frequencies are calculated in a finite displacement phonon calculation, thus, with this data, the heat capacity at a given temperature can easily be determined by converting these vibrational frequencies into vibrational temperatures and employing Equation 2.59.

$$C_{V,tot} = \frac{3}{2}\mathrm{R} + 0 + \frac{3}{2}\mathrm{R} + \mathrm{R}\sum_{\kappa=1}^{3N-3} \frac{\left(\frac{\Theta_{vib,\kappa}}{T}\right)^2 e^{\frac{\Theta_{vib,\kappa}}{T}}}{\left(e^{\frac{\Theta_{vib,\kappa}}{T}} - 1\right)^2}$$

Equation 2.59

In this manner, the effect of pressure on the heat capacities of a specific system is determined by performing a series of geometry optimisations at applied external pressures, phonon calculations are then performed on the resultant structures with Equation 2.59 then utilised to determine heat capacities.

2.6 References

1 Schrödinger, E. *Phys. Rev.* **1926**, *28*, 1049.
2 Rankin, D. W. H.; Mitzel, N. W.; Morrison, C. A. in *Structural Methods in Molecular Inorganic Chemistry,* John Wiley & Sons, Chichester, **2013**.
3 Atkins, P.; Friedman, R. in *Molecular Quantum Mechanics 4th edition*, Oxford University Press, New York, **2005**.
4 http://vergil.chemistry.gatech.edu/notes/
5 McQuarrie, D. A.; Simon, J. D. in *Molecular Thermodynamics*, University Science Books, Sausalito, **1999**.
6 Parr, R. G.; Yang, W. in D*ensity-Functional Theory of Atoms and Molecules*, Oxford University Press, New York, **1989**.
7 Szabo, N. S.; Ostlund, A. in *Modern Quantum Chemistry*, McGraw-Hill, New York, **1985**.
8 McWeeny, R. in *Methods of Molecular Quantum Mechanics*, Academic Press, London, **1992**.
9 Slater, J. C. *Phys. Rev.* **1929**, *34*, 1293.
10 Burke, K. *J. Chem. Phys.* **2012**, *136*, 15091.
11 Hohenberg, P.; Kohn, W. *Phys. Rev. B* **1964**, *136*, 864.
12 Thomas, L. H. *Math. Proc. Cambridge Philos. Soc.* **1927**, *23*, 542.
13 Fermi, E. *Z. Phys. A: Hadrons Nucl.* **1928**, *48*, 73.
14 Becke, A. D. *J. Chem. Phys.* **1993**, *98*, 5648..
15 Perdew, J. P.; Burke, K.; Ernzerhof, M. *Phys. Rev. Lett.* **1996**, *77*, 3865.
16 Perdew, J. P.; Burke, K.; Ernzerhof, M. *Phys. Rev. Lett.* **1997**, *78*, 1396.

17 Perdew, J. P. in *Electronic Structure of Solids*, Eds.: Ziesche, P.; Eschrig, H., Akademie Verlag, Berlin, **1991**.
18 Perdew, J. P.; Chevary, J. A.; Vosko, S. H.; Jackson, K. A.; Singh, D. J.; Fiolhais, C. *Phys. Rev. B* **1992**, *46*, 6671.
19 Becke, A. D. *Phys. Rev. A* **1988**, *38*, 3098.
20 Lee, C.; Yang, W.; Parr, R. G. *Phys. Rev. B* **1988**, *37*, 785.
21 Miehlich, B.; Savin, A.; Stoll, H.; Preuss, H. *Chem. Phys. Lett.* **1989**, *157*, 200.
22 Martin, R. M. in E*lectronic Structure: Basic Theory and Practical Methods*, Cambridge University Press, Cambridge, **2004**.
23 Personal communication courtesy of Michal Kochman.
24 Cohen, M. L.; Heine, V. in *Solid State Physics vol. 24*, Academic Press, New York, **1970**.
25 Image courtesy of www.wikipedia.com, the image has been released into the public domain.
26 Monkhorst, H. J.; Pack, J. D. *Phys. Rev. B* **1976**, *13*, 5188.
27 Jones, R. O.; Gunnarsson, O. *Rev. Mod. Phys.* **1989**, *61*, 689.
28 Dion, M.; Rydberg, H.; Schroeder, E.; Langreth, D. C.; Lundqvist, B. I. *Phys. Rev. Lett.* **2004**, *92*, 246401.
29 Langreth, D. C.; Lundqvist, B. I.; Chakarova-Kack, S. D.; Cooper, V. R.; Dion, M.; Hyldgaard, P.; Kelkkanen, A.; Kleis, J.; Kong, L. Z.; Li, S.; Moses, P. G.; Murray, E.; Puzder, A.; Rydberg, H.; Schroeder, E.; Thonhauser, T. J. *Phys. Condens. Matter* **2009**, *21*, 084203.
30 Lin, I. C.; Coutinho-Neto, M. D.; Felsenheimer, C. n Lilienfeld, O. A.; Tavernelli, I.; Rothlisberger, U. *Phys. Rev. B* **2007**, *75*, 205131.
31 Tavernelli, I.; Lin, I. C.; Rothlisberger, U. *Phys. Rev. B* **2009**, *79*, 045106.
32 Grimme, S. *J. Comput. Chem*. **2006**, *27*, 1787.
33 Tkatchenko, A.; Scheffler, M. *Phys. Rev. Lett*. **2009**, *102*, 073005.
34 Jurecka, P.; Cerny, J.; Hobza, P.; Salahub, D. R. *J. Comput. Chem.* **2007**, *28*, 555.
35 Ortmann, F.; Bechstedt, F.; Schmidt, W. D. *Phys. Rev. B*. **2006**, *73*, 205101.
36 London, F. *Trans. Faraday Soc.* **1937**, *33*, 8.
37 Wu, Q.; Yang, W. *J. Chem. Phys*., **2002**, *116*, 515.
38 Fischer, T. H.; Almlof, J. *J. Phys. Chem.* **1992**, *96*, 9768.
39 Hellmann, H. in *Einführung in die Quantenchemie*, Franz Deuticke, Leipzig, 1937.
40 Feynman, R. P. *Phys. Rev.* **1939**, *56*, 340.
41 Fiolhais, C.; Nogueira, F.; Marques, M., in *A Primer in Density Functional Theory*, Springer-Verlag, Berlin Heidelberg, **2003**.
42 Frank, W.; Elsässer, C.; Fähnle, M. *Phys. Rev. Lett.* **1995**, *74*, 1791.
43 Lee, J. C., in *Thermal Physics: Entropy and Free Energies 2nd Edition*, World Scientific, Singapore, **2011**.
44 Maczek, A., in *Statistical Thermodynamics*, Oxford Chemistry Primers, Oxford University Press, New York, **1998**.

Chapter 3

Experimental Techniques

3 Experimental Techniques

3.1 Merrill-Bassett Diamond Anvil Cell

High-pressure Raman spectroscopic studies were performed using a gasketed diamond anvil cell (DAC). The DAC used in this work (Figure 3.1) is based on the opposed anvils developments proposed by Merrill and Bassett.[1] The basic principle of the device is relatively simple, a sample is placed between two opposing flat diamond faces (culets) and the sample is subjected to high pressures when a force pushes the opposing anvils together. The transparency of diamond over a wide range of the electromagnetic spectrum, combined with its hardness, makes it an ideal material for an anvil. This transparency allows visual observation, in addition to *in situ* diffraction (crystallography) and spectroscopic analysis of samples contained within the cell.

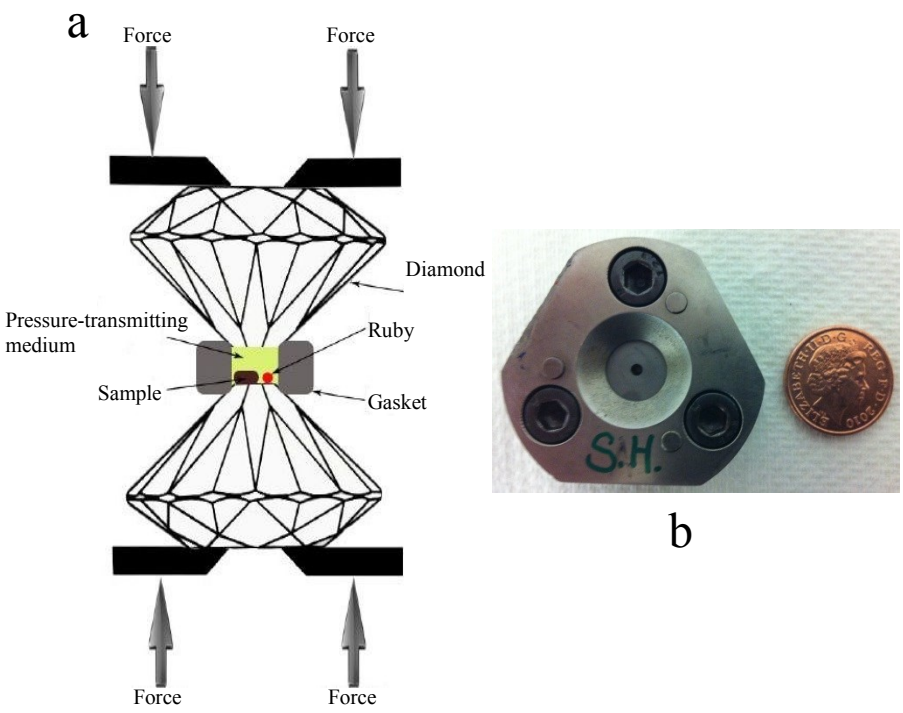

Figure 3.1 (a) schematic representation of the principles of the DAC. (b) photograph of the Merrill-Bassett DAC used in this study alongside a one penny (GBP) coin, highlighting the simplicity and size of the DAC.

The DAC is ~5 cm in diameter and comprises of two gem-quality diamonds (culet diameter 600 μm) attached to beryllium or steel backing plates. A small

cylindrical hole in the centre of these backing plates facilitates visual observation of the sample as well as access to electromagnetic radiation. The backing plates are then held in a stainless steel casing by small screws which allow the alignment of the two anvils. A gasket is placed between the two culets and the two halves are then forced together simply by tightening three Allen screws attached to the steel casing. The sample chamber is essentially just a metal plate with a hole in the middle (the gasket). A ~250 μm thick (1 cm by 1cm) square of metal (usually tungsten or stainless steel) is placed between the two aligned diamonds and pre-indented (by tightening the Allen screws) to a thickness of ~100 μm, during this pre-indentation process the gasket extrudes outwards, around the culets sealing the sample chamber. A hole (diameter 300 μm) is then drilled in the centre of the pre-indentation by spark erosion, thus creating the sample chamber. The cell configuration described above allows pressures up to ~12 GPa to be achieved, but the pressure attainable in a DAC can be substantially higher (pressures >250 GPa) by reducing the hole size and thickness of the gasket and the diameter of the diamond culets.

The sample is loaded into the sample chamber, alongside a piece of ruby and the pressure-transmitting medium (PTM). The ruby is used as a pressure calibrant, with the ruby fluorescence method being utilised to measure the pressure within the cell.[2] The PTM is an encapsulating fluid (that does not react with the sample and does not solidify within the pressure range studied) that facilitates hydrostatic conditions by transforming the uni-axial force (of the Allen screws) driving the anvils together into a homogenous pressure in all directions. In these studies a 4:1 mixture of methanol:ethanol was used as PTM, which has been shown to remain truly hydrostatic to ~9.8 GPa.[3]

3.2 Spectroscopic Techniques

3.2.1 Raman Spectroscopy

Raman spectroscopy was used to determine characteristic solid-state vibrational frequencies of the compounds of interest. These characteristic vibrational modes give structural information as different structural groups vibrate at different frequencies. In addition, if all vibrational modes, both internal and lattice, of a

crystal are known, then statistical thermodynamics can be used to calculate heat capacities.

Traditionally, Raman spectroscopy has been less widely used than the more popular (but complementary) infrared (IR) spectroscopy technique. The main reason IR has historically been favoured over Raman is simply due to instrumentation. However, recent advances in instrument technologies have simplified the Raman equipment, thus Raman spectroscopy is now relatively straightforward and ideally suited for high pressure studies.

Raman spectroscopy measures the inelastic scattering of radiation that occurs after a monochromatic beam of electromagnetic radiation has irradiated a sample. The majority of the radiation incident on the sample either passes straight through the sample or may be absorbed by the sample depending on its functional properties and the wavelength of radiation used. A small percentage of the radiation, around 0.1%, undergoes Rayleigh scattering (elastic scattering) and an even smaller fraction, one photon in 10^6 or 10^7 undergoes Raman scattering.[4]

There are two possibilities in inelastic scattering; either energy is transferred from the photon of radiation to the molecule, thus the photon is scattered with a lower energy and frequency, and longer wavelength (Stokes scattering). The other possibility is that radiation is transferred from the molecule to the photon, giving a scattered photon with increased energy, thus shorter wavelength (anti-Stokes scattering).[5] This is illustrated in Figure 3.2.

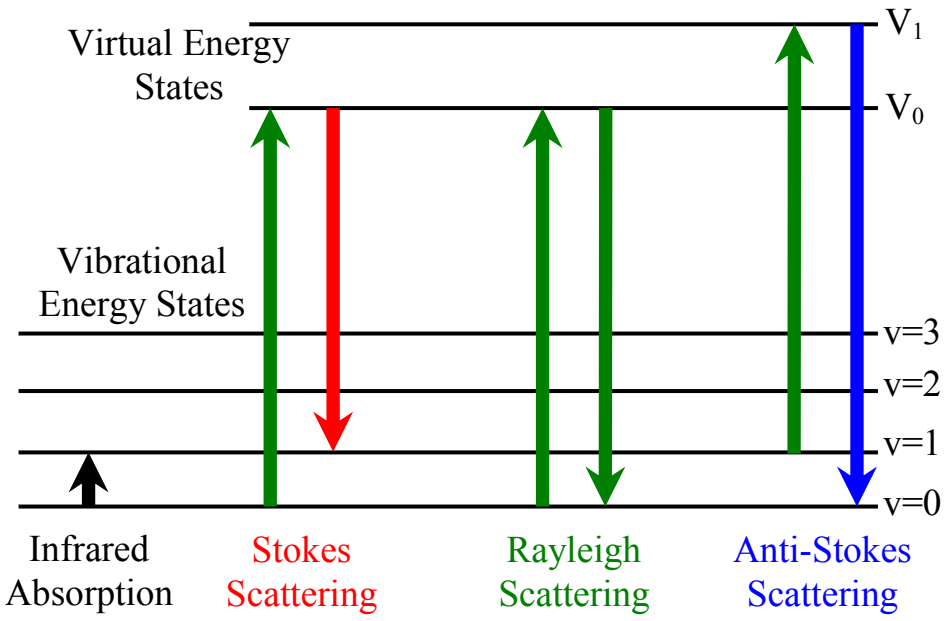

Figure 3.2 Diagram showing the mechanism for IR absorption, Stokes, anti-Stokes and Rayleigh scattering.[6]

Generally Raman spectra are plotted such that the Rayleigh line lies at 0 cm^{-1}. Using this scale, the band positions due to Raman scattering will lie at frequencies that correspond to the energy levels of different normal modes. For a vibrational mode to be Raman active, the vibration must satisfy the selection rule ($\Delta v = \pm 1$). In addition the polarisability tensor of the molecule must change with the vibrational motion. This is best imagined as the ease with which the electron cloud of the molecule is distorted (*i.e.* polarised). Thus Raman spectroscopy provides information that is complementary to IR spectroscopy.

3.2.2 Inelastic Neutron Scattering

3.2.2.1 Inelastic Neutron Scattering Description

A complementary approach to optical Raman and IR spectroscopy is inelastic neutron scattering (INS). In INS an incident beam of neutrons[**] strikes a sample, and the neutrons are then scattered by the nuclei in the sample. The neutrons can undergo several types of scattering, including: elastic scattering (analogous to Rayleigh scattering in Raman spectroscopy), inelastic scattering, coherent scattering

[**] Note, the neutron is an elementary particle with zero charge. It undergoes the phenomenon of wave-particle duality. In INS the neutron is regarded as a particle, however the scattered neutron is treated theoretically as a spherical wave.

and incoherent scattering. Coherent scattering arises from interference of the scattered waves from different nuclei of the same type, and is measured in diffraction experiments. Incoherent scattering arises when the natural isotopic and spin mixture within the sample destroys local order and reduces the degree of interference between the scattered waves. Inelastic scattering occurs when the incident neutron and the sample exchange energy; it is incoherent inelastic scattering that is detected in an INS experiment. The INS technique poses several advantages over the optical spectroscopies. These include:

(i) INS spectra are not subject to the rules of optical selection

Thus all vibrations (fundamental, overtones and combination modes) are active in INS and, in principle, measurable.

(ii) INS spectra are particularly sensitive to vibrations involving hydrogen atoms

Optical spectroscopy is most sensitive to vibrations involving heavier atoms (because of the larger number of electrons), but as the incoherent neutron cross section (σ)[††] of hydrogen is uniquely high, INS spectra are dominated by modes involving hydrogen motion.

(iii) neutrons are penetrating – photons are not

As neutrons penetrate deeply (in the order of millimetres) INS results are naturally weighted to the measurement of bulk properties.

(iv) wide spectral range

INS spectrometers cover the whole molecular vibrational range of interest (16 – 4000 cm^{-1}). Furthermore the lower energy range (<400 cm^{-1}) is particularly accessible, a region that is more difficult experimentally for optical spectroscopy.

[††] Neutron scattering cross sections describe the likelihood of interaction between the incident neutron and the nuclei within the sample. The incoherent neutron scattering cross sections of ^{1}H, ^{2}D, ^{12}C, ^{13}C, ^{14}N and ^{16}O are; 80.27, 2.05, 0, 0.034, 0.5 and 0 barn respectively. It can be seen that the incoherent cross section of ^{1}H dominates that of all other nuclei, thus INS is uniquely sensitive to vibrations involving hydrogen motion.

(v) INS spectra are readily and accurately modelled

Measured INS intensities are straightforwardly related to the atomic displacements of the scattering atom (eigenvector of the vibration, described in Section 3.2.2.4), which are conveniently calculated using modern *ab initio* computational chemistry phonon calculations.

3.2.2.2 Neutron Sources

There are two different types of neutron source used for research purposes; reactor sources and spallation sources. [7,8] At reactor sources, neutrons are generated by nuclear fission of ^{235}U to produce a continuous wave of high-energy neutrons which are subsequently moderated to produce thermal neutrons. At a spallation source, short pulses of energetic protons (generated using a synchrotron) bombard a heavy metal target (such as tantalum or tungsten) triggering a cascade of high-energy neutrons, and due to the fact a pulsed proton beam is used to generate the neutrons, a pulsed neutron beam is produced. The INS experiments carried out in this work were performed at ISIS Neutron and Muon Facility, STFC Rutherford Appleton Laboratory, UK (a neutron spallation source), thus further description will be given for pulsed spallation sources only.

In a spallation source, protons hit the nuclei in the target material and trigger an intra-nuclear cascade, exciting individual nuclei into highly excited states. These excited nuclei must then release the excess energy, which is achieved by 'evaporating' nucleons (the majority of which are neutrons). Some of these neutrons will then go on to trigger further reactions, the rest will leave the target creating the neutron pulse. Each high-energy proton delivered to the target results in an excess of approximately 15 neutrons, resulting in an intense neutron pulse.

The resultant neutrons are high-energy neutrons with energies of ~2 MeV (often termed epithermal neutrons). In order to be experimentally useful, the neutrons need to be slowed down, which is achieved by a moderator. The moderator consists of a medium with atoms of similar mass to neutrons (*i.e.* ^{1}H or ^{2}D). Thus the neutrons undergo multiple inelastic collisions with the medium resulting in a significant transfer of momentum from the neutron to the medium thereby slowing

the neutrons to useful kinetic energies. These are known as thermal neutrons. The thermalised neutrons are slowed to a distribution of velocities (given by the Maxwell-Boltzmann distribution) and each different moderator medium produces neutrons with peak neutron fluxes at different energies. For example, water moderators produce peak fluxes at ~200 cm^{-1}, methane at ~70 cm^{-1} and dihydrogen (H_2) at ~40 cm^{-1}.

3.2.2.3 TOSCA Instrument

The instrument used for INS spectroscopy in this work was the TOSCA instrument at ISIS. TOSCA is an indirect geometry time-of-flight (ToF) spectrometer which operates at cryogenic temperatures (~10 – 20 K).[9] This indirect geometry ToF means that the energy spectrum of the sample is scanned by fixing the final energy of the neutrons and scanning the incident energies. The source of the neutrons for TOSCA is a white beam from a water moderator (as described in the previous section). TOSCA contains both forward and backward scattering detectors. For the backward scattering detectors, the neutrons that are inelastically backscattered through an angle = 45° or 135° impinge on a graphite crystal – the analyser crystal. Equation 3.1 states Bragg's law where λ is the wavelength (of the scattered neutron), d is the inter-planar distance (of the graphite crystal) and θ is the scattering angle.

$$\lambda = 2d \sin\theta$$

Equation 3.1

In this case, since d and θ are constant, only one neutron λ (and its higher orders, $\lambda/2$, $\lambda/3$ etc.) will satisfy the Bragg condition and be scattered by the graphite crystal, the remainder of the neutrons will pass through the analyser and be absorbed by the spectrometer's shielding. Subsequently, the scattered neutrons are passed through a beryllium filter which acts as a long-pass filter, scattering away the neutrons with multiples of the fundamental λ, with the remaining neutrons detected by ^{3}He filled detector tubes. The net result of using the graphite crystal in series with the beryllium filter is to essentially create a narrow band-pass filter.

The kinetic energy of a neutron is given by Equation 3.2.

$$E = \frac{1}{2} \mathrm{m_n} \boldsymbol{v}^2 \Rightarrow \boldsymbol{v} = \sqrt{\frac{2E}{\mathrm{m_n}}}$$

Equation 3.2

where $\boldsymbol{v}$ is the velocity and $\mathrm{m_n}$ is the mass of a neutron. If the energy transferred to the sample, E_{trans}, is defined as the difference between the initial (E_{i}) and final (E_{f}) energies of the neutrons. The total time, t_{tot}, is the difference between the time taken for the incident neutron to travel from moderator→sample (over distance $\mathrm{l_i}$), t_{i}, and the time taken for the scattered neutron to travel from sample→analyser→detector (over distance $\mathrm{l_f}$), t_{f}. Then as time equals distance divided by velocity, Equation 3.3 can be derived.

$$t_{tot} = \frac{\mathrm{l_i}}{\boldsymbol{v}_i} + \frac{\mathrm{l_f}}{\boldsymbol{v}_f} \Rightarrow = \frac{\mathrm{l_i}}{\sqrt{\frac{2E_i}{\mathrm{m_n}}}} + \frac{\mathrm{l_f}}{\sqrt{\frac{2E_f}{\mathrm{m_n}}}}$$

Equation 3.3

Thus, as E_{f}, l_{i} and l_{f} are all known (and fixed), then the time of arrival at the detector uniquely defines the incident energy of the neutron, hence the energy transferred to the sample, E_{trans}.

The above explanation of how the scattered neutrons are detected can be simplified by the schematic shown in Figure 3.3.

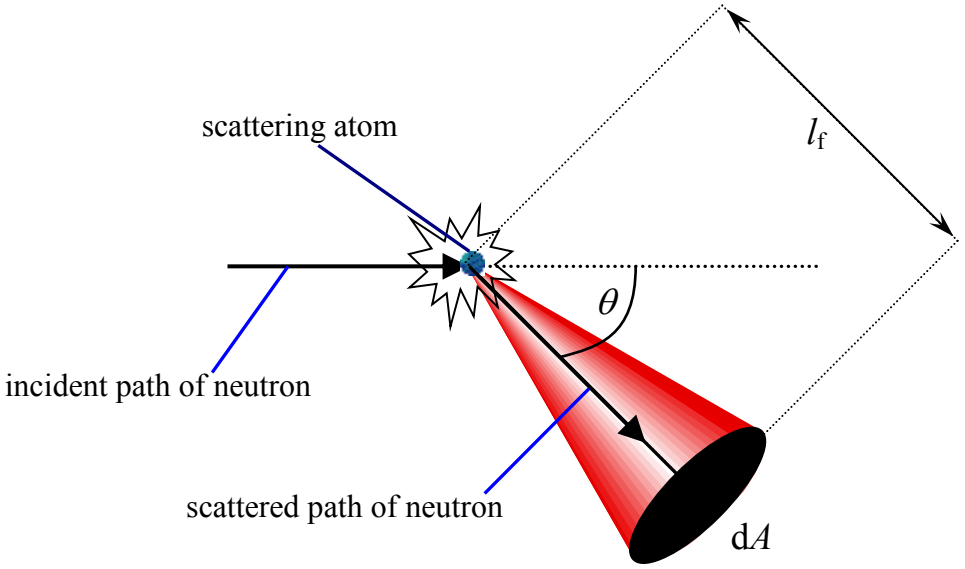

Figure 3.3 A schematic diagram of a simple scattering measurement. The incident neutrons strike a sample, a proportion of which are scattered through an angle θ into the detector with area dA, at a distance l_f from the sample.

The solid angle, dΩ can then be defined by Equation 3.4:

$$d\Omega = \frac{dA}{l_f^2}$$

Equation 3.4

The intensity of a sample's response in inelastic neutron scattering is, therefore, known as a function of energy and since there are multiple detector positions, also as a function of solid angle. Thus, the observable quantity in an INS experiment is the rate of change of the scattering cross section with respect to the final energy (E_f), and solid angle (dΩ) - the double differential scattering cross section. To understand the form of this double differential scattering cross section, the changes that occur during the scattering process must be related to how the initial state of the system is transformed into the final state of the system.[10]

3.2.2.4 The Scattering Law

A complete derivation regarding the origin of the scattering law is not within the scope of this thesis. Instead only the law itself and the practical application are described here. However, a complete description and derivation of the scattering law can be found in Reference 10.

As is the case for other spectroscopic techniques, INS is difficult to perform on the basis of absolute measurements, and so only the relative strengths of the spectral intensities are measured. The calculated relative intensity (termed the scaled scattering factor, $S^{\bullet}(Q,\omega_v)$) of the v^{th} mode determined at a momentum transfer, $\boldsymbol{Q}$, and a neutron energy loss, $E_{trans} \equiv \omega_v$, is given by Equation 3.5:

$$S^{\bullet}(\boldsymbol{Q},\omega_v)_m^n = y\sigma_m \frac{\left[\left(\boldsymbol{Q}\bullet {}^{v}\boldsymbol{u}_m\right)^2\right]^n}{n!} e^{-\left(\boldsymbol{Q}\bullet\sum_v {}^{v}\boldsymbol{u}_m\right)^2}$$

Equation 3.5

where n indicates the final state of the mode that has been excited (elastic; n = 0, fundamental mode (1←0 transition); n = 1, 1st overtone (2←0 transition); n = 2, etc.), ${}^{v}\boldsymbol{u}_m$ is the displacement vector for atom m in mode v and y is a linear factor (of units barn cm) which effectively converts the actual units of $S^{\bullet}(Q,\omega_v)$ (barn^{-1} cm^{-1}) into scaled dimensionless units. In Equation 3.5 the two main parts are the pre-exponential term and the exponential term.

The pre-exponential term is proportional to $\boldsymbol{Q}^2\boldsymbol{u}^2$ which increases as the momentum transferred from the neutron to the sample and/or the scattering atom's atomic displacement increases. As $\boldsymbol{Q}$ is fixed by the spectrometer, determination of $S^{\bullet}(\boldsymbol{Q},\omega)$ allows the atomic displacements (eigenvector of a vibrational mode) to be extracted. The exponential term is known as the Debye-Waller factor and it decreases faster with $\boldsymbol{Q}^2\boldsymbol{u}^2$ than the pre-exponential increases. Additionally, since the atomic displacements are temperature dependent, $\boldsymbol{Q}^2\boldsymbol{u}^2$ has significant temperature dependence. Thus, in order to maximise the observed spectral intensities, INS studies are carried out at cryogenic temperatures (to minimise $\boldsymbol{u}$).

Thus in summary, the output from an INS experiment is a plot of $S^{\bullet}(\boldsymbol{Q},\omega)_{tot}$ versus the neutron energy loss (E_{trans} or ω_v). As the scattering factor is directly related to the observed intensities, this explains why the intensity of a mode (at eigenvalue, ω) in an INS spectra gives information about not only the eigenvalue, but also the eigenvector of the vibration.

3.3 Differential Scanning Calorimetry

3.3.1 Principles of Differential Scanning Calorimetry

Differential scanning calorimetry (DSC) is a thermal analysis technique,[11] in which the energy changes that occur as a sample is heated, cooled or held isothermally are recorded, together with the temperature at which these changes occur. The sample material under study can be characterised for melting processes, crystallisation processes (phase changes in general), measurement of glass transitions as well a range of more complex events. The basic outline of a DSC experiment is as follows. A sample of known weight is encapsulated within a sample holder, which is placed into a furnace alongside a reference material (also in the same type of sample holder as the sample). The furnace temperature is then scanned at a known scan rate. The DSC analyser independently measures the temperature of the reference and the sample, and records the difference in the amount of heat required to increase the temperature of the sample with respect to the reference material, as a function of temperature.

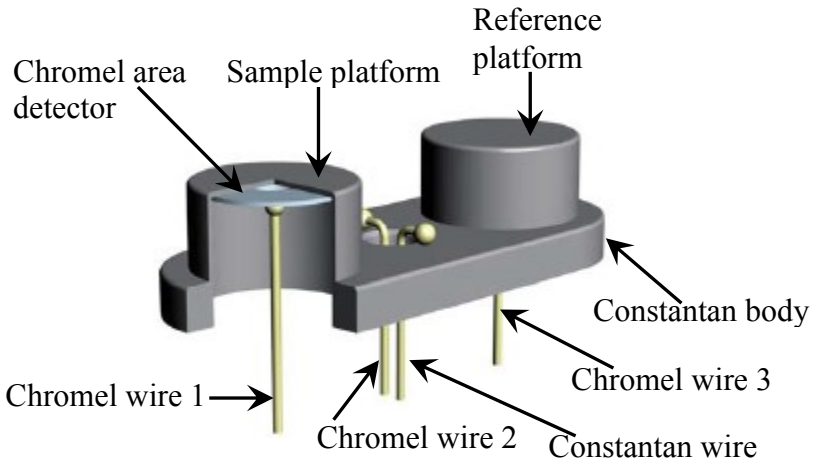

Figure 3.4 Example of the DSC analyser used in this work.[12]

An example of a DSC analyser is shown in Figure 3.4. The DSC analyser essentially consists of three independent thermocouples contained within a furnace. The Constantan wire / Chromel wire 2 pair combine to act as the furnace thermocouple, which controls the temperature of the furnace. The encapsulated sample and reference are placed on their respective platforms. These platforms are

each on the bridge between the Constantan body and Chromel area detectors (with attached Chromel wires), thus the temperature response of the sample and reference materials can be measure independently of each other. The overall heat flow of the sample is then measured as the difference in the sample's temperature response, with respect to the temperature response of the reference.

3.3.2 Practical Aspects of DSC

There are several practical issues to consider when performing DSC experiments. These include encapsulation, temperature range, scan rate, sample size and the purge gas used.

Encapsulation

Samples are encapsulated within a DSC pan to provide good thermal conductance to the sample and to contain the sample contents. This prevents contamination of the analyser and ensures that the sample is in good thermal contact with the furnace. A variety of different DSC pans are available for use, depending on the experimental conditions to be used (sample type and size, temperature range, pressure). Pans come in different sizes, are made from different materials (such as aluminium, copper, gold, platinum and graphite) and can be hermetically or non-hermetically sealed. This flexibility allows for a wide range of sample materials to be studied.

Temperature range

The starting temperature of the scan should be well below the beginning of the first transition within the sample. This allows time for the initial transient (which is explained in the next section) to settle and a period of flat baseline to be established so that the sample transition can be seen clearly. The upper temperature of the scan should be below the decomposition temperature of the sample.

Scan rate

The choice of scan rate may affect several aspects:

- Sensitivity – the faster the scan rate the greater the sensitivity. As DSC measures the flow of energy, during a fast scan the flow of

energy increases, over a short period of time, thereby increasing the peak intensity.

- Resolution – the faster the scan rate the lower the resolution. As the scan rate is increased, the thermal gradient across the sample increases, consequently reducing resolution. Thermal gradients across a sample can be reduced by decreasing the sample size and improving the thermal contact of the sample with the DSC pan.

- Transition kinetics – kinetically slow events may not go to completion if a fast scan rate is used. Furthermore, the kinetically slow event may be shifted to a higher temperature with fast scan rate, and consequently can occur more rapidly.

- Analysis time – the faster the scan rate used, the quicker the experiment.

All of these factors need to be considered in order to obtain the optimum scan rate for the specific experiment, traditionally the most common scan rate used by thermal analysts is 10 °C min^{-1}.

Purge gas

Purge gases are used to control the sample environment, remove volatiles from the system and to prevent contamination. Additionally, purge gases reduce detector noise by preventing convection currents within the system. Several types of gas can be used including nitrogen, air, argon and helium.

Sample size

The size of sample used in DSC experiments is determined by the type of sample used and what is trying to be measured. Typically, for pharmaceutical materials 1 – 3 mg of sample is sufficient, however, for very weak transitions and accurate heat of fusion measurements more sample may be needed.

3.3.3 Data Interpretation

An annotated DSC thermogram is shown in Figure 3.5, with the important elements highlighted; the transient slope of the baseline, the onset of melting, the peak resulting from melting and a step-down in baseline after a phase transition.

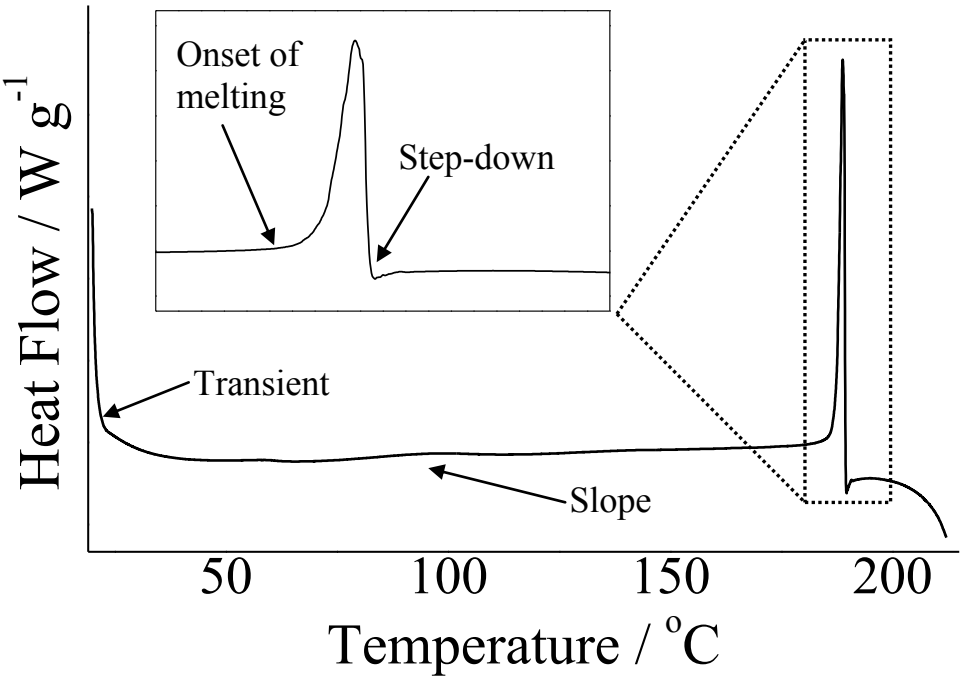

Figure 3.5 Annotated DSC thermogram (endothermic events up) displaying the melting of a solid sample.

The transient is an artefact at the start of every single DSC experiment (in fact it occurs every time the rate of heating is changed). At the beginning of the run, it takes a short period of time for the energy to be transferred to the sample and reference in order to produce the required heating rate, thus there is always a period of slight instability before a stable baseline is established, this period of instability is known as the transient.

After the initial transient, and before the thermal event, the baseline is established. This baseline is not necessarily completely straight, if the thermal mass of the sample and reference are not exactly matched then the heat flow curve will slope as a manifestation of the changes in heat capacity of the sample compared to the reference, this may result in a positive or negative slope.

The scale on the *y*-axis in Figure 3.5 has endothermic events up, thus the peak seen in Figure 3.5 is an endothermic event, in this case the melting of the sample. As can be seen from the enlarged inset of the peak in Figure 3.5, melting does not produce a symmetrical peak shape. The reason for this is easily understood if we consider what happens in a melting process:

- When melting begins, the sample will essentially remain at the melting temperature whilst the solid and liquid are in equilibrium and melting progresses
- This process results in a peak with a straight leading edge, with slope that reflects the rate of energy transfer to the sample
- The peak maximum then represents the end of the equilibrium melting region
- The trace then drops rapidly back to the baseline, with the energy under the tail of the peak resulting from the energy needed to heat the resulting liquid to the temperature of the furnace

From this description it can easily be seen that the melting point of the sample is the onset temperature of the peak, and not the peak maximum. The area under the peak is the heat of fusion of the melting process.

On some occasions (as exemplified by Figure 3.5) the baseline before and after the melting event are at different values. This occurs when the heat capacity of the sample after the melt is noticeably different from that of the sample before the melt, resulting in a peak with an obvious step underneath.

As mentioned earlier, the area under the peak represents the heat of fusion of the melting event. There are numerous alternatives for choice of integration limits, and care needs to be taken when selecting these. There is no one standard way to integrate the peak(s), it is down to the operator to decide the limits, the important point is that the limits are chosen in a reproducible manner.

3.4 References

1 Merrill, L.; Bassett, W. A. *Rev. Sci. Instrum.* **1974**, 45, 290.

2 Piermarini, G. J.; Block, S.; Barnett, J. D.; Forman, R. A. *J. App. Phys.* **1975**, 46, 2774.

3 Varga, T.; Wilkinson, A. P.; Angel, R. J. *Rev. Sci. Instrum.* **2003**, *74*, 4564.

4 Browne, W. R.; McGarvey, J. J. *Coord. Chem. Rev.*, **251**, 2007, 454.

5 Wood, R. W. *Nature*, 1928, **122**, 349.

6 Hollas, J. M. in *Modern Spectroscopy 4th Edition*, John Wiley & Sons, Chichester, **2004**.

7 Skold, K.; Price, D. L. in *Methods of Experimental Physics Vol. 23 Neutron Scattering Part A*, Academic Press, London, **1986**.

8 Windsor, C. G. in *Pulsed Neutron Scattering*, Taylor and Francis, London, **1981**.

9 Parker, S. F.; Carlile, C. J.; Pike, T. G.; Tomkinson, J.; Newport, R. J.; Andreani C. Ricci, F. P.; Sacchetti, F.; Zoppi, M. Physica B **1998**, 241-243, 154.; Colognesi, D.; Celli, M.; Cilloco, F.; Newport, R. J.; Parker, S. F.; Rossi-Albertini, V.; Sacchetti, F.; Tomkinson, J.; Zoppi, M., *Applied Physics A - Materials Science & Processing* **2002,** *S74*, S64.

10 Mitchell, P. C. H.; Parker, S. F.; Ramirez-Cuesta, A. J.; Tompkinson, J. in *Vibrational Spectroscopy with Neutrons with Applications in Chemistry, Biology, Materials Science and Catalysis*, World Scientific, Singapore, **2005**.

11 Gabbott, P. in *Principles and Application of Thermal Analysis*, Blackwell Publishing, Oxford, **2008**.

12 www.tainstruments.com DSC brochure.

Chapter 4

High-Pressure Computational Investigations of Ammonium Perchlorate

4 High-Pressure Computational Investigations of Ammonium Perchlorate

4.1 Introduction

Ammonium perchlorate (AP) is an energetic oxidiser that is widely used in solid rocket motors.[1,2,3] AP is particularly important in the defence and space aviation industries. Some example systems utilising AP (or rather, ammonium perchlorate composite propellants, which include a fuel such as aluminium powder, the oxidiser AP and a binder) include; the Trident I C-4 and Polaris family of intercontinental ballistic missiles, the boosters for NASA space shuttles as well as several military and commercial satellite vehicles such as Delta IV, Atlas V and Titan IV. AP has widespread use as it is cheap to manufacture and contains a large amount of oxygen that is converted entirely into stable gaseous products during combustion (and thus produces very good performance). However, AP also has its limitations, for example, combustion of AP produces vast quantities of hydrochloric acid (HCl). Furthermore, ammonium perchlorate is highly soluble in water, and the perchlorate ion can affect thyroid gland function on account of it being mistakenly taken up in place of iodide. For these reasons, there is considerable research into alternative 'green propellants' for use instead of AP – an example is ammonium dinitramide. However, while alternative oxidisers exist, significant cost, availability, environmental and performance issues remain for these 'green propellants' and these have so far prevented their use in fielded weapon systems and launch vehicles. As AP still has widespread use, a complete understanding of its chemical and mechanical properties is vital.

At ambient pressure and temperature, AP crystallises in the orthorhombic crystal system, space group *Pnma* (see Figure 4.1). Variable temperature studies indicate that, at least up to 78 K, the ammonium ions undergo increasingly large amplitude rotational oscillations about definite equilibrium positions such that they exhibit essentially free rotation.[1,2,3] On heating to above 511-513 K, a reversible phase transition to a cubic structure has been observed in which there is almost unrestricted rotational reorientation of the perchlorate ions.[4]

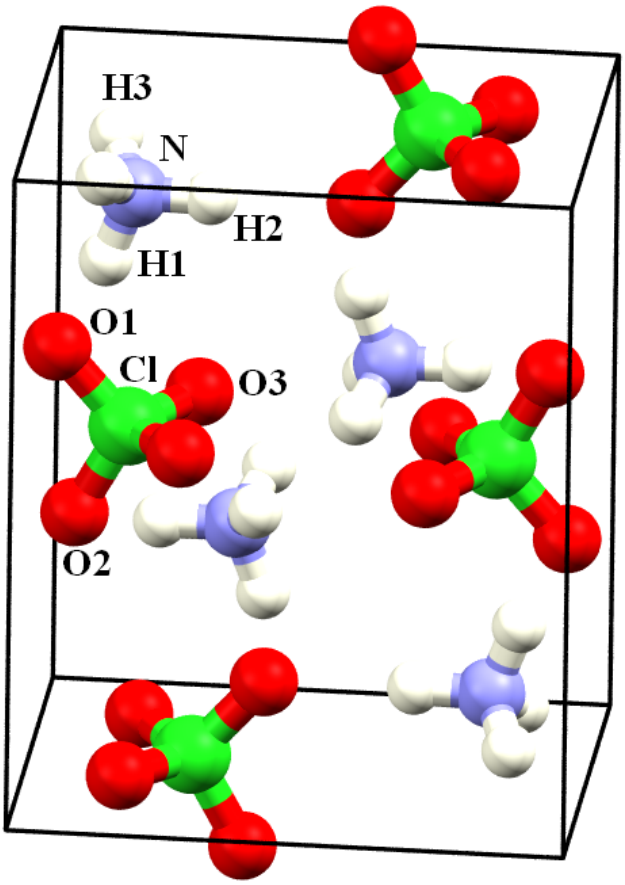

Figure 4.1 Unit cell for AP at ambient pressure (phase I).

By contrast, the structural behaviour of AP at high pressures was, until recently, relatively poorly understood and several studies in the literature appear to contradict each other. The first high-pressure study by Bridgman identified a very small change in volume at 3.1 GPa when a sample of AP was subjected to shear experiments at elevated temperatures.[5] The orthorhombic-to-cubic transition that occurs at 511 K at ambient pressure has been followed as a function of pressure up to 0.4 GPa, and this study reported a very strong pressure dependence (216 K GPa^{-1}) of the transition,[6] but subsequent optical studies determined that it was only weakly pressure-dependent.[7] These studies also reported the pressure dependence of the solid-liquid transition and claimed that there was no evidence for a high-pressure phase transition up to 26 GPa.[7] A powder X-ray diffraction study up to 5.0 GPa, combined with a shock compression study of the bulk speed of sound, identified no discernible phase changes up to 3.57 GPa, but by 4.70 GPa some alteration in the diffraction pattern was observed that was indicative of a phase transition. The new diffraction pattern, however, proved impossible to index.[8] An infrared study by Brill

et al. noted the disappearance of the vibrational band at 939 cm^{-1} associated with the ν_1 mode of the ClO_4^- group at pressures between 1.0-2.4 GPa, and tentatively assigned this to the orthorhombic-to-cubic phase transition.[9] The response of single crystals of AP to shockwaves up to 6.2 GPa has also been studied, but under these conditions no features were observed that could be identified as a shock-induced, sustained chemical reaction or phase transformation.[10] A subsequent study used these data to construct a thermo-mechanical model for shock compression normal to the (210) and (001) crystal planes and suggested that any phase transition occurred either with a negligible change in volume or with very slow kinetics.[11] Peiris *et al*. investigated the effects of pressures up to 5.6 GPa on AP using powder X-ray diffraction and IR and Raman spectroscopy.[12] Discontinuities observed in the Raman spectra at pressures of approximately 0.9 GPa and 3.0 GPa were attributed to phase transitions. New peaks were also observed in the X-ray diffraction pattern above 0.9 GPa that could not be indexed to the orthorhombic structure. The intensities of these new peaks increased up to 2.9 GPa, but above 3.0 GPa all of the peaks observed at lower pressure disappeared completely and a new set of peaks appeared that persisted up to 5.6 GPa, the limit of the study. Unfortunately, the authors were unable to index either of the patterns associated with the new high-pressure phases. The pressure-volume data up to 2.9 GPa obtained from the X-ray measurements were used to calculate a bulk modulus of 16.0 ± 0.2 GPa.[12] With the advances in techniques for the collection and data analysis of high-pressure diffraction data, Hunter *et al.* were, for the first time, able to obtain structural information at the molecular level for AP at elevated pressures.[13] Detailed structural information was obtained up to ~8 GPa using a combination of X-ray and Neutron diffraction techniques. The authors identified a first-order phase transition at 3.98 GPa under hydrostatic conditions. The new high-pressure structure (denoted phase II) was successfully solved and refined with space group *Pnma*.[13]

A complementary approach to experiment is atomistic simulation. Simulations can provide an effective way to model the properties and structures of crystalline materials. Zhu *et al.* recently performed an ambient-pressure DFT study of AP,[14] followed up by a hydrostatic compression study.[15] However, it is noteworthy that the authors used the incorrect crystal structure for their

computational model – the structure with space group $Pna2_1$ was used rather than the structure with space group *Pnma*. Recently, new dispersion correction schemes have been developed to augment traditional density functional theory.[16,17] Although AP is an ionic material, and therefore the contribution towards intermolecular bonding from dispersion may be expected to be quite low, there is evidence that the ions are linked through a hydrogen bonding network. Thus, an exploration of how well these dispersion correction schemes simulate the structure and properties of AP is worthy of investigation.[18,19]

This work was partly funded by QinetiQ, and one of the objectives was for this work to provide relevant data that can be used as input variables for Group Interactive Modelling (GIM).[20] Key parameters include cohesive energy (lattice energy), heat capacities and the effect of high-pressures on physical and mechanical properties.

4.2 Aims

Given the recent structural characterisation of the high-pressure behaviour of AP and the incorrect starting structure used in previous DFT studies, in addition to the project objectives identified by QinetiQ, the aims of this work were:

- to investigate the high-pressure Raman properties of AP
- to perform DFT calculations (at ambient and applied hydrostatic pressures) on crystalline AP using the correct starting structure
- in the process, to take the opportunity to investigate the performance of two different types of pseudopotential (as this work involves calculations at high pressure, the choice of pseudopotential is an important factor to consider in the simulations as the pseudopotential approximations describe the core electrons at ambient pressure, as an external pressure is applied different pseudopotentials will have individual performances as a function of pressure)

- to investigate the performance of a number of different DFT dispersion correction schemes at describing the high pressure structure and properties of AP
- to calculate the lattice energy of AP

4.3 Experimental

4.3.1 Raman Spectroscopy Studies

Raman measurements were conducted at ambient temperature on a powdered sample of AP compressed in a Merrill-Bassett DAC (40° half-opening angle), [21] equipped with 600 μm culets and a tungsten gasket with a 300 μm hole. A 4:1 mixture of methanol/ethanol was used as a hydrostatic PTM. A small ruby chip was also loaded into the cell as the pressure calibrant, with the ruby fluorescence method being utilised to measure the pressure. [22] Raman spectra were recorded on a Jobin-Yvon LabRam 300 spectrometer equipped with a 50 mW He-Ne laser of wavelength 632.8 nm.

4.3.2 Computational Methods

Structure optimisations (at ambient pressure and under hydrostatic externally applied pressure conditions) and vibrational frequency calculations were performed using density functional theory (DFT) and the plane-wave pseudopotential method as implemented in CASTEP version 5.5,[23] utilising the dispersion correction schemes of Grimme[16] and Tkatchenko & Scheffler[17]. Treatment of electronic exchange and correlation was handled by the generalised gradient approximation (GGA) formalised by Perdew, Burke and Ernzerhof (PBE).[24] The performance of two different types of pseudopotentials were tested [Vanderbilt 00PBE,[25] and on-the-fly (OTF)[26]]; the plane-wave cut-off energy used throughout was 650 eV, which ensured that total energies were converged to less than 5 meV per atom for both types of pseudopotential. Brillouin zone sampling was obtained using a 2 × 3 × 3 (4 k-point) M-P[27] grid. The structure was relaxed [using the BFGS[28] method] to allow both atomic coordinates and unit cell vectors to optimise simultaneously while constraining space group geometry (convergence criteria: maximum change in

system energy = 2 x 10^{-5} eV, maximum root-mean-square (RMS) force = 0.01 eV $Å^{-1}$, maximum RMS stress = 0.01 GPa and maximum RMS displacement = 0.002 Å). Following successful geometry optimisation, external hydrostatic pressures were applied from 0–3.5 GPa, in 0.5 GPa increments (and later, at pressures corresponding to available experimental data). Phonon frequencies (at the gamma point in k-space) for the optimised structures were then calculated by finite displacement methods.[29] In order to create potentials wells to determine lattice energies, single-point energy (SPE) calculations were performed on the experimental structure of AP for each scheme being investigated. Further SPE calculations on structures with smaller/larger volumes were performed by isotropically decreasing/increasing the experimental lattice parameters as described in Section 2.4.10.1.

4.4 Results and Discussion

4.4.1 Investigation into Choice of Computational Scheme

A comparison between the performance of conventional DFT and DFT-D for unit cell optimisation was performed by considering three different correction schemes: (i) no dispersion correction (NDC), (ii) the dispersion correction developed by Grimme[16] (G06) and (iii) the dispersion correction developed by Tkatchenko & Scheffler[17] (TS).

Furthermore, two different types of pseudopotential were also investigated, on-the-fly (OTF) CASTEP pseudopotentials and Vanderbilt-type ultrasoft pseudopotentials (00PBE). Both of these pseudopotentials are of the 'ultrasoft' type, however they have been optimised slightly differently resulting on slightly different core radii, r_c (above r_c the pseudopotential has exactly the same form as the all-electron wavefunction).[‡‡] Because of the different parameterisation of each pseudopotential each type will perform slightly differently, resulting in the calculation of slightly different optimised structures. For high pressure calculations, one also needs to consider the sum of the core radii of ion pair *ij*, $r_{c,ij}$, with respect to

[‡‡] r_c for the OTF pseudopotentials are: H = 0.425 Å, N = 0.741 Å, O = 0.531 Å and Cl = 0.902 Å. Corresponding r_c for the 00PBE pseudopotentials are: H = 0.423 Å, N = 0.740 Å, O = 0.529 Å and Cl = 0.900 Å.

the interatomic distances (bond length) of atoms *i* and *j*, $R_{i\text{-}j}$. If $r_{c,ij} >$, $R_{i\text{-}j}$ then the pseudopotentials are no longer applicable for use. Throughout the current investigation, the shortest calculated H-N and Cl-O bond lengths (at a pressure of 8.13 GPa) were $R_{H\text{-}N}$ = 1.0280 Å and $R_{Cl\text{-}O}$ = 1.4376 Å, respectively. The $r_{c,ij}$ for the OTF pseudopotentials are $r_{c,HN}$ = 1.166 Å and $r_{c,ClO}$ = 1.433 Å, with corresponding values for the 00PBE pseudopotentials being $r_{c,HN}$ = 1.163 Å and $r_{c,ClO}$ = 1.429 Å. Thus for all calculations performed in this study, all interatomic distances were greater than the sum of the pseudopotentials core radii, and both types of pseudopotential are applicable for use in these high-pressure calculations.

4.4.1.1 Convergence Testing

Convergence testing is usually performed to determine the optimum computational parameters to use when performing geometry optimisation calculations. DFT methods use functionals to approximate the effects of exchange and correlation so that the Schrödinger equation can be (approximately) solved, hence the ground state energy of the system determined. As the number of k-points and E_{cut} are increased the calculated ground state energy tends towards the 'real' value. However increasing the number of k-points and E_{cut} increases the computational expense. Thus a trade-off between computational accuracy and expense must be implemented; this is enforced by use of convergence criterion. In this study a convergence criterion of energy difference <5 meV per atom is used. This is only ~0.00005% of the total system energy, thus this criterion ensures that the greater accuracy obtained from using a more complete basis set is negligible compared to the extra computational expense.

Convergence testing with respect to both k-point sampling and E_{cut} was performed. First, the number of k-points to be used was determined by fixing the E_{cut} (to 400 eV) and performing single point energy calculations using differing numbers of k-points. TABLE 4.1 displays the results of the k-point convergence testing for OTF pseudopotentials. Similar results were obtained using 00PBE pseudopotentials. It is apparent that irrespective of the k-point mesh used, all system energies are calculated within 5 meV per atom of each other thus the number of k-

points used is unimportant. Thus for all further calculations a spacing of < 0.06 $Å^{-1}$ was used.

spacing ($Å^{-1}$)	*number k-points*	*energy (eV)*	*energy per atom (eV)*
0.015	120	-10085.70877	-252.1427
0.02	60	-10085.70517	-252.1426
0.025	36	-10085.71204	-252.1428
0.03	18	-10085.7005	-252.1425
0.04	12	-10085.70434	-252.1426
0.045	8	-10085.69298	-252.1423
0.05	8	-10085.69151	-252.1423
0.06	4	-10085.73416	-252.1434
0.07	2	-10085.71095	-252.1428

TABLE 4.1 Calculated system energies of crystalline AP as determined using differing k-point meshes while fixing the E_{cut} at 400 eV.

To determine the optimum E_{cut} needed, a series of single point energy calculations were performed on the AP crystal while systematically increasing E_{cut}. The results are plotted in Figure 4.2 for OTF pseudopotentials with the corresponding results obtained for 00PBE pseudopotentials plotted in Figure 4.3. It is apparent that the convergence criterion (energy difference <5 meV) is met at 600 eV using OTF pseudopotentials. However, for the 00PBE pseudopotentials, convergence is not reached until an E_{cut} of 650 eV. Thus to ensure a commensurate comparison of the performance of each pseudopotential all further calculations for each type of pseudopotential were performed with E_{cut} of 650 eV (at which the convergence criteria are met for both types of pseudopotential).

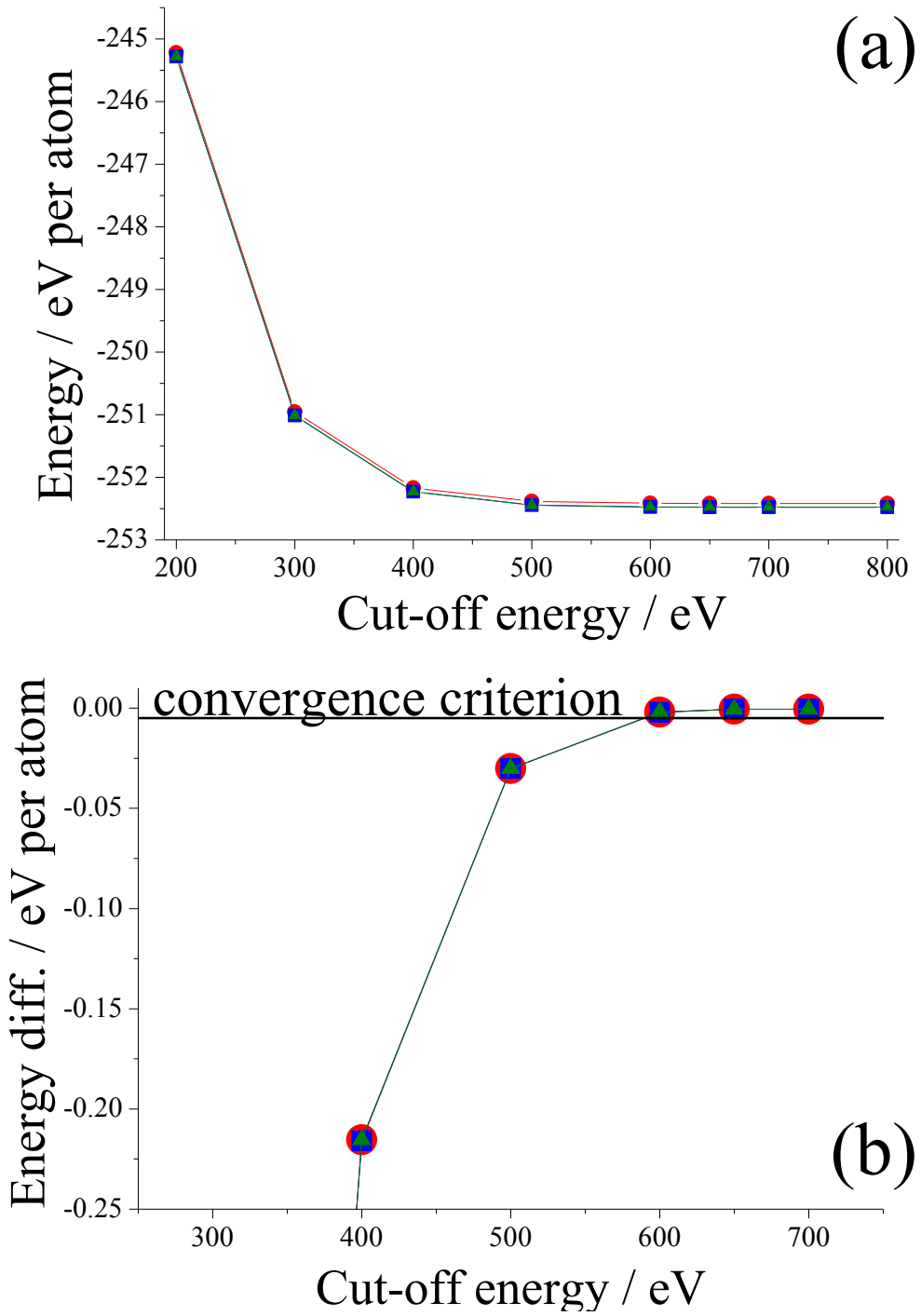

Figure 4.2 System energy per atom as a function of E_{cut} calculated using OTF pseudopotentials. NDC scheme: **red circle**, TS scheme: **blue square**, G06 scheme: **green triangle**. (a) displays the calculated system energies per atom against the E_{cut} used. (b) the energy difference of successive E_{cut} values are plotted such that the point labelled 400 eV is the difference in calculated energies between the 400 and 500 eV calculations, the point at 500 eV is the difference between the 500 and 600 eV calculations, *etc*.

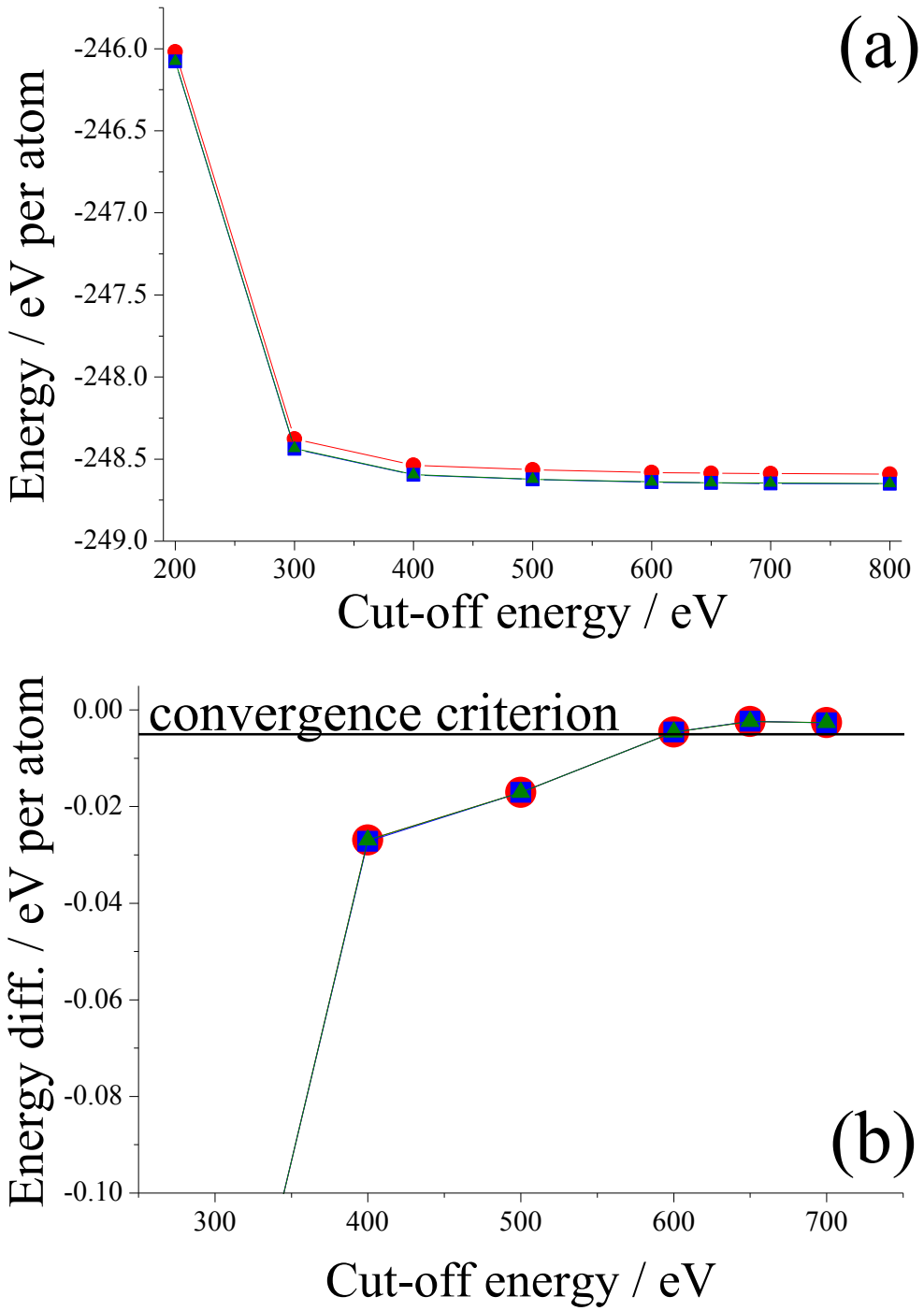

Figure 4.3 System energy per atom as a function of E_{cut} calculated using 00PBE pseudopotentials. NDC scheme: **red circle**, TS scheme: **blue square**, G06 scheme: **green triangle**. (a) displays the calculated system energies per atom against the E_{cut} used (b) the energy difference of successive E_{cut} values are plotted such that the point labelled 400 eV is the difference in calculated energies between the 400 and 500 eV calculations, , the point at 500 eV is the difference between the 500 and 600 eV calculations, *etc*.

4.4.1.2 Internal Geometries

In all simulations all N-H and Cl-O bond lengths and H-N-H and O-Cl-O bond angles are calculated within 2% of the experimental values (calculation to within 2% of experiment is considered as accurate) at ambient and under high-pressure conditions. As an example, the calculated bond lengths and angles at ambient pressure using OTF pseudopotentials are compared with experiment in TABLE 4.2. These results demonstrate no superiority between choice of pseudopotential or DFT-D scheme.

Bond	*Experiment*	*NDC*	*TS*	*G06*
Length (Å)				
N—H1	1.028	1.041	1.040	1.039
N—H2	1.028	1.041	1.040	1.039
N—H3	1.029	1.034	1.034	1.034
N—H4	1.027	1.043	1.041	1.042
Cl—O1	1.439	1.457	1.454	1.454
Cl—O2	1.439	1.457	1.454	1.454
Cl—O3	1.438	1.456	1.455	1.457
Cl—O4	1.437	1.445	1.444	1.444
Angle (deg.)				
H1—N—H2	109.38	108.66	108.45	108.50
H1—N—H3	109.50	110.42	110.40	110.21
H1—N—H4	109.49	108.30	108.61	109.05
H2—N—H3	109.49	110.42	110.40	110.21
H2—N—H4	109.50	108.30	108.61	109.05
H3—N—H4	109.46	110.66	110.33	109.79
O1—Cl—O2	109.03	108.80	108.73	108.85
O1—Cl—O3	109.53	108.88	108.95	108.89
O1—Cl—O4	109.60	110.07	110.11	110.13
O2—Cl—O3	109.53	108.88	108.95	108.89
O2—Cl—O4	109.60	110.07	110.11	110.13
O3—Cl—O4	109.53	110.11	109.97	109.94

TABLE 4.2 Experimental and calculated bond lengths (Å) and angles (degrees) of crystalline AP at ambient pressure.

4.4.1.3 Crystal Geometries

Compression studies in the region 0.0–3.5 GPa were performed allowing atomic positions and unit cell vectors to optimise simultaneously, whilst preserving crystal symmetry.

The effect of pressure on the lattice parameters for the three DFT schemes are compared to the experimental data of Hunter *et al.*[13] as shown in Figure 4.4. From this, it can be seen that all calculations underestimate the ambient pressure *a*-axis lattice parameter: the NDC scheme by 2.7%; the TS scheme by 5.8%; and the G06 scheme by 5.6% using OTF pseudopotentials (with the corresponding values for the 00PBE pseudopotentials being 2.9, 6.0 and 5.8%, respectively). As pressure is applied the *a*-axis lattice parameter decreases monotonically for both types of pseudopotential, which follows the experimental trend. The OTF pseudopotentials show a steady compression rate, in contrast to the 00PBE pseudopotentials which tended towards more erratic predictions in the 1.0-2.5 GPa pressure region for all three DFT schemes. However, regardless of how favourable the compression trend is, both types of pseudopotential produce similar overall compression parameters between 0.0–3.5 GPa. The experimental compression ratio at 3.5 GPa, a/a_0 (where a_0 is the length of unit cell parameter a at 0 GPa) is 0.944;[13] corresponding a/a_0 ratios calculated using OTF pseudopotentials are 0.939, 0.953 and 0.951 for the NDC, TS and G06 schemes, respectively (with the corresponding values for the 00PBE pseudopotentials being 0.932, 0.947 and 0.946).

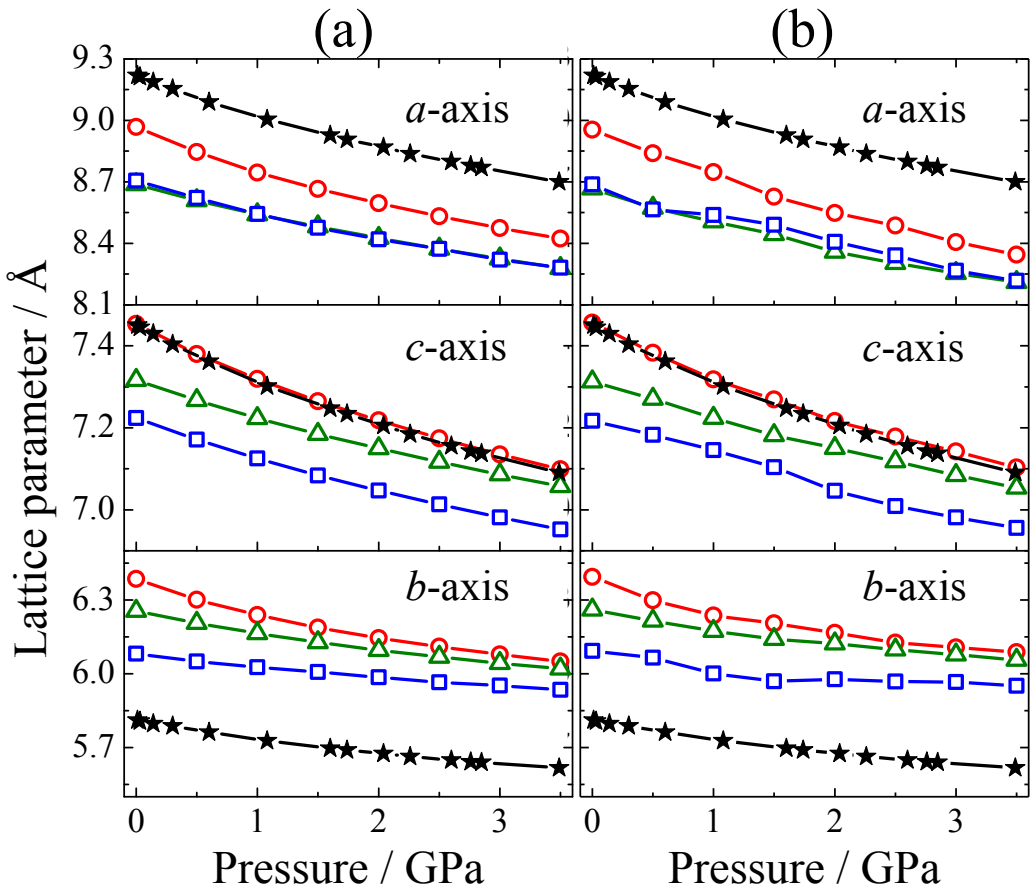

Figure 4.4 Lattice parameters as a function of hydrostatic pressure for crystalline AP. NDC scheme: **red circle**, TS scheme: **blue square**, G06 scheme: **green triangle** and experimental[13]: **black star**. (a) OTF pseudopotentials, (b) 00PBE pseudopotentials.

All three functionals overestimate the *b*-axis lattice parameter: the NDC scheme by 9.9%, the TS scheme by 7.6% and the G06 scheme by 4.7% at ambient pressure using OTF pseudopotentials (with the corresponding values for the 00PBE pseudopotentials being 10.0, 7.7 and 4.9%). Consistent with experimental results,[13] the *b*-axis lattice parameter decreases monotonically for both types of pseudopotential. As in the case of the *a*-axis, the OTF pseudopotentials replicate the trend of smooth compression observed experimentally, while the 00PBE pseudopotentials deviate from the experimental trend. The experimental compression ratio of the *b*-axis at 3.5 GPa, b/b_0 is 0.967;[13] corresponding b/b_0 ratios calculated using OTF pseudopotentials are 0.948, 0.963 and 0.976 for the NDC, TS and G06 schemes, respectively (with the corresponding values for the 00PBE pseudopotentials being 0.952, 0.967 and 0.977).

For the compression of the *c*-axis with respect to pressure, the two dispersion corrections underestimate the *c*-axis lattice parameter. Using the OTF pseudopotentials at ambient pressure, the difference between the calculated and experimental[13] *c*-axes are 0.0% using the NDC scheme, -1.8% for the TS scheme and -3.0% using the G06 scheme (with the corresponding values for the 00PBE pseudopotentials being 0.1, -1.9 and -3.1%). The trends in the compression behaviour of the *c*-axis are analogous to those found for the *a*- and *b*- axes. The experimental compression ratio of the *c*-axis at 3.5 GPa, c/c_0 is 0.952;[13] corresponding c/c_0 ratios calculated using OTF pseudopotentials are 0.952, 0.965 and 0.962 for the NDC, TS and G06 schemes, respectively (with the corresponding values for the 00PBE pseudopotentials being 0.953, 0.965 and 0.964).

Figure 4.5 depicts the overall unit cell volume compression as a function of pressure. The compression results are compared with experiment and are fitted to 3rd order Birch-Murnaghan (B-M) equations of state (EoS) of the form given in Equation 4.1:[30]

$$P = 3B_0 f_E (1+2f_E)^{\frac{5}{2}}\left(1+\frac{3}{2}(B'-4)f_E+\frac{3}{2}\left(B_0B''+(B'-4)(B'-3)+\frac{35}{9}\right)f_E^2\right)$$

Equation 4.1

where P is the pressure at a given volume, V, B_0 is the bulk modulus (compressibility) of the material, B' and B'' are the first and second pressure derivatives of B_0, and f_E is the Eulerian strain and is given by Equation 4.2:

$$f_E = \frac{\left(\frac{V_0}{V}\right)^{\frac{2}{3}}-1}{2}$$

Equation 4.2

where V_0 is the zero-pressure volume. Overall, this yields a three-parameter EoS (with V_0, B_0 and B') with an implied value of B'' given by Equation 4.3.[31]

$$B'' = \frac{-1}{B_0}\left((3-B')(4-B')+\frac{35}{9}\right)$$

Equation 4.3

The results indicate that at ambient pressure, the unit cell volumes differ from experiment by +7.0%, -0.4% and -4.2% for NDC, TS and G06 respectively using OTF pseudopotentials (with the corresponding values for the 00PBE pseudopotentials being +7.0, -0.6 and -4.3%). Inspection of these unit cell volumes in isolation implies that the TS dispersion correction provides a very good model, nonetheless a good computational model must accurately describe not only the cell size, but also the cell shape. The TS functional attains this favourable unit cell volume by significantly underestimating the *a*-axis and overestimating the *b*-axis, thereby predicting the 'correct' unit cell volume through cancellation of errors.

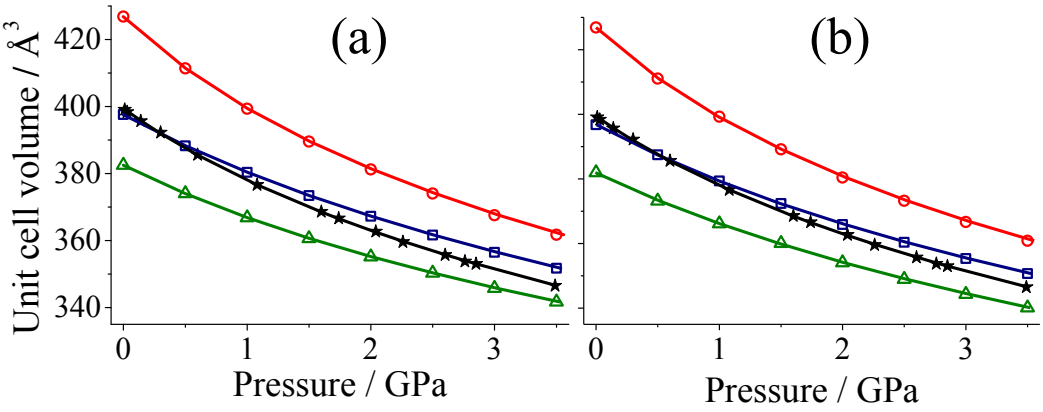

Figure 4.5 Unit-cell volume as a function of pressure fitted with 3rd order B-M EoS for crystalline AP. NDC: **red circle**, TS: **blue square**, G06: **green triangle** and experimental[13]: **black star**. (a) OTF pseudopotentials, (b) 00PBE pseudopotentials.

As the degree of compression was increased, the inaccuracy of the predicted unit cell volume diminished using the NDC scheme. These results mirror those obtained by Byrd *et al.*[32] and Conroy *et al.*[33] who concluded that as the degree of compression is increased, the intermolecular interactions become more important and thus conventional DFT is better able to describe accurately the intermolecular interactions and so gives a better agreement with experiment.

	Experiment[13]	NDC	TS	G06
V_0 (Å^3)	399.33(20)	426.87	397.53	382.50
B_0 (GPa)	14.91(25)	11.96	19.91	20.50
B'	7.32(23)	7.12	5.96	7.53

TABLE 4.3 Experimental and calculated 3rd order B-M EoS parameters of crystalline AP over the pressure range 0-3.5 GPa.

An appropriate way to compare the simulated compression of the overall unit cell (*i.e.* both cell shape and volume) with experiment is to calculate an EoS. TABLE 4.3 shows that the NDC scheme provides the best agreement with experiment for both B_0 and B'. Although the curvature of the EoS predicted by the TS and G06 schemes are respectable, both significantly overestimate the bulk modulus.

These compression results have determined that:

(i) the OTF pseudopotentials perform better than the 00PBE pseudopotentials in describing the high pressure structural behaviour of AP. This is exemplified by the fact that the OTF pseudopotentials reproduce monotonic compression for all lattice parameters in agreement with the experimentally determined trend, whereas the 00PBE pseudopotentials tend to produce erratic results in the 1.0-2.5 GPa pressure region.

(ii) this study has established that no significant improvement in the calculation of crystal geometries of AP are obtained by employing DFT-D corrections. In fact, all three schemes investigated here (conventional DFT [NDC scheme], and the dispersion corrections proposed by Grimme[16] [G06 scheme] and Tkatchenko & Scheffler[17] [TS scheme]) cannot accurately describe the structure of AP. All schemes calculate lattice parameters with percentage differences from experiment of ~ -3–6% for the *a*-axis, ~ +5–10% for the *b*-axis and ~ -0–3% for the *c*-axis. These results suggest that although there is experimental evidence that the ions in AP are linked through a H-bond network the dispersive contribution to intermolecular interactions in AP is indeed low, and the structure is dominated by Coulombic interactions that these DFT methods cannot accurately describe.

(iii) irrespective of how accurately the various DFT schemes describe the overall structure of AP, the predictions for the rate of compression is much better; values obtained for the compression of all lattice vectors are within 2% of experimental values between 0.0–3.5 GPa, additionally EoS parameters are calculated in reasonable agreement to those experimentally determined.

4.4.1.4 Vibrational Properties

A comprehensive study of the experimental gamma-point vibrational modes including mode symmetry has been performed elsewhere.[18] From this it was observed that in the condensed phase of AP, the molecular ions (of symmetry T_d) are placed on a site of lower (C_s) symmetry. Thus, the mode character for the isolated tetrahedral ion (T_d) undergoes site splitting, shown in Equation 4.4:

$$\begin{aligned} &T_d \rightarrow C_s, \\ &A_1(\nu_1) \rightarrow A', \\ &E(\nu_2) \rightarrow A' + A'', \\ &T_2(\nu_3, \nu_4) \rightarrow 2A' + A''. \end{aligned}$$

Equation 4.4

The degeneracies of the E and T_2 modes are therefore lifted as a result of a reduction in local site symmetry. The space group of AP (*Pnma* or D_{16}^{2h}) has four formula units in the unit cell (Figure 4.1) and so the expected modes are found from the correlation shown in Equation 4.5:

$$\begin{aligned} &4A_1 \rightarrow 4A' \rightarrow A_g + B_{2g} + B_{1u} + B_{3u}, \\ &4E \rightarrow \begin{cases} 4A' \rightarrow A_g + B_{2g} + B_{1u} + B_{3u} \\ 4A'' \rightarrow A_u + B_{2u} + B_{1g} + B_{3g} \end{cases}, \\ &4T_2 \rightarrow \begin{cases} 4A' \rightarrow A_g + B_{2g} + B_{1u} + B_{3u} \\ 4A' \rightarrow A_g + B_{2g} + B_{1u} + B_{3u} \\ 4A'' \rightarrow A_u + B_{2u} + B_{1g} + B_{3g} \end{cases}. \end{aligned}$$

Equation 4.5

The total number of modes in a crystal lattice is $3N$, where N is the number of atoms in the unit cell. Thus for AP, which has 40 atoms in the unit cell, there are 120 calculated modes. Of these, the first three correspond to acoustic modes which represent the three translations of the unit cell (assigned to symmetry species B_{1u}, B_{2u} and B_{3u}) and should have zero frequency at the gamma-point. From Equation 4.5 it is apparent that the remaining 117 optical modes must conform to four symmetric stretching modes, eight symmetric bending modes, twelve asymmetric stretching modes, and twelve asymmetric bending modes, *i.e.* 36 internal modes each for NH_4^+ and ClO_4^-. The 45 remaining modes are lattice modes, of symmetry $6B_{1g} + 6B_{2g} +$

$6B_{3g} + 6A_g + 5B_{1u} + 5B_{2u} + 5B_{3u} + 6A_u$. For the D_{16}^{2h} (*Pnma*) space group only the *gerade* modes (i.e. B_{1g}, B_{2g}, B_{3g} and A_g) are Raman active. (Note full tables of all 120 modes calculated at each pressure value for each DFT scheme and type of pseudopotential can be found on the Supplementary Information CD, in addition, also contained on the CD are the experimental Raman data, the computationally calculated structures and the CASTEP output files for the geometry optimisations, the lattice energy calculations, and the phonon calculations).

This group theoretical analysis relates to the equilibrium (0 K) structure, but in reality the number of peaks observed experimentally will vary with temperature, as random reorientation of the ions will eventually cause the observed site and correlation splittings to be motionally averaged.[34] Experimentally, Prask *et al.*[18] have identified 22 of the 24 possible Raman-active lattice modes predicted by group theory, 15 of the 18 Raman active ClO_4^- modes, and 15 of 18 possible NH_4^+ modes.

Label	Exp.[18] ν	Symmetry $\left(D_{16}^{2h}\right)$	NDC ν	TS ν	G06 ν
M_1	34.5	B_{1g}	54.5	69.1	52.8
M_2	50.5	B_{3g}	58.9	68.3	59.4
M_3	60	A_g	49.6	63.9	60.6
M_4	65	B_{3g}	67.6	81.5	96.3
M_5	65	B_{2g}	72.3	77.8	76.7
M_6	70.3	A_g	66.5	82.7	79.6
M_7	81	B_{1g}	59.7	84.2	75.1
M_8	82	B_{3g}	79.9	97.9	102.6
M_9	93.5	A_g	84.0	102.6	95.5
M_{10}	97	B_{1g}	70.2	97.9	108.9
M_{11}	112	B_{3g}	136.9	175.2	134.4
M_{12}	113	B_{1g}	134.0	163.4	136.7
M_{13}	115	B_{2g}	73.0	94.5	90.4
M_{14}	118	B_{2g}	94.7	117.6	123.2
M_{15}	157.5	A_g	135.4	160.4	157.8
M_{16}	158	B_{2g}	169.5	195.5	195.6
M_{17}	168	B_{3g}	238.1	228.1	195.4
M_{18}	174	B_{1g}	232.0	220.1	182.3
M_{19}	175	A_g	163.6	193.1	194.6
M_{20}	199	B_{2g}	195.3	215.7	213.3
M_{21}	220	A_g	289.4	297.4	295.1
M_{22}	232	B_{2g}	294.3	298.9	295.3

TABLE 4.4 Experimental and calculated Raman active lattice vibrational modes of AP. All frequencies, **ν**, are in cm^{-1}.

The computational results obtained in this study (using OTF pseudopotentials) are compared with all 22 of the lattice modes as shown in TABLE 4.4 (for phonon calculation results using 00PBE pseudopotentials please see the Supplementary Information CD). Due to the fact that the computational models of AP do not accurately reproduce the unit cell shape and size, the predicted lattice modes show some variation from experiment. The NDC scheme (using the OTF pseudopotentials) predicts only seven lattice modes within 10% of experiment, whereas the TS scheme predicts only six modes and the G06 scheme eight modes within this error range. A further four, seven and five modes for each respective scheme are within 20% of experiment. Thus, eleven lattice modes for the NDC scheme, nine modes for the TS scheme and nine modes for the G06 scheme differ from experiment by more than 20%. The 00PBE pseudopotentials did not perform as well; only six, three and three modes were within 10%, with eleven, nineteen and

sixteen modes differing from experiment by more than 20% for the NDC, TS and G06 schemes, respectively.

Mode (T_d ion)	Label	Exp.[18] **ν**	Symmetry $\left(D_{16}^{2h}\right)$	NDC **ν**	TS **ν**	G06 **ν**
E (ν_2)	M_{23}	464	B_{3g}	442.8	446.6	444.0
Symmetric	M_{24}	464	B_{1g}	445.1	449.0	447.6
bend	M_{25}	467.5	A_g	446.1	451.0	449.9
	M_{26}	467.5	B_{2g}	446.1	451.0	450.4
T_2 (ν_4)	M_{27}	624	B_{3g}	596.0	597.8	596.6
Asymmetric	M_{28}	624.5	A_g	594.7	596.9	597.0
bend	M_{29}	629.5	B_{2g}	599.4	603.0	603.3
	M_{30}	637	A_g	617.1	621.0	619.2
	M_{31}	643	B_{2g}	621.3	625.5	623.9
A_1 (ν_1) Symmetric stretch	M_{32}	941.5	A_g	907.8	914.7	910.8
T_2 (ν_3)	M_{33}	1070	A_g	1036.7	1041.5	1034.4
Asymmetric	M_{34}	1080	B_{3g}	1061.1	1069.3	1070.5
stretch	M_{35}	1104	B_{2g}	1076.5	1086.4	1082.5
	M_{36}	1118	A_g	1092.1	1096.2	1097.5
	M_{37}	1139	B_{2g}	1111.7	1117.2	1117.8

TABLE 4.5 Experimental and calculated Raman-active vibrational modes of the perchlorate ion of AP. All frequencies, **ν**, are in cm^{-1}.

The computational calculations fared better at reproducing the internal geometries of AP, and this is also reflected in the calculation of the internal vibrational modes. TABLE 4.5 compares the calculated and experimental Raman-active modes (using OTF pseudopotentials) for the perchlorate ion under ambient-pressure conditions. The NDC scheme predicts all modes to within 2% of the experimental values at ambient pressure using the 00PBE pseudopotentials, corresponding results for the OTF pseudopotentials are predicted within 5%. The TS scheme predicts all modes within 2.5% except for the symmetric bending modes which are calculated to within 5% using the 00PBE pseudopotentials, all modes are predicted within 4.5% of experiment using the OTF pseudopotentials. The G06 scheme predicts frequencies within 2.5% and 4% of experiment for 00PBE and OTF pseudopotentials, respectively.

All internal modes associated with the ammonium ion (reported in TABLE 4.6) were calculated to within 5% of experiment irrespective of the choice of pseudopotentials or dispersion-correction scheme. These results suggest that, in contrast to the results obtained for internal geometries and unit cell shape and size (where generally the OTF pseudopotentials provide better agreement with experiment), at ambient pressure it is the 00PBE pseudopotentials that generally fair better in comparison to the experimental values. This is particularly true for the internal modes of the perchlorate ion. It should be noted that, the computationally calculated phonon data appear to suggest a possible miss-assignment of the experimental data for the NH_4^+ symmetric bending modes. All three schemes, using both types of pseudopotential, suggest that the symmetries of the B_{1g} mode (M_{43}) and the B_{3g} mode (M_{44}) should be swapped. Thus it is suggested that M_{43} has symmetry B_{3g} and that M_{44} has symmetry B_{1g}.

Mode (T_d ion)	Label	Exp.[18] **ν**	Symmetry $\left(D_{16}^{2h}\right)$	NDC **ν**	TS **ν**	G06 **ν**
T_2 (ν_4)	M_{38}	1409	A_g	1403.3	1409.0	1398.0
Asymmetric	M_{39}	1409	B_{2g}	1405.6	1408.3	1396.2
bend	M_{40}	1422	B_{1g}	1412.5	1412.0	1403.0
	M_{41}	1422	B_{3g}	1415.9	1414.0	1403.9
	M_{42}	1427	A_g	1447.1	1438.3	1426.3
E (ν_2)	M_{43}	1665	B_{1g}	1655.7	1653.5	1640.5
Symmetric	M_{44}	1673	B_{3g}	1643.7	1641.4	1627.2
bend	M_{45}	1687	B_{2g}	1665.7	1667.4	1654.4
	M_{46}	1695	A_g	1681.1	1684.2	1670.9
A_1 (ν_1)						
Symmetric	M_{47}	3201	A_g	3262.2	3281.2	3260.5
stretch	M_{48}	3206	B_{2g}	3267.9	3287.3	3267.2
T_2 (ν_3)	M_{49}	3262	A_g	3313.0	3330.9	3332.3
Asymmetric	M_{50}	3292	B_{1g}	3344.6	3358.5	3370.6
stretch	M_{51}	3327	A_g	3453.4	3455.9	3453.8
	M_{52}	3343	B_{2g}	3463.5	3466.4	3464.0

TABLE 4.6 Experimental and calculated Raman active ammonium ion vibrational modes of AP. All frequencies are, **ν**, in cm^{-1}.

The preceding results have demonstrated that the 00PBE ultrasoft pseudopotentials are unable to describe accurately the high-pressure behaviour of AP. For this reason, the following discussion comparing calculated high-pressure

vibrational properties with high-pressure experimental Raman spectra focuses only on the results obtained using OTF pseudopotentials.

To augment previously published experimental data,[12] Raman measurements as a function of pressure were collected as part of this work.[§§,35] The observed peaks in the room-temperature Raman spectra are listed as a function of pressure in TABLE 4.7. A typical (assigned) spectrum obtained inside a DAC is shown in Figure 4.6 alongside a spectrum of polycrystalline AP on a glass slide. The nine experimentally determined room-temperature modes encompass seventeen calculated (0 K) modes. The contribution of the calculated modes to each of the experimental room temperature modes is noted in the labelling of each mode. Thus for example, in the final column in TABLE 4.7, the label $M_{47\text{-}48}$, denotes that this experimental mode incorporates both of the computationally derived NH_4^+ symmetric stretching modes A_g (M_{47}) and B_{2g} (M_{48}).

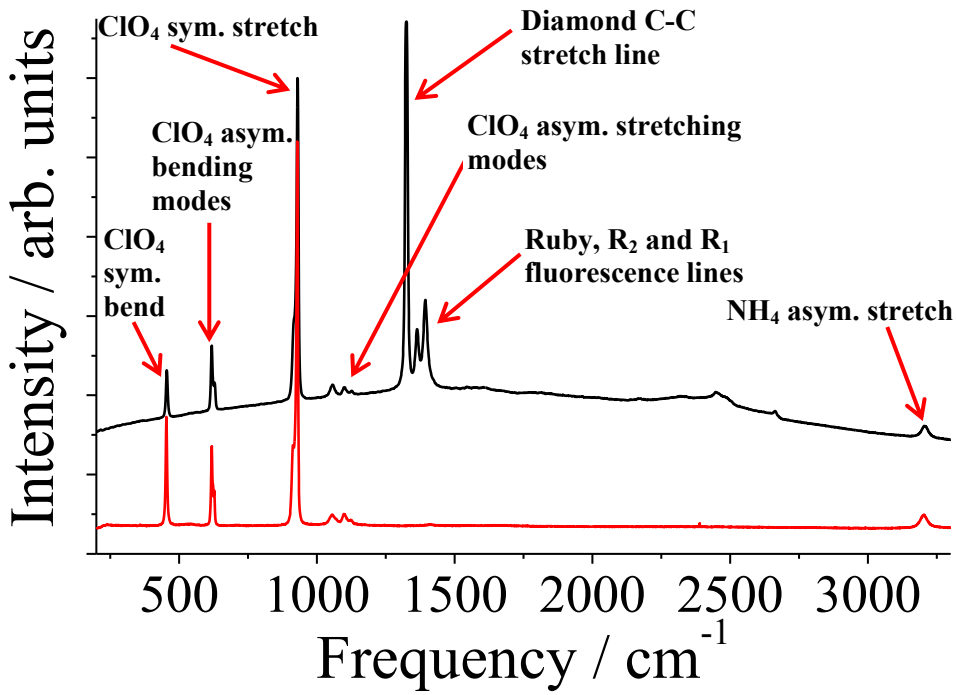

Figure 4.6 Typical room-temperature Raman spectra of AP collected using the Jobin-Yvon LabRam 300 spectrometer. **Black** powder sample in a DAC, **red** powder sample on glass slide.

[§§] Peiris *et al.*[12] have performed Raman measurements as a function of pressure. In the study Fluorinert FC-75 was used as PTM. However, careful studies by Varga *et al.*[§§] demonstrated that Fluorinert FC-75 remains truly hydrostatic only up to 1.2 GPa. Thus the assumed hydrostaticity of the Raman measurements made by Peiris *et al.*[12] at pressures above 1.3 GPa are questionable.

Pressure (GPa)	M_{23-26}	M_{27-28}	M_{29}	M_{30-31}	M_{32}	M_{33}[a] (M_{33-34})[b]	M_{34-35}[a] (M_{35-36})[b]	M_{36-37}[a] (M_{37})[b]	M_{47-48}
	ν	**ν**	**ν**	**ν**	**ν**	**ν**	**ν**	**ν**	**ν**
0.26	456	619	624	629	931	1058	1100	1127	3208
0.72	456	618	623	692	932	1060	1100	1128	3212
1.26	458	619	627	632	935	1064	1104	1131	3217
1.72	460	620	626	633	937	1067	1105	1133	3221
2.09	461	621	628	634	939	1070	1109	1135	3224
2.38	462	622	629	635	941	1073	1110	1137	3226
3.13	465	625	633	640	944	1076	1113	1141	3234
3.72	466	625	633	640	946	1079	1113	1143	3238

TABLE 4.7 The pressure response of the Raman-active experimental vibrational frequencies of AP (this work). All frequencies, **ν**, are in cm^{-1}. [a] Combination of modes predicted by computational models. [b] Combination of modes assigned experimentally by Prask *et al.*[18]

Figure 4.7 depicts the typical effect of pressure on one of the vibrational modes, *i.e.* the asymmetric bending mode of the perchlorate ion labelled M_{32} (note the shoulder in this figure corresponds to an overtone of the symmetric bending mode of the perchlorate ion). All experimentally observed modes harden linearly with pressure; this was also observed from computations (see Figure 4.8 and Figure 4.9), where the effect of pressure on all frequencies was calculated using the NDC scheme.

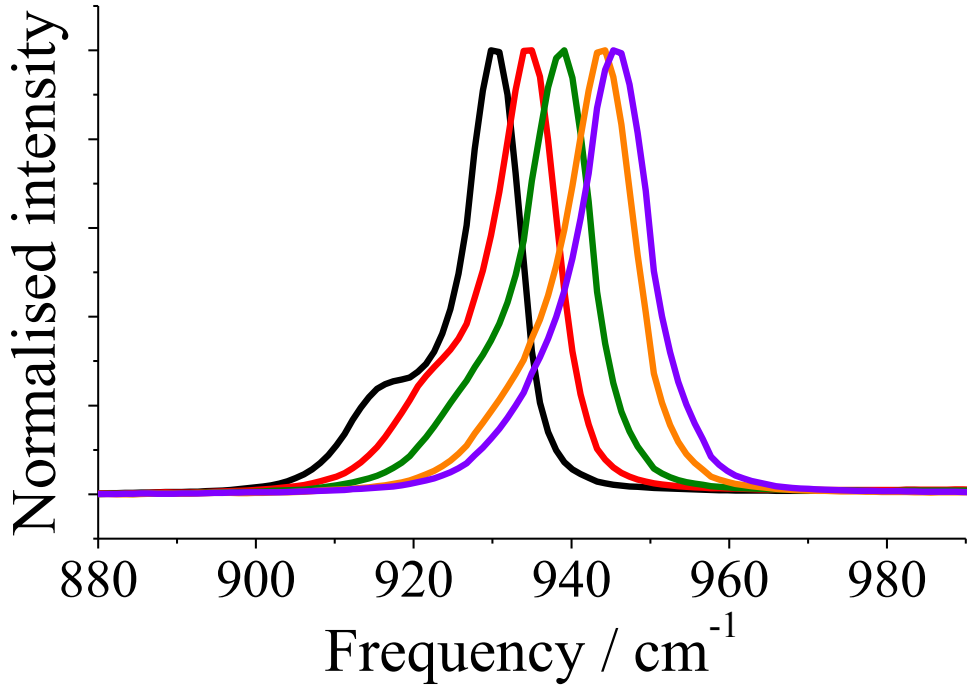

Figure 4.7 Raman spectra displaying the pressure induced shift of the symmetric stretching mode of the perchlorate ion. 0.26 GPa: **black**; 1.26 GPa: **red**; 2.09 GPa: **green**; 3.13 GPa: **orange**; 3.72 GPa: **purple**.

In the Raman experiments, with the exception of the symmetric stretch, all the modes associated with the ammonium ion were very broad (due to the large amplitude oscillations of the ions) and thus could not be resolved. This is consistent with previous findings.[18] For the symmetric stretching mode, the effect of temperature has caused the correlation splitting to disappear, and therefore only one peak was observed, which incorporates both the A_g (M_{47}) and the B_{2g} (M_{48}) low temperature modes. The symmetric stretching mode of the perchlorate ion, M_{32}, is also a singlet as only one low-temperature mode contributes to the room temperature mode. $M_{23\text{-}26}$ is the symmetric bending mode of the perchlorate ion; it is a single peak as both site- and correlation-splittings have been motionally averaged due to temperature. Three ClO_4^- asymmetric bending modes are observed ($M_{27\text{-}28}$, M_{29} and $M_{30\text{-}31}$), thus implying that although the correlation splitting has been averaged, site splitting still exists at room temperature for the asymmetric bending modes. The same is true for the asymmetric stretching modes; again three modes are observed in the Raman spectrum at room temperature. Unlike the asymmetric bending modes, which combine in a fashion in agreement with the low-temperature experiment,[18] for the asymmetric stretching modes, the contributing modes to each peak differ between those predicted by the computational model and the experimental assignments. TABLE 4.7 depicts both scenarios; (a) M_{33}, $M_{34\text{-}35}$ and $M_{36\text{-}37}$ as predicted by the computational models and (b) $M_{33\text{-}34}$, $M_{35\text{-}36}$ and M_{37} as assigned experimentally by Prask *et al*..[18]

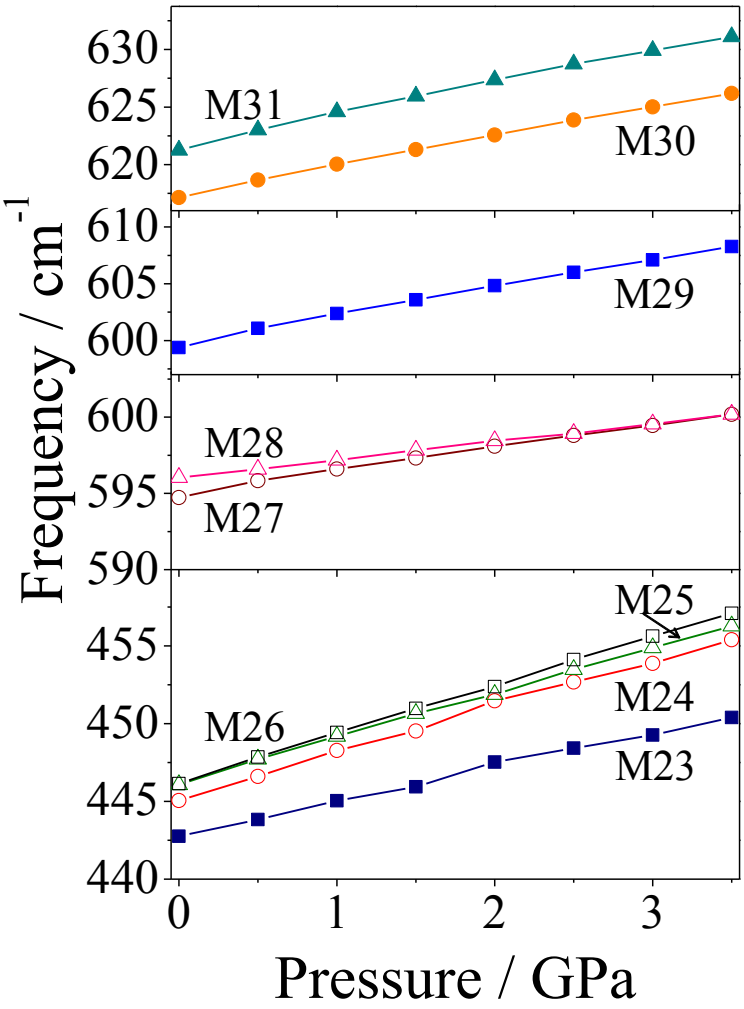

Figure 4.8 Pressure-induced shifts of vibrational frequencies associated with the ClO_4^- bending modes of crystalline AP calculated using the NDC scheme.

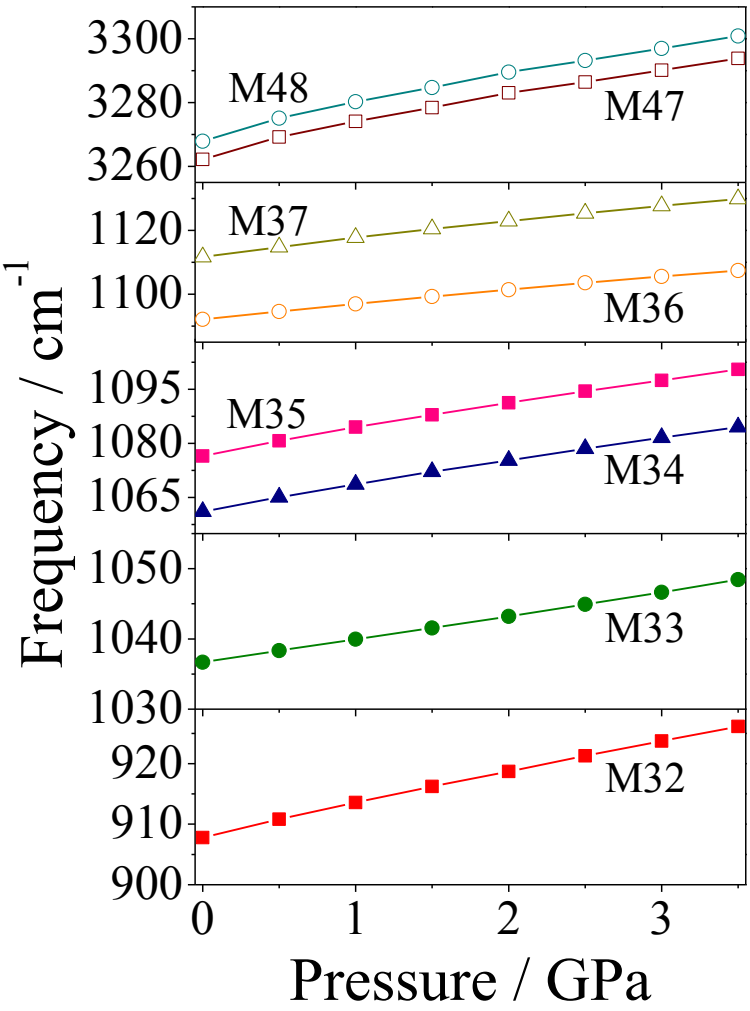

Figure 4.9 Pressure-induced shifts of vibrational frequencies associated with the ClO_4^- stretching modes and the NH_4^+ symmetric stretching modes of crystalline AP calculated using the NDC scheme.

Coefficients of mode hardening in units of cm^{-1} GPa^{-1} (*i.e.* the shift in frequency of each mode due to applied pressure) for both the experimental and computational vibrational frequencies are compared in TABLE 4.8. From this, it is shown, that the experimentally calculated coefficients are generally well reproduced by all computational models. The NDC and TS schemes produce very similar results for all perchlorate ion modes (all modes in TABLE 4.8 except for M_{47-48}), and all schemes predict the coefficients for the perchlorate ion symmetric (M_{23-26}), and asymmetric bending modes (M_{27-28}, M_{29}, M_{30-31}) within 0.9 cm^{-1} GPa^{-1} of experiment. For the symmetric stretching mode (M_{32}) both the TS and NDC schemes predict the pressure induced shift coefficient within 0.6 cm^{-1} GPa^{-1}, while the prediction using the G06 scheme is inferior, with a difference of 1.1 cm^{-1} GPa^{-1}.

However, the situation as described above regarding the perchlorate ion asymmetric stretching modes is not so straightforward. Irrespective of which scheme is used, all computational models predict the third asymmetric stretching mode (M_{36-37}, M_{37}) within 0.8 cm^{-1} GPa^{-1}, which is in good agreement with experiment. When combining the peaks as predicted by the computational models, rather large deviations from experimental predictions are obtained; the computationally calculated coefficients for M_{33} differ from experiment by 3.1, 2.6 and 1.7 cm^{-1} GPa^{-1} for the NDC, TS and G06 schemes, respectively. However, significantly improved agreement with experiment is obtained when combining modes M_{33} and M_{34} (as assigned experimentally by Prask *et al.*) with differences of only 1.4, 1.4 and 0.8 cm^{-1} GPa^{-1} for the NDC, TS and G06 schemes. The same effect is observed for the M_{34-35}/M_{35-36} mode; differences from experiment for the NDC, TS and G06 schemes reduce from 2.3, 1.8 and 2.5 cm^{-1} GPa^{-1} for the M_{34-35} to 1.2, 0.9 and 1.0 cm^{-1} GPa^{-1} for the M_{35-36} combination, respectively.

Mode	Exp. (This work)	NDC	TS	G06
M_{23-26}	3.2	2.8	2.9	3.9
M_{27-28}	2.2	1.4	1.4	1.9
M_{29}	3.0	2.5	2.4	2.7
M_{30-31}	3.6	2.7	2.7	3.1
M_{32}	4.6	5.2	5.2	5.7
M_{33}[a]	6.4	3.3	3.8	4.7
M_{33-34}[b]		5.0	5.0	5.6
M_{34-35}[a]	4.4	6.7	6.2	6.9
M_{35-36}[b]		5.6	5.3	5.4
M_{36-37}[a]	4.9	4.8	4.7	4.1
M_{37}[b]		5.2	5.1	4.4
M_{47-48}	8.8	9.1	5.8	10.3

TABLE 4.8 Experimental and calculated coefficients (cm^{-1} GPa^{-1}) for the pressure-induced shifts of the internal vibrational modes of crystalline AP. [a] Combination of modes predicted by computational models. [b] Combination of modes assigned experimentally by Prask *et al.*[18]

In summary, phonon calculations as a function of pressure have been performed together with an experimental high-pressure Raman study. These results demonstrate that:

(i) the largest errors in calculation of the vibrational modes occur in the lattice-mode region. This is not unexpected as the unit cell is not accurately

described using DFT methods. However, the internal vibrational modes are calculated in good agreement with experiment due to the fact that DFT methods accurately calculate the internal geometries of AP

(ii) no significant differences were identified between the various DFT schemes in the calculation of the vibrational frequencies

(iii) the comprehensive vibrational mode analysis performed in this study has identified a possible experimental miss-assignment by Prask *et al*.[18] in the symmetries of two of the ammonium ion symmetric bending modes

(iv) an experimental linear pressure dependence for the pressure induced shifts of all vibrational modes in the Raman spectra of AP has been highlighted, with the corresponding shifts calculated to be in good agreement with experiment for all three DFT schemes investigated

4.4.2 Computational Compression Study on Phase I and Phase II

Having determined that the 'on-the-fly' pseudopotentials perform better for high-pressure calculations of AP, further hydrostatic-compression calculations were performed (using OTF pseudopotentials) to explore whether the various DFT schemes are able to differentiate between the two phases of AP (I and II).

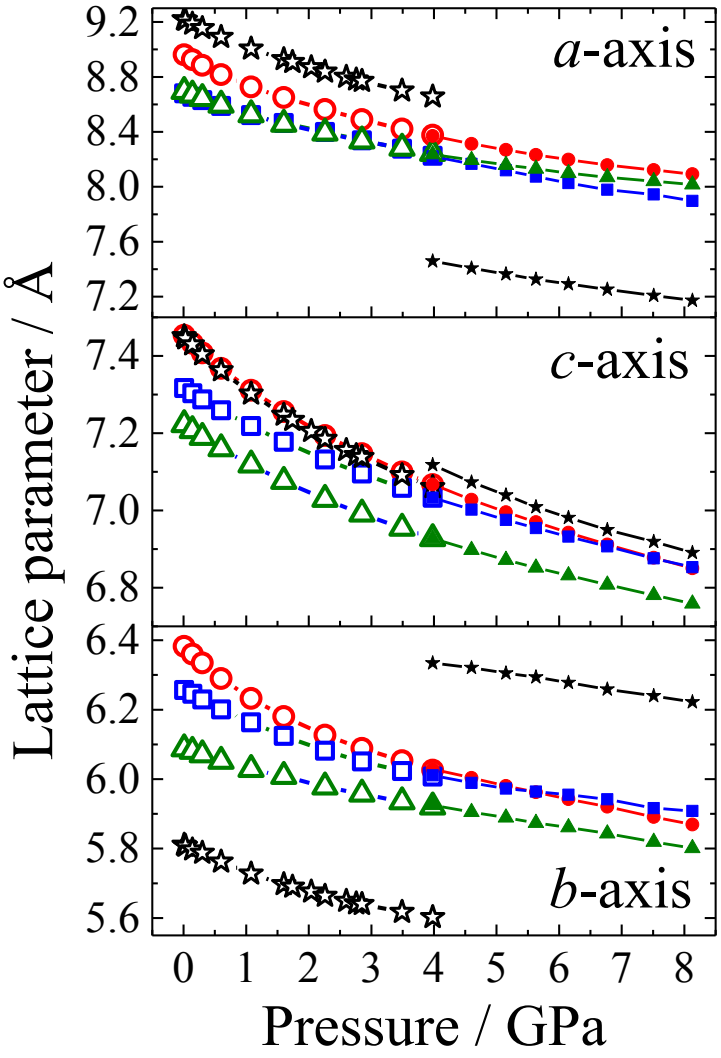

Figure 4.10 Lattice parameters as a function of hydrostatic pressure for crystalline AP. NDC scheme: **red circle**, TS scheme: **blue square**, G06 scheme: **green triangle** and experiment:[13] **black star**. Open symbols phase I, closed symbols, phase II.

Figure 4.10 displays the calculated lattice parameters as a function of pressure compared with available experimental data. In addition, the calculated and experimentally determined unit-cell volumes for phases I and II are presented in Figure 4.11. The calculated open symbol points are optimisation results starting from the ambient-pressure (phase I) structure, whereas the solid points are the optimisation results using the recently refined high-pressure (phase II) structure.[13] For the experimental data, the open and closed symbols represent phases I and II, respectively.

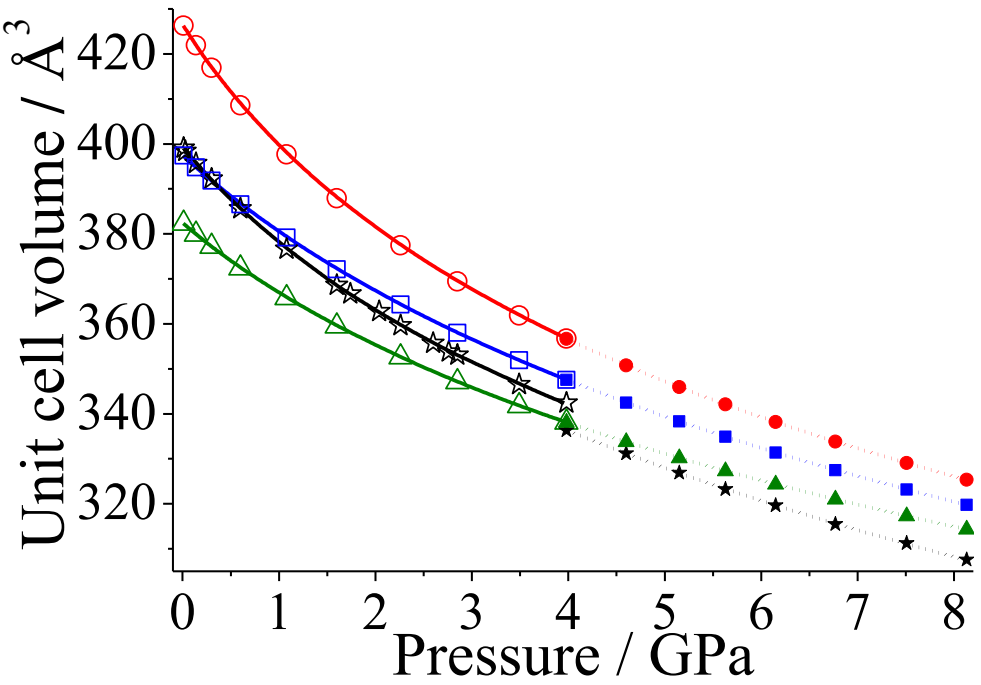

Figure 4.11 Unit cell volume as a function of pressure fitted with 3rd order B-M EoS (Equation 4.1) for crystalline AP. NDC: **red circle**, TS: **blue square**, G06: **green triangle** and experimental: **black star**. Open symbols phase I, closed symbols, phase II.

It is apparent from these figures that all three computational schemes cannot distinguish between the structures of phase I and phase II, with the same computational structure produced regardless of starting structure. This result is not unexpected considering the structural similarity between the experimental phase I and phase II structures and the inability of the DFT method to describe accurately the structure of AP.

4.2.3 Prediction of Lattice Energy

The lattice energy of AP has been predicted using the NDC, TS and G06 schemes by constructing potential wells as described in Section 2.4.10.1. Figure 4.4 shows the calculated potential wells obtained for phase I AP.

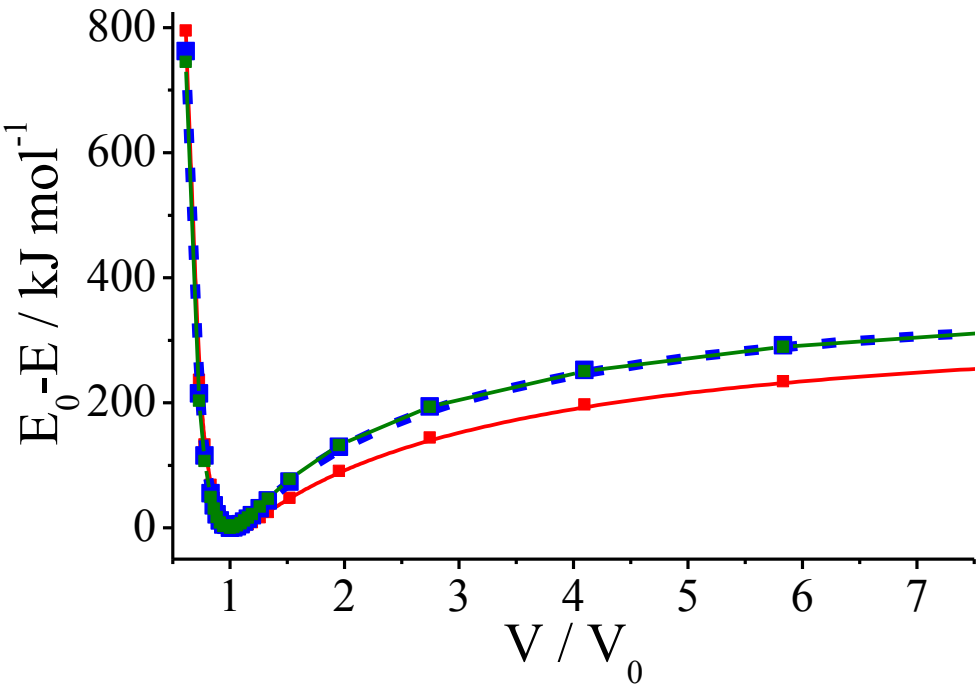

Figure 4.12 Calculated potential wells for AP fitted with Lennard-Jones type potentials. **Red square** NDC, **blue square** TS and, **green square** G06 schemes, respectively.

As the difference in energy (E_0-E in units of kJ mol^{-1}) is plotted in Figure 4.12, rather than the actual system energies, the calculated variable *E* (from Equation 2.32, described in Chapter 2) is the magnitude of the lattice energy. Thus, the lattice energies calculated using the NDC, TS and G06 schemes are shown in TABLE 4.9, in addition to the other fitting parameters, A – D from Equation 2.32.

	Variable A	*Variable B*	*Variable C*	*Variable D*	E_L (kJ mol^{-1})
NDC	141.46	0.68	5.53	0.65	-376.23
TS	164.44	0.66	5.62	0.76	-417.24
G06	168.42	0.67	5.43	0.77	-419.54

TABLE 4.9 Calculated lattice energies and fitting variables as determined from Equation 2.32, of AP for the NDC, TS and G06 schemes.

The enthalpy of sublimation of AP [$\Delta H_{sub}(NH_4ClO_{4(s)})$] has been experimentally determined by several different methods, with values of ΔH_{sub} ranging from 234.3 – 254.4 kJ mol^{-1}.[36,37,38,39,40,41] All of the aforementioned values of ΔH_{sub} were determined on the assumption that sublimation occurs by the dissociation process in the following equation:

$$NH_4ClO_{4\,(s)} \rightleftharpoons NH_{3\,(g)} + HClO_{4\,(g)}$$

Equation 4.6

Thus, AP sublimes entirely through the dissociation process on the surface of the crystal.[42] Hence, the experimental sublimation enthalpy is not comparable to the calculated lattice energies due to the mechanism of sublimation.

To provide an analogous 'experimental' result to the computed lattice energy, a Born-Haber cycle for the lattice energy of AP has been produced (Figure 4.13). For the purposes of the Born-Haber cycle, the mean of the six reported values, with standard deviation error (240.7 ± 7.4 kJ mol^{-1}) has been used as the ΔH_{sub} of AP. The following experimental values have been used: the bond dissociation enthalpy of the O-H bond in perchloric acid, D_0 (H-OClO$_{3(g)}$) [449.4 ± 25.5 kJ mol^{-1}],[43] the electron affinity of the perchlorate molecule, E_{ea} (ClO$_{4(g)}$) [-506.56 ± 9.65 kJ mol^{-1}],[44] the proton affinity of ammonia, E_{pa} (NH$_{3(g)}$) [-859 ± 2 kJ mol^{-1}],[45] and the ionisation enthalpy of hydrogen, IE (H$_{(g)}$) [1312.05 kJ mol^{-1}].[46]

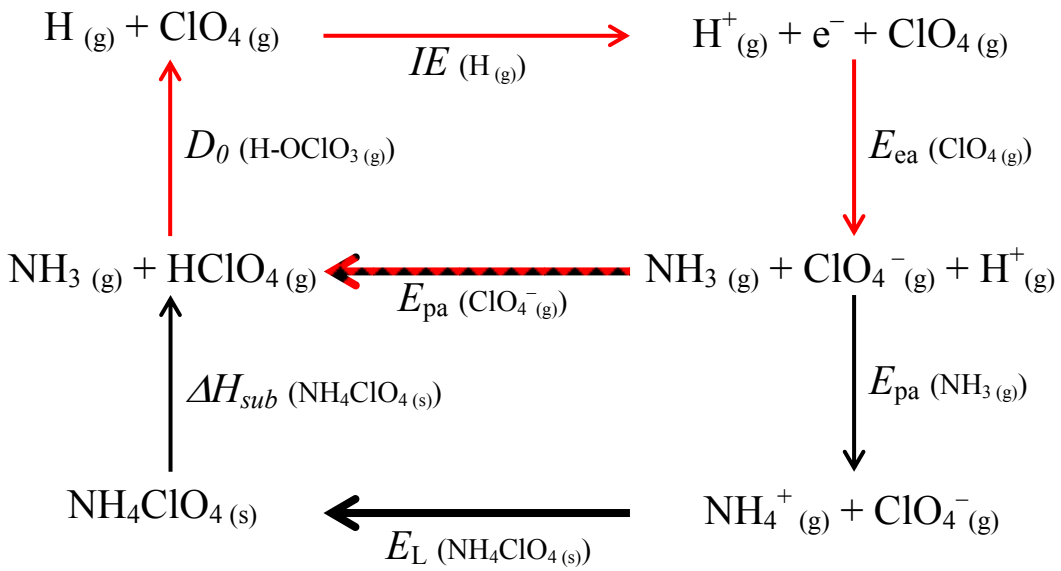

Figure 4.13 Born-Haber cycle of AP.

By following the black circuit of the Born-Haber cycle in Figure 4.13, it can be seen that the 'experimental' lattice energy for AP can be determined from Equation 4.7:

$$E_{\mathrm{L}}\,(NH_4ClO_{4(s)}) \;=\; -\,E_{\mathrm{pa}}\,(NH_{3(g)}) \;+\; E_{\mathrm{pa}}\,(ClO_4^{-}{}_{(g)}) \;-\; \Delta H_{sub}(NH_4ClO_{4(s)})$$

Equation 4.7

However, $E_{\mathrm{pa}}\,(ClO_4^{-}{}_{(g)})$ is unknown, and so first one must follow the red circuit of the Born-Haber cycle in Figure 4.13, hence, the proton affinity of the perchlorate ion, $E_{\mathrm{pa}}\,(ClO_4^{-}{}_{(g)})$, can be determined using Equation 4.8; yielding a value of -1254.89 ± 27.26 kJ mol^{-1}.

$$E_{\mathrm{pa}}\,(ClO_4^{-}{}_{(g)}) \;=\; -\,E_{\mathrm{ea}}\,(ClO_{4(g)}) \;-\; IE\,(H_{(g)}) \;-\; D_0\,(H\text{-}OClO_{3(g)})$$

Equation 4.8

It follows that by utilising the result from Equation 4.8 in Equation 4.7, the black circuit is completed and the 'experimental' lattice energy for AP can be determined, yielding a value of -636.6 ± 28.3 kJ mol^{-1}.

An alternate method for the prediction of the lattice energy is to use the Kapustinskii Equation[47] as shown in Equation 4.9:

$$E_{\mathrm{L}} = \frac{120{,}200m|Z_a||Z_c|}{r_a + r_c}\left(1 - \frac{34.5}{r_a + r_c}\right)$$

Equation 4.9

where the lattice energy E_{L} is given in units of kJ mol^{-1}, m is the number of ions in the formula of the compound, r_a and r_c are the ionic radii of the anion and the cation in units of pm and Z_a and Z_c are their charges, respectively.

The literature values of the ionic radii for the ammonium and perchlorate ions are 136 ± 19 and 225 ± 19 pm, respectively.[48] Hence, the lattice energy for AP predicted by the Kapustinskii equation is -602.29 ± 44.83 kJ mol^{-1}. Thus, the 'experimental' lattice energies proposed by the Born-Haber cycle and the Kapustinskii equation agree within error, and are also in agreement with the previously reported Ewald summation result of 601.66 kJ mol^{-1}, collectively providing a good estimate of the actual (experimental) lattice energy.

Comparison of the computationally predicted lattice energies of -376.23, -417.24 and -419.54 kJ mol^{-1} for the NDC, TS and G06 schemes, respectively, with the 'experimental' lattice energy shows that all of the computational methods

significantly underestimate the lattice energy. This is perhaps not an unexpected result as the preceding structural study has shown that all three schemes cannot describe accurately the intermolecular (electrostatic) interactions in AP. Admittedly, the DFT-D dispersion correction schemes predict lattice energies slightly closer to the 'experimental' value, however, in line with the structural and vibrational predictions, implementation of DFT-D rather than DFT does not provide a significant increase in accuracy of the prediction of the lattice energy for AP.

4.5 Conclusions

Density functional theory studies of the hydrostatic compression of AP have been performed in the region of 0.0-3.5 GPa in order to compare the performances of different pseudopotentials and DFT dispersion correction schemes in the calculation of crystal geometries and vibrational frequencies at high pressure. The results demonstrate that the choice of pseudopotential used for high-pressure calculations is important and highlight that 00PBE ultrasoft pseudopotentials are unable to describe accurately the high-pressure compression behaviour of AP. Using 'on-the-fly' (OTF) pseudopotentials generated using the CASTEP code reproduces the experimental compression behaviour of phase I for all DFT dispersion correction schemes used.

This study has highlighted the fact that the DFT methods investigated here cannot accurately predict the structure of AP. This suggests that although there is experimental evidence that the ions in AP are linked weakly through a hydrogen bonding network, the dispersive contribution to the lattice energy of AP is small with coulombic interactions dominating over dispersive intermolecular forces. However, irrespective of how well each scheme describes the intermolecular interactions of AP, the modelling of EoS parameters (B_0 and B') proved successful, particularly for the NDC scheme, where good agreement with experiment was obtained.

The high-pressure vibrational properties of crystalline AP have been studied using Raman spectroscopy, elucidating that all Raman-active vibrational modes undergo linear pressure-induced (blue-) shifts with applied hydrostatic pressure. Similarly, this was confirmed computationally as the results of the comprehensive

vibrational mode analysis produced pressure-induced shifts in good agreement with experimental data.

This study has established that no significant improvement in the calculation of crystal geometries and vibrational properties of AP are obtained by employing DFT-D corrections. Furthermore, the ability of the differing computational models to differentiate between phase I and phase II was investigated, but as the DFT methods do not accurately describe the intermolecular interactions in AP, all three models were unable to differentiate between the structural differences between the two phases.

To provide input data for group interaction modelling (GIM) DFT methods have been used to predict the lattice energy of AP, furthermore approximate 'experimental' values of the lattice energy were determined using Born-Haber cycles and the Kapustinskii equation. The predicted lattice energies are in poor agreement with the 'experimental' values. Nevertheless, the lattice energy determined by the Born-Haber cycle (-636.6 ± 28.3 kJ mol^{-1}) should be a good approximation of the actual experimental lattice energy of AP, and thus provides valuable information that can be used in the GIM.

4.6 Further Work

This study has highlighted the limitations of the DFT method for describing ionic interactions; they are not properly described. In the future, to accurately model the structure of AP and similar ionic materials, one could use classical modelling methods, such as an experimentally parameterised force-field. However, this would require significant work to develop, in addition, force-fields are generally non-transferable to other systems (except perhaps those with extremely similar intermolecular interactions). As the development of dispersion correction methods for use in DFT is a very active research field, and new procedures are constantly being implemented, the computational expense of higher-level DFT dispersion correction methods (such as XDM,[49] van der Waals density functionals,[50] or adiabatic-connection fluctuation-dissipation theorem methods[51,52]) is continually decreasing. In addition, different dispersion correction methods are developed with

different parameterisation, and thus other methods may be more suitable for the accurate description of the AP structure. Hence, in the near future it may be (computationally) cost-effective to investigate the capability of such methods to adequately describe the intermolecular interactions of AP.

4.7 References

1 Jacobs, P. W. M.; Whitehead, H. M. *Chem. Rev.* **1969**, *69*, 551.
2 Politzer, P.; Lane, P. *J. Mol. Strut.* **1998**, *454*, 229.
3 Brill, T. B.; Budenz, B. T. *Progr. Astronaut. Aeronaut.* **2000**, *185*, 3.
4 Stammler, M.; Bruenner, R.S.; Schmidt, W.; Orcutt, D. *Adv. X-ray Anal.* **1966**, *9*, 170.
5 Bridgman, P. W. *Proc. Amer. Acad. Arts Sci.* **1937**, *72*, 45.
6 Richter, P. W.; Pistorius, C. F. W. T. *J. Solid State Chem.* **1971**, *3*, 434.
7 Foltz, M. F.; Maienschein, J. L. *Mater. Lett*. **1995**, *24*, 407.
8 Sandstrom, F. W.; Persson, P. A.; Olinger, B. *AIP Conference Proceedings* **1994**, *309*, 1409.
9 Brill, T. B.; Goetz, F. *Papers in Astronaut. Aeronaut.* **1978**, *63*, 3.
10 Yuan, G.; Feng, R.; Gupta, Y. M.; Zimmerman, K. A. *J. Appl. Phys.* **2000**, *88*, 2371.
11 Winey, J. M.; Gruzdkov, Y. A.; Dreger, Z. A.; Jensen, B. J.; Gupta, Y. M. *J. Appl. Phys.* **2002**, *91*, 5650.
12 Peiris, S. M.; Pangilinan, G. I.; Russell, T. P. *J. Phys. Chem. A* **2000**, *104*, 11188.
13 Hunter, S.; Davidson, A. J.; Morrison, C. A.; Pulham, C. R.; Richardson, P.; Farrow, M. J.; Marshall, W. G.; Lennie, A. R.; Gould, P.J. *J. Phys. Chem. C* **2011**, *115*, 18782.
14 Zhu, W.; Wei, T.; Zhu, W.; Xiao, H. *J. Phys. Chem. A* **2008**, *112*, 4688.
15 Zhu, W.; Zhang, X.; Zhu, W.; Xiao, H. *Phys. Chem. Chem. Phys.* **2008**, *10*, 7318.
16 Grimme, S. *J. Comput. Chem.* **2006**, *27*, 1787.
17 Tkatchenko, A.; Scheffler, M. *Phys. Rev. Lett.* **2009**, *102*, 073005.
18 Prask, H. J.; Choi, C. S.; Chesser, N. J.; Rosasco, G. J. *J. Chem Phys.* **1988**, *88*, 5106.
19 Choi, C. S; Prask, H. J.; Prince, E. *J. Chem Phys.* **1974**, *61*, 3523.
20 Porter, D. in *Group Interaction Modelling of Polymer Properties*, Marcel Dekker, New York, **1995**.
21 Merrill, L.; Bassett, W. A. *Rev. Sci. Instrum.* **1974**, 45, 290.
22 Piermarini, G. J.; Block, S.; Barnett, J. D.; Forman, R. A. *J. App. Phys.* **1975**, *46*, 2774.
23 Clark, S. J.; Segall, M. D.; Pickard, C. J.; Hasnip, P. J.; Probert, M. J.; Refson, K.; Payne, M. C. *Z. Krystallogr.* **2005**, *220*, 567.
24 Perdew, J. P.; Burke, K.; Ernzerhof, M. *Phys. Rev. Lett.* **1996**, *77*, 3865.
25 Vanderbilt, D. *Phys. Rev. B* **1990**, *41*, 7892.
26 Vackar, J.; Hytha, M.; Simunek, A. *Phys. Rev. B* **1998**, *58*, 12712.

27 Monkhorst, H. J.; Pack, J D. *Phys. Rev. B* **1976**, *13*, 5188.
28 Fischer, T. H.; Almlof, J. *J. Phys. Chem.* **1992**, *96*, 9768.
29 Frank, W.; Elsässer, C.; Fähnle, M. *Phys. Rev. Lett.* **1995**, *74*, 1791.
30 Birch, F.; *Phys. Rev.* **1947**, *71*, 809.
31 Anderson, O. L. in *Equations of States of Solids for Geophysics and Ceramic Science*, Oxford University Press, Oxford, **1995**.
32 Byrd, E. F. C.; Rice, B. M. *J. Phys. Chem. C* **2007**, *111*, 2787.
33 Conroy, M. W.; Oleynik, I. I.; ZybinS. V.; White, C. T. *J. App. Phys.* **2008**, *104*, 053506.
34 Oxtoby, W. *Annu. Rev. Phys. Chem.* **1981**, *32*, 77.
35 Varga, T,; Wilkinson, A. P.; Angel, R. J. *Rev. Sci. Instrum.* **2003**, *74*, 4564.
36 Powling, J.; Smith, W. A. W. *Combust. Flame* **1962**, *6*, 173.
37 Powling, J.; Smith, W. A. W. *Combust. Flame* **1963**, *7*, 269.
38 Inami, S. H.; Rosser, W. A.; Wise, H. *J. Phys. Chem.* **1963**, *67*, 1077.
39 Pearson, G. S. *Advan. Inorg. Chem. Radiochem.* **1966**, *8*, 177.
40 Davies, J. V.; Jacobs, P. W. M.; Russell-Jones, A. *Trans. Faraday Soc.* **1967**, *63*, 1737.
41 Jacobs, P. W. M.; Russell-Jones, A. *J. Phys. Chem.* **1968**, *72*, 202.
42 A.G. Keenan and R. F. Siegmund in *Thermal Decomposition of Ammonium Perchlorate*, Special Report No. 6 (AD673542), Office of Naval Research, **1968**.
43 Meyer, M. M.; Kass, S. R. *J. Phys. Chem. A* **2010**, *114*, 4086.
44 Wang, X.- B.; Wang L.- S. *J. Chem Phys.* **2000**, *113*, 10928.
45 Jenkins, H. D. B.; Morris, D. F. C. *J. Chem. Soc., Faraday Trans. 2* **1984**, *80*, 1167.
46 http://webbook.nist.gov/
47 House, J. E. in *Inorganic Chemistry 2nd Edition*, Academic Press, Elsevier, Amsterdam, **2013**.
48 Roobottom, H. K.; Jenkins, H. D. B.; Passmore, J. Glasser, L. *J. Chem Educ.* **1999**, *76*, 1570.
49 Becke, A. D.; Johnson, E. R. *J. Chem. Phys.* **2007**, *127*, 154108.
50 Lee, K.; Murray, E. D.; Kong, L., Lundqvist, B. I.; Langreth, D. C. *Phys. Rev. B* **2010**, *82*, 081101.
51 Dobson, J. F.; Dinte, B, P. *Phys. Rev. Lett.* **1991**, *44*, 4032.; Furche, F.; Van Voorhis, V. *J. Chem. Phys.* **2005**, *122*, 164106.
52 Ángyán, J. G.; Liu, R.; Toulouse, J.; Jansen, G. *J. Chem. Theory Comput.* **2011**, *7*, 3116.; Hesselmann, A. *Phys. Rev. A* **2012**, *85*, 012517.

Chapter 5

DFT-D Investigations of Various Polymorphs of RDX

5 DFT-D Investigations of Various Polymorphs of RDX

5.1 Introduction

RDX (cyclotrimethylenetrinitramine) is a secondary high explosive commonly used in military applications - its structure is shown in Figure 5.1. At ambient temperature and pressure, the thermodynamically stable phase is the α-form, the crystal structure of which has been determined by both single crystal X-ray[1] and neutron diffraction studies.[2] The ambient-pressure vibrational properties of α-RDX have been extensively studied by polarised Raman spectroscopy,[3,4,5] and more recently by inelastic neutron scattering (INS).[6] At ambient pressure there also exists a metastable β-form of RDX, which was first identified in 1950 by McCrone[7] and has subsequently been studied using vibrational spectroscopy.[8,9] On account of its high metastability with respect to the α-form, it was only recently structurally characterised.[10] There has been a long-standing assumption that β-RDX could only be grown from high boiling solvents,[7,8] but Infante-Castillo *et al*.[11] demonstrated on the basis of Raman spectra that α-RDX can undergo a solid-solid phase transition to β-RDX upon heating. Furthermore, Goldberg *et al.* performed a comprehensive investigation into crystal growth of β-RDX and demonstrated that the β-form can consistently be obtained from a wide range of solvents using the technique of drop-cast crystallisation.[12]

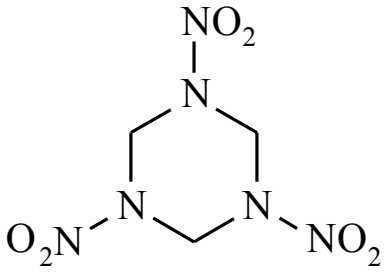

Figure 5.1 Molecular structure of RDX.

Compression of the α-form to pressures exceeding 3.9 GPa at ambient temperature induces a phase transition to the γ-form, which has been structurally characterised by neutron powder diffraction and single crystal X-ray diffraction.[13]

Vibrational studies at elevated pressures include Raman studies at ambient temperature that explored the effect of hydrostatic compression on the vibrational properties of both α- and γ-forms of RDX.[14,15] Ciezak & Jenkins used spectroscopic methods to obtain a P-T phase diagram of RDX.[16] Raman and far-infrared spectroscopic studies suggest a further high-pressure polymorph at pressures >17.8 GPa, denoted as the δ-form,[16,17] but the crystal structure of this δ-form is currently unknown. Millar *et al*. recently characterised a high-pressure/high-temperature polymorph, ε-RDX (obtained by compression of RDX through the α → γ phase transition then heating to 448 K), using a combination of diffraction techniques.[18] The Raman spectra of ε-RDX have also been reported.[19,20] The phase diagram of RDX elucidated by considering the data obtained from all these studies is shown in Figure 5.2.

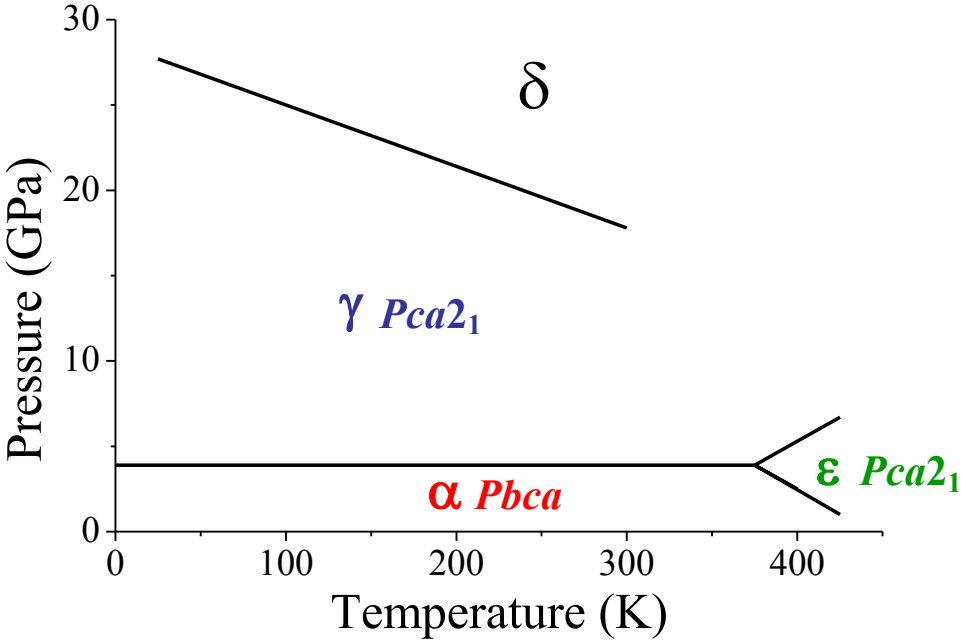

Figure 5.2 Pressure-Temperature phase diagram for RDX labelled with thermodynamically stable phases in each regime and space group symmetry if known.

A complementary approach to experiment is atomistic simulation, which provides an effective way to model the properties and structure of crystalline materials. The suitability of density functional theory (DFT) for studying energetic molecular materials has been reported in depth.[21,22,23] It is well known that conventional DFT methods cannot provide reliable results for intermolecular interactions in systems for which vdW or dispersion interactions are the major

component. Byrd *et al.* studied a series of energetic materials at ambient pressure and found poor agreement with experiment, with errors as high as 9.6% for the calculation of lattice parameters.[21] A subsequent study demonstrated that an increase in pressure diminishes the importance of the dispersion interactions relative to the increasing contribution of the repulsive interactions.[22] As the external pressure applied to the simulation cell increased, the inaccuracies of the predicted intermolecular distances and lattice parameters relative to experimental data decreased, to the extent that good agreement with experiment was produced for pressures greater than 6-7 GPa.[21,22]

Shimojo *et al.*[24] have shown that the dispersion correction proposed by Grimme (2006)[25] accounts accurately for the dispersion interactions for the α-RDX crystal in the high-pressure regime (0 – 15 GPa), while incurring little additional computational overhead. In addition, the authors determined that the non-empirical van der Waals density-functional (vdW-DF) method also provides an accurate description of the vdW interactions, but requires orders-of-magnitude more computational resource.[24] Similarly, Sorescu *et al.* performed theoretical predictions of the responses of the crystallographic lattice parameters to pressure for ten energetic molecular crystals, including the α- and γ-forms of RDX.[26] They concluded that the dispersion-corrected density functional theory method (DFT-D) as parameterised by Grimme[25] provides significant improvements for the description of intermolecular interactions in molecular crystals at both ambient and high pressures relative to conventional DFT. Balu *et al.* investigated the performance of dispersion-corrected atom-centered pseudopotentials (DCACP's) at describing the ambient-pressure crystal structure of several energetic materials and demonstrated excellent agreement with experiment, giving results that were comparable to DFT-D studies.[27]

5.2 Aims

Given the recent increase in understanding of the polymorphism of RDX (recent structural characterisation of the high-pressure/high-temperature ε-RDX and advances in the techniques for producing β-RDX) and the successful implementation

of dispersion corrections to accurately describe the structure of RDX, the aims of this work were:

- to obtain complete ambient pressure vibrational information of α-RDX by means of inelastic neutron scattering spectroscopy
- to demonstrate the capability of the DFT-D functional parameterised by Grimme[25] to accurately reproduce the structure, vibrational and thermo-chemical properties of various forms of RDX at ambient pressure
- to attempt to determine the enthalpy of fusion of the highly metastable β-form of RDX, in the process further validating the predictive capability of the computational model used in this study
- to perform the first ever computational compression study on the newly structurally characterised ε-polymorph of RDX
- to investigate the suitability of the DFT-D functional parameterised by Grimme[25] to accurately predict the high-pressure structure and vibrational properties of the α-, γ- and ε-polymorphs of RDX
- to utilise the results of phonon calculations to predict the effect of pressure on the heat capacities of RDX to provide insight to the requirements of potential experimental techniques for measuring heat capacities at elevated pressure

5.3 Experimental

5.3.1 Computational Methods

Structure optimisations (at ambient pressure and under hydrostatic externally applied pressure conditions) and vibrational frequency calculations were performed using density functional theory plus dispersion (DFT-D) coupled to the plane-wave pseudopotential method, as implemented in CASTEP version 5.5.[28] The dispersion correction scheme of Grimme[25] was utilised throughout. Treatment of electronic

exchange and correlation was handled by the generalised gradient approximation (GGA) formalised by Perdew, Burke and Ernzerhof (PBE).[29] On-the-fly (OTF) [30] pseudopotentials were generated using CASTEP expressed at an E_{cut} of 700 eV, which ensured convergence of lattice parameters and total energies to less than 1 meV per atom. Brillouin zone sampling was obtained using M-P[31] grids of $2 \times 2 \times 3$, $2 \times 3 \times 2$ and $3 \times 2 \times 2$ for the α-, γ- and ε-polymorphs, respectively (all resulting in 2 k-points in the irreducible Brillouin zone). The structures were relaxed [using the BFGS[32] method] to allow both atomic coordinates and unit cell vectors to optimise simultaneously whilst constraining space group geometry. The following convergence criteria were applied: maximum change in system energy = 2×10^{-5} eV, maximum RMS force = 0.025 eV $Å^{-1}$, maximum RMS stress = 0.01 GPa and maximum RMS displacement = 0.002 Å. Following successful geometry optimisation, external hydrostatic pressures were applied at pressures corresponding to the available experimental data. Phonon frequencies (at the gamma point in k-space) for the optimised structures were then calculated by finite displacement methods.[33] In order to create potentials wells to determine lattice energies, single-point energy (SPE) calculations were performed on the experimental structure of α-RDX using both DFT and DFT-D methods. Further SPE calculations on structures with smaller/larger volumes were performed by isotropically decreasing/increasing the experimental lattice parameters as described in Section 2.4.10.1. The preceding methodology was then repeated for the crystal structure of β-RDX.

5.3.2 Inelastic Neutron Scattering

INS spectra (24-4000 cm^{-1}) were recorded using the TOSCA[34] instrument at the ISIS Neutron and Muon Facility, which has an energy resolution of ~1.25% of the energy transfer. Approximately 4.0 g of polycrystalline α-RDX (Bridgwater Type I, Class 5 ~ 10-30 μm) was loaded into an aluminium sample can and cooled to $T < 20$ K in a conventional closed cycle refrigerator. Spectra were recorded for 3–6 h. INS data were visualised and compared to the simulated spectra of the DFT-D calculations using the aCLIMAX program.[35]

5.3.3 Differential Scanning Calorimetry

Samples of α-RDX (Bridgwater Type I, Class 5 ~ 10-30 μm) were loaded into aluminium pans (TA Instruments Tzero^{TM} series) and hermetically sealed and weighed (0.153 – 0.261 mg). β-RDX was obtained by crystallisation from the melt. Thermograms were obtained on a TA Instruments Q2000 DSC module with heat flow recorded using a Tzero^{TM} cell. The apparatus was calibrated using indium. Measurements were performed from 20 °C to 215 °C with a heating rate of 10 °C min^{-1}. A helium gas flow of 50 ml min^{-1} was maintained through the furnace during measurements. The resulting DSC traces were analysed by means of the TA Universal Analysis Software.[36]

5.3.4 X-Ray Powder Diffraction

Samples of α-RDX (Bridgwater Type I, Class 5 ~ 10-30 μm) were densely packed into 0.7 mm diameter thin-walled glass capillaries. X-ray powder diffraction data were collected on Beam-line I11 (HRPD) at the Diamond Light Source (λ = 0.826136(2) Å).[37,38]

5.4 Results and Discussion

5.4.1 Ambient-Pressure Behaviour

5.4.1.1 Structure and Spectroscopic Properties of α-RDX

α-RDX crystallises in the orthorhombic crystal system with space group *Pbca*: the unit cell contains eight RDX molecules, giving a total of 168 atoms. The results of the geometry optimisation compared to available experiment and previous DFT and DFT-D studies are shown in TABLE 5.1. All lattice parameters agree with experimental values[2] to within 1.3%, and the overall unit cell volume differs from the experimental volume by only 0.3%. These results are consistent with previous

DFT-D studies,[***24,26] and confirm that the Grimme dispersion correction can describe accurately the intermolecular interactions in the α-RDX crystal.

Parameter	Exp.[2]	DFT[22]	DFT-D[26]	DFT-D
a (Å)	13.182[2]	13.688 (3.8)	13.237 (0.4)	13.282 (0.8)
b (Å)	11.574[2]	11.933 (3.1)	11.391 (-1.6)	11.419 (-1.3)
c (Å)	10.709[2]	11.538 (7.7)	10.770 (0.6)	10.736 (0.3)
V (Å^3)	1633.86[5]	1884.52 (15.3)	1623.94 (-0.6)	1628.27 (-0.3)

TABLE 5.1 Comparison of the crystallographic parameters for α-RDX calculated at ambient pressure using the DFT-D method alongside results obtained from ambient temperature experimental and previous DFT and DFT-D studies. The numbers in square brackets are the estimated standard deviations of experimental values, the values in parentheses are the percentage error deviations from experimental values.

Following the geometry optimisation, a comprehensive, finite displacement phonon calculation (including symmetry) was performed to obtain the vibrational properties of α-RDX. The phonon calculation was performed at only the gamma point in k-space as the material is an insulator and thus the dispersion of phonon energies throughout k-space is assumed to be negligible. Due to the large number of calculated and experimental modes a detailed comparison has not been presented here; instead a numerical comparison of the calculated modes compared to the experimental Raman spectra published by Haycraft *et al*.[5] is displayed in TABLE 5.2. A full list of calculated vibrational modes with experimental comparisons from both Haycraft *et al*.[5] and Dreger & Gupta[14] can be found on the Supplementary Information CD (in addition, also contained on the CD are the computationally calculated structures and the CASTEP output files for the geometry optimisations and phonon calculations, and the statistical thermodynamics solver spread sheet). TABLE 5.2 shows that the majority of the calculated Raman-active vibrational modes are in good agreement (<2.5% difference) with experimental values.

[***] Although the current and previous DFT-D calculations both used the same dispersion correction scheme, the difference in the calculated geometries arises from the fact that different pseudopotentials were used in each study.

	α-RDX	γ-RDX	ε-RDX
No. Exp. modes	186[5]	76[14]	47[19]
>10%	5	0	3
5 – 10%	16	6	4
2.5 – 5%	49	8	9
<2.5%	116	62	31

TABLE 5.2 Numerical comparison, showing the number of calculated Raman-active modes that fall within a certain percentage of the experimental values.

The simulation also agrees very well with the INS spectrum obtained during the course of this work. The experimental INS spectrum determined in this work is, in turn, in good agreement with the previously published INS experiments performed on α-RDX by Ciezak *et al.* (43 – 1299 cm^{-1}), and extends the wavenumber range for these measurements (24 – 4000 cm^{-1}). INS spectra provide a unique way to assess the quality of the computational phonon calculations. This is because the eigenvalues of a vibration are a function of the molecule's structure and the intramolecular forces, and correspond to the energies lost by the neutron. Furthermore, the intensity of the observed transition is a function of the eigenvector and the momentum lost by the neutron (as explained in Section 3.2.2.4).[39] Thus by comparing the calculated spectra to the experimental INS spectra it is possible to assess how well both the wavenumber and the eigenvector of each mode are calculated. In Figure 5.3 the calculated INS spectrum of α-RDX calculated using DFT-D is compared to the ambient-pressure experimental INS spectrum recorded using the TOSCA instrument.[34] From this it is apparent that the computed and experimental spectra show excellent agreement, both for the transition energies and for the intensities of the lattice and internal modes.

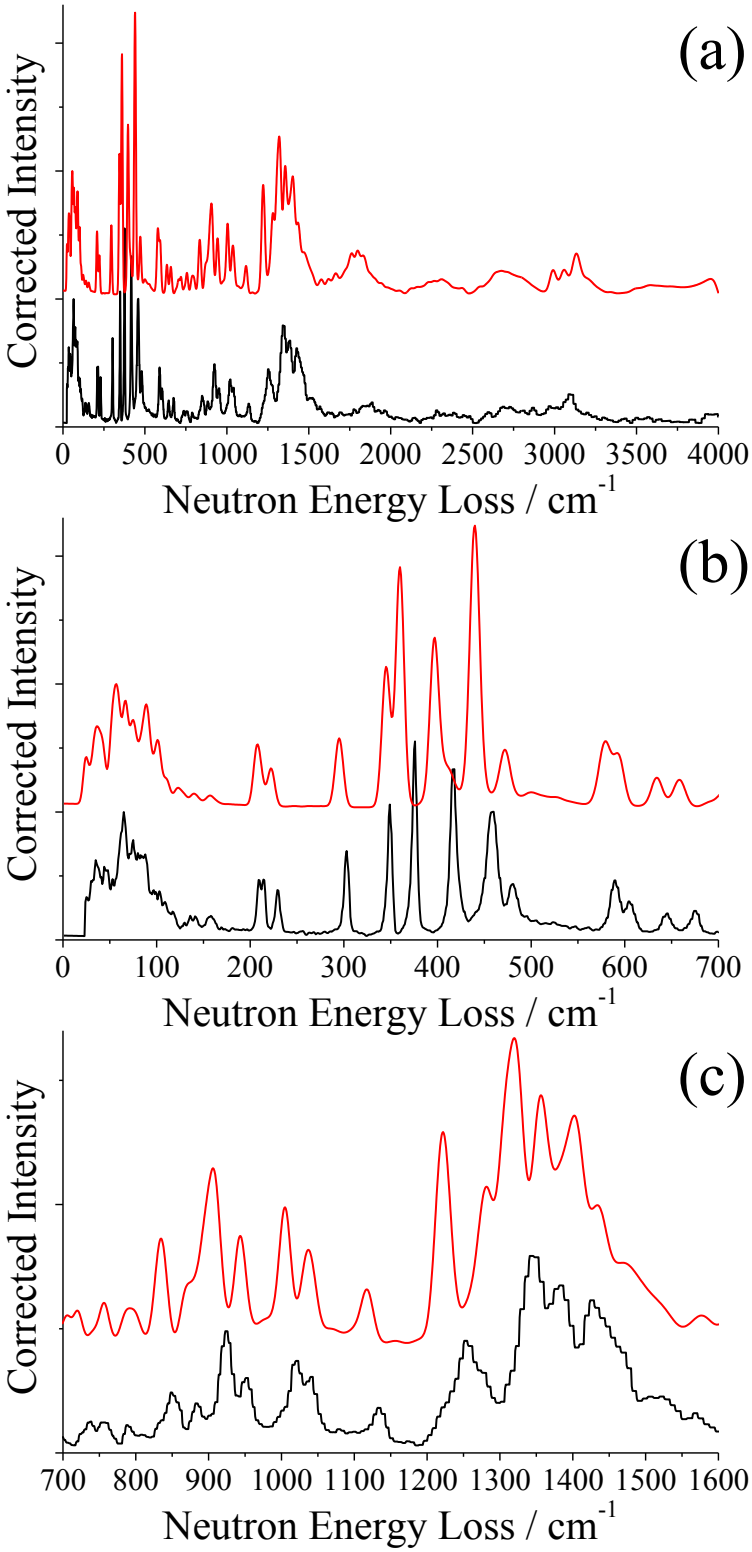

Figure 5.3 Experimental (**black**) and calculated (**red**) INS spectra of α-RDX at ambient pressure in the regions (a) 0 – 4000 cm^{-1}, (b) 0 – 700 cm^{-1}, (c) 700 – 1600 cm^{-1}.

The excellent agreement between experiment and theory for the crystallographic lattice parameters and for the vibrational frequencies and intensities

gives confidence that the computational model used in this study accurately describes both the intramolecular and intermolecular interactions in crystalline α-RDX.

5.4.1.2 Calculation of Lattice Energies of α- and β-RDX

Figure 5.4 shows the calculated potential wells obtained for α-RDX using DFT and DFT-D methods, and the potential well obtained using the DFT-D method for the β-form of RDX.

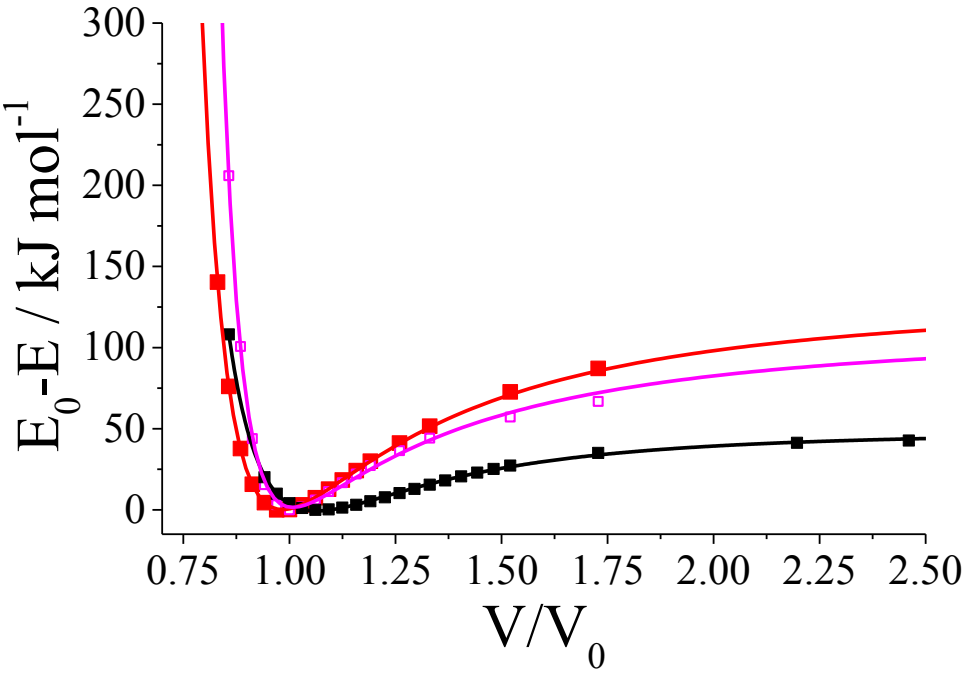

Figure 5.4 Calculated potential wells for α- and β-RDX fitted with Lennard-Jones type potentials. **Black square** α-RDX DFT, **red square** α-RDX DFT-D and, **pink square** β-RDX DFT-D.

The sublimation enthalpy is the difference between the enthalpies in the gaseous and solid states, as shown in Equation 5.1.

$$\Delta H_{sub} = H_{gas} - H_{solid}$$

Equation 5.1

Assuming that the gas is ideal and that the Dulong-Petit Law holds for the solid then each degree of freedom contributes 1/2 R*T* to the enthalpy of the system. Thus as there are three translational and three rotational kinetic degrees of freedom, H_{gas} is given by Equation 5.2, where the final R*T* term accounts for *PV* (in accordance with the ideal gas law).

$$H_{gas} = \frac{3}{2}\mathrm{R}T + \frac{3}{2}\mathrm{R}T + \mathrm{R}T$$

Equation 5.2

In the solid state, there are three degrees of freedom for both the kinetic and potential energy components of the translational and librational oscillations, in addition to the intramolecular component of internal energy (the lattice energy, E_L). Thus H_{solid} is given by Equation 5.3:

$$H_{solid} = 3\mathrm{R}T + 3\mathrm{R}T + E_L$$

Equation 5.3

It follows that by inserting Equation 5.2 and Equation 5.3 into Equation 5.1, that the lattice energy, E_L, can be related to the enthalpy of sublimation, ΔH_{sub}, by Equation 5.4.

$$-E_L = \Delta H_{sub} + 2\mathrm{R}T$$

Equation 5.4

However, due to the nature of the experimental methods used to determine enthalpies of sublimation, the absolute temperatures at which ΔH_{sub} are measured are often unknown. As a result, the relationship above is often simplified to that shown in Equation 5.5, in order to compare calculated lattice energies to experimentally determined sublimation enthalpies.[40,41,42,43,44,45]

$$-E_L \approx \Delta H_{sub}$$

Equation 5.5

The enthalpy of sublimation for α-RDX has been independently determined experimentally by Rogers[46] to be 130.12 kJ mol^{-1} and by Rosen *et al.*[47] to be 130.16 kJ mol^{-1}. As stated above, this work directly compares the calculated E_L and the experimentally determined ΔH_{sub} (as shown by Equation 5.5), but it should be noted that a correction of a few kJ mol^{-1} has been neglected in order to be able to make this approximation.

In TABLE 5.3 the lattice energies for α-RDX calculated using DFT (GGA-PBE) and DFT-D methods (derived from variable E from Equation 2.32) are compared to the experimentally determined enthalpies of sublimation , in addition to

the other fitting parameters, A – D from Equation 2.32. DFT seriously underestimates the lattice energy of α-RDX, again demonstrating that this model cannot describe accurately the intermolecular interactions within crystalline RDX. By contrast, the E_L calculated using DFT-D (-130.06 kJ mol^{-1}) is in excellent agreement with experiment. Previous calculations by Perger *et al,*[48] investigated the predictive power of multiple functionals with differing basis sets and different levels of theory and showed that both HF and DFT-GGA methods significantly underestimate the lattice energy (HF: 40.4 – 65.0 kJ mol^{-1}, B3LYP: 36.3 – 43.1 kJ mol^{-1}, GGA: 57.8 – 63.3 kJ mol^{-1}). Hu *et al*.[49] and Wang *et al*.[50] both calculated the enthalpy of sublimation of α-RDX, with predictions of 109.7 and 100.4 kJ mol^{-1}, respectively. The most accurate prediction to date was obtained using the COMPASS force field, which predicted the lattice energy of α-RDX to be -116.7 kJ mol^{-1}.[51]

	Var. A	*Var. B*	*Var. C*	*Var. D*	E_L (kJ mol^{-1})	ΔH_s (kJ mol^{-1})
α-RDX	32.35	0.90	12.83	3.36	48.15	
α-RDX	56.98	0.83	9.84	2.25	130.06	
α-RDX						130.12
α-RDX						130.16
β-RDX	41.62	0.88	17.68	2.21	109.71	

TABLE 5.3 Calculated lattice energies an fitting variables from Equation 2.32, of α-RDX using both DFT & DFT-D methods compared to experimental heats of sublimation, along with the predicted lattice energy for β-RDX.

The successes of the DFT-D approach prompted the calculation of the E_L for β-RDX (the calculated potential well is shown in Figure 5.4, with parameters from the Lennard-Jones type fit shown in TABLE 5.3, giving a predicted lattice energy of -109.71 kJ mol^{-1}). This result predicts that the experimental -E_L (ΔH_{sub}) of β-RDX is approximately 20 kJ mol^{-1} more positive than that of α-RDX. This is an unusually large difference between polymorphs of a molecular crystal – energy differences are typically less than 10 kJ mol^{-1}.[52,53,54] However, this is by no means the first observation of a large energy difference between polymorphs; the drug Efavirenz ((4*S*)-6-chloro-4-cyclopropylethynyl-4-trifluromethyl-1,4-dihydro-2*H*-3,1-benzoxazin-2-one) crystallises in multiple polymorphic forms, and recent DSC

experiments have shown that the enthalpies of fusion of these different forms vary considerably, the difference between Form I and Form III being over 17 kJ mol^{-1}.[55] Similarly, studies on a simple N, N'- diaryl urea derivative (1-(3-Methylsulfanylphenyl)-3-pyridin-2-ylurea) determined a difference in the enthalpies of fusion of 23.4 kJ mol^{-1} between the thermodynamically stable Form IV and the metastable Form I.[56]

5.4.1.3 Experimental Determination of Enthalpy of Fusion of β-RDX

The enthalpy of fusion of α-RDX has been previously experimentally determined using DSC by Hall (35.65 ± 2.51 kJ mol^{-1}),[57] Kishore (30.71 ± 0.29 kJ mol^{-1}),[58] and Zeman (32.90 ± 0.73 kJ mol^{-1}).[59]

The challenge in measuring ΔH_{fus} for β-RDX is its high degree of metastability, illustrated by the observation that any mechanical manipulation of the β-form results in immediate transformation to the α-form.[8,12] The β-form can be reproducibly obtained by drop-cast recrystallisation, *i.e.* evaporation of dilute solutions of RDX in solvents such as DMSO. In this way Goldberg *et al*. obtained DSC traces for the β-form and identified its melting temperature as 188 °C, but did not report its enthalpy of fusion.[12] The authors also commented on the influence of scale on the crystallisation of the β-form - crystallisation of samples from higher concentration drops increased the propensity for the α-form to crystallise.[12]

Note: X-ray diffraction studies were performed by Prof. Colin Pulham (The University of Edinburgh).

The approach of this work was to crystallise the β-form from the melt, first using X-ray powder diffraction to identify unequivocally that the β-form is formed in this way. To this end powder diffraction patterns of the α-form contained in a 0.7 mm thin-walled glass capillary were recorded until just before the melting point (477 K) – all were consistent with the α-form. It was only after complete melting of the sample and cooling to ambient temperature that the characteristic diffraction pattern of the β-form was obtained, albeit with very pronounced preferred orientation which affects the observed intensities (see Figure 5.5). This contrasts somewhat with the results of Infante-Castillo *et al*.,[11] who reported that the α → β transition

occurred *via* a solid-solid transition, but this may be a consequence of the different methods of containment of the sample in the two experiments. Nevertheless, it did prove possible to obtain samples of the β-form in a reproducible manner by cooling from the melt, and so this was the strategy adopted for the DSC experiments in this work. To this end, a sample of α-RDX was first heated in a sealed aluminium pan to just beyond the melting point of the α-form (204 °C) and then cooled to ambient temperature. However, initial experiments using quantities of 2-3 mg of RDX were unsuccessful – invariably only the α-form crystallised. It was only when samples of mass <~0.25 mg were used that reproducible crystallisation of the β-form could be achieved. Thus crystallisation of the β-form from the melt also appears to be strongly affected by scale in a similar way to the drop-cast recrystallisation of RDX from solution.[12]

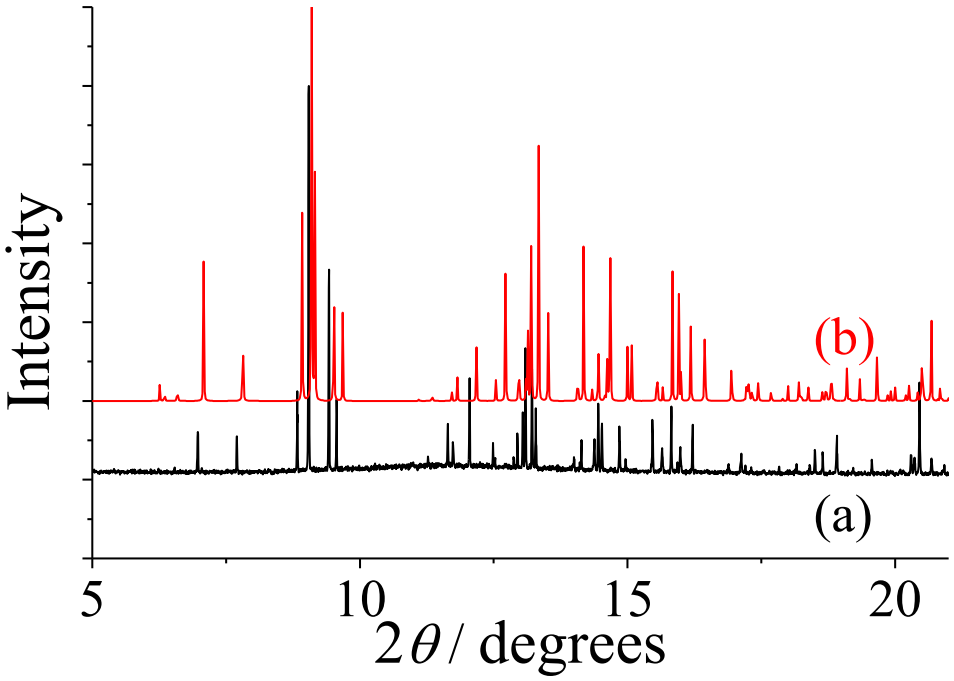

Figure 5.5 Powder X-ray diffraction patterns of (a) RDX recrystallised from the melt and then cooled to 298 K and (b) simulated powder pattern of the single crystal X-ray diffraction structure of β-RDX at 150 K. (λ = 0.826136(2) Å)

A typical DSC thermogram obtained for β-RDX is shown in Figure 5.6 (all other thermograms that were recorded can be found in the Appendix Figures A5.1 – A5.4). Upon heating from 20 °C to 210 °C, an endothermic peak was observed with

an onset temperature of 186.7 ± 0.8 °C, indicative of melting of the β-form, and in agreement with the results of Goldberg *et al*.[12]

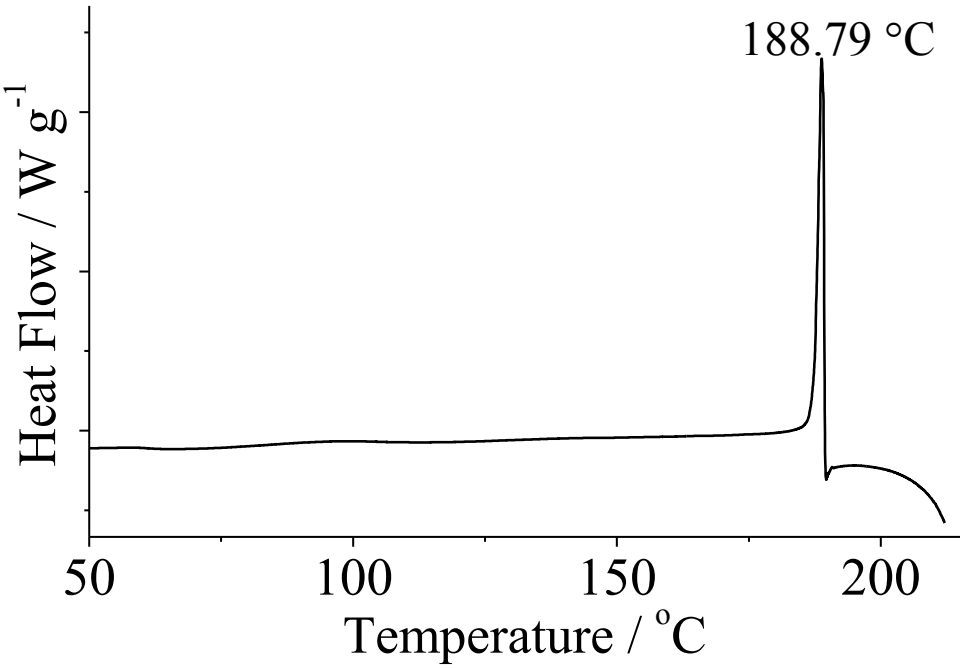

Figure 5.6 Typical DSC thermograph, obtained at a heating rate of 10 °C per minute for β-RDX (sample mass 0.153 mg). Scale: endothermic up.

The observed characteristics of fusion determined for five samples of β-RDX are shown in TABLE 5.4. From this sample set, the mean and standard deviation for the onset temperature (or melting point), peak temperature and ΔH_{fus} have been determined as 186.7 ± 0.8 °C, 188.5 ± 0.4 °C and 12.63 ± 0.28 kJ mol^{-1}, respectively. This represents the first experimental determination of the enthalpy of fusion of β-RDX.

Mass (mg)	Onset T (°C)	Peak T (°C)	Peak area (J g^{-1})	$\Delta H°_{fus}$ (kJ mol^{-1})
0.153	187.5	188.8	58.66	13.02
0.184	186.4	188.8	55.99	12.44
0.184	186.2	188.1	56.65	12.58
0.194	185.8	188.0	55.48	12.32
0.261	187.5	188.9	57.50	12.77
Mean	**186.7 ± 0.8**	**188.5 ± 0.4**	**56.86 ± 1.26**	**12.63 ± 0.28**

TABLE 5.4 Observed characteristics of fusion for β-RDX samples.

A pertinent comparison between the calculated lattice energies and experimentally determined data can be obtained by comparing the difference between the calculated lattice energies with the difference in the experimentally determined enthalpies of fusion for α- and β-RDX, for in this way any errors due to the omission of zero-point energy corrections will cancel. This gives a difference of 20.35 kJ mol^{-1} from the simulations, in excellent agreement to the difference of 20.46 ± 0.92 kJ mol^{-1} obtained from the difference between the experimental ΔH_{fus} of β-RDX (determined in this study) and the average of the literature values quoted above for ΔH_{fus} of α-RDX (33.086 ± 0.877 kJ mol^{-1}).

With a knowledge of this difference in the enthalpies of fusion, it can be subtracted from the enthalpy of sublimation of α-RDX, to determine the 'experimental' lattice energy of β-RDX, producing an 'experimental' lattice energy of -109.68 ± 1.27 kJ mol^{-1}. The lattice energy of β-RDX predicted earlier in this study by DFT-D (-109.71 kJ mol^{-1}) is in excellent agreement with this experimental determination, which serves to highlight the predictive power of a good computational model.

These experimental findings may have considerable implications for polymorph prediction strategies,[60] where large numbers of possible structures are generated, and those that are not within ~10 kJ mol^{-1} of the lowest energy structure are typically discarded. The observed β-RDX polymorph in this study would be overlooked in such a screening, highlighting that care must be taken when choosing selection criteria in some polymorph prediction studies.

5.4.2 High-Pressure Behaviour of the α- γ- and ε-Polymorphs of RDX

5.4.2.1 Effect of Pressure on Lattice Parameters

The effect of pressure on the lattice parameters of the α- and γ-forms of RDX is shown in Figure 5.7. The results are in very close agreement with a previous computational DFT-D study,[26] and are, in turn, in excellent agreement with experimental values.[61] The lattice parameters are calculated to lie within 1.6% and 1.1% (for α-RDX and γ-RDX, respectively) of the experimental values determined

by Oswald *et al.*[61] and all unit-cell volumes (shown in Figure 5.8) for α-RDX are calculated to lie within 1.3% of experiment, with the largest deviation from the experimental γ-RDX volumes being just 0.9%.

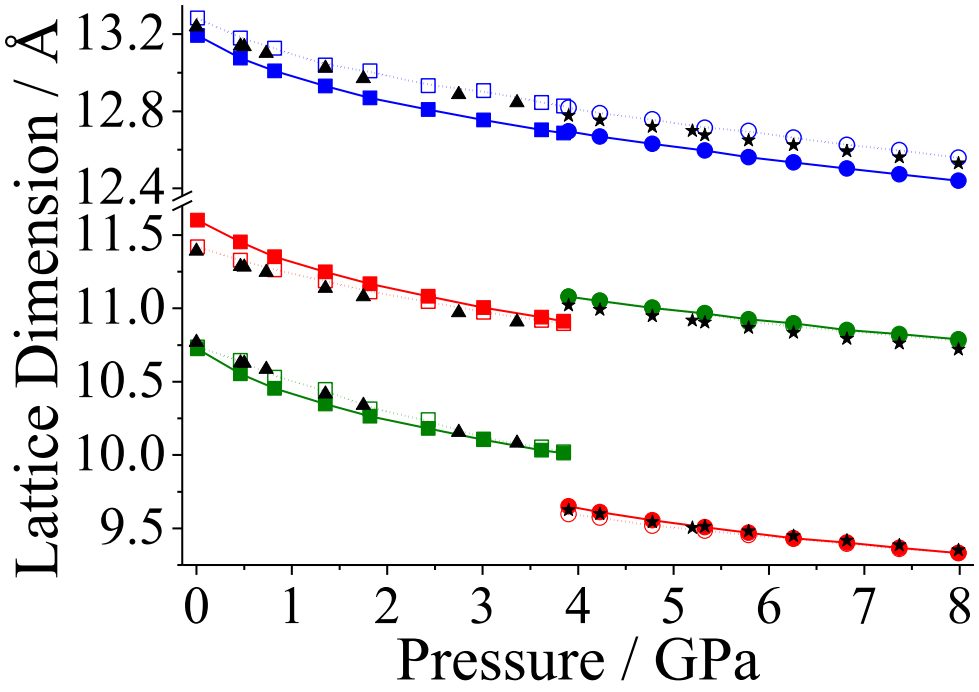

Figure 5.7 Lattice parameters as a function of hydrostatic pressure for the α- and γ-forms of RDX. Square: α-RDX, circle: γ-RDX. Solid symbol: experimental,[61] open symbol: computational. **Blue**: *a*-axis, **red**: *b*-axis, **green**: *c*-axis. **Black** triangles and stars; previous DFT-D results for α- and γ-RDX, respectively.[26]

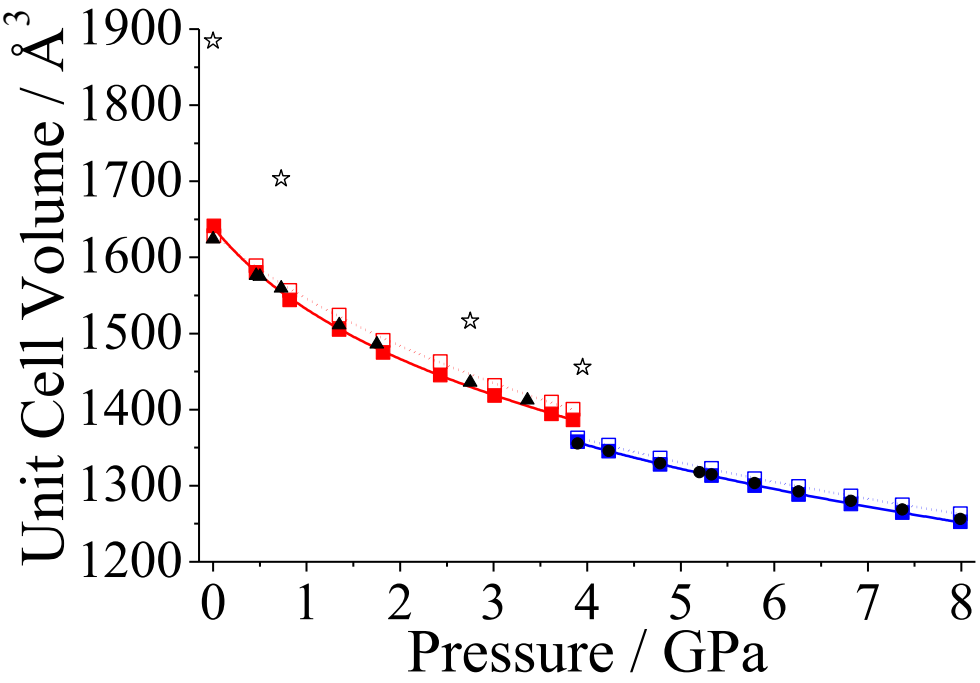

Figure 5.8 Unit-cell volumes as a function of pressure fitted with 3rd order B-M EoS (Equation 4.1). **Red**: α-RDX, **blue**: γ-RDX. Open symbol: computational (this work), closed symbol: experimental.[61] **Black** star: α-RDX DFT,[22] **black** triangle and circle: α- & γ-RDX DFT-D Sorescu & Rice.[26]

5.4.2.2 Compression of ε-RDX

This work presents the first computational compression study of the recently characterised high-temperature/high-pressure polymorph, ε-RDX. Figure 5.9 shows that the experimental[10] lattice parameters and compression behaviour are reproduced well by the DFT-D method. The *a*-axis is consistently overestimated by ~1%, the *b*-axis is initially overestimated by 0.5%, and upon compression the overestimation gradually rises, with a maximum difference of 1.3% at 4.64 GPa. Calculation of the *c*-axis is initially underestimated by 1.8% at 0.99 GPa but as the pressure is increased the difference compared to experiment decreases to only 1.0% at 5.04 GPa, the maximum pressure of the experimental study.

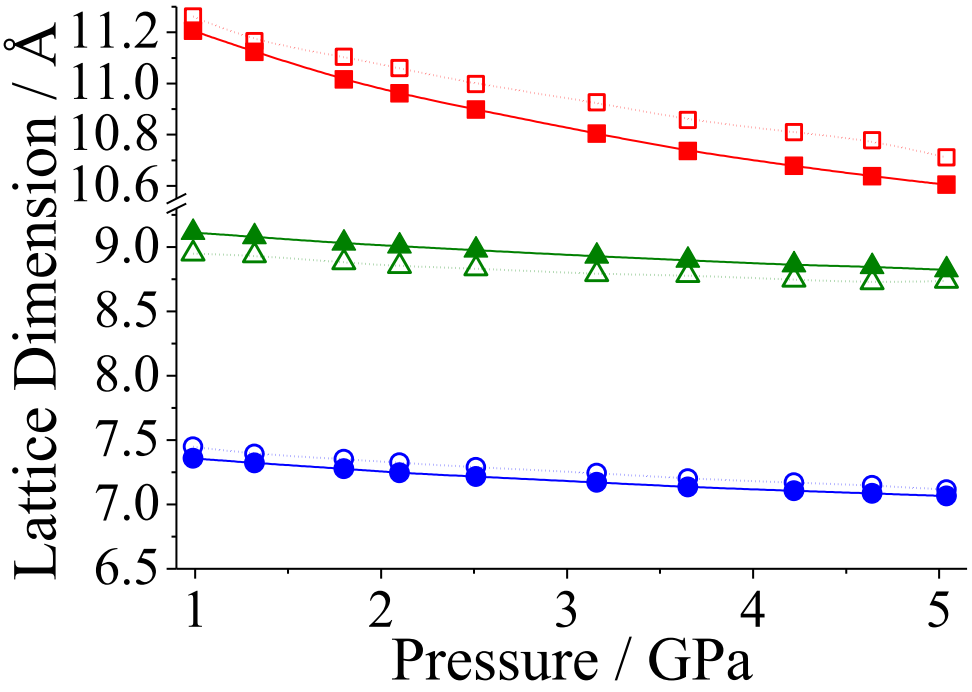

Figure 5.9 Variation of lattice parameters as a function of hydrostatic pressure for crystalline ε-RDX. **Blue circle** *a*-, **red square** *b*- and, **green triangle** *c*- vectors (solid symbol: experimental,[10] open symbol: computational).

Figure 5.10 depicts the overall unit cell volume compression as a function of pressure for ε-RDX. The compression results are compared to experiment[10] and are fitted to Murnaghan[62] EoS as shown in Equation 5.6:

$$P = \frac{B_0}{B'}\left[\left(\frac{V_0}{V}\right)^{B'} - 1\right]$$

Equation 5.6

The unit-cell volumes as a function of pressure for ε-RDX were calculated in excellent agreement with experiment, with deviations of no more than 0.9% over the pressure range studied.

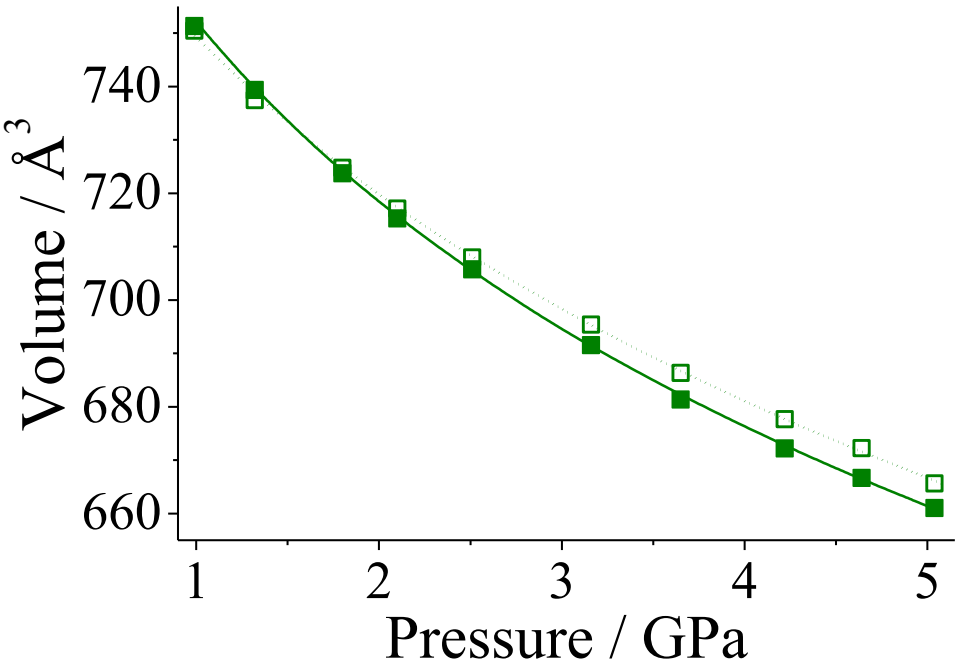

Figure 5.10 Unit cell volumes as a function of pressure for ε-RDX, fitted to Murnaghan[62] EoS (solid symbol: experimental,[10] open symbol: computational).

The calculated EoS, presented in TABLE 5.5, highlight the quality of the simulated results. Results obtained for all three polymorphs are shown alongside their experimentally-derived counterparts, along with previous DFT-D results by Sorescu and Rice.[26] It can be seen that both this work and the DFT-D calculations by Sorescu and Rice[26] slightly underestimate the compressibility of α-RDX. This is primarily due to the initial underestimation of the unit cell volume at ambient pressure for both computational studies, in conjunction with the subsequent slight overestimation at elevated pressures. However, for both γ- and ε-RDX, the computational models in this work generate B_0 values in excellent agreement with experimental values.

		V_0 (Å^3)	B_0 (GPa)	B'
α-RDX	Exp.[61]	1639.8 (5.8)	10.10 (1.18)	11.00 (1.65)
	DFT-D	1630.7 (3.7)	15.54 (1.08)	6.46 (0.82)
	Ref. 26	1625.6	13.99	7.80
γ-RDX	Exp.[61]	1616.1 (8.0)	9.50 (0.41)	11.00 (fixed)
	DFT-D	1616.1 (fixed)	9.17 (0.20)	12.63 (0.36)
	Ref. 26	1555.0	16.72	8.03
ε-RDX	Exp.[10]	808.3 (7.6)	10.34 (1.74)	7.78 (0.65)
	DFT-D	799.3 (6.4)	10.63 (2.25)	12.32 (2.51)

TABLE 5.5 Experimental and calculated 3rd order B-M (Equation 4.1, α- and γ-RDX) and Murnaghan (Equation 5.6, ε-RDX) EoS parameters of crystalline RDX.

5.4.2.3 High-Pressure Vibrational Properties

High-pressure vibrational mode calculations have also been performed for α-, γ- and ε-RDX. Due to experimental limitations, it has not been possible to obtain experimental INS spectra for γ- and ε-RDX. However, the calculated high-pressure vibrational properties of α-, γ- and ε-RDX are compared to available high-pressure Raman spectra published by Dreger & Gupta.[14,19] A numerical comparison of the simulated results with the available experimental data for γ-RDX (at 4 GPa) and ε-RDX (at 1 GPa) is provided previously in TABLE 5.2. This shows that the computational model appears to be capable of reliably predicting the vibrational properties of several polymorphs of RDX over a range of pressures.

The results of the high-pressure phonon calculations, and corresponding experimental values for α-, γ- and ε-RDX, can be found on the Supplementary Information CD. Computed INS spectra for γ- and ε-RDX, compared to computed spectra of α-RDX at similar pressures, can be found in the Appendix Figures A5.5 and A5.6.

5.4.2.4 Prediction of Heat Capacities

The successes of the DFT-D model for the prediction of lattice energies, compression behaviour and vibrational properties of RDX, give confidence that the model is capable of predicting properties that have not yet been experimentally measured.

The preceding phonon calculations utilised Hooke's law (Force = 1/2 -k$\boldsymbol{x}$, where k is the spring constant) and implemented the harmonic approximation (Energy = 1/2 k$\boldsymbol{x}^2$), which assumes that the vibrations are symmetric.[63] Thus as the heat capacities are being predicted at non-zero temperatures (at approximately room temperature), one needs to ensure that the harmonic approximation is still valid at these temperatures. This can be achieved by inspection of the height of the potential well that is reasonably symmetric. Figure 5.11 displays a comparison of the Lennard-Jones type potential well calculated using DFT-D for α-RDX (the fit of the potential well created to calculate the lattice energy in Section 5.4.1.2) with a symmetric x^2 function.[†††] It can be seen from Figure 5.11(b) that the well is reasonably symmetric at least up to a height that is energy equivalent to a temperature of 600 K; hence the harmonic approximation is still valid at the temperatures being used for these heat capacity predictions.

[†††] Or rather, a function that varies with $(x-1)^2$ to normalise the curve to $V/V_0 = 1$.

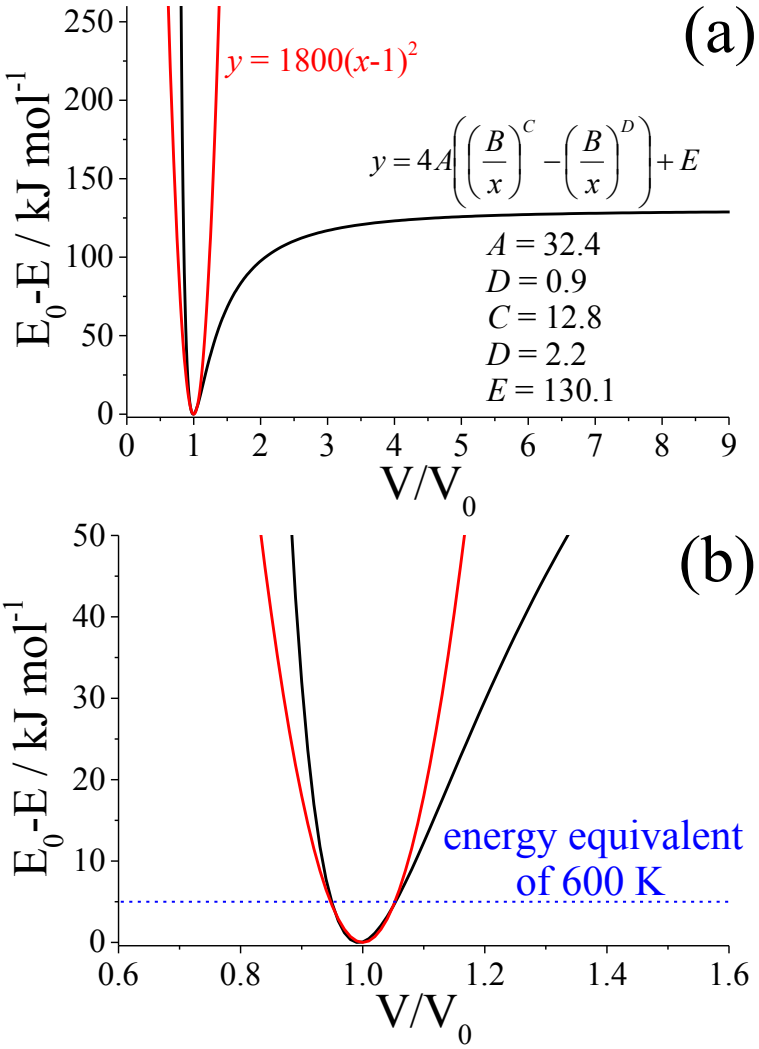

Figure 5.11 DFT-D calculated Lennard-Jones types potential wells compared to parabolic function to asses height of well that is reasonably symmetric. (a) Potential well and parabolic function annotated with relevant functions and fitting parameters. (b) Close up to highlight the symmetry at the base of the potential well.

Hence, by utilising the results of the phonon calculations, the variation in heat capacities as a function of pressure (C_V) for the α-, γ- and ε-forms of RDX have been predicted. As well as providing valuable predictions about the effect of pressure on the heat capacities, these results provide insight into the requirements of potential experimental techniques for measuring heat capacities at elevated pressures. The heat capacity at a given pressure can be calculated using Equation 2.59, which is described in Chapter 2.

Figure 5.12 displays the calculated variation in heat capacities at 295 K in the 0 – 8 GPa pressure range for α-, γ- and ε-RDX. The calculated heat capacity for α-RDX at ambient pressure at this temperature is 216.17 J K^{-1} mol^{-1} , close to the

experimental value of 231.68 J K^{-1} mol^{-1} determined by Miller.[64] As discussed previously, the phonon calculations were only performed at the gamma point in k-space, however as an estimate of the actual effect of phonon dispersion on the calculated heat capacities, phonon calculations at multiple points in k-space have been performed on a smaller test system (one molecule of α-RDX in a box), the results of which can be found in the Supplementary information. The standard deviation (as a percentage of the mean value) of the predicted heat capacities for the 8 k-points of the test system has been used to estimate the magnitude of the error in the calculated heat capacities at the gamma point in k-space of the full computational system, this error is shown as the error bars in Figure 5.12. These results confirm that the effect of phonon dispersion on the vibrational properties of RDX is indeed small and that the prediction of heat capacities using only the gamma point in k-space is valid.

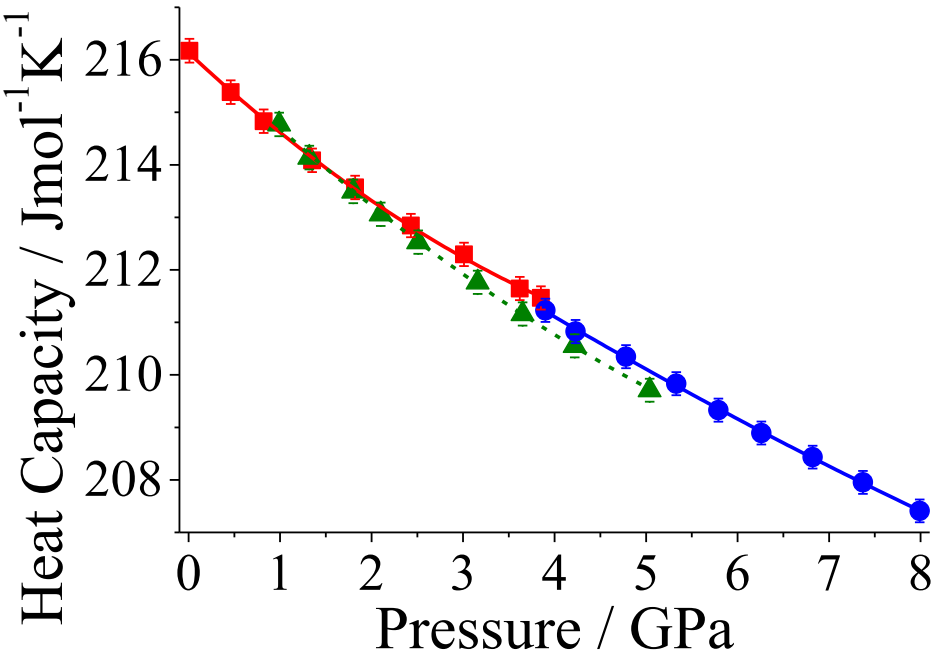

Figure 5.12 Calculated effect of pressure on the heat capacities at *T*= 295 K of α-RDX (**red square**), γ-RDX (**blue circle**) and ε-RDX (**green triangle**). The error bars provide an estimate (as determined from the standard deviation of phonon dispersion calculations on a smaller test system) of the effect of phonon dispersion on the calculated (gamma point only) heat capacities.

Figure 5.12 shows that the effect of pressure on the heat capacities for all three polymorphs is only approximately -1 J K^{-1} mol^{-1} GPa^{-1} (in comparison to a temperature dependence of approximately 0.6 J K^{-2} mol^{-1} for α-RDX).[64,65] In

addition, at the α-γ phase transition the discontinuity is only 0.25 J K^{-1} mol^{-1}. These results illustrate that there is only a weak pressure dependence of heat capacities for all three forms of RDX studied here. Thus to determine experimentally the effect of pressure on the heat capacities of materials such as RDX, a very sensitive method will be needed. Furthermore, these results highlight that pressure does not play a major role in influencing the deflagration-to-detonation transition; instead the major influence is temperature as heat capacities are highly temperature dependent.

5.5 Conclusions

DFT-D calculations have been utilised to describe accurately the structure and properties of several polymorphs of the organic molecular crystal RDX. At ambient pressure the DFT-D model predicted all of the lattice parameters of α-RDX to lie within 1.3% of experiment,[2] commensurate with previous DFT-D studies.[24,26] Subsequent phonon calculations generated vibrational frequencies in good agreement with experimental Raman spectra. From the results of the phonon calculations, an INS spectrum was plotted and compared with the experimental spectrum determined in this work. Eigenvalues and eigenvectors were well replicated by the model.

The lattice energy of α-RDX was calculated to be -130.06 kJ mol^{-1}, in excellent agreement with the experimental ΔH_{sub} value of 130.14 kJ mol^{-1}.

The good agreement between theory and experiment for α-RDX prompted use of the DFT-D model to predict the lattice energy of the metastable β-form of RDX (-109.71 kJ mol^{-1}) and this was found to be 20.35 kJ mol^{-1} more positive than that for α-RDX.

As part of the study, the first experimental determination of the enthalpy of fusion, ΔH_{fus}, of the highly metastable β-RDX was performed. The characteristics of fusion for β-RDX were determined to be 186.7 ± 0.8 °C, 188.5 ± 0.4 °C and 12.63 ± 0.28 kJ mol^{-1} for the onset temperature (or melting point), peak temperature and ΔH_{fus}, respectively. The difference in experimental ΔH_{fus} for the α- and β-forms of RDX is 20.46 ± 0.92 kJ mol^{-1}, in excellent agreement with the computationally predicted difference in lattice energies. These findings may have considerable

implications for polymorph prediction strategies, where structures not within ~10 kJ mol^{-1} of the lowest energy structure are typically discarded. The observed β-RDX polymorph in this study would be overlooked in such a screening, highlighting that care must be taken when choosing selection criteria in some polymorph prediction studies.

The high-pressure behaviour of RDX was also investigated. DFT-D hydrostatic compression studies included the α- and γ-forms of RDX, with structures produced that were in good agreement with experimental values,[61] and a previous DFT-D study.[26] Moreover, the first computational study of the recently characterised ε-form of RDX has been performed. The experimental high-pressure behaviour of ε-RDX was reproduced well by the computational model, with the calculated bulk modulus (10.63 GPa) in excellent agreement with the experimentally determined value of 10.34 ± 1.74 GPa.

The vibrational properties as a function of pressure were calculated for the α-, γ- and ε-forms of RDX, and were found to be in very good agreement with available experimental data. The results of the phonon calculations were then used to predict the effect of pressure on the heat capacities of the α-, γ- and ε-forms of RDX. These predictions suggest a very weak pressure dependence of heat capacities for all crystal forms of RDX studied, and in particular highlighted a very small (0.25 $J\ K^{-1}\ mol^{-1}$) discontinuity at the α-γ phase transition. These results indicate that the experimental determination of the effect of pressure on the heat capacities of materials such as RDX is likely to be a very challenging task, and would require the use of a very sensitive technique.

This comprehensive study of selected polymorphic forms of crystalline RDX at ambient and applied high-pressures has shown that the DFT-D model performs extremely well over a range of conditions, and is able to describe accurately intramolecular and intermolecular interactions and thus the structure and properties of the organic molecular crystal RDX.

5.6 Further Work

This study has highlighted that the DFT-D model proposed by Grimme can describe accurately the intramolecular and intermolecular interactions in various polymorphs of the energetic nitramine RDX. Further investigation into the transferability of the Grimme DFT-D model at describing the high-pressure structure and properties of other structurally similar energetic nitramine crystalline materials would be prudent to confirm the validity of the model.

5.7 References

1 Hakey, P.; Oullette, W.; Zubieta, J.; Korter, T. *Acta Crystallogr., Sect. E: Struct. Rep. Online* **2008**, *64,* o1428.

2 Choi, C. S.; Prince, E. *Acta Crystallogr., Sect. B: Struct. Crystallogr. Cryst. Chem.* **1972**, *28*, 2857.

3 Rey-Lafon, M.; Trinquecoste, C.; Cavagnat, R.; Forel, M. T. *J. Chim. Phys. Phys.-Chim. Biol*. **1971**, *68*, 1533.

4 Rey-Lafon, M.; Trinquecoste, C.; Cavagnat, R.; Forel, M. T. *J. Chim. Phys. Phys.-Chim. Biol*. **1971**, *68*, 1573.

5 Haycraft, J. J.; Stevens, L. L.; Eckhardt, C. J. *J. Appl. Phys*. **2006**, *100*, 053508.

6 Ciezak, J. A.; Trevino, S. F. *J. Phys. Chem. A* **2006**, *110*, 5149.

7 McCrone, W. C. *Anal. Chem.* **1950**, *22*, 954.

8 Karpowicz, R. J.; Serglo, S. T.;and Brill, T. B. *Ind. Eng. Chem. Prod. Res. Dev*. **1983**, *22*, 363.

9 Karpowicz, R. J.; Brill, T. B. *J. Phys. Chem*. **1984**, *88*, 348.

10 Millar, D. I. A.; Oswald, I. D. H.; Barry, C.; Francis, D. J.; Marshall, W. G.; Pulham, C. R.; Cumming, A. S. *Chem. Commun.* **2009**, *5*, 562.

11 Infante-Castillo, R.; Pacheco-Londoño, L. C.; Hernández-Rivera, S. P. *J. Mol. Struct*. **2010**, *970*, 51.

12 Goldberg, I. G.; Swift, J. A. *Cryst. Growth Des*. **2012**, *12*, 1040.

13 Davidson, A. J.; Oswald, I. D. H.; Francis, D. J.; Lennie, A. R.; Marshall, W. G.; Millar, D. I. A.; Pulham, C. R.; Warren, J. E.; Cumming, A. S. *CrystEngComm* **2008**, *10*, 162.

14 Dreger, Z. A.; Gupta, Y. M. *J. Phys Chem B* **2007**, *111*, 3893.

15 Zheng, X.; Zhao, J.; Tan, D.; Liu, C.; Song, Y.; Yang, Y. *Propell. Explos. Pyrothech*. **2011**, *36*, 22.

16 Ciezak, J. A.; Jenkins, T. A.; Liu, Z.; Hemley, R. J. *J. Phys. Chem. A* **2007**, *111*, 59.

17 Ciezak, J. A.; Jenkins *Propell. Explos. Pyrotech.* **2008**, *33*, 390.

18 Millar, D. I. A.; Oswald, I. D. H.; Barry, C.; Francis, D. J.; Marshall, W. G.; Pulham, C. R.; Cumming, A. S. *Chem. Commun.* **2010**, *46*, 5662.

19 Dreger, Z. A.; Gupta, Y. M. *J. Phys Chem A* **2010**, *114*, 7038.

20 Dreger, Z. A.; Gupta, Y. M. *J. Phys Chem A* **2010**, *114*, 8099.
21 Byrd, E. C. F.; Scuseria, G. E.; Chabalowski, C. F. *J. Phys. Chem. B* **2004**, *108*, 13100.
22 Byrd, E. C. F.; Rice, B. M. *J. Phys. Chem. C* **2007**, *111*, 2787.
23 Miao, M. S.; Dreger, Z. A.; Winey, J. M.; Gupta, Y. M. *J. Phys. Chem. A* **2008**, *112*, 12228.; Cui, H. L.; Ji, G. F.; Chen, X. R.; Zhu, W. H.; Zhao, F.; Wen, Y.; Wei, D. Q. *J. Phys. Chem. A* **2010**, *114*, 1082.; Zerilli, F. J.; Kuklja, M. M. *J. Phys. Chem. A* **2010**, *114*, 5372.
24 Shimojo, F.; Wu, Z.; Nakano. A.; Kalia, R. K.; Vashisgta, P. *J. Chem. Phys.* **2010**, *132*, 094106.
25 Grimme, S. *J. Comput. Chem.* **2006**, *27*, 1787.
26 Sorescu, D. C.; Rice, B. M. *J. Phys. Chem. C* **2010**, *114*, 6734.
27 Balu, R.; Byrd, E. C. F.; Rice, B. M. *J. Phys. Chem. B* **2011**, *115*, 803.
28 Clark, S. J.; Segall, M. D.; Pickard, C. J.; Hasnip, P. J.; Probert, M. J.; Refson, K.; Payne, M. C. *Z. Krystallogr.* **2005**, *220*, 567.
29 Perdew, J. P.; Burke, K.; Ernzerhof, M. *Phys. Rev. Lett.* **1996**, *77*, 3865.
30 Vackar, J.; Hytha, M.; Simunek, A. *Phys. Rev. B* **1998**, *58*, 12712.
31 Monkhorst, H. J.; Pack, J D. *Phys. Rev. B* **1976**, *13*, 5188.
32 Fischer, T. H.; Almlof, J. *J. Phys. Chem.* **1992**, *96*, 9768.
33 Frank, W.; Elsässer, C.; Fähnle, M. *Phys. Rev. Lett.* **1995**, *74*, 1791.
34 Parker, S. F.; Carlile, C. J.; Pike, T. G.; Tomkinson, J.; Newport, R. J.; Andreani C. Ricci, F. P.; Sacchetti, F.; Zoppi, M. *Physica B* **1998**, *241-243*, 154.; Colognesi, D.; Celli, M.; Cilloco, F.; Newport, R. J.; Parker, S. F.; Rossi-Albertini, V.; Sacchetti, F.; Tomkinson, J.; Zoppi, M., *Applied Physics A - Materials Science & Processing* **2002,** *S74*, S64.
35 Ramirez-Cuesta, A. J. *Comput. Phys. Commun.* **2004**, *157*, 226.
36 www.tainstruments.com
37 Tang, C. C.; Thompson, S. P.; Hill, T. P.; Wilkin, T. R.; Wagner, U. H. *Z. Kristallogr. Suppl.* **2007**, *26*, 153.
38 Thompson, S. P.; Parker, J. E.; Potter, J.; Hill, T. P.; Birt, A.; Cobb, T. M.; Yuan, F.; Tang, C. C. *Rev. Sci. Instrum.* **2009**, *80*, 075107.
39 Mitchell, P. C. H.; Parker, S. F.; Ramirez-Cuesta, A. J.; Tomkinson, J. in *Vibrational Spectroscopy with Neutrons with applications in Chemistry, Materials Science and Catalysis*, World Scientific, Singapore, **2005**.
40 Hagler, A.T.; Huler, E.; Lifson, S. *J. Am. Chem. Soc.* **1974**, *96*, 5319.
41 Sandman, D. J.; Epstein, A. J.; Chickos, J. S.; Ketchum, J.; Fu, J. S.; Scheraga, H. A. *J. Chem. Phys.* **1979**, *70*, 305.
42 Pertsin, A. J.; Kitaigorodsky, A. I. in *The atom-atom potential method applications to organic molecular solids*, Springer, Berlin, **1987**.
43 Osborn, J. C.; York, P. *J. Mol Struct.* **1999**, *474*, 43.
44 Bisker-Leib, V.; Doherty, M. F. *Cryst. Growth Des*. **2001**, *1*, 455.
45 Ouvrard, C.; Mitchell, J. B. O. *Acta Crystallogr., Sect. B: Struct. Sci.* **2003**, *59*, 676.
46 Rogers, J. T. *Holston Defence Corporation, Kingsport, TN, Report HDC-20P-26-SER-B, CPIA Abstract 73-1016, AD 904-410L, U-B*, **1962**.
47 Rosen, J.; Dickinson, C. *J. Chem. Eng. Data*, **1969**, *14*, 120.

48 Perger, W. F.; Pandey, R.; Blanco, M. A.; Zhao, *J. Chem. Phys. Lett*. **2004**, *388*, 175.
49 Hu, A.; Larade, B.; Dudiy, S.; Abou-Rachid, H.; Lussier, L.-S.; Guo, H. *Propell. Explos. Pyrotech.* **2007**, *32*, 331.
50 Wang, F.; Du, H.-C.; Zhang, J.-Y.; Gong, X.-D. *J. Phys. Chem. A* **2011**, *115*, 11852.
51 Zhu, W.; Xiao, J.; Zhu, W.; Xia, H. *J. Hazard. Mat.* **2009**, *164*, 1082.
52 Kitaigorodskii, A. I. in *Molecular Crystals and Molecules*, Academic Press, New York and London, **1973**.
53 Chickos, J. S.; Braton, C. M.; Hesse, D. G.; Liebman, J. F. *J. Org. Chem*. **1991**, *56*, 927.
54 Boese, R.; Downs, A. J.; Greene, T. M.; Hall, A. W.; Morrison, C. A.; Parsons, S. *Organometallics* **2003***, 22*, 2450.
55 Chadha, R.; Arora, P.; Saini, A.; Tain, D. S. *J. Pharm. Pharmaceut. Sci*. **2012**, *15*, 234.
56 Fucke, K.; Quereshi, N.; Yufit, D. S.; Howard, J. A.K.; Steed, T. W. *Cryst. Growth Des*. **2010**, *10*, 880.
57 Hall, P. G. *Trans. Faraday Soc.* **1971**, *67*, 556.
58 Kishore, K. *Def. Sci J.* **1978**, *28*, 59.
59 Zeman, S. *Thermochim. Acta* **1997**, *302*, 11.
60 An extensive list inventory of methodologies used for crystal structure prediction can be found in the three blind tests carried out by the CCSD. (i) Lommerse, J. P. M.; Motherwell, W. D. S.; Ammon, H. L.; Dunitz, J. D.; Gavezzotti, A.; Hofmann, D. W.; Leusen, F. J.; Mooij, W. T. M.; Price, S. L.; Schweizer, B.; Schmidt, M. U.; van Eijck, B. P.; Verwer, P.; Williams, D. E. *Acta Crystallogr., Sect. B: Struct. Sci.* **2000**, *56*, 697. (ii) Motherwell, W. D. S.; Ammon, H. L.; Dunitz, J. D.; Dzyabchenko, A.; Erk, P.; Gavezzotti, A.; Hofmann, D. W. M.; Leusen, F. J. J.; Lommerse, J. P. M.; Mooij, W. T. M.; Price, S. L.; Scheraga, H.; Schweizer, B.; Schmidt, M. U.; van Eijck, B. P.; Verwer, P.; Williams, D. E. *Acta Crystallogr., Sect. B: Struct. Sci.* **2002**, *58*, 647. (iii) Day, G. M.; Motherwell, W. D. S.; Ammon, H. L.; Boerrigter, S. X. M.; Della Valle, R. G.; Venuti, E.; Dzyabchenko, A.; Dunitz, J. D.; Schweizer, B.; van Eijck, B. P.; Erk, P.; Facelli, J. C.; Bazterra, V. E.; Ferraro, M. B.; Hofmann, D. W. M.; Leusen, F. J. J.; Liang, C.; Pantelides, C. C.; Karamertzanis, P. G.; Price, S. L.; Lewis, T. C.; Nowell, H.; Torrisi, A.; Scheraga, H. A.; Arnautova, Y. A.; Schmidt, M. U.; Verwer, P. *Acta Crystallogr., Sect. B: Struct. Sci.* **2005**, *61*, 511.
61 Oswald, I. D. H.; Millar, D. I. A.; Davidson, A. J.; Francis, D. J.; Marshall, W. G.; Pulham, C. R.; Cumming, A. S.; Lennie, A. R.; Warren, J. E. *High Pressure Res.* **2010**, *30*, 280.
62 Murnaghan, F. D. *Am. J. Math.* **1937**, *59*, 235.
63 Halliday, D.; Resnick, R.; Walker, J. in *Principles of Physics, Extended*, John Wiley & Sons, Chichester, **2011**.
64 Miller, M. S. *J. Thermophys. Heat Tansfer*, **1994**, *8*, 803.
65 Shoemaker, R. L.; Stark, J. A.; Taylor, R. E. *High Temperatures High Pressures* **1985**, *17*, 429.

Chapter 6

Further Investigation of the DFT-D Model: Studies of HMX and FOX-7

6 Further Investigation of the DFT-D Model: Studies of HMX and FOX-7

6.1 Introduction

HMX (cyclotetramethylenetetranitramine, Figure 6.1) is a secondary high explosive that is similar to RDX, and which is used almost exclusively in military applications. Due to the higher molecular weight of HMX with respect to RDX, HMX has greater thermal stability. It also has a greater detonation velocity due to the increased density of HMX with respect to RDX (β-HMX – 1.91 g cm^{-3}, 9100 m s^{-1}; α-RDX - 1.82 g cm^{-3}, 8750 m s^{-1}). HMX is known to exist in four crystalline phases, all of which can be crystallised from solution at ambient pressure, depending on the crystallisation rate and temperature.[1] They are denoted as the α, β, γ and δ forms: the γ-form is not a true polymorph of HMX, it is a hydrate. At ambient temperature and pressure, β-HMX is the most stable form, with the stability order, β > α > γ > δ under ambient conditions.[2] Single crystal X-ray,[3,4,5] and neutron diffraction[6] studies show that β-HMX crystallises in the monoclinic crystal system with space group $P2_1/c$.

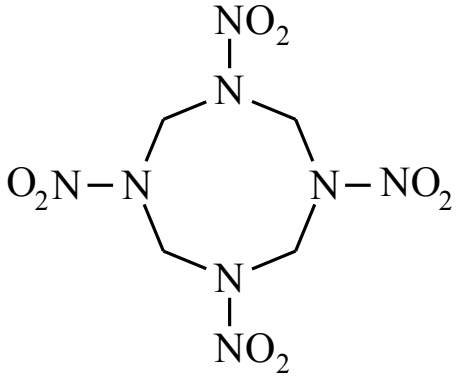

Figure 6.1 Molecular structure of HMX.

The structure of the α-form, stable between 377 and 429 K, was determined by single crystal X-ray diffraction to have an orthorhombic unit cell, with space group *Fdd*2.[4] Cobbledick & Small solved the structure of the δ-form, stable at temperatures > 429 K, in the space group $P6_1$.[7] The γ-form is usually formed under

conditions of rapid crystallisation. Main *et al.* identified γ-HMX as a hydrated form which crystallises in the monoclinic crystal system with space group *Pn*.[8]

To date, no high-pressure polymorphic forms of HMX have been structurally characterised, although evidence for existence of high-pressure forms has been proposed. Yoo & Cynn suggest that β-HMX undergoes two phase transitions under 'hydrostatic compression'.[9] Combined angle-resolved synchrotron X-ray diffraction and micro-Raman spectroscopic studies up to 45 GPa with argon as the PTM suggest a conformational transition at 12 GPa with no apparent abrupt volume change and a discontinuous transition at 27 GPa with a 4% volume change. Similarly, Gump and Peiris performed an angle-dispersive high-pressure synchrotron X-ray diffraction compression study (0 – 5.42 GPa) on β-HMX utilising n-hexane as the PTM.[10] These studies were preceded by the investigation by Olinger *et. al.* who examined the effect of pressure of β-HMX using X-ray crystallography with 4:1 methanol:ethanol as the PTM.[11] These studies have determined a range of values for the bulk modulus for the compression of the β-form, ranging from 10.6 to 21.0 GPa.

The stability to pressure of each polymorphic form has been studied by a combination of IR and Raman spectroscopy. This study identified that the β-form of HMX is stable to compression up to 5.4 GPa (the limit of the study), and the α-form is stable up to 4.2 GPa, albeit with some reversible intensity changes with applied pressure. The study also highlighted that upon compression above 0.55 GPa, γ-HMX converts to the β-form and at an applied pressure of only 0.05 GPa, δ-HMX converts to a mixture of the α- and β-forms. In the same study the authors published assigned ambient pressure IR spectra (600 – 1700 cm^{-1}) of all four polymorphs of HMX. In an additional publication, Goetz and Brill reported the ambient pressure Raman spectra for α-, β-, γ- and δ-HMX.[12] Iqbal *et. al.* performed a combined IR and Raman study on β-HMX and its isotopic isomers (HMX-$^{15}NO_2$, HMX-$^{15}N(NO_2)$, HMX-^{13}C (50%) and HMX-d_8) to present fully assigned IR and Raman spectra (0 – 4000 cm^{-1}).[13] More recently, Brand *et. al.*[14] carried out a combined theoretical and experimental study of the IR vibrational spectra of α-, β- and δ-HMX. In addition, Stevens *et. al.*[15] performed single-crystal polarised Raman

experiments on β-HMX and were able to distinguish the fundamental modes by careful assignment of the combination and overtone modes. Both of these studies are in good agreement with previous experimental results.

The insensitive high explosive 1,1-diamino-2,2-dinitroethylene (DADNE or FOX-7), shown in Figure 6.2a was developed in 1998 and shows much promise as a potential substitute for triaminotrinitrobenzene (TATB) (due to increased performance of FOX-7 with respect to TATB, detonation velocity: FOX-7 8870 m s^{-1};[16] TATB 7350 m s^{-1}.[17]) and also as a reduced sensitivity substitute for RDX. The material is bright yellow and has a layered graphitic, vdW-bonded structure between layers and a far more strongly interacting hydrogen bonded zig-zagging structure within each layer, shown in Figure 6.2b.[18,19,20]

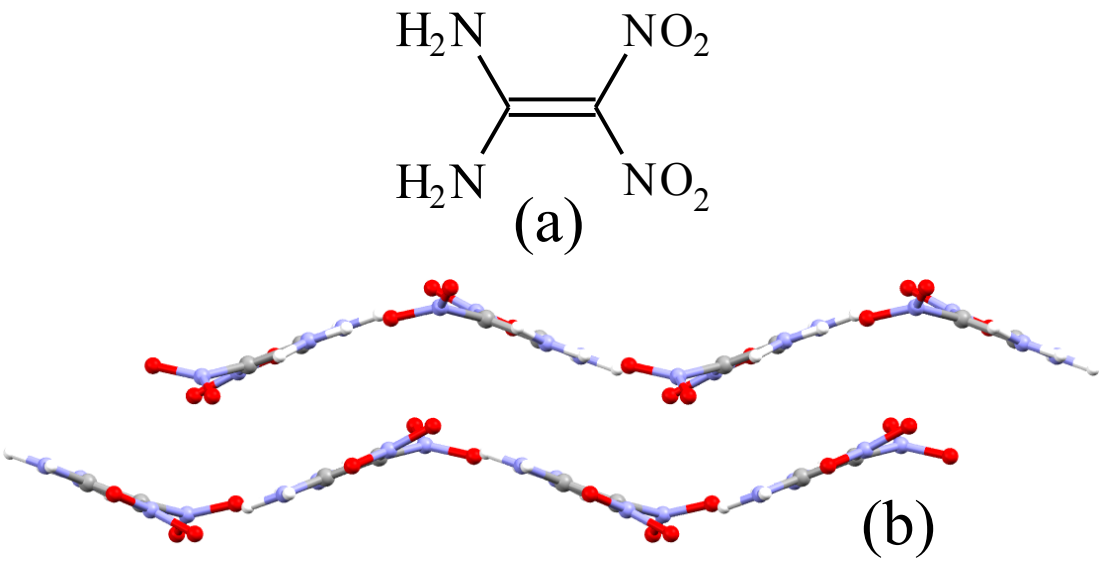

Figure 6.2 (a) Molecular structure of FOX-7. (b) Solid-state structure of FOX-7.

There are three structurally characterised phases (α, β, and γ) at ambient pressure. The α form (monoclinic, $P2_1/n$ symmetry)[19] is the most stable under ambient conditions. When heated beyond 389 K at ambient pressure, a fully reversible transformation into the β-form occurs (orthorhombic, $P2_12_12_1$ symmetry),[19] which then converts to the γ-form (monoclinic, $P2_1/n$ symmetry)[21] upon further heating above 446 K. Upon cooling of the γ-form to below 348 K, the sample directly, but incompletely reverts to the α phase.[22]

The application of non-hydrostatic pressures (at ambient temperature) causes a transition to a quasi-amorphous phase above ~4.5 GPa, which is apparently irreversible and may be related to molecular decomposition. The authors noted that this phase transition may be dependent upon the state of shear stress within the sample.[23,24] FOX-7 has also been investigated at both high-temperature and high pressure under non-hydrostatic conditions.[25] The authors identified that a transition into the amorphous phase occurs beyond 280°C near 2 GPa. Further pressure and temperature cycling suggests that the sample transformed reversibly into and out of the amorphous phase near the phase line, contrary to earlier reports of molecular decomposition.[25]

Unlike HMX which has been widely studied using vibrational spectroscopy, FOX-7 has not been extensively investigated, due to its relatively recent identification as an energetic material. The compression studies highlighted previously also reported Raman data, pressure-induced changes were observed above 1 GPa but were not believed to represent a phase transition.[23,24] Furthermore, the initial synthesis and characterisation of FOX-7 reported IR spectra at ambient pressure.[26] Recently, Pravica *et al.* performed a high-pressure far- and mid-infrared study of FOX-7 up to 28 GPa.[27] The authors present evidence for at least two, possibly three, phase transitions. Spectral changes near 2 GPa suggest a phase transition, similar to results highlighted previously, but discounted by Peiris *et al.*[24] Furthermore the phase transition articulated by Peiris *et al.* near 5 GPa is confirmed in the recent study. The authors noted that this transition may be sluggish, completing at ~10 GPa, otherwise FOX-7 undergoes a further phase transition at 10 GPa. Contrary to the earlier reports of pressure-induced molecular decomposition, this study observed that FOX-7 survives pressure cycling to 28 GPa.[27]

There have been several DFT studies on crystalline HMX[28,29,30,31,32] and FOX-7,[33,34] but as described in the previous chapter, DFT is unable to accurately describe the intermolecular interactions of the molecular systems such as the nitramine crystals being studied here, without the implementation of some sort of dispersion correction. TABLE 6.1 and TABLE 6.2 display comparisons of previous

DFT studies of HMX and FOX-7 with the experimental crystal structures, illustrating the inaccuracy of DFT to accurately describe the ambient crystal structures of β-HMX and α-FOX-7.

	a (Å)	*b* (Å)	*c* (Å)	β (deg.)	*V* (Å^3)
Exp. Ref.6* Temp = R.T.	6.533	11.030	8.699	124.45	516.90
Ref. 28 (GGA/PBE)	6.314	11.102	7.395	102.69	505.71
Ref. 29 (GGA/PBE)	6.762	11.461	8.865	123.8	570.6
Ref. 30 (GGA/PW91)	6.78	11.48	9.19	125.02	585.57
Ref. 30, 31 (LDA/CA-PZ)	6.43	10.34	8.61	124.23	473.81
Ref. 32 (GGA/PW91)	6.860	11.517	8.929	122.8	593.3

TABLE 6.1 Comparison of previous DFT studies of HMX. * Note: no estimated standard deviations given for the experimental crystal structure.

	a (Å)	*b* (Å)	*c* (Å)	β (deg.)	*V* (Å^3)
Exp. Ref. 20 Temp = R.T.	6.934(1)	6.623(1)	11.312(1)	90.065(13)	519.47(1)
Ref. 33 (GGA/PBE)	6.74	6.18	11.05	90.69	460.5
Ref. 33 (LDA/PZ)	7.19	7.54	11.49	91.96	623.0
Ref. 34 (GGA/PBE)	6.89	6.50	11.24	91.06	503.3

TABLE 6.2 Comparison of previous DFT studies of FOX-7. The values in parentheses are estimated standard deviations.

There have been several different approaches to implement dispersion corrections in order to describe accurately the structure and properties of crystalline nitramines. Sorescu and Rice performed theoretical DFT-D predictions at ambient and elevated pressures of the crystallographic properties of ten energetic molecular crystals, including the β- and δ-forms of HMX as well as α-FOX-7.[35] They concluded that the dispersion-corrected density functional theory method (DFT-D) as parameterised by Grimme[36] provides significant improvements for description of intermolecular interactions in molecular crystals at both ambient and high pressures (although the authors did not study the effect of pressure for α-FOX-7) relative to

conventional DFT. Balu *et al.*[37] investigated the performance of dispersion-corrected atom-centered pseudopotentials (DCACP's) at describing the ambient-pressure crystal structures of several energetic materials (including HMX, but not FOX-7), showing excellent agreement with experiment, rivalling the results of DFT-D studies. Additionally, for β-HMX there have been two independent studies that have implemented the quasi-harmonic approximation in combination with a DFT-D dispersion correction, in order to predict equilibrium volumes and properties at non-zero temperatures, termed DFT-D+T.[38,39] Utilising the dispersion correction proposed by Neumann and Perrin[40] (which is similar to that of Grimme), Landerville *et. al.*[38] determined that the DFT-D+T method improved the prediction of the unit-cell volumes of β-HMX and α-FOX-7 over conventional DFT and DFT-D. The determined DFT, DFT-D and DFT-D+T volumes for β-HMX were 556.07, 500.77 and 519.41 $Å^3$, respectively (+7.75%, -3.12% and +0.49% difference to the experimental[6] volume of 516.90 $Å^3$). Similarly, for α-FOX-7 the determined DFT, DFT-D and DFT-D+T volumes were 585.08, 502.87 and 513.72 $Å^3$, respectively (+12.01%, -3.73% and -1.65% difference to the experimental[20] volume of 522.33 $Å^3$) However, no information about individual cell parameters was given, and so although the overall predicted volumes are in excellent agreement with experiment for DFT-D+T, the accuracy of the structural predictions is not clear. Using a similar method, Wu *et. al.*[39] utilised the Grimme dispersion correction to predict the structure and properties of β-HMX. In this case, the authors determined that the best agreement with experiment for predicting the unit cell shape and volume was obtained by the DFT-D method rather than DFT-D+T, as shown in TABLE 6.3 . At ambient pressure the DFT-D method predicted all lattice parameters and unit cell volume within 1% of experiment.

	Exp. Ref. 6	*Ref. 39 DFT*	*Ref. 39 DFT+T*	*Ref. 39 DFT-D*	*Ref. 39 DFT-D+T*
a (Å)	6.533	6.90	7.07	6.56	6.63
b (Å)	11.030	11.65	11.93	10.97	11.08
c (Å)	8.699	9.15	9.34	8.70	8.80
β (deg.)	124.45	124.5	124.6	124.4	124.5
V (Å^3)	516.90	608.1	653.6	517.4	534.1

TABLE 6.3 Comparison of the calculated structures and properties of β-HMX using different DFT and DFT-D methods. The temperature for DFT+T and DFT-D+T calculations was 300 K.

6.2 Aims

Given the successful implementation of dispersion corrections to describe accurately the structure and properties of various RDX polymorphs (Chapter 5), the ambiguity regarding experimental hydrostatic compression data and the incomplete characterisation of vibrational properties for β-HMX and α-FOX-7, together with the desire to investigate the factors affecting the deflagration-to-detonation transition, the aims of this work were:

- to perform the first inelastic neutron scattering studies on β-HMX and α-FOX-7 and thus obtain complete ambient pressure vibrational information
- to provide further credence that the DFT-D functional parameterised by Grimme[25] can describe accurately the structure and properties of crystalline nitramine energetic materials
- to predict the effect of pressure on the heat capacities of β-HMX and α-FOX-7

6.3 Experimental

6.3.1 Sample Preparation

Crystalline samples of β-HMX used for INS studies were kindly provided by Dr. Bernard Garatay (QinetiQ, Fort Halstead). Crystalline samples of α-FOX-7 used for INS studies were kindly provided by Dstl, Fort Halstead. Deuterated HMX and FOX-7 were synthesised by Dr. David Millar (School of Chemistry, University of

Edinburgh). HMX was deuterated following the preparation given by Bulusu *et al*.[41] Deuterated FOX-7 was prepared by treatment with NaOD in D_2O, followed by neutralisation with D_2SO_4.

6.3.2 Neutron Powder Diffraction

A lightly ground sample (*ca.* 100 mg) of deuterated powder (β-HMX or α-FOX-7) was loaded into an encapsulated TiZr gasket,[42] together with a small quantity of 4:1 perdeuterated methanol/ethanol as a PTM and a sample of lead as pressure calibrant. The resulting capsule assembly was then compressed within a type V3b Paris-Edinburgh press[43] equipped with standard single toroid anvils with cemented WC cores (Ni binder). The P-E press ram pressure was monitored and varied by means of a computer controlled hydraulic system. High-pressure neutron powder diffraction data were collected using the PEARL/HiPr and POLARIS diffractometers at the UK spallation neutron source, ISIS Neutron and Muon facility, located at the STFC Rutherford Appleton Laboratory.[44] Time-of-flight neutron powder diffraction data suitable for structure refinement were obtained by electronically focusing the individual detector element spectra from the 2θ=90° detector banks. The resulting summed pattern was then normalised with respect to the incident beam monitor and the scattering from a standard vanadium calibration sample. Lastly, the diffraction pattern intensity scale was corrected for the wavelength and scattering-angle dependence of the neutron attenuation by the anvil (WC) and gasket (TiZr) materials. Full-profile Rietveld refinements of the TOF neutron powder diffraction patterns were carried out using the GSAS package.[45] Sample pressures were calculated from the refined lead lattice parameters and the room-temperature EoS for lead as derived by Decker[46] with an uncertainty of ± 0.05 GPa. Data collection times per pressure point ranged between 1 and 6 hours at an equivalent of 165 μA ISIS proton current.

6.3.3 Inelastic Neutron Scattering

INS spectra (24-4000 cm^{-1}) were recorded using the TOSCA[47] instrument at the ISIS Neutron and Muon facility, which has an energy resolution of ~1.25%. Approximately 3.2 g of polycrystalline β-HMX (Type A ~ 200-400 μm) and 1.8 g of

polycrystalline α-FOX-7 were loaded into aluminium sample cans and cooled to T < 20 K in a conventional closed cycle refrigerator, and spectra were recorded for 3–6 h (at an equivalent of 165 μA ISIS proton current). INS data were visualised and compared to the simulated spectra of the DFT-D calculations using the aCLIMAX program.[48]

6.3.4 Computational Methods

Structure optimisations (at ambient pressure and under hydrostatic externally applied pressure conditions) and vibrational frequency calculations were performed using density functional theory plus dispersion (DFT-D) and the plane-wave pseudopotential method as implemented in CASTEP version 5.5,[49] utilising the dispersion correction scheme of Grimme.[36] Treatment of electronic exchange and correlation was handled by the generalised gradient approximation (GGA) formalised by Perdew, Burke and Ernzerhof (PBE).[50] On-the-fly (OTF)[51] pseudopotentials generated using the CASTEP code were used; the plane-wave cut-off energies used throughout were 700 eV and 650 eV for β-HMX and α-FOX-7, respectively, which ensured convergence of both lattice parameters and total energies (to less than 5 meV per unit cell). Brouillon zone sampling was obtained using M-P[52] grids of 2 × 1 × 2 for β-HMX and 2 × 3 × 1 for α-FOX-7 (both resulting in 2 k-points). The structures were relaxed [using the BFGS[53] method] to allow both atomic coordinates and unit cell vectors to optimise simultaneously while constraining space group geometry (convergence criteria: maximum change in system energy = 2 x 10^{-5} eV, maximum RMS force = 0.025 eV $Å^{-1}$, maximum RMS stress = 0.01 GPa and maximum RMS displacement = 0.002 Å). Following successful geometry optimisation of the experimental starting structures external hydrostatic pressures were applied at pressures corresponding to available experimental data. Phonon frequencies (at the gamma point in k-space) for the optimised structures were then calculated by finite displacement methods.[54]

6.4 Results and Discussion

6.4.1 Crystallographic Data

Note: all neutron and X-ray diffraction studies were performed by Dr. Alistair J. Davidson (The School of Chemistry, University of Edinburgh) and Dr. William G. Marshall (ISIS Neutron and Muon Facility.) Data were refined by Mr. Paul Coster (The School of Chemistry, University of Edinburgh).

This work uses (as yet) unpublished experimental neutron powder diffraction data as high-pressure experimental comparisons. The data in these neutron powder diffraction studies were collected using 4:1 methanol/ethanol as the PTM on account of it remaining truly hydrostatic up to pressures of *ca.* 9.8 GPa.[55] The data were collected and refined as described in Section 6.3.2.

TABLE 6.4 lists the lattice parameters obtained from Rietveld refinements for the compression of β-HMX. Fitting statistics, wR_p and χ^2 are listed for each pressure, furthermore, plots of the experimental lattice parameters and unit-cell volumes can be found in Figure 6.3 and Figure 6.4.*

Pressure (GPa)	***a*** (Å)	***b*** (Å)	***c*** (Å)	*β* (deg.)	*V* (Å^3)	wR_p	χ^2
0.00	6.5298(7)	11.0284(11)	8.6909(11)	124.391(7)	516.47(4)	3.80	1.21
0.19	6.5050(9)	10.9532(15)	8.6759(15)	124.581(9)	508.95(6)	5.70	1.14
0.32	6.4884(9)	10.9152(15)	8.6597(15)	124.672(10)	504.39(6)	5.95	1.19
0.55	6.4634(6)	10.8451(10)	8.6384(10)	124.794(7)	497.26(4)	3.62	1.18
0.99	6.4273(6)	10.7419(10)	8.6073(10)	124.933(6)	487.19(4)	3.81	1.23
1.57	6.3837(6)	10.6206(10)	8.5686(10)	125.077(7)	475.43(4)	3.87	1.20
2.11	6.3528(4)	10.5297(7)	8.5378(7)	125.148(5)	466.99(3)	2.67	1.32
2.69	6.3222(6)	10.4389(9)	8.5098(10)	125.209(6)	458.87(4)	3.68	1.15
3.31	6.2932(6)	10.3469(9)	8.4850(9)	125.267(6)	451.10(4)	3.73	1.17
3.93	6.2681(5)	10.2636(7)	8.4628(7)	125.313(5)	444.27(3)	2.77	1.29
4.65	6.2416(7)	10.1803(9)	8.4407(9)	125.335(7)	437.53(4)	3.83	1.21
5.45	6.2171(6)	10.0989(9)	8.4211(10)	125.356(7)	431.22(4)	3.78	1.18
6.22	6.1957(5)	10.0240(7)	8.4068(8)	125.388(5)	425.65(3)	2.89	1.27
7.04	6.1743(7)	9.9477(10)	8.3921(11)	125.403(7)	420.13(3)	3.75	1.15
7.77	6.1565(8)	9.8806(11)	8.3805(12)	125.424(7)	415.42(4)	4.23	1.20
8.54	6.1387(7)	9.8177(9)	8.3693(9)	125.401(4)	411.14(3)	3.12	1.31

TABLE 6.4 Variation in the unit-cell parameters of β-HMX with pressure. The values in parentheses are estimated standard deviations.

* The weighted R-factor, wR_p, represents the minimisation of the difference between the calculated and observed patterns, while χ^2 is a comparison of wR_p to the statistically expected value R_{exp}. Typically, for powder patterns consistent with the model, wR_p should be <~5% and χ^2 as close to 1 as possible. Throughout the course of a powder refinement, however, these values may yield erroneously low values, especially with data suffering from a high background or broadened diffraction peaks. It is often the case that visual inspection of the diffraction profile and difference curve is the best assessment for the quality of the refinement.

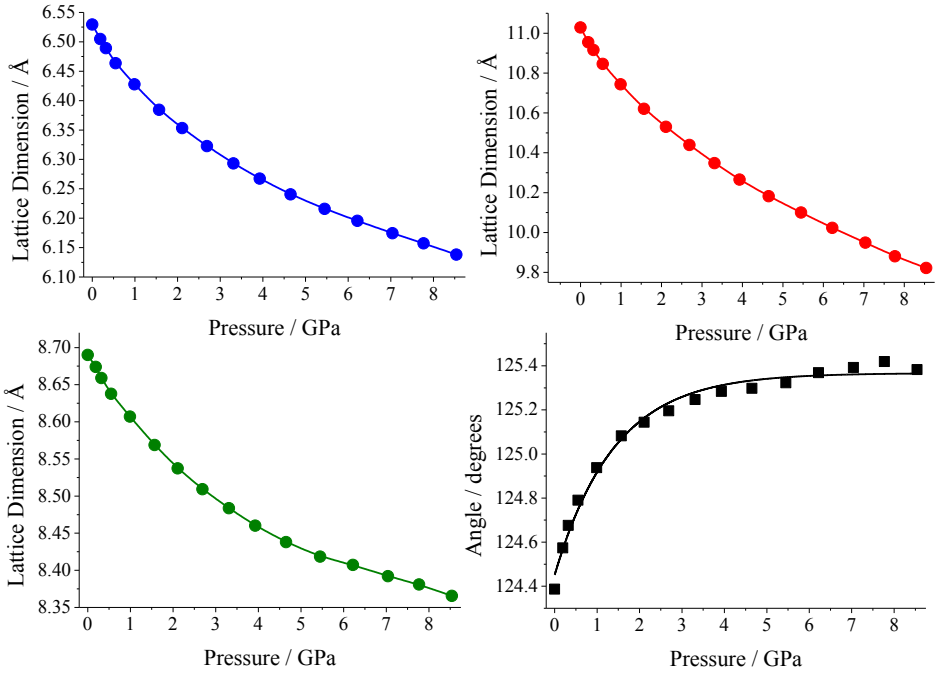

Figure 6.3 Lattice parameters of β-HMX as a function of hydrostatic pressure for the experimental data reported in TABLE 6.4. **Blue**: *a*-axis, **red**: *b*-axis, **green**: *c*-axis **black**: beta-angle.

The change in unit-cell volume as a function of pressure can be fitted to a 3rd order B-M[56] EoS (Equation 4.1), with parameters V_0 = 516.65(1.31) Å ^{3}, B_0 = 11.82(0.81) GPa, and B' = 12.10(0.82). Previous experimentally determined EoS parameters are compared to those calculated in this study in TABLE 6.5. As explained previously in Chapter 3, perhaps the most important variable in isothermal direct compression experiments is the choice of PTM. Angel et. al. determined that argon only remains truly hydrostatic to ~1.9 GPa.[55] Additionally *n*-hexane freezes at 1.04 GPa, thus at higher pressures the applied pressure across the sample material is inhomogeneous creating non-hydrostatic conditions. Thus the studies by Yoo and Cynn[9] and Gump and Peiris[10] were not performed under hydrostatic conditions throughout the whole pressure range. This explains the discrepancy between the bulk moduli between the four studies. The (unpublished) neutron powder diffraction compression data, and the experiment performed by Olinger *et. al.*[11] both utilised 4:1 methanol/ethanol as the PTM, which remained hydrostatic throughout the whole pressure range studied, and the resultant bulk moduli are in excellent agreement (within experimental error) of each other. The other two studies report larger bulk moduli, i.e. HMX under non-hydrostatic conditions is less compressible than under hydrostatic conditions. Ironically Yoo and Cynn[9] reached the same conclusion by

comparison of their 'hydrostatic' experiments using argon as the PTM with respect to compression of β-HMX with no PTM.

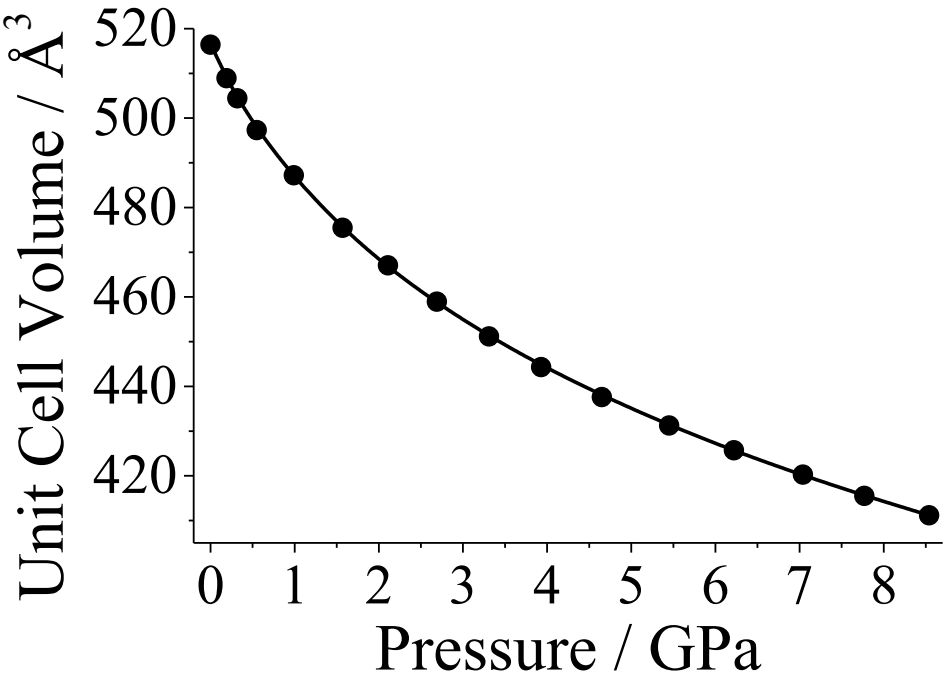

Figure 6.4 Unit-cell volume of β-HMX as a function of hydrostatic pressure for the experimental data reported in TABLE 6.4 fitted with 3rd order B-M EoS (Equation 4.1).

	B_0 (GPa)	B'
This work	11.82(0.81)	12.10(0.82)
Ref. 9	16.0(2.5)	7.3(1.4)
Ref. 10	21.0(1.0)	7.4(1.7)
Ref. 11	10.6(1.7)	18.1(3.4)

TABLE 6.5 Comparison of calculated bulk moduli and pressure derivative of the bulk moduli values for this work (Neutron powder diffraction, 4:1 methanol:ethanol PTM, 0.00 – 8.54 GPa), Yoo and Cynn data - Ref. 9 (X-ray powder diffraction, argon PTM, 0 – 12 GPa), Gump and Peiris data – Ref. 10 (X-ray powder diffraction, n-hexane PTM, 0.00 – 5.42 GPa) and Olinger et. al. data – Ref. 11 (X-ray powder diffraction, 4:1 methanol:ethanol PTM, 0 – 7.5 GPa).

To summarise, the experimental high-pressure neutron powder diffraction study is complementary to previous X-ray diffraction experiments. The EoS is in excellent agreement with previous hydrostatic studies, indicating that deuteration of β-HMX does not affect its compression behaviour, and thus these data are suitable for use as an experimental comparison to the computational simulations.

To date no hydrostatic compression diffraction studies of α-FOX-7 have been presented in the literature. TABLE 6.6 lists an amalgamation of unpublished data obtained from multiple neutron powder diffraction experiments, displaying the lattice

parameters obtained from Rietveld refinements for the compression of α-FOX-7, with fitting statistics, wR_p and χ^2, furthermore, plots of the experimental lattice parameters and unit-cell volumes can be found in Figure 6.5and Figure 6.6.

Pressure (GPa)	***a*** *(Å)*	***b*** *(Å)*	***c*** *(Å)*	*β (deg.)*	*V (Å^3)*	wR_p	χ^2
0.00*	6.9400(2)	6.6280(1)	11.3287(4)	90.595(3)	521.07(2)	3.29	9.30
0.09*	6.9255(10)	6.5759(6)	11.3050(22)	90.547(14)	514.82(10)	0.70	10.06
0.38*	6.9014(9)	6.5052(5)	11.2701(19)	90.471(13)	505.96(9)	0.70	10.83
0.47#	6.8956(6)	6.5014(3)	11.2660(14)	90.483(9)	505.05(6)	1.29	3.34
0.68*	6.8735(10)	6.4349(6)	11.2264(21)	90.395(15)	496.54(10)	0.76	11.37
1.33#	6.8371(6)	6.3428(3)	11.1698(13)	90.318(10)	484.39(6)	1.30	3.61
1.34*	6.8335(9)	6.3271(5)	11.1630(19)	90.321(14)	482.64(9)	0.72	10.52
1.73#	6.8146(6)	6.2842(3)	11.1294(12)	90.267(9)	476.60(6)	1.32	3.50
1.89*	6.8046(8)	6.2531(5)	11.1121(17)	90.263(13)	472.81(8)	0.70	9.74
2.20#	6.7905(6)	6.2243(3)	11.0877(12)	90.224(9)	468.63(6)	1.26	3.47
2.36#	6.7835(6)	6.2058(3)	11.0722(12)	90.198(9)	466.10(5)	1.29	3.49
2.47#	6.7810(13)	6.1955(6)	11.0697(24)	90.202(19)	465.06(11)	1.07	8.83
2.58#	6.7783(9)	6.1865(4)	11.0614(16)	90.188(13)	463.84(7)	1.17	5.60
2.64*	6.7670(8)	6.1641(5)	11.0516(15)	90.184(12)	460.99(7)	0.72	10.04
2.79#	6.7622(10)	6.1562(5)	11.0438(18)	90.147(15)	459.75(8)	1.17	7.43
3.30#	6.7482(16)	6.1170(7)	11.0092(27)	90.102(21)	454.44(12)	1.40	7.60
3.63*	6.7321(11)	6.0788(6)	10.9849(22)	90.113(18)	449.54(10)	0.89	14.49
4.14#	6.7291(29)	6.0629(12)	10.9555(47)	90.142(38)	446.96(21)	3.13	17.00

TABLE 6.6 Variation in the unit-cell parameters of α-FOX-7 with pressure, the values in parentheses are estimated standard deviations. * signifies data collection using the POLARIS instrument, # signifies data collection using the PEARL/HiPr instrument.

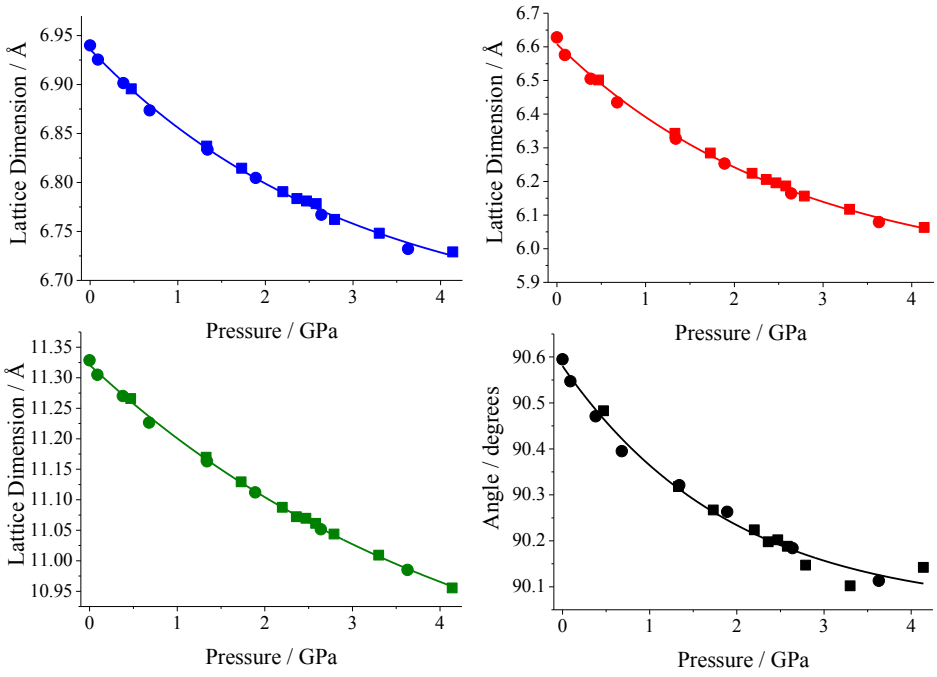

Figure 6.5 Lattice parameters of α-FOX-7 as a function of hydrostatic pressure for the experimental data reported in TABLE 6.6. **Blue**: *a*-axis, **red**: *b*-axis, **green**: *c*-axis **black**: beta-angle. Circle: POLARIS instrument data, Square: PEARL instrument data.

The change in unit-cell volume as a function of pressure for α-FOX-7 can be fitted to a 3rd order B-M[56] EoS (Equation 4.1), with parameters V_0 = 521.07(0.04) Å^3, B_0 = 11.81(0.47) GPa, and B' = 11.41 (0.95).

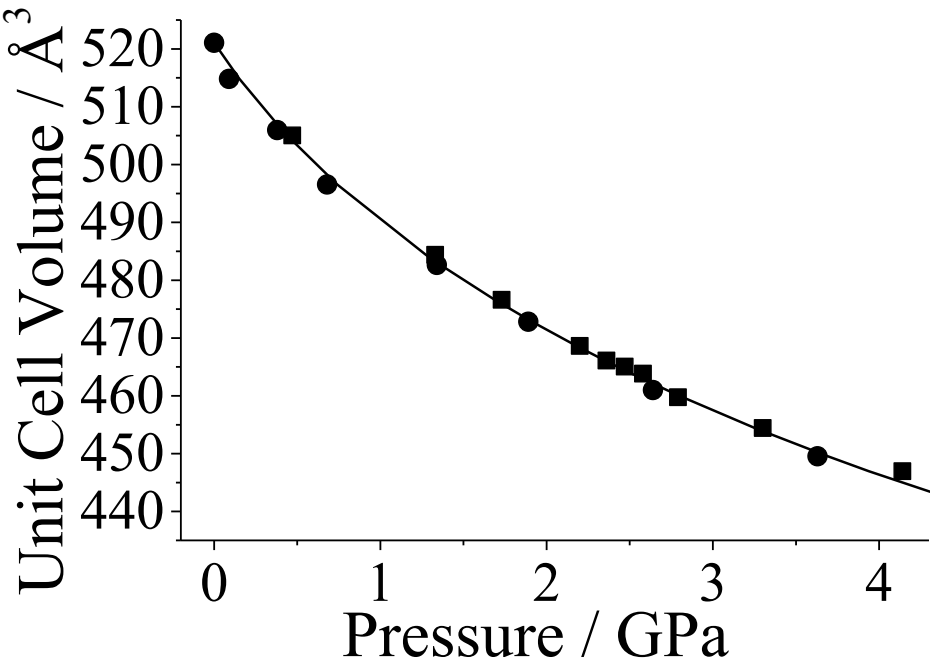

Figure 6.6 Unit-cell volume of α-FOX-7 as a function of hydrostatic pressure for the experimental data reported in TABLE 6.6 fitted with 3rd order B-M EoS (Equation 4.1). Circle: POLARIS instrument data, Square: PEARL instrument data.

6.4.2 Ambient-Pressure Computational Behaviour

6.4.2.1 Structure of β-HMX and α-FOX-7

β-HMX crystallises in the monoclinic crystal system with space group $P2_1/c$: the unit cell contains 2 HMX molecules, giving a total of 56 atoms. The results of the geometry optimisation are compared to available experiment and previous dispersion correction studies as shown in TABLE 6.7. All lattice parameters agree with experimental values to within 1.5%, and the overall unit-cell volume differs from experiment by only 0.6%. These results are consistent with previous DFT-D studies[†] and confirm that the Grimme dispersion correction can accurately describe the intermolecular interactions in the β-HMX crystal.

[†] The current and previous DFT-D (Ref. 35) calculations both used the same dispersion correction scheme, the difference in the calculated geometries arises from the fact that different pseudopotentials

Parameter	Exp.* Ref. 6	DFT-D Ref. 39	DFT-D Ref. 35	DFT-D (This work)
a (Å)	6.533	6.56 (0.4)	6.540 (0.1)	6.5489 (0.2)
b (Å)	11.030	10.97 (-0.5)	10.811 (-2.0)	10.8597 (-1.5)
c (Å)	8.699	8.70 (0.0)	8.742 (0.5)	8.7538 (0.6)
β (deg.)	124.45	124.4 (0.0)	124.28 (-0.1)	124.373 (-0.1)
V (Å^3)	516.90	517.4 (0.1)	510.79 (-1.2)	514.01 (-0.6)

TABLE 6.7 Comparison of the crystallographic parameters of β-HMX calculated at ambient pressure using the DFT-D method alongside results obtained from experiment and previous DFT-D studies. * Note: no estimated standard deviations given for the experimental crystal structure. The values in parentheses are the percentage error deviations from experimental values.

Similarly, α-FOX-7 crystallises in the monoclinic crystal system with space group $P2_1/n$: the unit cell contains 4 FOX-7 molecules, giving a total of 56 atoms. The results of the geometry optimisation are compared to available experimental data and a previous dispersion correction study as shown in TABLE 6.8. All lattice parameters agree with experimental data to within 1.5%, and the overall unit cell volume differs from experiment by only 0.6%. These results are consistent with previous DFT-D studies† and confirm that the Grimme dispersion correction can accurately describe the intermolecular interactions in the α-FOX-7 crystal.

Parameter	Exp. Ref. 20	DFT-D Ref. 35	DFT-D (This work)
a (Å)	6.9340[7]	6.8973 (-0.63)	7.0049 (0.92)
b (Å)	6.6228[8]	6.4488 (-1.83)	6.4738 (-1.45)
c (Å)	11.3119[13]	11.2919 (-0.20)	11.3091 (-0.05)
β (deg.)	90.065[13]	90.98 (0.47)	90.946 (0.44)
V (Å^3)	519.47[1]	508.74 (-1.39)	512.78 (-0.60)

TABLE 6.8 Comparison of the crystallographic parameters of FOX-7 calculated at ambient pressure using the DFT-D method alongside results obtained from experiment and previous DFT-D studies. The numbers in square brackets are the estimated standard deviations of experimental values, the values in parentheses are the percentage error deviations from experimental values.

were used in each study. The calculations in Ref. 39 implemented the dispersion correction of Neumann and Perrin.

6.4.2.2 Vibrational Properties

Following the geometry optimisations, comprehensive finite displacement phonon calculations (including symmetry) were performed to obtain the vibrational properties of β-HMX and α-FOX-7. The phonon calculation was performed at only the gamma point in k-space as the materials are insulators and thus the dispersion of phonon energies throughout k-space is assumed to be negligible. TABLE 6.9 shows a comparison of the calculated fundamental modes for β-HMX with literature IR and Raman spectra, in addition to the experimental INS spectra determined in this study. Likewise, the assigned fundamental modes for α-FOX-7 are compared to the INS spectra determined in this study in TABLE 6.10.

TABLE 6.9 and TABLE 6.10 show that the majority of the calculated fundamental vibrational modes are in good agreement (<2.5% difference) with experimental frequencies and in turn show that the INS spectra determined in this study are in good agreement with previous IR and Raman spectra.

*Mode**	*Activity*	*DFT-D*	*INS (this work)*	*Raman Ref. 12*	*Raman Ref. 13*	*IR Ref. 12*	*IR Ref. 2*	*Assignment*
		ν	**ν**	**ν**	**ν**	**ν**	**ν**	
4	Raman	44.5	36	32	36			lattice
5	IR	51.4	41					
6	Raman	66.7	45	60	36			
7	IR	67.9	56				59	
8	Raman	74.0	58		65			
9	Raman	76.5	73	78	65			
11	Raman	88.4	80		81			
12	IR	92.5	83				90	
18	Raman	106.6	109		96			
10	IR	84.1	75				79	NO_2 wag
13	IR	96.2	84					
14	Raman	99.0	91	92	81			
15	Raman	101.7	100	127	97			
16	IR	103.9	103					NO_2 wag
17	IR	105.0	106				110	
20	Raman	126.2	124	134	130			
22	Raman	133.1	130		130			
19	IR	123.4	122				126	NO_2 rot.
21	IR	132.4	130		130			
25	Raman	146.8	154	142	139			
26	Raman	155.5	156		149			
23-24	IR	143.0	144				140	NO_2 rot.
27-28	Raman	164.6	164	151	155			
29	IR	168.1	171				152	ring def.
30	IR	172.5	174				158	
35-36	Raman	222.4	183				183	
31-32	IR	180.1	192		181			NO_2 rot.
33-34	Raman	193.5	230	230	231			
37-38	IR	238.0	235				224	ring def.
39	Raman	269.1	280	281	283			

*Mode**	*Activity*	*DFT-D*	*INS (this work)*	*Raman Ref. 12*	*Raman Ref. 13*	*IR Ref. 12*	*IR Ref. 2*	*Assignment*
		ν	**ν**	**ν**	**ν**	**ν**	**ν**	
40	Raman	270.0	281		283			
41-42	Raman	306.1	320	312	316, 318			ring def.
43-44	IR	343.7	357					
45-46	Raman	359.7	365	358	363, 364			ring def.
47	IR	374.0	383					
48	IR	376.5	385				385	
49-50	Raman	406.0	415	412	415, 417			ring def.
51-52	IR	412.7	417				420	
55-56	IR	425.7	441				441	
57-58	Raman	581.1	601	597	598, 600			ring def.
59-60	IR	585.9					605	
61-62	IR	609.3	631				630	ring def.
67-68	Raman	643.4		662	662, 663			
63-64	Raman	625.5	650	638	640			ring def.
65-66	IR	640.7	664			660, 668	660	
69-70	Raman	698.9	719	721	722			ring def.
79-80	IR	750.5	763			752, 758	755	
71-72	IR	721.8						$N\text{-}NO_2$ umb.
73-74	Raman	723.2						
75, 77	IR	727.8	763			769	762, 773	$N\text{-}NO_2$ umb.
76, 78	Raman	729.5		759	762, 763			
81-82	IR	815.4	835			827	833	asym. ring st.
83-84	Raman	824.2		834	834, 836			
85-86	IR	860.7	882			871	872	sym. ring st.
87-88	Raman	872.1		881	884			
89-90	IR	931.9	960			945	948	NN st., CH_2 rock
91, 95	Raman	944.0		950	953			
92, 94	Raman	944.9	974	965	966, 967			NN st., CH_2 rock
93, 96	IR	948.9				965	966	
97, 100	Raman	1084.8	1098	1080, 1090	1080, 1088			NN st., CH_2 rock
98-99	IR	1086.6				1090	1089	
101-102	IR	1131.9	1155			1146	1145	NC st., CH_2 tw.
103-104	Raman	1156.7	1178	1168	1170			
105-106	Raman	1191.8	1202	1190	1190, 1192			NC st., CH_2 wag
107-108	IR	1202.4				1205	1203	
109-110	IR	1224.8	1250			1240	1269	NC st., CH_2 tw.
111-112	Raman	1234.1		1248	1250, 1251			
113-114	Raman	1279.3		1268	1268, 1270			NO_2 sym. st., CH_2 tw.
115-116	IR	1289.9				1280	1281, 1288	
117, 120	IR	1299.0					1298	NO_2 sym. st., CH_2 tw.

*Mode**	*Activity*	*DFT-D*	*INS (this work)*	*Raman Ref. 12*	*Raman Ref. 13*	*IR Ref. 12*	*IR Ref. 2*	*Assignment*
		ν	**ν**	**ν**	**ν**	**ν**	**ν**	
118-119	Raman	1300.5			1310			
	Raman	1316.2	1361	1312	1315,			CH_2 tw.
121, 125					1318			
129-130	IR	1365.5						
122, 124	IR	1313.8	1334			1320	1325	CH_2 tw.
	Raman	1323.2		1368	1368,			
123, 126					1369			
127-128	Raman	1339.8		1350	1351			CH_2 wag
131-132	IR	1379.0				1348	1348	
	IR	1384.1	1424			1397	1395,	CH_2 wag
133-134							1401	
135-136	Raman	1398.7		1418	1420			
	Raman	1436.0	1467	1452,	1461			CH_2 sci.
141, 143				1460				
142, 144	IR	1441.4					1463	
	Raman	1593.0		1525,	1535			NO_2 asym. st.
145, 147				1532				
	IR	1598.3				1540	1533,	
146, 148							1538	
	IR	1629.2				1570	1565,	NO_2 asym. st.
149, 152							1573	
	Raman	1629.0		1558,	1560,			
150-151				1568	1570			
153-154	Raman	3023.1	3038	2992	2994			CH_2 sym. st.
155-156	IR	3023.5					2978	
157-158	IR	3131.1					2983	CH_2 sym. st.
159-160	Raman	3131.9						
161, 163	IR	3084.9	3069				3027	CH_2 asym. st.
162, 164	Raman	3085.5		3028	3028			
165-166	IR	3089.9					3037	CH_2 asym. st.
167-168	Raman	3090.4		3037	3038			

TABLE 6.9 Assigned spectrum of the computationally calculated fundamental modes for β-HMX compared with previous IR and Raman spectroscopy spectra, in addition to the INS spectrum reported in this work. * Where there are multiple modes, the DFT-D value stated is an average of the contributing modes. rot. = rotation, def. = deformation, umb. = umbrella, asym. = asymmetric, sym. = symmetric, st. = stretch, tw. = twist, and sci. = scissors. All frequencies, **ν**, are in units of cm^{-1}.

Furthermore, comparisons of experimental combination and overtone bands with their identifiable computationally calculated counterparts can be found in the Appendix, Tables A6.1 and A6.2 for β-HMX and α-FOX-7, respectively.

*Mode**	*DFT-D*	*INS (this work)*	*Assignment*
	ν	**ν**	
4	29.3	27	lattice
5	48.1	46	lattice
6	57.9	53	lattice
7	60.1	58	lattice
8	67.3	64	lattice
9	76.3	69	lattice
10	77.1	72	lattice
11	81.5	79	lattice
12	86.5	85	lattice
13	91.7	88	lattice
14-15	93.4	95	lattice
16	97.3	97	lattice
17-20	100.1	103	lattice
21-22	109.3	112	lattice
25	119.6	117	CN_2 wag, NO_2 twist
23-24	113.5	122	CN_2 wag, NO_2 twist
26-27	122.9	138	CN_2 wag, NO_2 twist
28	124.4	145	lattice
29	128.9	148	lattice
30	130.9	150	CN_2 wag, NO_2 twist
31	145.4	162	NO_2 twist
32	150.6	164	NO_2 twist
35-36	165.7	177	CN_2 wag, NO_2 twist
37-38	256.1	238	CN_2 wag
39-40	263.8	241	CN_2 wag
41-44	319.5	317	CN_2 scissors
45-48	326.6	327	CN_2 wag
49-52	384.6	388	CN_2 wag
53-56	445.4	453	CN_2 scissors
57-60	455.8	464	CN_2 scissors
61-64	476.5	474	CN_2 scissors, NH_2 twist
65-66	558.8	529	NH_2 wag
67-68	599.6	559	NH_2 wag
71-72	611.5	584	NH_2 wag
69,70,73,74	610.9	602	CN_2 scissors
75-76,77-78	639.6	627	NH_2 wag
79-82,83-84	671.9	679	CN_2 wag, NH_2 twist; NH_2 wag
85-88	715.3	720	CN_2 wag
89-92	740.6	742	CN_2 wag
93-96	765.1	769	NO_2 scissors, NH_2 twist
97-100	783.9	784	NH_2 twist
101-104	837.3	808	NO_2 scissors, NH_2 rock
105-108	1017.8	1036	NH_2 wag
109-112	1068.7	1068	NH_2 wag
113-116	1148.5	1134	CN_2 asymmetric stretch
117-120	1167.6	1146	CC stretch, NH_2 wag
121-124	1251.7	1260	CN_2 asymmetric stretch, NH_2 wag
125-128	1368.6	1371	CN_2 symmetric stretch
129-132	1413.2	1392	NO_2 asymmetric stretch, NH_2 scissors
133-136	1480.6	1463	NO_2 asymmetric stretch, NH_2 scissors
141-142	1517.4	1485	CC stretch, NO_2 asymmetric stretch, NH_2 scissors
145-148	1573.8	1538	NO_2 asymmetric stretch, NH_2 scissors
153-160	3421.5	3331	NH_2 symmetric stretch
161-168	3556.9	3432	NH_2 asymmetric stretch

TABLE 6.10 Assigned spectrum of the computationally calculated fundamental modes for α-FOX-7 compared to the INS spectrum reported in this work. * Where there are multiple modes, the DFT-D value stated is an average of the contributing modes. All frequencies, **ν**, are in units of cm^{-1}.

In Figure 6.7 and Figure 6.8 the calculated INS spectra of β-HMX and α-FOX-7 calculated using DFT-D, are compared to the experimental INS spectra measured on the TOSCA instrument at ISIS[34] (in addition, annotated comparisons of the experimental and computational INS spectra can be found in the Supplementary Information CD for both β-HMX and α-FOX-7). From these comparisons it can be readily seen that the computed and experimental spectra show excellent agreement, both for neutron energy loss and for the phonon mode intensities.

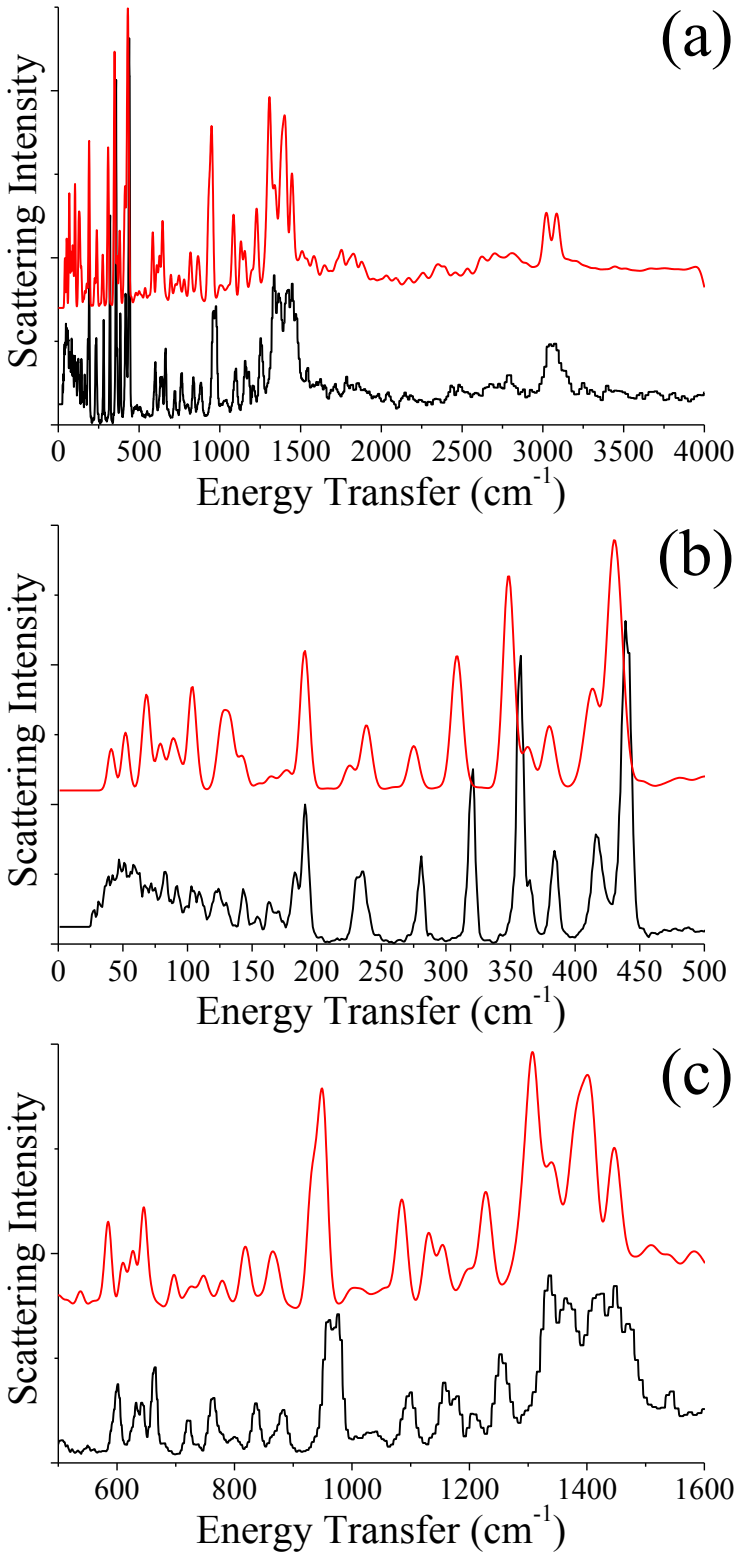

Figure 6.7 Experimental (**black**) and computationally calculated (**red**) INS spectra of β-HMX at ambient pressure. (a) 0 – 4000 cm^{-1}, (b) 0 – 500 cm^{-1}, (c) 500 – 1600 cm^{-1}.

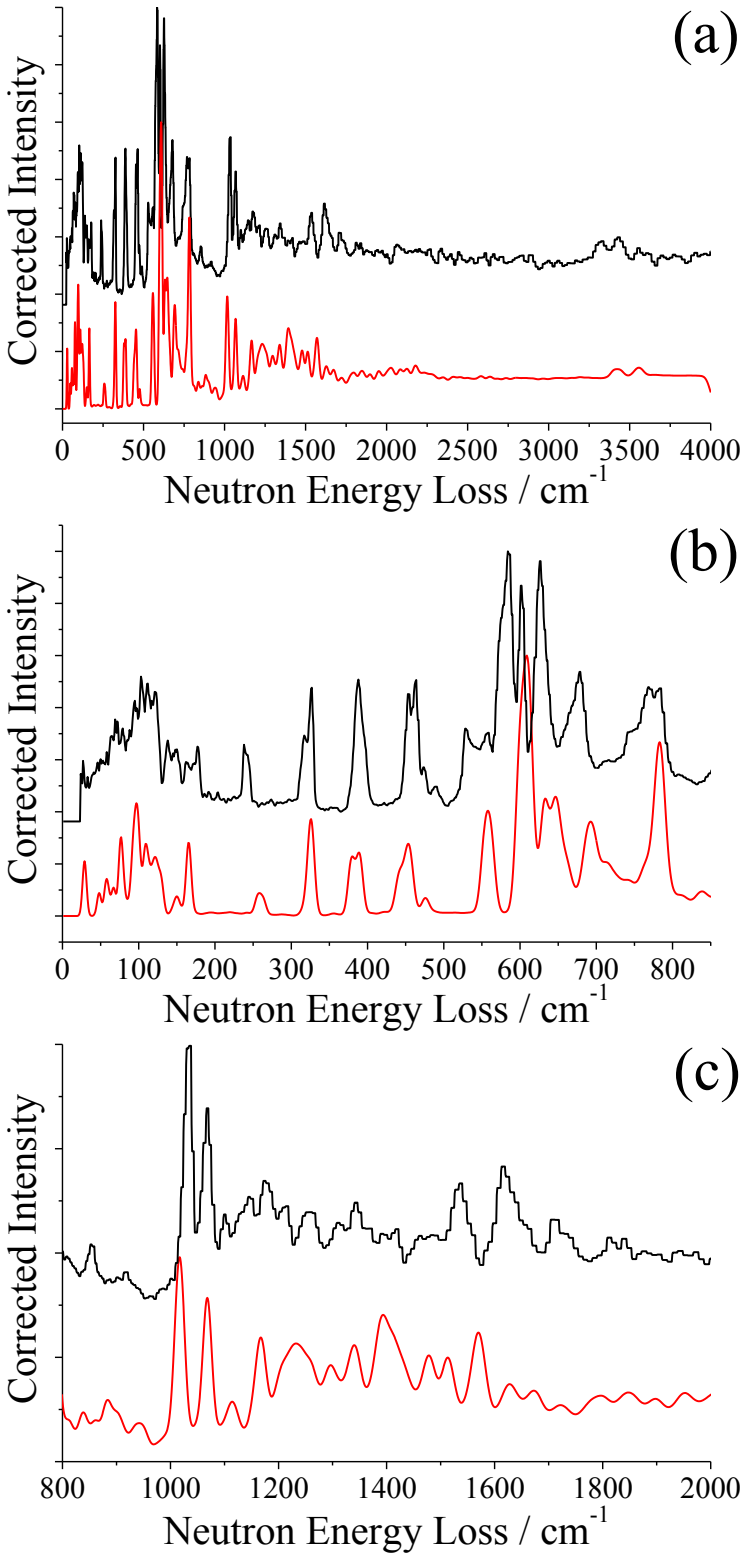

Figure 6.8 Experimental (**black**) and computationally calculated (**red**) INS spectra of α-FOX-7 at ambient pressure. (a) 0 – 4000 cm^{-1}, (b) 0 – 850 cm^{-1}, (c) 800 – 2000 cm^{-1}.

The excellent agreement between experiment and theory both for the crystallographic lattice parameters and for the vibrational frequencies and intensities

for β-HMX and α-FOX-7, confirm the conclusion reached during the study of crystalline RDX, that the computational model accurately describes both the intra- and intermolecular interactions in these nitramine crystals.

6.4.3 Compression Behaviour of β-HMX and α-FOX-7

6.4.3.1 Effect of Pressure on Lattice Parameters

Figure 6.9 shows that the experimental lattice parameters and compression behaviour are reproduced well by the DFT-D method. For β-HMX the *a*-axis is consistently overestimated by ~0.4%, the *b*-axis is initially underestimated by 1.5% and upon compression the overestimation gradually rises, with a maximum difference of 2.4% at 8.54 GPa. Similarly, the *c*-axis is initially overestimated by 0.7% at ambient pressure, as the pressure is increased the difference compared to experiment increases to 2.4% at 8.54 GPa. It can readily be seen from Figure 6.9a that the computational model used in this study provides comparable results to the previous computational DFT-D compression study performed by Sorescu and Rice.[35]

The *a*-axis of α-FOX-7 is initially overestimated by ~1.0% at ambient pressure, but as the pressure is increased the difference to experiment gradually decreases, with an error of only 0.1% at 4.14 GPa, the maximum pressure of the study. Analogous to the behaviour of the *a*-axis, the error in the calculation of the *b*-axis decreases with increasing pressure, an underestimation of 2.3% at ambient reduces to only 1.6% at 4.14 GPa. The *c*-axis is initially underestimated computationally at low pressure, then slightly overestimated at greater degrees of compression, however, the difference compared to experiment is never more the 0.3%.

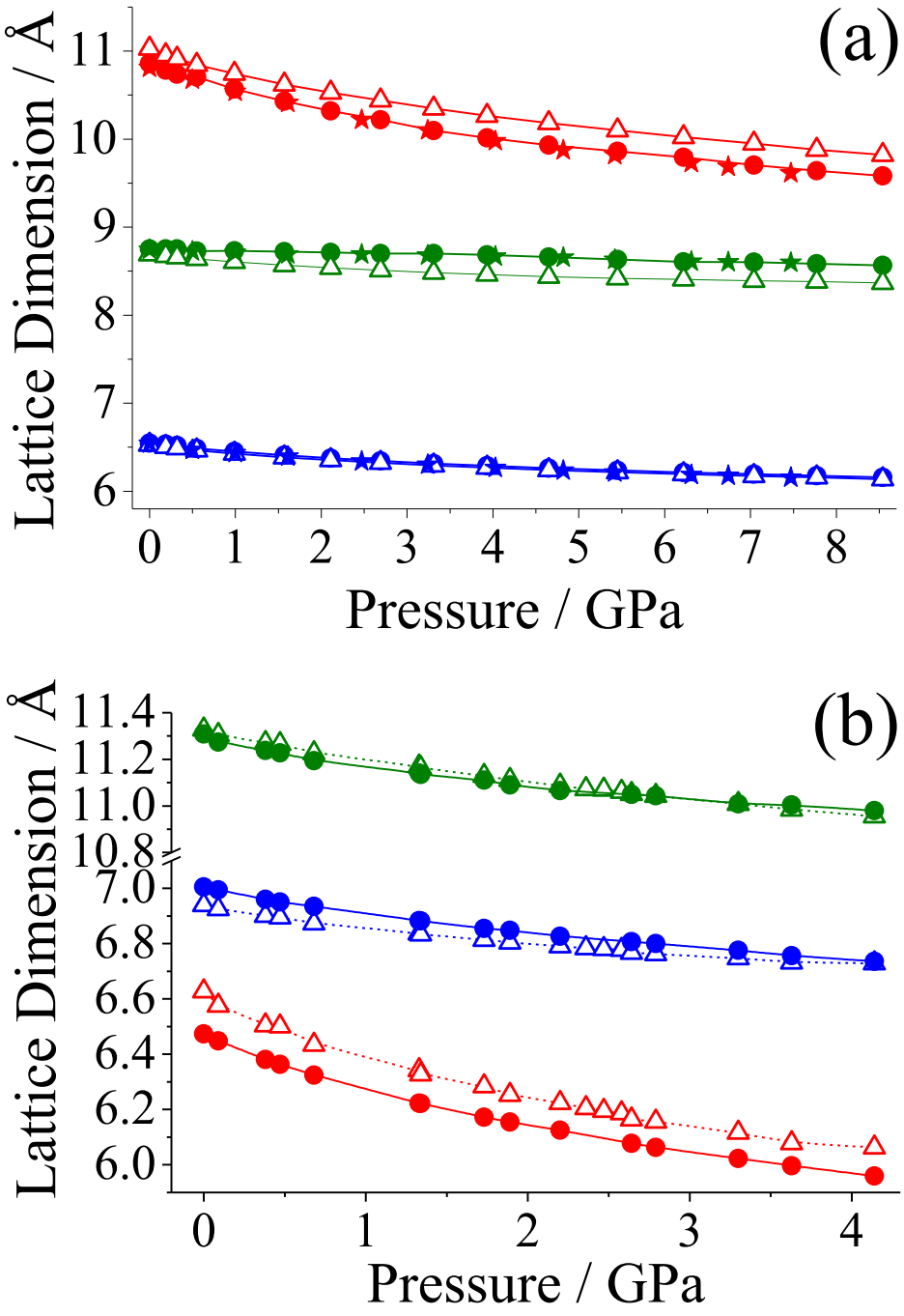

Figure 6.9 Lattice parameters as a function of hydrostatic pressure. Triangle: experiment (unpublished data reported in this work), circle: DFT-D (this work), star: DFT-D Ref. 35. **Blue**: *a*-axis, **red**: *b*-axis, **green**: *c*-axis. (a) β-HMX, (b) α-FOX-7.

Figure 6.10 demonstrates that the experimental trends for the effect of pressure on the *β*-angle of the unit cells of both β-HMX and α-FOX-7 are successfully reproduced by the computational models. The *β*-angle of β-HMX is consistently calculated to lie within 0.4% of experimental values, similarly the

β-angle of α-FOX-7 was calculated to lie within 0.2% of experimental values throughout the whole pressure range. Furthermore, inspection of Figure 6.10a shows that this study produces a computational compression trend for β-HMX in superior agreement to experiment than the trend predicted by the previous DFT-D study.[35]

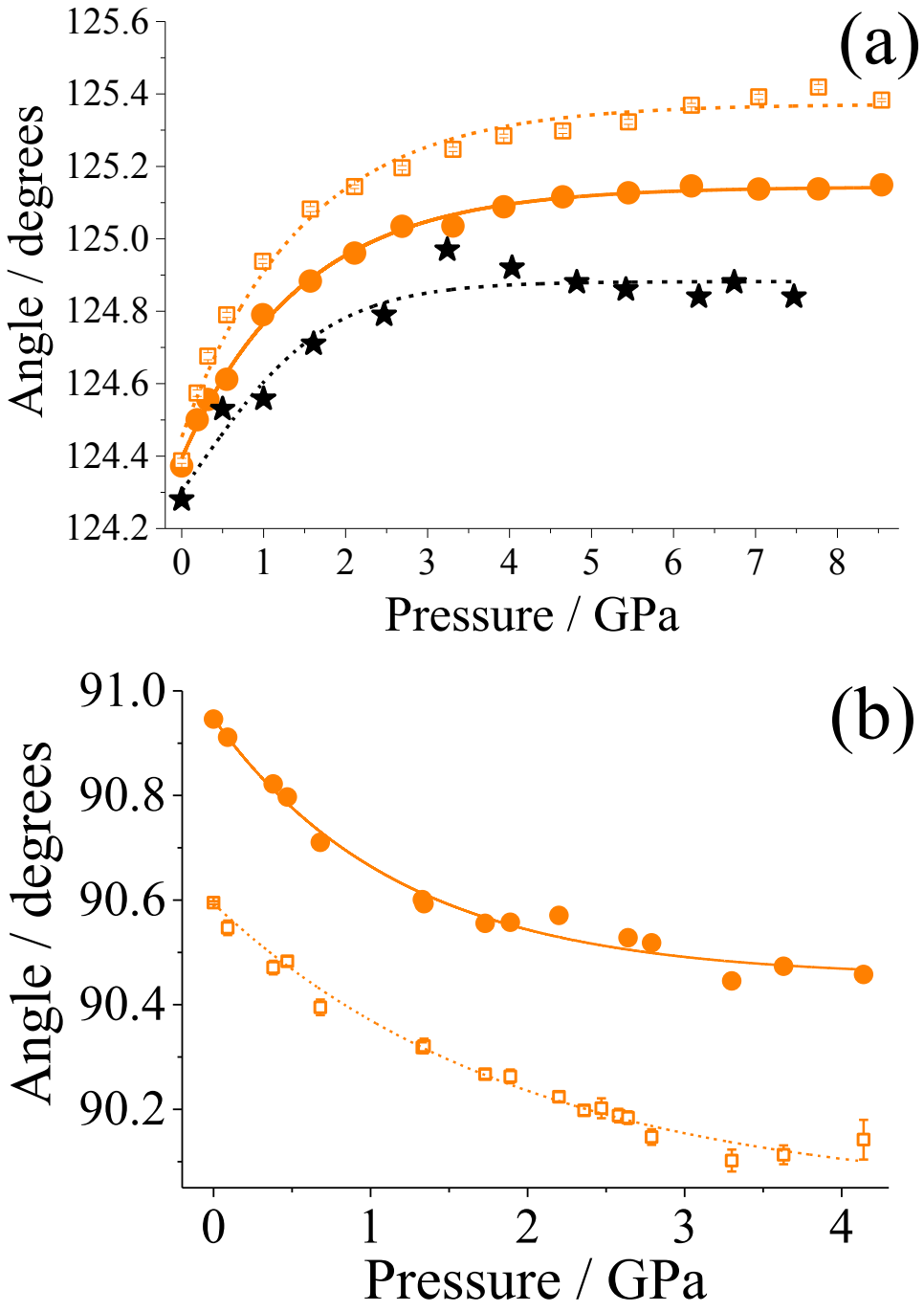

Figure 6.10 β-angle as a function of hydrostatic pressure. Square: experiment (unpublished data reported in this work), circle: DFT-D (this work), star: DFT-D Ref. 35. (a) β-HMX, (b) α-FOX-7. (Note for these and subsequent figures the error bars on the data points are similar to or less than the size of the data points.)

Figure 6.11 depicts the overall unit-cell volume compression as a function of pressure for β-HMX the results are compared to experimental values and are fitted with 3rd order B-M EoS.[56] The unit-cell volumes as a function of pressure for β-HMX were calculated in excellent agreement with experiment, with deviations of no more than 0.8% over the pressure range studied.

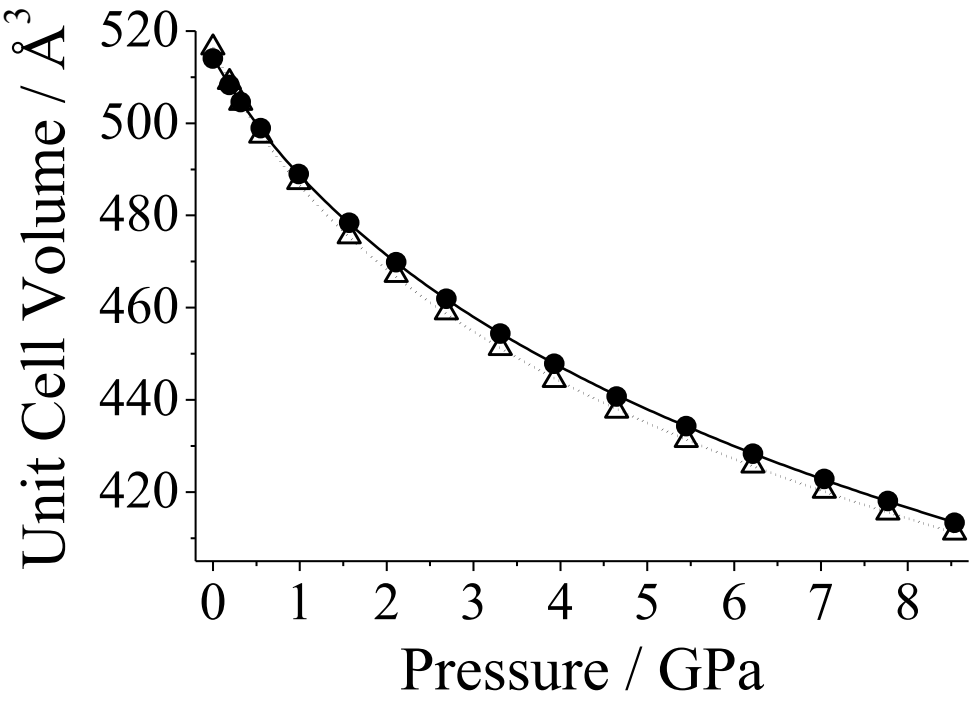

Figure 6.11 Unit-cell volume as a function of hydrostatic pressure for β-HMX fitted with 3rd order B-M EoS (Equation 4.1). Triangle: experiment (unpublished data reported in this work), circle: DFT-D (this work).

The calculated EoS parameters are presented in TABLE 6.11, alongside their experimentally-derived counterparts, in addition to previous DFT-D results by Sorescu and Rice.[35] It can be seen that both this work and the DFT-D calculations by Sorescu and Rice slightly underestimate the compressibility of β-HMX. This is primarily due to the initial underestimation of the unit cell volume at ambient pressure for both computational studies, in conjunction with the subsequent slight overestimation at elevated pressures. Nonetheless, the calculated EoS parameters agree well with experiment, furthermore the EoS parameters calculated in this study agree with experiment as well as or better than previous DFT-D and DFT-D+T computational studies.[35,39]

	V_0 (Å^3)	B_0 (GPa)	B'
Exp. (Unpublished data, this work)	516.65(1.31)	11.82(0.81)	12.10(0.82)
DFT-D (This work)	514.29(0.27)	15.57(0.21)	9.29(0.14)
DFT-D Ref. 35	510.91(0.38)	16.20(0.30)	8.78(0.19)
DFT-D+T Ref. 38*	519.41	16.74	7.78

TABLE 6.11 Experimental and computational 3rd order B-M[56] EoS (Equation 4.1) parameters of crystalline β-HMX. The values in parentheses are estimated standard deviations. * No estimated standard deviations reported in this study.

Similarly, Figure 6.12 depicts the overall unit-cell volume compression as a function of pressure for α-FOX-7, the results are compared to experimental values and are fitted with 3rd order B-M EoS.[56] The unit-cell volumes as a function of pressure were calculated in excellent agreement with experiment, the calculated volumes throughout the whole pressure range underestimated experimental values by no more than 1.7%.

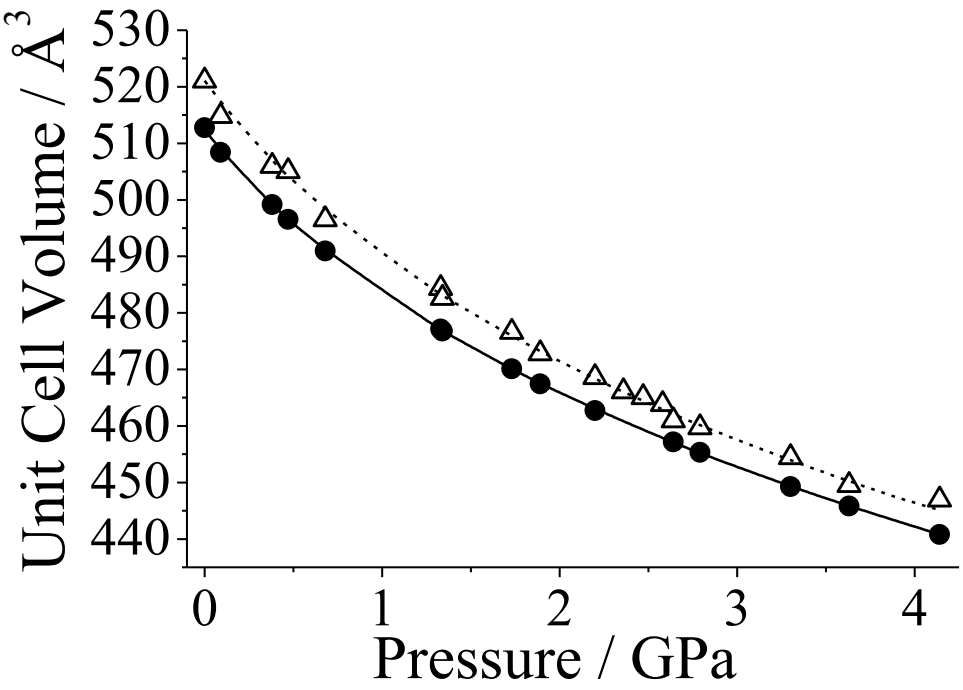

Figure 6.12 Unit-cell volume as a function of hydrostatic pressure for α-FOX-7 fitted with 3rd order B-M EoS (Equation 4.1). Triangle: experiment (unpublished data reported in this work), circle: DFT-D (this work).

The calculated EoS parameters are presented in TABLE 6.11, alongside their experimentally-derived counterparts and previous computational DFT-D+T results. Although the initial zero-pressure volume is slightly underestimated computationally

in this study, which the DFT-D+T method reproduces better, it can readily be seen that the overall experimental compression trend is reproduced extremely well using DFT-D, exemplified by the fact that the calculated B_0 and B' values agree (within error) with those experimentally determined, where the DFT-D+T method significantly underestimates the compressibility of α-FOX-7 in this pressure range.

	V_0 (Å^3)	B_0 (GPa)	B'
Exp. (Unpublished data, this work)	521.07(0.04)	11.81(0.47)	11.41(0.95)
DFT-D (This work)	512.37(0.23)	12.46(0.20)	12.01(0.26)
DFT-D+T Ref. 38*	518.28	18.41	6.12

TABLE 6.12 Experimental and computational 3rd order B-M[56] EoS parameters (Equation 4.1) of crystalline α-FOX-7. The values in parentheses are estimated standard deviations. * No estimated standard deviations reported in this study.

6.4.3.2 High-Pressure Vibrational Properties

High-pressure vibrational mode calculations have also been performed for β-HMX and α-FOX-7. Complete results of the high-pressure phonon calculations can be found in the Supplementary Information CD (in addition, also contained on the CD are the experimental crystallographic information files [cifs], the computationally calculated structures and the CASTEP output files for the geometry optimisations and phonon calculations, and statistical thermodynamics solver spread sheets for each compound studied). Although there is experimental information about the effect of pressure on the vibrational frequencies of β-HMX,[2] unfortunately, the reported data are limited (information for only 7 modes) and span only a very small pressure range (0.33 GPa). Hence they are not directly comparable to the calculated results. In addition, there are currently no published pressure-induced shift values for α-FOX-7. Nevertheless, the effect of pressure on the vibrational frequencies have been calculated (or rather the effect of changing volume on the vibrational properties), represented by the Grüneisen parameters, γ. The larger the magnitude of γ, the greater the effect that changing the volume has on the vibrational properties. Furthermore, a positive value indicates mode-hardening with pressure (blue-shift) and red-shifts are represented with negative values of γ.

Inspection of the high-pressure phonon calculation results (contained on the Supplementary Information CD) highlight that the vast majority of the calculated modes shift towards higher energies (mode-harden), as is generally expected upon compression. However, for α-FOX-7 both the NH_2 wagging modes (ω = ~1010-1070 cm^{-1}) and the NH_2 stretching modes (ω = ~3380-3580 cm^{-1}) exhibit negative Grüneisen parameters (red-shift with increasing pressure). These observations are in qualitative agreement with the recent experimental high-pressure far- and mid-IR study performed by Pravica *et al.*,[27] and concur with the authors' conclusions that the decrease in vibrational frequencies are a result of decreasing intermolecular distances with pressure and hence an increase in intermolecular hydrogen bonding. This complex interplay of intra- and intermolecular interactions (that are ultimately responsible for shock-initiated chemical reactions) may explain the insensitivity of FOX-7, particularly in comparison to RDX and HMX (which do not have extensive intermolecular hydrogen bonding networks).

The $N\text{-}NO_2$ umbrella modes of β-HMX also display slight red-shifts in frequency with increasing pressure. However, rather than this being a consequence of increased intermolecular hydrogen bonding as is manifested for α-FOX-7, past studies would suggest that the vibrational energies of these $N\text{-}NO_2$ umbrella modes are generally unaffected by pressure (in the pressure range studied here).[30,39] Instead, the slightly negative γ parameters may well arise due to serendipitous ring conformation changes.

6.4.3.3 Prediction of Heat Capacities

Similar to the predictions for the polymorphs of RDX in the previous chapter, the effect of high pressures on the heat capacities (at constant volume, C_V) of β-HMX and α-FOX-7 have been predicted by utilising the results of the phonon calculations and implementing Equation 2.59. The phonon calculations were only performed at the gamma point in k-space, however as an estimate of the actual effect of phonon dispersion on the calculated heat capacities, phonon calculations at multiple points in k-space have been performed on a smaller test system (either one molecule of β-HMX or α-FOX-7 in a box), the results of which can be found in the

Supplementary information. The standard deviations (as a percentage of the mean value) of the predicted heat capacities for the 8 k-points of each test system has been used to estimate the magnitude of the errors in the calculated heat capacities at the gamma point in k-space of the full computational systems, these errors are shown as the error bars in Figure 6.13 and Figure 6.14.

Figure 6.13 displays the calculated variation in heat capacities at 315 K in the 0–8.54 GPa pressure range for β-HMX. The calculated heat capacity for β-HMX at ambient pressure at this temperature is 280.06 J K^{-1} mol^{-1} , only a 11.6% difference to the experimental value of 316.72 J K^{-1} mol^{-1} determined by Shoemaker *et al*.[57]

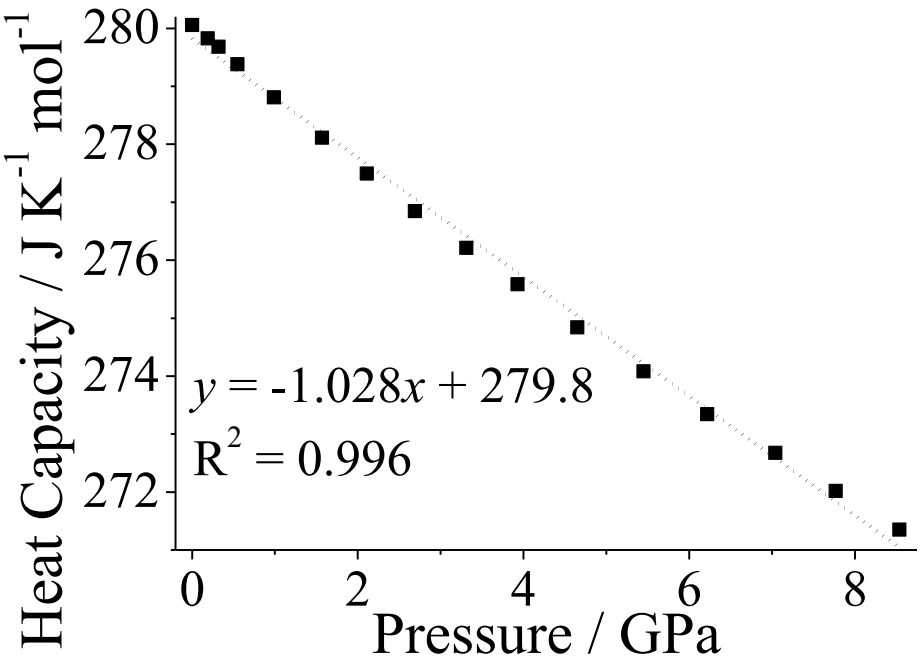

Figure 6.13 Calculated effect of pressure on the heat capacities at *T*= 315 K of β-HMX. The error bars provide an estimate (as determined from the standard deviation of phonon dispersion calculations on a smaller test system) of the effect of phonon dispersion on the calculated (gamma point only) heat capacities – in this case, the error bars are actually smaller than the symbols displaying the points.

To date, there has been no experimental determination of C_V (at ambient or high-pressure) for α-FOX-7, nevertheless the heat capacities as a function of pressure have been determined for α-FOX-7, as shown in Figure 6.14.

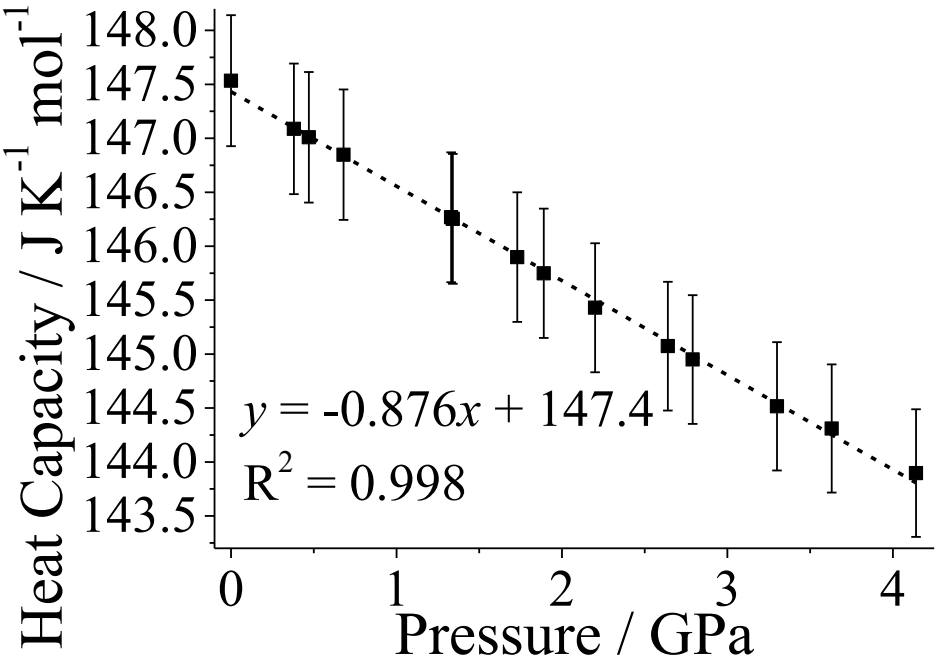

Figure 6.14 Calculated effect of pressure on the heat capacities at T= 300 K of α-FOX-7. The error bars provide an estimate (as determined from the standard deviation of phonon dispersion calculations on a smaller test system) of the effect of phonon dispersion on the calculated (gamma point only) heat capacities.

These results validate the conclusions from the previous chapter, that the pressure dependence of the heat capacities of these types of crystalline nitramines is very small (only approximately -1 J K^{-1} mol^{-1} GPa^{-1} for RDX, HMX and FOX-7, in comparison to temperature dependences of approximately 0.6 and 0.8 J K^{-2} mol^{-1} for α-RDX[64,58] and β-HMX,[64] respectively).

6.5 Conclusions

This work presents data for the hydrostatic compression of both deuterated β-HMX and α-FOX-7 performed using neutron powder diffraction on the PEARL/HiPr and POLARIS instruments at the ISIS Neutron and Muon facility. Compression of deuterated β-HMX provides complementary data to previous X-ray diffraction experiments. The resulting 3rd order B-M[56] EoS produced (V_0 = 516.65(1.31) $Å^3$, B_0 = 11.82(0.81) GPa, and B' = 12.10(0.82), in the 0 – 8.54 GPa range) is in excellent agreement with the previous hydrostatic study, indicating that deuteration of β-HMX does not affect its compression behaviour. In addition, this work presents the first truly hydrostatic compression data for α-FOX-7, generating a

3rd order B-M[56] EoS in the 0 – 4.14 GPa range with parameters: V_0 = 521.07(0.04) Å^3, B_0 = 11.81(0.47) GPa, and B' = 11.41 (0.95).

This work reports the first experimental determinations of the INS spectra of both β-HMX and α-FOX-7. Both spectra are consistent with previous Raman and IR studies and (particularly for α-FOX-7) expand on the known ambient pressure vibrational information, providing a more complete assignment of the vibrational properties.

DFT-D calculations have been utilised to describe accurately the structure and properties of both β-HMX and α-FOX-7. For both systems studied, at ambient pressure, the DFT-D models predicted all of the lattice parameters to lie within 1.5% and overall unit-cell volumes to lie within 0.6% of experimental values,[6,20] commensurate with previous DFT-D studies.[35,39] Subsequent phonon calculations generated vibrational frequencies in good agreement with experimental vibrational spectra. From the results of the phonon calculations, INS spectra were plotted and compared with the experimentally determined spectra. Eigenvalues and eigenvectors were well replicated by the models.

The DFT-D hydrostatic compression studies for both β-HMX and α-FOX-7 reproduced the experimental compression trends, producing 3rd order B-M EoS in excellent agreement with experiment. Furthermore, the vibrational properties as a function of pressure were calculated, and were found to be in very good agreement with available experimental data. The results of the phonon calculations were then used to predict the effect of pressure on the heat capacities of β-HMX and α-FOX-7. These predictions suggest a very weak pressure dependence of heat capacities (approximately -1 J K^{-1} mol^{-1} GPa^{-1}) for the nitramine crystals studied here.

All of these favourable comparisons with experiment for both β-HMX and α-FOX-7, at ambient and applied high pressures provide further validation of the conclusions reached during the study of crystalline RDX (in Chapter 5) that the Grimme DFT-D model performs extremely well over a range of conditions, and is able to describe accurately intramolecular and intermolecular interactions and thus the structure and properties of the organic molecular nitramine crystals.

6.6 References

1 Cady, H. H.; Smith L. C. in *Studies on the Polymorphs of HMX*, LAMS-2652 TID-4500, **1961**.
2 Goetz, F.; Brill, T. B.; Ferraro, J. R. *J. Phys. Chem.* **1978**, *82*, 1912.
3 Eiland, P. F.; Pepinsky, R. *Z. Krystallogr.,* **1955**, *106*, 273.
4 Cady, H. H.; Larson, A. C.; Kromer, D. T. *Acta Cryst.*, **1963**, *16*, 617.
5 Kohno, Y.; Maekawa, K.; Azuma, N.; Tsuchioka, T.; Hashizume, T.; Imamura, A. *Kogyo Kayaku*, **1992**, *53*, 227.
6 Choi, C. S.; Boutin, H. P. *Acta Cryst. B*, **1970**, *26*, 1235.
7 Cobbledick, R. E.; Small, R. W. H. *Acta Cryst. B*, **1974**, *30*, 1918.
8 Main, P.; Cobbledick, R. E.; Small, R. W. H. *Acta Cryst. C*, **1985**, *41*, 1351.
9 Yoo, C. S.; Cynn, H. *J. Phys. Chem.,* **1999**, *111*, 10229.
10 Gump, J. C.; Peiris, S. M., *J. App. Phys*. **2005**, *98*, 053513.
11 Olinger, B.; Roof, B.; Cady, H. *Actes du Symposium International sur le Comportement des Millieux Denses sous Hautes Pressions Dynamiques*, Paris **1978**.
12 Goetz, F.; Brill, T. B. *J. Phys. Chem*. **1979**, *83*, 340.
13 Iqbal, Z.; Bulusu, S.; Autera, J. R. *J. Chem. Phys.* **1974**, *60*, 221.
14 Brand, H. V.; Rabie, R. L.; Funk, D. J.; Diaz-Acosta, I.; Pulay, P, Lippert, T. K. *J. Phys. Chem. B* **2002**, *106*, 10594.
15 Stevens, L. L.; Haycraft, J. J.; Eckhardt, C. *J. Cryst. Growth Des.* **2005**, *5*, 2060.
16 Klapötke, T. A. in *Chemistry of High-Energy Materials*, Walter de Gruyter, Berlin and New York, **2011**.
17 Cooper, P. W. in *Explosives Engineering*, Wiley-VCH, New York, **1996**.
18 Kjellstrom, A.; Latypov, N.; Eldsater, C.; Eriksson, L. in *FOI Swedish Defense Research Agency Technical Report No. SE-147 25*, Tumba, **2005**.
19 Evers, J.; Klapötke, T. M.; Mayer, P.; Oehlinger, G.; Welch, J. *Inorg. Chem.* **2006**, *45*, 4996.
20 Bemm, U.; Ostmark, H. *Acta Cryst. C* **1998**, *54*, 1997.
21 Crawford, M. J.; Evers, J.; Göbel, M.; Klapötke, T. M.; Mayer, P.; Oehlinger, G.; Welch, J. M. *Propell. Explos. Pyrotech.* **2007**, *32*, 478.
22 Kempa, P. B.; Herrmann, M. *Z. Kristallogr. Proc.* **2011**, *1*, 481.
23 Peiris, S. M.; Pangilinan, G. I.; Zerilli, F. J.; Russell, T. P.; *Shock Conp. Cond. Matter* **2002**, *CP620*, 181.
24 Peiris, S. M.; Wong, C. P.; Zerilli, F. J. *J. Chem. Phys.* **2004**, *120*, 8060.
25 Pravica, M.; Galley, M.; Park, C.; Ruiz, H.; Wojno, J. *High Press. Res.* **2011**, *31*, 80.
26 Latypov, N. V.; Bergman, J.; Langlet, A.; Bemm, U. W. *Tetrahedron* **1998**, *54*, 11525.
27 Pravica, M.; Liu, Y.; Robinson, J.;Velisavljevic, N.; Liu, Z.; Galley, M. *J. Appl. Phys.* **2012**, *111*, 103534.
28 Chen, J.; Long, Y.; Liu, Y. G.; Nie, F. D.; Sun, J. S. *Sci. China Phys. Mech. Astron.* **2011**, *54*, 831.
29 Cui, H. -L.; Ji, G. -F.; Chen, X. -R.; Zhu, W. -H.; Zhao, F.; Wen, Y.; Wei, D. -Q. *J. Phys. Chem. A* **2010**, *114*, 1082.

30 Lu, L. -Y.; Wei, D. -Q.; Chen, X. -R.; Lian, D.; Ji, G. -F.; Zhang, Q. -M.; Gong, Z. -Z. *Mol. Phys.* **2008**, *106*, 2569.
31 Lian, D.; Lu, L. -Y.; Wei, D. -Q.; Zhang, Q. -M.; Gong, Z. -Z.; Guo, Y. -X. *Chinese Phys. Lett.* **2008**, *25*, 899.
32 Byrd, E. F. C.; Rice, B. M. *J. Phys. Chem. C* **2007**, *111*, 2787.
33 Zhai, J.; Liu, H. *Comp. Mater. Sci.* **2008**, *42*, 698.
34 Hu, A.; Larade, B.; Abou-Rachid, H.; Lussier, L.-S.; Guo, H. *Propell. Explos. Pyrotech.* **2006**, *31*, 355.
35 Sorescu, D. C.; Rice, B. M. *J. Phys. Chem. C* **2010**, *114*, 6734.
36 Grimme, S. *J. Comput. Chem.* **2006**, *27*, 1787.
37 Balu, R.; Byrd, E. C. F.; Rice, B. M. *J. Phys. Chem. B* **2011**, *115*, 803.
38 Landerville, A. C.; Conroy, M. W.; Budzevich, M. M.; Lin, Y.; White, C. T.; Oleynik, I. I. *App. Phys. Lett.* **2010**, *97*, 251908.
39 Wu, Z.; Kalia, R. K.; Nakano, A.; Vashishta, P. *J. Chem. Phys.* **2011**, *134*, 204509.
40 Neumann, M. A.; Perrin, M. -A. *J. Phys. Chem. B* **2005**, *109*, 15531.
41 Bulusu, S.; Autera, J.; Axenrod, T. *J. Labelled Compd. Radiopharm.* **1980**, *17*, 707.
42 Marshall, W. G.; Francis, D. J. *J. App. Cryst.* **2002**, *35*, 122.
43 Besson, J. M.; Nelmes, R. J.; Hamel, G.; Loveday, J. S.; Weill, G.; Hull, S. *Physica B* **1992**, *180-181*, 907.
44 http://www.isis.stfc.ac.uk/.
45 Larson, A. C.; Von Dreele, R. B. in *General Structure Analysis System (GSAS)*; Los Alamos National Laboratory Report, LAUR 86-748, **2000**.
46 Decker, D. L. *J. App. Phys.* **1971**, *42*, 3239.
47 Colognesi, D.; Celli, M.; Cilloco, F.; Newport, R. J.; Parker, S. F.; Rossi-Albertini, V.; Sacchetti, F.; Tomkinson, J.; Zoppi, M. *Appl. Phys. A: Mater. Sci. Process.* **2002**, *S74* , S64.
48 Ramirez-Cuesta, A. J. *Comput. Phys. Commun.* **2004**, *157*, 226.
49 Clark, S. J.; Segall, M. D.; Pickard, C. J.; Hasnip, P. J.; Probert, M. J.; Refson, K.; Payne, M. C. Z. Krystallogr. **2005**, *220*, 567.
50 Perdew, J. P.; Burke, K.; Ernzerhof, M. *Phys. Rev. Lett.* **1996**, *77*, 3865.
51 Vackar, J.; Hytha, M.; Simunek, A. *Phys. Rev. B* **1998**, *58*, 12712.
52 Monkhorst, H. J.; Pack, J D. *Phys. Rev. B* **1976**, *13*, 5188.
53 Fischer, T. H.; Almlof, J. *J. Phys. Chem.* **1992**, *96*, 9768.
54 Frank, W.; Elsässer, C.; Fähnle, M. *Phys. Rev. Lett.* **1995**, *74*, 1791.
55 Angel, R. J.; Bujak, M.; Zhao, J.; Gatta, G. D.; Jacobsen, S. D. *J. Appl. Cryst*. **2007**, *40*, 26.
56 Birch, F.; *Phys. Rev.* **1947**, *71*, 809.
57 Shoemaker, R. L.; Stark, J. A.; Taylor, R. E. *High Temperatures High Pressures* **1985**, *17*, 429.
58 Miller, M. S. *J. Thermophys. Heat Tansfer*, **1994**, *8*, 803.

Chapter 7

Prediction of the Hydrostatic Compression Behaviour of CL-20

7 Prediction of the Hydrostatic Compression Behaviour of CL-20

7.1 Introduction

The polycyclic nitramine CL-20 (2,4,6,8,10,12-hexanitro-2,4,6,8,10,12-hexaazaisowurtzitane, Figure 7.1) is so named on account of its development at China Lake, USA. CL-20 was first synthesised in 1987[1] and is the most powerful explosive in current use, although some concerns remain over its sensitivity to detonation.[2] Its high performance and high density have been attributed to the 1:1 ratio of C atoms to nitramine groups and to its caged molecular structure.[3] CL-20 is known to exist in four crystalline phases at ambient pressure, denoted as the α, β, γ and ε forms.[1] At ambient temperature and pressure, ε-CL-20 is the most stable form (and is the form used in commercial propellants), with the stability order, ε > γ > α > β under ambient conditions.[4,5] Subsequently, the α-form has been shown to be a hydrate, rather than a true polymorph of CL-20.[1] Single crystal X-ray diffraction studies have been used to structurally characterise each of these forms. The α-form crystallises in the orthorhombic crystal system, with space group *Pbca*, both the β- and γ-forms crystallise in the monoclinic crystal system, with space groups of $Pb2_1a$ and $P2_1/n$, respectively, and ε-CL-20 crystallises in the monoclinic crystal system, with space group $P2_1/n$.[1,3]

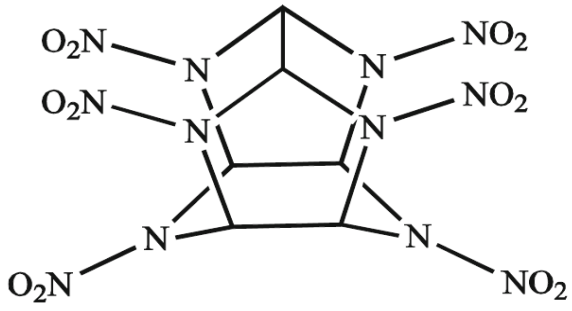

Figure 7.1 Molecular structure of CL-20.[6]

Russell *et al*. identified a high-pressure polymorph (denoted ζ-CL-20) using a combination of energy-dispersive X-ray diffraction, FT-IR spectroscopy and

polarised light microscopy by compression of γ-CL-20 to pressures exceeding 0.7 GPa, but attempts to determine its structure were unsuccessful.[7,8] Recently, Millar *et al.* successfully determined the structure of the high-pressure ζ-form using a combination of single crystal X-ray and powder diffraction techniques, and showed that it crystallises in the $P2_1/n$ space group. The high-pressure behaviour of the ε-form of CL-20 was first explored with angle-dispersive high-pressure synchrotron X-ray diffraction (0 – 5.57 GPa) utilising Dow Corning 200 Fluid (1 cSt) as the pressure-transmitting medium (PTM) and ruby fluorescence as the pressure calibrant, and no further transition from this form was observed.[9] A spectroscopic study[9] probed the behaviour of the ε-form up to 27 GPa, and suggested that a sluggish transition occurred between 4.5 and 6.4 GPa to what the authors suggest to be the γ-form. Subsequent compression led to a further phase transition at ~18.7 GPa, the authors suggest that this is the ζ-form.[10]

There have been several reports of the vibrational spectra of the various polymorphs of CL-20,[1,1011,12,13] but to date there been no thorough vibrational investigations (such as polarised Raman spectroscopy) detailing a complete list of fundamental and lattice modes including symmetry.

As described in the previous chapters, a complementary approach to experiment is atomistic simulation, which provides an effective way to model the properties and structure of crystalline materials. There have been multiple DFT studies on crystalline CL-20.[14,15] However, as described in the previous chapters, DFT is unable to accurately describe the intermolecular interactions of the molecular systems such as the nitramine crystals being studied here, without the implementation of some sort of dispersion correction.

To date, there have been several different approaches to implementing dispersion corrections to attempt to describe accurately the intermolecular interactions at ambient and high-pressures in molecular organic crystals such as those being investigated in this work. These different approaches include; dispersion-corrected atom-centered pseudopotentials (DCACP's),[16] non-empirical van der Waals density-functional (vdW-DF),[17] dispersion-corrected density functional theory (DFT-D, implementing corrections proposed by both Grimme,[18] and Neumann and

Perrin[19]),[17,20,21,22] and dispersion-corrected density functional theory in conjunction with the quasi-harmonic approximation (DFT-D+T).[21,22] Energetic materials of interest investigated throughout these works include, among others; RDX,[16,17,20,21] HMX,[16,20,21,22] FOX-7,[20,21] TATB,[16,20,21] PETN,[16,20,21] NM,[20,21] and CL-20.[20] The studies all concluded that the dispersion-corrected methods provide significant improvements for the description of intermolecular interactions in molecular crystals at both ambient and high pressures relative to conventional DFT.

It is apparent from this list of previous dispersion-corrected studies, that thus far, there has been only one study on CL-20. Sorescu and Rice performed theoretical DFT-D predictions (implementing the dispersion correction parameterised by Grimme[18]), at ambient and elevated pressures, of the crystallographic properties of ten energetic molecular crystals, including ε-CL-20.[20] For the hydrostatic compression of ε-CL-20, predictions were only made in the 0 – 2.7 GPa pressure range, due to available experimental comparisons.

7.2 Aims

Given the successful implementation of dispersion corrections to describe accurately the structure and properties of various RDX polymorphs (Chapter 5) and β-HMX and α-FOX-7 (Chapter 6), the ambiguity of previous experimental compression data, and the desire to investigate the factors affecting the DDT, the aims of this work were:

- to demonstrate that the DFT-D model can predict the hydrostatic compression behaviour of ε-CL-20, and in turn be used as a tool to guide experimental endeavours;
- to perform the first inelastic neutron scattering studies on ε-CL-20, to obtain complete ambient pressure vibrational information;
- to predict the effect of pressure on the heat capacities of ε-CL-20.

7.3 Experimental

7.3.1 Sample Preparation

Crystalline samples of ε-CL-20 used for INS, X-ray diffraction and Neutron diffraction studies were kindly provided by Dr. Bernard Garatay (QinetiQ, Fort Halstead).

7.3.2 X-ray Powder Diffraction

Samples of ε-CL-20 were finely ground and loaded into a Merrill-Bassett DAC (40° half-opening angle), [23] equipped with 400 μm culets and a tungsten gasket with a 200 μm hole. A 4:1 mixture of methanol/ethanol was used as a hydrostatic PTM. A 2-3 μm diameter ruby sphere was also loaded into the cell as the pressure calibrant, with the ruby fluorescence method being utilised to measure the pressure.[24] Compression data were then collected from the samples at beam-lines I11 and I15 at the Diamond Light Source, located at the STFC Rutherford Appleton Laboratory. An identical set up was used in both cases, which has been explained elsewhere.[25] In both cases a wavelength of approximately 0.4 Å was used, and the distance between the sample and detector was optimised to allow the maximum amount of crystallographic information to be collected. Data were integrated from the two-dimensional image plates MAR345 format, to powder diffraction chi plots with Fit2D.[26] Data were then exported from this format into GSAS[27] for Rietveld refinement.

7.3.3 Neutron Powder Diffraction

A lightly ground sample (*ca.* 100 mg) of ε-CL-20 was loaded into an encapsulated TiZr gasket,[28] together with a small quantity of 4:1 perdeuterated methanol/ethanol as PTM and a sample of lead as the pressure calibrant. The resulting capsule assembly was then compressed within a type V3b Paris-Edinburgh press[29] equipped with standard single toroid anvils with cemented WC cores (Ni binder). The Paris-Edinburgh press ram pressure was monitored and varied by means of a computer controlled hydraulic system. High-pressure neutron powder diffraction data for ε-CL-20 were collected using the PEARL/HiPr diffractometer at

the UK spallation neutron source, ISIS Neutron and Muon facility, located at the STFC Rutherford Appleton Laboratory.[30] Time-of-flight neutron powder diffraction data suitable for structure refinement were obtained by electronically focusing the individual detector element spectra from the PEARL/HiPr 2θ=90° detector banks. The resulting summed pattern was then normalised with respect to the incident beam monitor and the scattering from a standard vanadium calibration sample. Lastly, the diffraction pattern intensity scale was corrected for the wavelength and scattering-angle dependence of the neutron attenuation by the anvil (WC) and gasket (TiZr) materials. Full-profile Rietveld refinements of the TOF neutron powder diffraction patterns were carried out using the GSAS package.[27] Sample pressures were calculated from the refined lead lattice parameters and the room-temperature EoS for lead as derived by Decker[31] with an uncertainty of ± 0.05 GPa. Data collection times per pressure point ranged between 1 and 6 hours at an equivalent of 165 μA ISIS proton current.

7.3.4 Inelastic Neutron Scattering

INS spectra (24-4000 cm^{-1}) were recorded using the TOSCA[32] instrument at the ISIS Neutron and Muon facility, which has an energy resolution of ~1.25%. Approximately 2.5 g of polycrystalline ε-CL-20 was loaded into an aluminium sample can and cooled to T < 20 K in a conventional closed cycle refrigerator, and spectra were recorded for 3–6 h (at an equivalent of 165 μA ISIS proton current). INS data were visualised and compared to the simulated spectra of the DFT-D calculations using the aCLIMAX program.[33]

7.3.5 Computational Methods

Structure optimisations (at ambient pressure and under hydrostatic externally applied pressure conditions) and vibrational frequency calculations were performed using density functional theory plus dispersion (DFT-D) and the plane-wave pseudopotential method as implemented in CASTEP version 5.5,[34] utilising the dispersion correction scheme of Grimme.[35] Treatment of electronic exchange and correlation was handled by the generalised gradient approximation (GGA) formalised by Perdew, Burke and Ernzerhof (PBE).[36] On-the-fly (OTF) [37]

pseudopotentials generated using the CASTEP code were used; the plane-wave cut-off energy used throughout was 650 eV, which ensured convergence of both lattice parameters and total energies (to less than 5 meV per unit cell). Brouillon zone sampling was obtained using M-P[38] grids of 2 × 2 × 2 (2 k-points). The structures were relaxed [using the BFGS[39] method] to allow both atomic coordinates and unit cell vectors to optimise simultaneously while constraining space group geometry (convergence criteria: maximum change in system energy = 2 x 10^{-5} eV, maximum RMS force = 0.025 eV $Å^{-1}$, maximum RMS stress = 0.01 GPa and maximum RMS displacement = 0.002 Å). Following successful geometry optimisation of the experimental starting structure [this work] (a = 8.8668 Å, b = 12.6021 Å, c = 13.3914 Å, β = 106.8907 degrees, hence V = 1431.81 $Å^3$) external hydrostatic pressures were applied at pressures corresponding to experimental data. Phonon frequencies (at the gamma point in k-space) for the optimised structures were then calculated by finite displacement methods.[40]

7.4 Results and Discussion

7.4.1 Ambient-Pressure Computational Behaviour

7.4.1.1 Structure of ε-CL-20

ε-CL-20 crystallises in the orthorhombic crystal system with space group $P2_1/n$: the unit cell contains 4 CL-20 molecules, giving a total of 144 atoms. The results of the geometry optimisation are compared to previous experiment and dispersion-corrected study as shown in TABLE 7.1. All lattice parameters agree with experiment to within 0.6%, and the overall unit cell volume differs from experiment by 1.7%. These results are broadly consistent with previous DFT-D studies, however differ slightly in the calculation of the *b*-axis. The previous DFT-D study underestimates the *b*-axis with respect to the experimentally determined value by 0.6%, whilst slighting overestimating the *a*- and *c*- axes. Similarly the DFT-D optimisation in this work also slightly overestimates the *a*- and *c*- axes, but in contrast overestimates (rather than underestimates in the case of the previous DFT-D study) the *b*-axis by 0.6%. Due to the slight overestimation of two lattice parameters, and underestimation of the third, the previous DFT-D study obtains a

fortuitous cancellation (albeit of slight) errors resulting in a favourable agreement of experimental unit cell volume. Nevertheless both DFT-D methods accurately reproduce all experimental lattice parameters and confirm that the Grimme dispersion correction can accurately describe the intermolecular interactions in the ε-CL-20 crystal.

Parameter	Exp. Ref. 3	DFT-D (This work)	DFT-D Ref. 20
a (Å)	8.863[1]	8.9189 (0.6)	8.9157 (0.6)
b (Å)	12.593[2]	12.6706 (0.6)	12.5171 (-0.6)
c (Å)	13.395[2]	13.4251 (0.2)	13.4132 (0.1)
β (deg.)	106.920[2]	106.559 (-0.3)	106.58 (-0.3)
V ($Å^3$)	1430.2[3]	1454.23 (1.7)	1434.68 (0.3)

TABLE 7.1 Comparison of the crystallographic parameters for ε-CL-20 calculated at ambient pressure using the DFT-D method alongside results obtained from previous experimental and DFT-D studies. The numbers in square brackets are the estimated standard deviations of experimental values, the values in parentheses are the percentage error deviations from experimental values.

7.4.1.2 Vibrational Properties

Following the geometry optimisations, a comprehensive finite displacement phonon calculation (including symmetry) was performed to obtain the vibrational properties of ε-CL-20. The phonon calculation was performed at only the gamma point in k-space as the material is an insulator and thus the dispersion of phonon energies throughout k-space is assumed to be negligible. TABLE 7.2 shows a comparison of the calculated fundamental modes for ε-CL-20 with the experimental INS spectra determined in this study (measured on the TOSCA[32] instrument at ISIS Neutron and Muon Facility), and demonstrates that the majority of the calculated fundamental vibrational modes are in good agreement (<2.5% difference) with experiment. Furthermore, a comparison of experimental INS combination and overtone bands with their identifiable computationally calculated counterparts can be found in the Appendix, Table A7.1.

In Figure 7.2 the calculated INS spectra of ε-CL-20 calculated using DFT-D, is compared to the experimentally determined INS spectrum (additional annotated comparisons of the experimental and computational INS spectra can be found on the Supplementary Information CD). From these comparisons it is clear that the

computed and experimental spectra show excellent agreement, both for neutron energy loss and for the intensities of the phonon modes.

*Mode**	*Comp.* **ν**	*INS (this work)* **ν**	*Mode**	*Comp.* **ν**	*INS (this work)* **ν**
4,5	33.8	28	97-100	257.3	266
6,7,8,9	36.7	33	101-104	293.4	306
10	41.2	40	105-108	302.0	314
11	44.2	43	109-112	307.9	318
12	45.3	46	113,114	336.7	339
13	47.3	50	115,116	338.7	349
14	50.9	53	117-124	360.9	376
15,16	55.5	57	125-128	374.8	386
17	58.1	61	129-132	397.3	412
18	63.4	65	133-136	440.1	450
19,20	66.2	69	137-140	458.5	469
21,22	69.5	72	141-144	516.7	528
23,24	77.6	78	145-148	553.3	572
25-28	79.8	84	149-152	567.8	584
29-33	84.8	88	153-156	575.3	595
34-36	90.3	93	157-160	593.5	607
37,38	99.1	103	161-164	613.1	629
39,40	103.4	105	165-172	633.2	648
40-42	104.8	109	173-176	647.0	665
43,44	109.4	111	177-180	687.2	681
45,46	112.7	116	181-188	706.0	709
47,48	115.7	119	189-200	717.1	727
49-52	119.4	126	201-212	724.4	753
53	123.0	136	213-216	765.9	796
54-56	128.2	139	217-220	776.6	808
57-59	132.8	145	221-232	804.1	836
60-62	135.5	149	233-236	830.4	862
63-64	139.2	152	237-240	867.7	888
65-66	140.7	156	257-260	931.2	924
67-70	151.1	164	241-256	905.1	947
71,72	156.4	169	261-268	952.5	991
73-75	159.4	173	269,270	1001.6	1021
76	162.5	177	271,272	1011.1	1031
77	172.8	183	273-280	1035.1	1057
78	173.8	188	281-284	1075.9	1095
79	193.3	194	285-296	1114.8	1145
80	197.3	199	297-312	1175.3	1222
81-84	206.5	214	313-332	1238.3	1259
85,86	211.2	226	333-360	1284.4	1310
87-88	216.8	233	361-372	1341.2	1351
89-92	244.0	253	373-384	1369.0	1391
93-96	248.2	262	409-432	3092.2	3060

TABLE 7.2 Comparison of the computationally calculated fundamental modes for ε-CL-20 compared to the INS spectrum reported in this work. * Where there are multiple modes, the DFT-D value stated is an average of the contributing modes. All frequencies, **ν**, are in units of cm^{-1}.

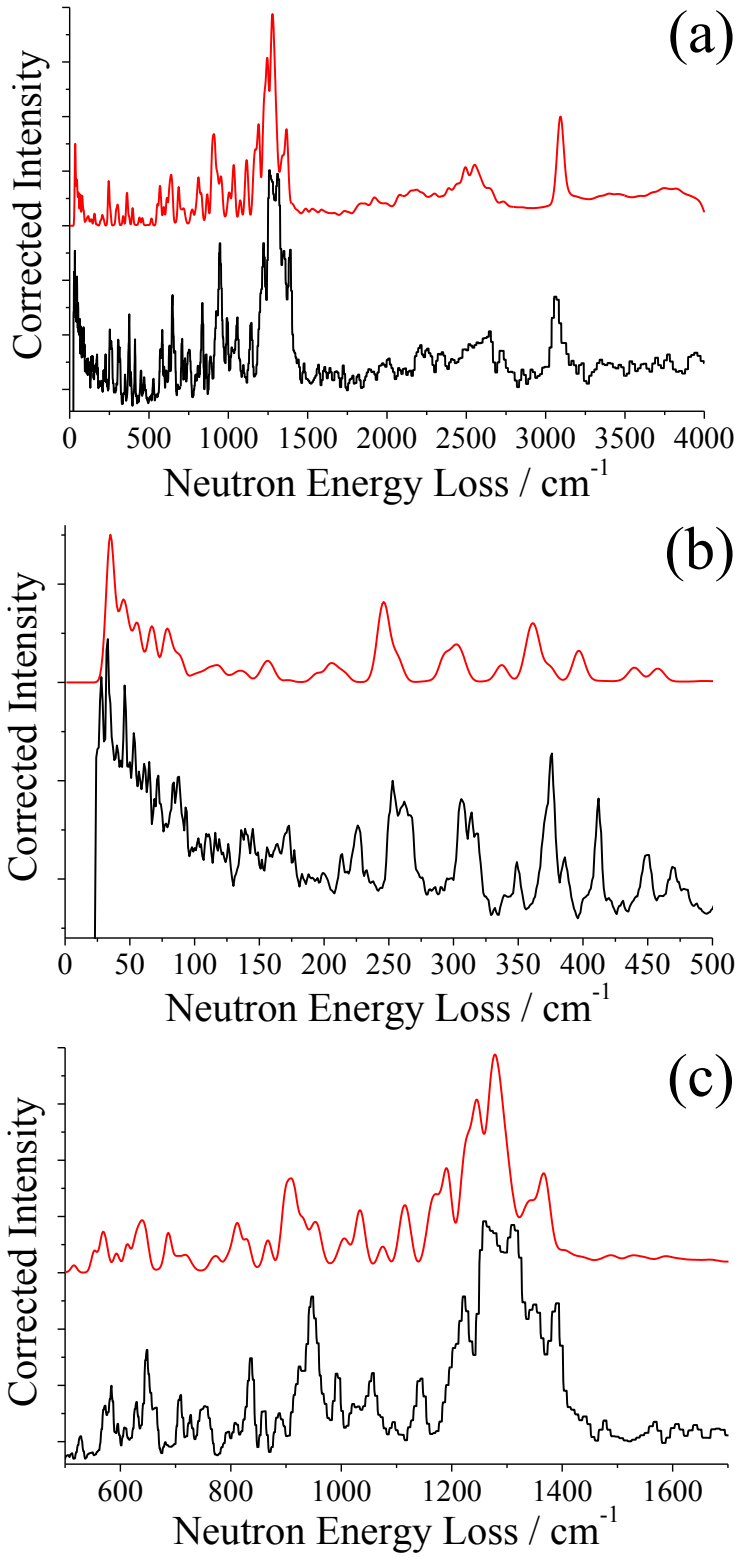

Figure 7.2 Experimental (**black**) and computationally calculated (**red**) INS spectra of ε-CL-20 at ambient pressure. (a) 0 – 4000 cm^{-1}, (b) 0 – 500 cm^{-1}, (c) 500 – 1700 cm^{-1}.

The excellent agreement between experiment and theory for the crystallographic lattice parameters and for the vibrational frequencies and intensities for ε-CL-20, confirm the conclusions ascertained during the studies of similar molecular energetic crystals in the previous chapters, that the computational model accurately describes both the intra- and intermolecular interactions in nitramine crystals.

7.4.2 High-Pressure Behaviour

7.4.2.1 Computational Compression

The effect of pressure on the lattice parameters of ε-CL-20 is shown in Figure 7.3, with the overall unit-cell volumes shown in Figure 7.4. The results are in very close agreement with the previous computational DFT-D study[20] for the *a*-axis, *c*-axis and *β*-angle, and differs in the calculation of the b-axis by ~1% as discussed in the previous section. Nevertheless the compression trends predicted by both studies are in excellent agreement.

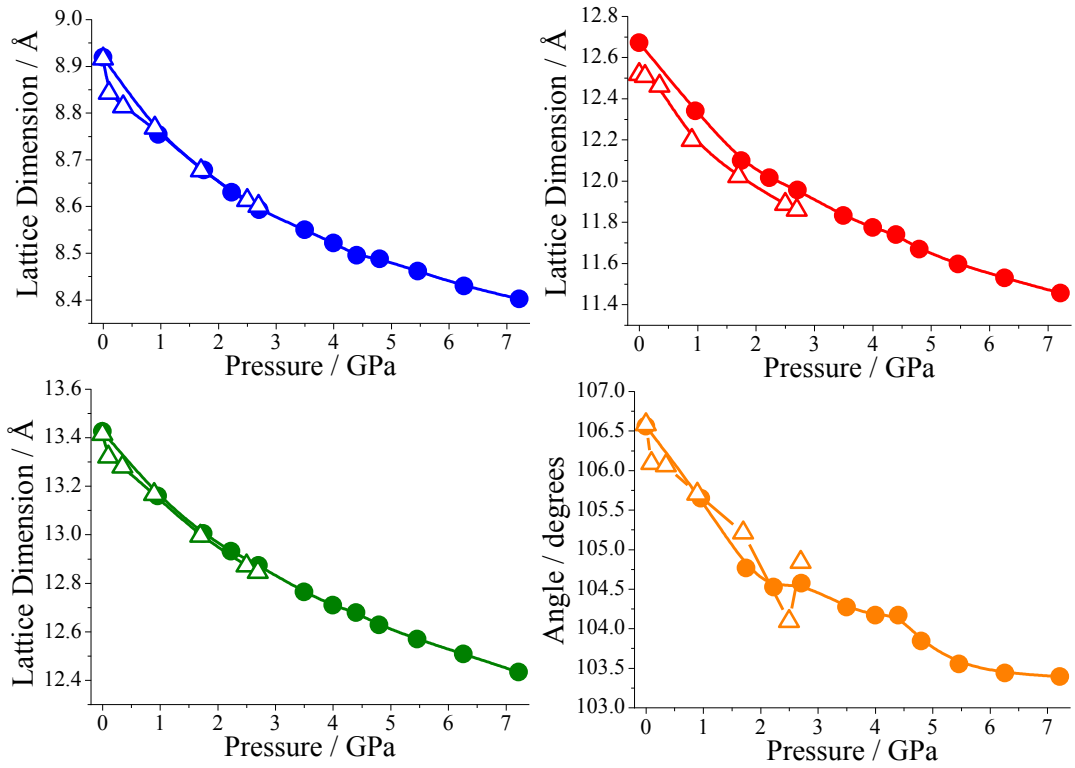

Figure 7.3 Lattice parameters as a function of hydrostatic pressure. Star: experiment,[9] circle: DFT-D (this work), triangle: DFT-D Ref. 20. **Blue**: *a*-axis, **red**: *b*-axis, **green**: *c*-axis, **orange**: β-angle.

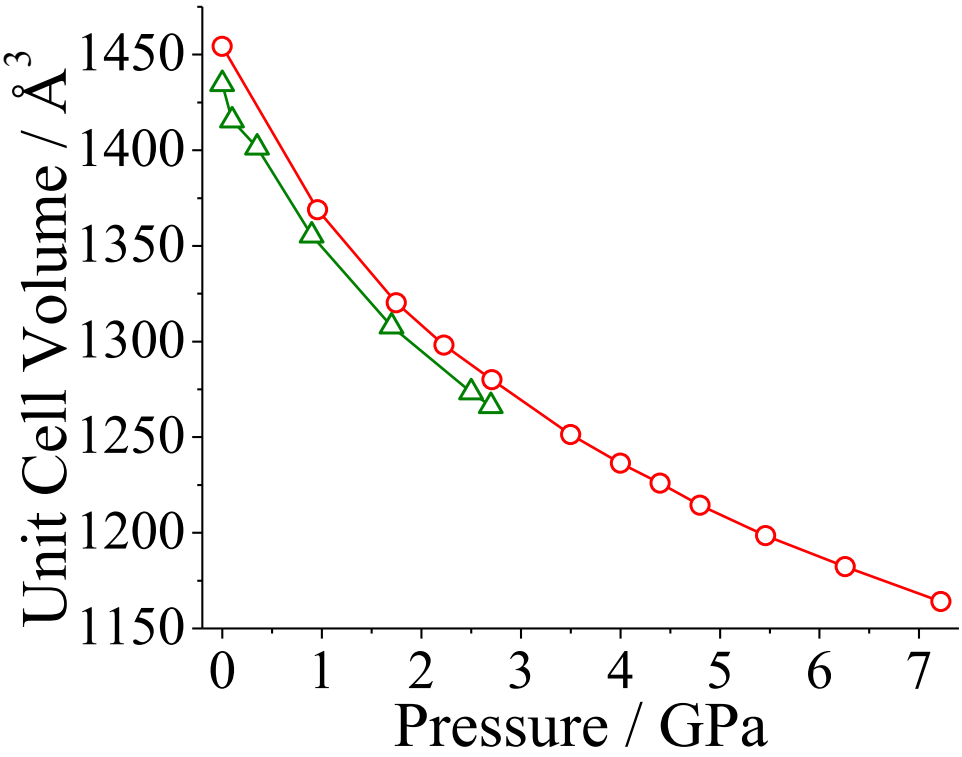

Figure 7.4 Unit cell volume as a function of hydrostatic pressure. Circle: DFT-D (this work), triangle: previous DFT-D Ref. 20.

Due to the accurate predictions of hydrostatic compression behaviour for all other nitramine crystals examined using the DFT-D method, (α-, γ- and ε-forms of RDX in Chapter 5, and β-HMX and α-FOX-7 in Chapter 6) there is confidence that the method will accurately predict the hydrostatic compression behaviour of the similar nitramine crystal, ε-CL-20.

7.4.2.2 High-Pressure X-ray Powder Diffraction

Note: The X-ray diffraction data were refined by Dr. Helen E. Maynard-Casely.

A previous experimental compression study has been performed which used Dow Corning Fluid 200 (1cSt) [silicone oil] as PTM. Angel *et al.*[41] reported that other similar silicone oils with kinematic viscosities in the rage of 0.65 – 37 cSt are only truly hydrostatic to pressures of ~0.9 GPa. Thus the experiment may not have been performed in truly hydrostatic conditions throughout the whole pressure range of the study.

For this reason, to endeavour to provide a hydrostatic compression study of ε-CL-20, myself and co-workers within the research group performed a further high-

pressure powder X-ray diffraction study utilising 4:1 methanol/ethanol as the PTM which remains truly hydrostatic up to *ca.* 9.8 GPa.[41]

Data were obtained for ε-CL-20 up to 9.8 GPa at Beamline I15, Diamond Light Source. At each pressure point the powder patterns were Rietveld refined with scale, lattice parameters, peak profiles and instrument parameters fitted to the data. The results of the refinements are displayed in TABLE 7.3, furthermore, plots of the experimental lattice parameters can be found in Figure 7.5 and Figure 7.6 displays the unit-cell volumes compared to the computationally calculated unit-cell volumes. Up to pressures of 7.2 GPa the data obtained was of such high quality that atomic coordinates of the ε-CL-20 molecule were also able to be refined (provided it was treated as a rigid molecule). All refinements throughout the whole pressure range studied were indexed to the ε-form of CL-20 and no transition was observed to the γ-form between 4.5 and 6.4 GPa as previously proposed.[10]

Pressure (GPa)	***a*** (Å)	***b*** (Å)	***c*** (Å)	*β* (deg.)	*V* ($Å^3$)
0.0(0)	8.8668(4)	12.6021(5)	13.3914(6)	106.8907(24)	1431.81(13)
0.96(2)	8.7016(10)	12.2946(14)	13.1268(16)	106.332(7)	1347.7(4)
1.75(2)	8.6597(12)	12.2013(16)	13.0443(15)	106.097(11)	1324.22(22)
2.23 (2)	8.642(1)	12.155(2)	13.008(2)	105.96(1)	1313.7(5)
2.71(2)	8.6090(17)	12.0775(21)	12.9382(26)	105.751(11)	1294.7(6)
3.50(2)	8.5658(21)	11.9713(27)	12.8456(32)	105.401(14)	1269.9(7)
4.00(2)	8.5405(20)	11.9197(31)	12.7949(24)	105.242(20)	1256.72(35)
4.40(2)	8.5289(35)	11.873(5)	12.764(5)	105.005(25)	1248.5(11)
4.80(2)	8.515(4)	11.825(5)	12.735(5)	104.824(26)	1239.5(11)
5.46(2)	8.504(4)	11.789(6)	12.711(6)	104.626(31)	1233.0(14)
6.26(2)	8.491(5)	11.744(7)	12.690(7)	104.469(32)	1225.5(15)
7.2(1)	8.477(6)	11.700(7)	12.658(7)	104.39(3)	1216.1(17)
8.5(1)	8.420(6)	11.631(9)	12.56(1)	104.97(5)	1188(2)
9.8(1)	8.381(6)	11.517(9)	12.47(1)	104.67(5)	1164(2)

TABLE 7.3 Variation in the unit cell parameters of ε-CL-20 with pressure, determined by X-ray powder diffraction. The values in parentheses are estimated standard deviations.

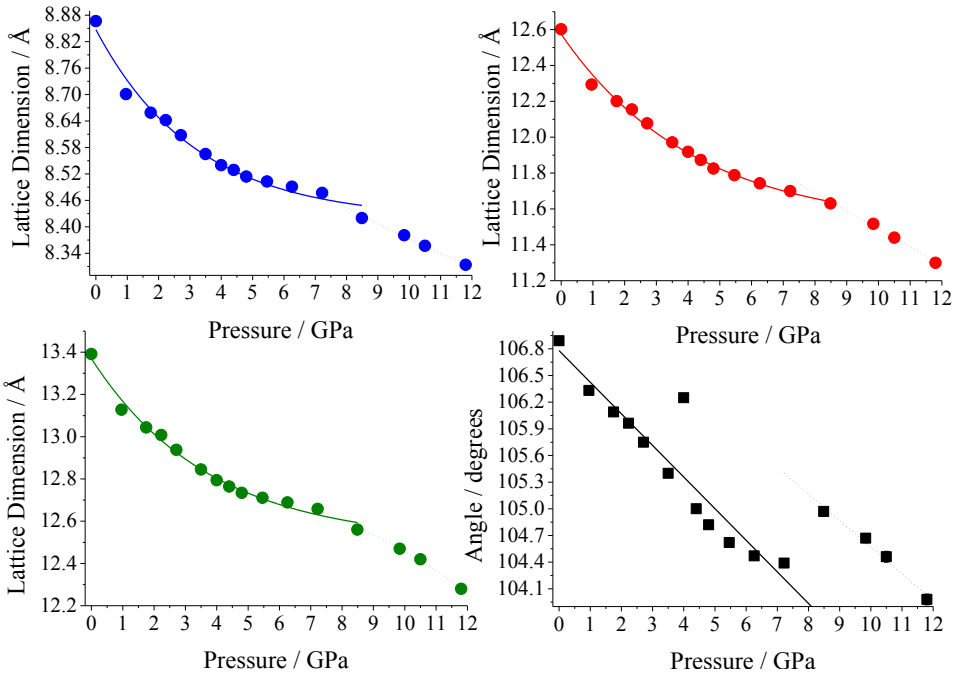

Figure 7.5 Lattice parameters of ε-CL-20 as a function of hydrostatic pressure for the experimental data reported in TABLE 7.3. **Blue**: *a*-axis, **red**: *b*-axis, **green**: *c*-axis **black**: beta-angle.

However, as depicted in Figure 7.6, significant deviations from the expected compression trend are observed for the X-ray powder diffraction results. The discrepancy cannot be attributed to non-hydrostatic conditions, as 4:1 methanol/ethanol remains truly hydrostatic up to *ca.* 9.8 GPa.[41] Furthermore, all powder patterns could be refined to the ε-form of CL-20 suggesting that any possible phase transition is very subtle. Nevertheless, based on the two curves used to fit the volumes, there does appear to be evidence for a phase transition at ~ 6.5-7.0 GPa that may be 2nd order.

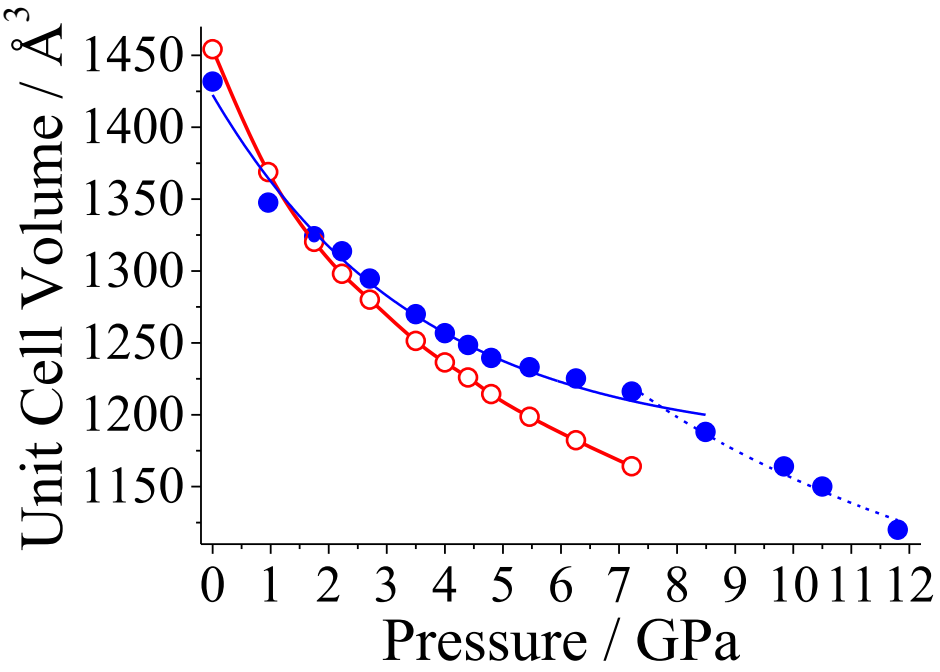

Figure 7.6 Unit-cell volume as a function of hydrostatic pressure for ε-CL-20 fitted with lines to guide the eye. **Blue**: experiment (unpublished X-ray data reported in this work), **red**: DFT-D (this work).

The apparent discrepancy between theory and experiment prompted a complementary neutron powder diffraction study.

7.4.2.3 High-Pressure Neutron Powder Diffraction

Note: all neutron and X-ray diffraction studies were collected by Dr. David I. A. Millar, and Prof. Colin Pulham (both The School of Chemistry, University of Edinburgh) and Dr. William G. Marshall (ISIS Neutron and Muon Facility) and refined by Mr. Paul Coster (The School of Chemistry, University of Edinburgh).

The neutron powder diffraction study of ε-CL-20 was performed utilising perdeuterated 4:1 methanol/ethanol as the PTM. It was not possible to deuterate the CL-20 sample, but on account of the small percentage of H in the sample the level of incoherent scattering was low.

Data were obtained for ε-CL-20 up to 7.12 GPa on the PEARL/HiPr instrument, ISIS Neutron and Muon facility, located at the STFC Rutherford Appleton Laboratory. At each pressure point the obtained powder patterns were Rietveld refined treating the CL-20 molecule as a rigid body, the results of the refinements displayed in TABLE 7.4. All refinements throughout the whole pressure

range studied could be fitted to the ε-form of CL-20 and no transition was observed to the γ-form between 4.5 and 6.4 GPa as previously proposed.[10]

Pressure (GPa)	***a*** *(Å)*	***b*** *(Å)*	***c*** *(Å)*	*β (deg.)*	*V (Å^3)*	*wR$_p$*	*χ^2*
0.00(2)	8.8629(9)	12.5959(15)	13.3794(14)	106.919(8)	1428.99(17)	2.50	0.961
0.20(2)	8.8135(9)	12.5109(15)	13.3117(14)	106.743(8)	1405.58(17)	2.89	0.954
0.40(2)	8.7737(8)	12.4429(13)	13.2519(13)	106.603(7)	1386.41(16)	2.58	0.862
0.69(2)	8.7290(8)	12.3548(13)	13.1804(13)	106.403(8)	1363.58(17)	2.68	0.888
0.99(2)	8.6897(8)	12.2765(12)	13.1118(13)	106.227(7)	1343.03(16)	2.70	0.841
1.29(2)	8.6565(8)	12.2036(13)	13.0493(13)	106.080(8)	1324.60(16)	2.67	0.805
1.60(2)	8.6241(8)	12.1368(13)	12.9940(13)	105.908(8)	1307.98(16)	2.65	0.870
2.00(2)	8.5914(6)	12.0630(10)	12.9305(10)	105.721(6)	1289.95(12)	2.19	1.061
2.38(2)	8.5611(7)	11.9946(12)	12.8694(12)	105.543(7)	1273.19(15)	2.72	0.872
2.81(2)	8.5324(8)	11.9253(12)	12.8097(13)	105.370(8)	1256.79(15)	2.84	0.847
3.32(3)	8.5006(8)	11.8533(12)	12.7377(13)	105.145(8)	1238.89(15)	2.60	0.865
4.38(3)	8.4483(8)	11.7222(12)	12.6200(12)	104.776(8)	1208.46(14)	2.77	1.191
5.14(3)	8.4151(8)	11.6396(13)	12.5463(11)	104.574(8)	1189.35(13)	2.95	1.099
5.68(3)	8.3934(10)	11.5900(16)	12.5001(13)	104.470(11)	1177.42(16)	3.29	1.007
6.19(3)	8.3733(8)	11.5466(13)	12.4566(10)	104.319(9)	1166.94(13)	3.20	1.342
6.65(3)	8.3591(9)	11.5074(16)	12.4220(13)	104.233(11)	1158.22(17)	3.68	0.999
7.12(4)	8.3421(10)	11.4671(17)	12.3905(14)	104.162(11)	1149.25(18)	3.70	0.990

TABLE 7.4 Variation in the unit cell parameters of ε-CL-20 with pressure, determined by neutron powder diffraction. The values in parentheses are estimated standard deviations.

Figure 7.7 shows that the compression trend determined from the neutron powder diffraction experiment is in excellent agreement to the hydrostatic compression trend predicted by the DFT-D method. Given that the X-ray diffraction experiment conducted by Peiris also fits the computational study, an explanation is required as to why the X-ray data collected on beamline I15 deviate so much from both the neutron experiment and the computational study. Inspection of Figure 7.7 indicates that the experimental unit-cell volumes obtained at the first two pressure points examined in the I15 X-ray study agree well with the hydrostatic compression trend from the neutron study. However, subsequent data points at higher pressures in the X-ray study deviate substantially from the true hydrostatic compression behaviour.

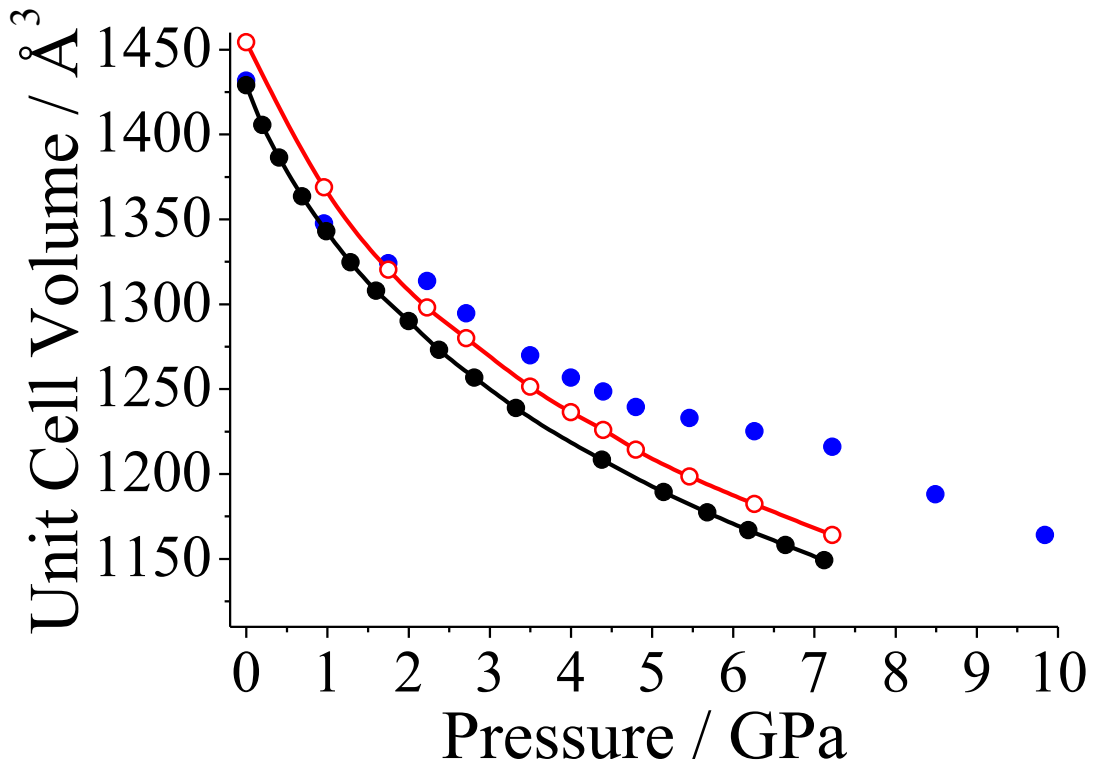

Figure 7.7 Unit-cell volume as a function of hydrostatic pressure for ε-CL-20 fitted with 3rd order B-M[56] EoS (Equation 4.1, for neutron and computational data sets only). **Blue**: experiment, X-ray (unpublished data reported in this work), **black**: experiment, neutron (unpublished data reported in this work), **red**: DFT-D (this work).

Since the ε-CL-20 used in the neutron powder compression study was not deuterated, the difference in compression behaviour cannot be as a result of deuteration. Likewise, the same PTM was used in both studies, ruling out possible differences in hydrostaticity or due to pressure induced reactions with the PTM. Consequently the only variable between the two experiments was the nature of the source used for diffraction experiments; synchrotron X-ray source or thermal neutrons. Thus the logical reason for the disparity in results obtained for the X-ray diffraction experiment is that the incident high flux of the synchrotron X-rays induced radiation damage of the ε-CL-20 sample. This explanation was later confirmed by further diffraction studies of ε-CL-20 at the same synchrotron source; prolonged irradiation with high-flux X-rays at ambient pressure and subsequent data collection of diffraction patterns on the irradiated region resulted in the determination of lattice parameters and unit-cell volumes very different from the known crystal structure. Furthermore, the degree of radiation damage increased with time. Hence the anomalous data from the high-pressure X-ray diffraction experiment arises from

an increase in the lattice parameters caused by localised radiation damage of the sample.

This investigation has demonstrated that the DFT-D computational model utilised in this study can not only reproduce experimentally determined hydrostatic compression behaviour (as in the case of the α-, γ- and ε-forms of RDX in Chapter 5, and β-HMX and α-FOX-7 in Chapter 6), but can be used to guide experimental endeavours.

7.4.2.4 Hydrostatic Compression Comparison

With confirmation that the neutron powder diffraction study truly represents the hydrostatic compression behaviour of ε-CL-20, for completeness an in-depth comparison is presented of the computationally predicted compression behaviour and the experimental neutron powder diffraction study.

Figure 7.8 shows that the experimental lattice vectors and compression behaviour are reproduced well by the DFT-D method. The experimentally determined values for the *a*- and *c*-axes are consistently overestimated computationally, by ~0.7% and ~0.4%, respectively. The *b*-axis is initially underestimated by only 0.6% and upon compression the disparity gradually reduces, with experiment and theory in agreement to within 0.1% at the maximum pressure of the study. In addition, the experimentally determined pressure-induced trend in variation of the β-angle is also reproduced by the computational model, albeit with some variation about the ideal trend. Nevertheless, differences in the experimentally determined angles are never more than ~1%.

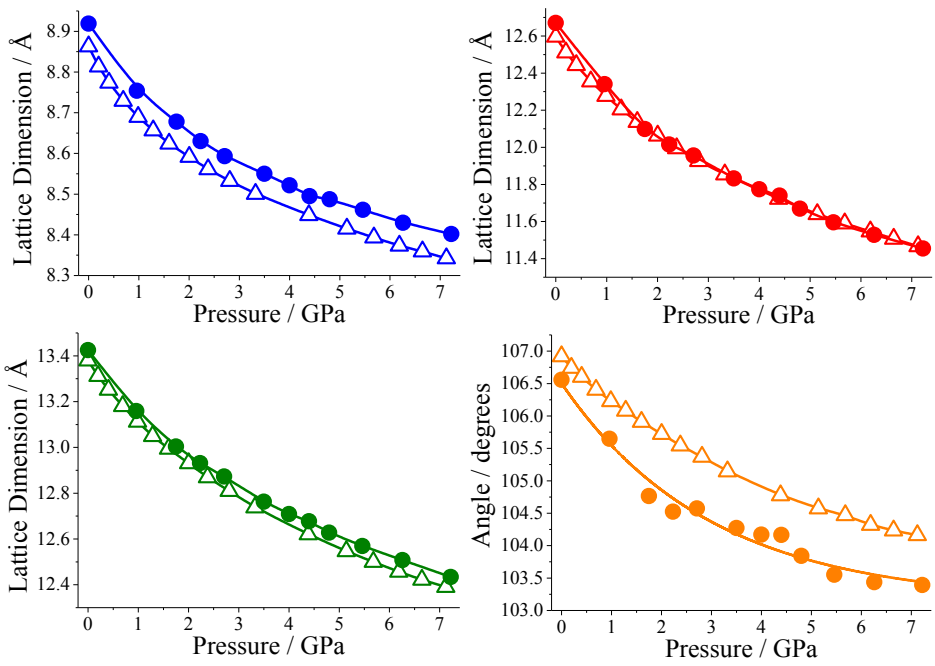

Figure 7.8 Lattice parameters as a function of hydrostatic pressure. Triangle: experiment (unpublished neutron data reported in this work), circle: DFT-D (this work). **Blue**: *a*-axis, **red**: *b*-axis, **green**: *c*-axis, **orange**: β-angle.

Referring back to Figure 7.7, as previously explained, the experimental and computational compression trends are in excellent agreement. The computational model consistently overestimates the experimentally determined (neutron powder diffraction) unit-cell volume (by 1.3 to 1.9%) throughout the whole pressure range studied. The overall compression trends were fitted with 3rd order B-M EoS, calculated EoS parameters are presented in TABLE 7.5 along with the previously determined experimental EoS by Gump & Peiris.[9]

	V_0 (Å^3)	B_0 (GPa)	B'
Exp. (Neutron data, this work)	1428.99(fixed)	11.39(0.13)	11.25(0.20)
Exp. Gump & Peiris, Ref 9*		13.6 (2.0)	11.7 (3.2)
DFT-D	1454.23(fixed)	10.81(0.18)	11.60(0.30)

TABLE 7.5 Experimental and computational 3rd order B-M[56] EoS (Equation 4.1) parameters of crystalline ε-CL-20 (0 – 7.2 GPa). The values in parentheses are estimated standard deviations. * EoS range, 0 – 5.57 GPa, zero-pressure volume, V_0 was not stated.

As would be expected from the visual comparison of unit cell volumes (in Figure 7.7), TABLE 7.5 shows that the EoS for the experimental (neutron) an computational DFT-D data are in excellent agreement for both bulk modulus (B_0)

and first derivative of bulk modulus (B'). TABLE 7.5 also displays the calculated EoS parameters for the Gump and Peiris[9] X-ray compression study. The larger bulk modulus determined for the Gump & Peiris data with respect to the neutron and DFT-D values (*i.e.* less compressible) gives further credence to the suggestion that the Gump & Peiris[9] study was not truly hydrostatic throughout the whole pressure range investigated.

7.4.2.5 Prediction of Heat Capacities

In order to predict the effect of pressure on the heat capacities of crystalline ε-CL-20, high-pressure vibrational mode calculations have also been performed. Complete results of the high-pressure phonon calculations can be found in the Supplementary Information CD (in addition the CD contains the experimental cifs, the computationally calculated structures and the CASTEP output files for the geometry optimisations and phonon calculations, and the statistical thermodynamics solver spread sheet). As explained in previous Chapters, the effect of high-pressure on the heat capacities (at constant volume, C_V) of ε-CL-20 have been predicted by utilising the results of the phonon calculations and implementing Equation 2.59, with error bars determined from phonon dispersion calculation on a small one-molecule test system. Figure 7.9 displays the calculated variation in heat capacities at 300 K in the 0 – 7.22 GPa pressure range for ε-CL-20. To date there has been no experimental determination of C_V for ε-CL-20.

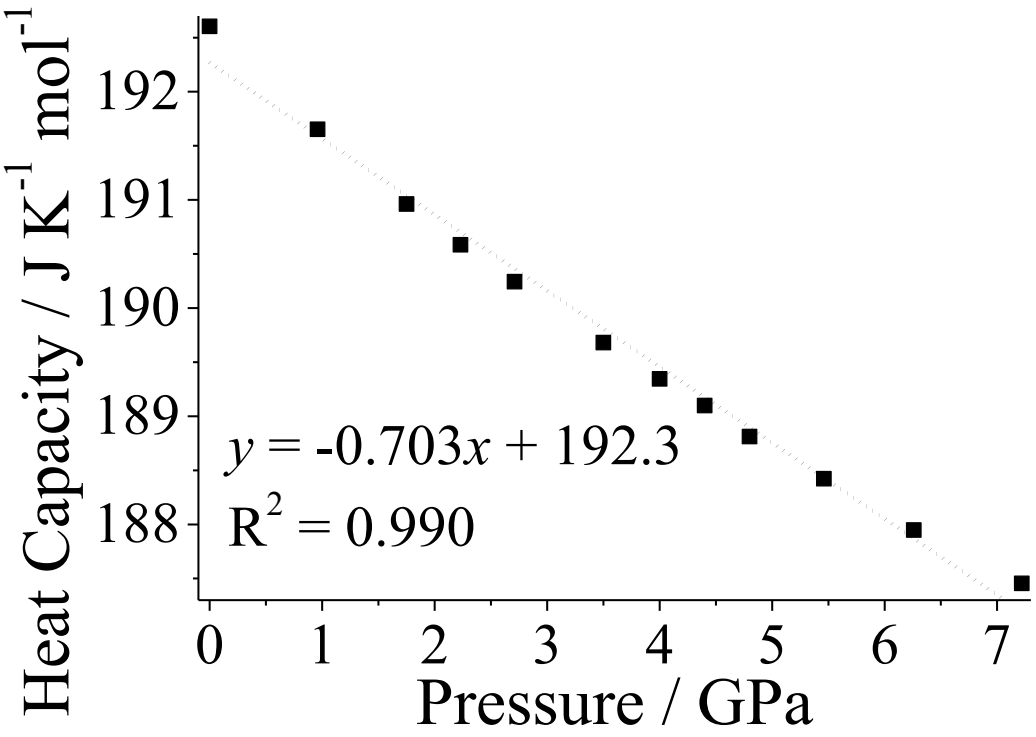

Figure 7.9 Calculated effect of pressure on the heat capacities at T= 300 K of ε-CL-20. The error bars provide an estimate (as determined from the standard deviation of phonon dispersion calculations on a smaller test system) of the effect of phonon dispersion on the calculated (gamma point only) heat capacities – in this case, the error bars are actually smaller than the symbols displaying the points.

In accordance with the results of studies on similar nitramines from previous chapters, the pressure dependence of the heat capacities of ε-CL-20 (and crystalline nitramines in general) is very small (only approximately -1 J K^{-1} mol^{-1} GPa^{-1}), in comparison to temperature dependences of approximately 0.7 J K^{-2} mol^{-1}.

7.5 Conclusions

DFT-D calculations have been utilised to describe accurately the structure and properties of ε-CL-20. At ambient pressure the DFT-D model predicted all of the lattice parameters of α-RDX to within 0.6% of experiment,[3] commensurate with previous DFT-D results.[20] Subsequent phonon calculations generated an INS spectrum in excellent agreement with the experimental spectrum also determined in this study. Eigenvalues and eigenvectors were well replicated by the model.

Subsequently the computational model was used to predict the high-pressure hydrostatic compression behaviour ε-CL-20. By virtue of the aforementioned results

and the confidence in the DFT-D method to predict accurately the hydrostatic compression behaviour of nitramine crystals (inspired by numerous previous favourable comparisons with experiment for the α-, γ- and ε-forms of RDX in Chapter 5, and β-HMX and α-FOX-7 in Chapter 6), the DFT-D hydrostatic compression study highlighted possible discrepancies within the hydrostatic experimental X-ray powder diffraction study presented in this work which consequently instigated a high-pressure neutron powder diffraction study of ε-CL-20.

The compression trend produced by the neutron powder diffraction study was in excellent agreement with the hydrostatic compression trend predicted by the DFT-D method. The combination of DFT-D and neutron results confirmed the fact that the X-ray powder diffraction study did not produce results consistent with hydrostatic compression, and furthermore established that during the high-pressure X-ray study, the ε-CL-20 was subjected to radiation damage. This investigation has demonstrated that the DFT-D computational model utilised in this study can not only reproduce experimentally determined hydrostatic compression behaviour, but can also be used to guide experimental endeavours.

The vibrational properties as a function of pressure were calculated, the results of which were then used to predict the effect of pressure on the heat capacities of ε-CL-20. These predictions confirm the trends determined in the previous chapters (for the α-, γ- and ε-forms of RDX in Chapter 5, and β-HMX and α-FOX-7 in Chapter 6) suggesting a very weak pressure dependence of heat capacities (approximately -1 J K^{-1} mol^{-1} GPa^{-1}) for the energetic nitramine materials investigated within this work.

7.6 References

1 Nielsen, A. T.; Chafin, A. P.; Christian, S. L.; Moore, D. W.; Nadler, M. P.; Nissan, R. A.; Vanderah, D. J.; Gilardi, R. D.; George, C. F.; Flippen-Anderson, J. L. *Tetrahedron* **1998**, *54*, 11793.

2 Simpson, R. L.; Urtiew, P. A.; Ornellas, D. L.; Moody, G. L.; Scribner, K. J.; Hoffmann, D. M. *Propell. Explos. Pyrothech*. **1997**, *22*, 249.

3 Bolotina, N. B.; Hardie, M. I.;Speer Jr., R. L.; Pinkerton, A. A. *J. Appl. Crystallogr*. **2004**, *37*, 808.

4 Foltz, M. F.; Coon, C. L.; Garcia, F.; Nichols III, A. L. *Propell. Explos. Pyrothech*. **1994**, *19*, 19.
5 Foltz, M. F.; Coon, C. L.; Garcia, F.; Nichols III, A. L. *Propell. Explos. Pyrothech*. **1994**, *19*, 133.
6 Image courtesy of www.wikipedia.com, the image has been released into the public domain.
7 Russell, T. P.; Miller, P. J.; Piermarini, G. J.; Block, S. J. Chem. Phys. **1992**, *96*, 5509.
8 Russell, T. P.; Miller, P. J.; Piermarini, G. J.; Block, S. J. Chem. Phys. **1993**, *97*, 1993.
9 Gump, J. C.; Peiris, S. M. *J. Appl. Phys*. **2008**, *104*, 083509.
10 Ciezak, J. A.; Jenkins, T. A.; Liu, Z.; Hemley, R, J. *Propell. Explos. Pyrotech.* **2007**, *32*, 472
11 McNesby, K. L.; Wolfe, J. E.; Morris, J. B.; Pesce-Rodriguez, R. A. *J. Raman Spectrosc.* **1994**, *25*, 75.
12 Fell, N. F.; Widder, J. M.; Medlin, S. V.; Morris, J. B.; Pesce-Rodriguez, R. A.; McNesby, K. L. *J. Raman Spectrosc.* **1996**, *27*, 97.
13 Goede, P.; Latypov, N. V.; Ostmark, H. *Propell. Explos. Pyrotech.* **2004**, *29*, 205.
14 Byrd, E. C. F.; Rice, B. M. *J. Phys. Chem. C* **2007**, *111*, 2787.
15 Xu, X. -J.; Zhu, W. -H.; Xiao, H. -M. *J. Phys. Chem. B* **2007**, *111*, 2090.
16 Balu, R.; Byrd, E. C. F.; Rice, B. M. *J. Phys. Chem. B* **2011**, *115*, 803.
17 Shimojo, F.; Wu, Z.; Nakano. A.; Kalia, R. K.; Vashisgta, P. *J. Chem. Phys.* **2010**, *132*, 094106.
18 Grimme, S. *J. Comput. Chem.* **2006**, *27*, 1787.
19 Neumann, M. A.; Perrin, M. -A. *J. Phys. Chem. B* **2005**, *109*, 15531.
20 Sorescu, D. C.; Rice, B. M. *J. Phys. Chem. C* **2010**, *114*, 6734.
21 Landerville, A. C.; Conroy, M. W.; Budzevich, M. M.; Lin, Y.; White, C. T.; Oleynik, I. I. *App. Phys. Lett.* **2010**, *97*, 251908.
22 Wu, Z.; Kalia, R. K.; Nakano, A.; Vashishta, P. *J. Chem. Phys.* **2011**, *134*, 204509.
23 Merrill, L.; Bassett, W. A. *Rev. Sci. Instrum.* **1974**, *45*, 290.
24 Piermarini, G. J.; Block, S.; Barnett, J. D.; Forman, R. A. *J. App. Phys.* **1975**, *46*, 2774.
25 Lennie, A.; Landy, D.; Robers, M.; Bushell-Wye, G. *J. Synchrotron Radiat.* **2007**, *14*, 433.
26 Hammersley, A. in *FIT2D: an introduction and overview*; ESRF Technical Report ESRF97HA02T, **1997**.
27 Larson, A. C.; Von Dreele, R. *General Structure Analysis System (GSAS)*; Los Alamos National Laboratory Report, LAUR 86-748, **2000**.
28 Marshall, W. G.; Francis, D. J. *J. App. Cryst.* **2002**, *35*, 122.
29 Besson, J. M.; Nelmes, R. J.; Hamel, G.; Loveday, J. S.; Weill, G.; Hull, S. *Physica B* **1992**, *180-181*, 907.
30 http://www.isis.stfc.ac.uk/
31 Decker, D. L. *J. App. Phys.* **1971**, *42*, 3239.

32 Colognesi, D.; Celli, M.; Cilloco, F.; Newport, R. J.; Parker, S. F.; Rossi-Albertini, V.; Sacchetti, F.; Tomkinson, J.; Zoppi, M. *Appl. Phys. A: Mater. Sci. Process.* **2002**, *S74* , S64.
33 Ramirez-Cuesta, A. J. *Comput. Phys. Commun.* **2004**, *157*, 226.
34 Clark, S. J.; Segall, M. D.; Pickard, C. J.; Hasnip, P. J.; Probert, M. J.; Refson, K.; Payne, M. C. Z. Krystallogr. **2005**, *220*, 567.
35 Grimme, S. *J. Comput. Chem.* **2006**, *27*, 1787.
36 Perdew, J. P.; Burke, K.; Ernzerhof, M. *Phys. Rev. Lett.* **1996**, *77*, 3865.
37 Vackar, J.; Hytha, M.; Simunek, A. *Phys. Rev. B* **1998**, *58*, 12712.
38 Monkhorst, H. J.; Pack, J D. *Phys. Rev. B* **1976**, *13*, 5188.
39 Fischer, T. H.; Almlof, J. *J. Phys. Chem.* **1992**, *96*, 9768.
40 Frank, W.; Elsässer, C.; Fähnle, M. *Phys. Rev. Lett.* **1995**, *74*, 1791.
41 Angel, R. J.; Bujak, M.; Zhao, J.; Gatta, G. D.; Jacobsen, S. D. *J. Appl. Cryst*. **2007**, *40*, 26.

Chapter 8

General Remarks

8 General Remarks

The work presented in this thesis has demonstrated that despite its relative simplicity, the DFT-D dispersion correction proposed by Grimme (2006) performs extremely well over a range of conditions, and is able to describe accurately intramolecular and intermolecular interactions and thus the structure and properties of the organic molecular nitramine crystals. The effect of high pressures on several polymorphs of RDX, β-HMX, α-FOX-7. ε-CL-20 and the ionic salt ammonium perchlorate have been studied computationally, augmented by various experimental investigations. The results of the structural optimisations and subsequent phonon calculations have been utilised in combination with statistical thermodynamics to predict the effect of pressure on the heat capacities of the energetic materials of interest. These predictions suggest a very weak pressure dependence of heat capacities for all nitramine crystals studied. Regardless of the magnitude of the pressure dependencies of the heat capacities of the energetic materials studied, this work has provided valuable information that can be used to better model the deflagration-to-detonation transition in the aforementioned materials and thus improve the safety of the energetic formulations.

Notably, the first experimental determination of the enthalpy of fusion, ΔH_{fus}, of the highly metastable β-RDX was performed as part of this study. Moreover, the DFT-D model was used to predict the lattice energies of the α- and β-forms of RDX, the difference in predicted lattice energies were found to be in excellent agreement to the difference in experimental enthalpies of fusion, further validating the ability of the DFT-D model to accurately describe the intermolecular interactions of this class of materials.

Furthermore the investigation of the hydrostatic compression of ε-CL-20 demonstrated that the DFT-D computational model utilised in this study can not only reproduce experimentally determined hydrostatic compression behaviour, but can also be used to guide experimental endeavours.

Unfortunately the DFT and DFT-D methods employed in this study do not accurately account for the intermolecular interactions in AP, furthermore this study established that no significant improvement in the calculation of crystal geometries and vibrational properties of AP are obtained by employing DFT-D corrections. In the future, to accurately model the structure of AP and similar ionic materials, one could use classical modelling methods, such as an experimentally parameterised force-field. However, as this requires significant work to develop, coupled with that fact that the force-field produced is generally non-transferable to other systems (except perhaps those with extremely similar intermolecular interactions) and the research being invested into alternatives for AP, it may not may be worthwhile to pursue this route.

As the field of developing dispersion correction methods for use in DFT is a very active research field, and new procedures are being implemented, the computational expense of higher-level DFT dispersion correction methods (such as XDM, specially developed van der Waals density functionals or adiabatic-connection fluctuation-dissipation theorem methods) is continually decreasing. In addition, different dispersion correction methods are developed with different parameterisation, and thus other methods may be more suitable for the accurate description of the AP structure. Hence, in the near future it may be (computationally) cost-effective to investigate the capability of such methods to adequately describe the intermolecular interactions of AP. The same is true for the further investigation of the nitramine crystals, although the simple DFT-D method utilised throughout this study provides an accurate descriptions of the intermolecular interactions (with all experimental lattice parameters at ambient and high-pressures reproduced to with ~2%), there is still room for improvement, and so future studies could investigate the performance of other dispersion corrections at describing the high-pressure structure and properties of not only the energetic materials studied here, but also other materials of interest in which dispersion interactions play a vital role in determining its crystal structure.

Chapter 9

Appendix : Extra figures and further information

9 Appendix : Extra Figures and Further Information

9.1 Chapter 5 Additional Information

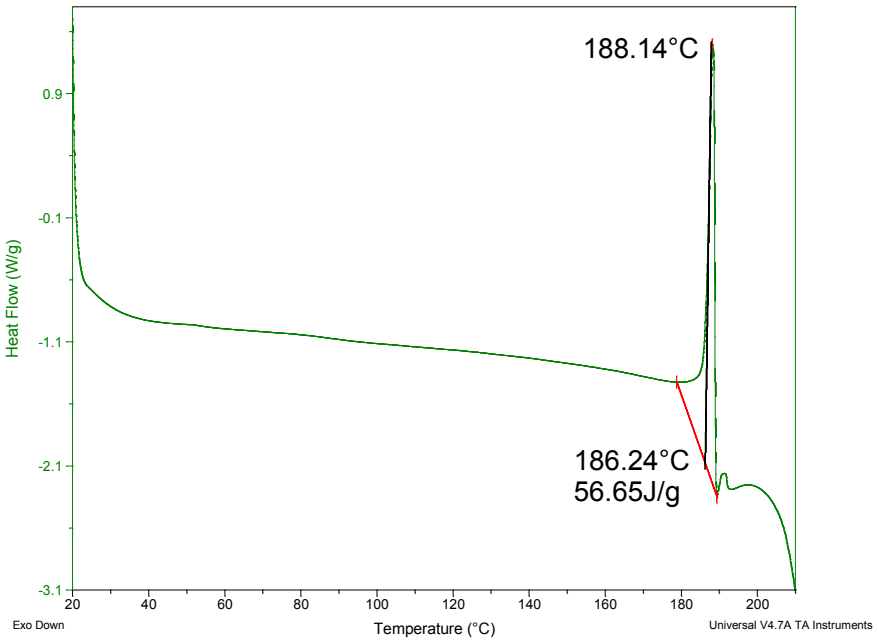

Figure A5.1 DSC Thermograph (10 °C min^{-1}) for β-RDX (sample mass 0.184 mg).

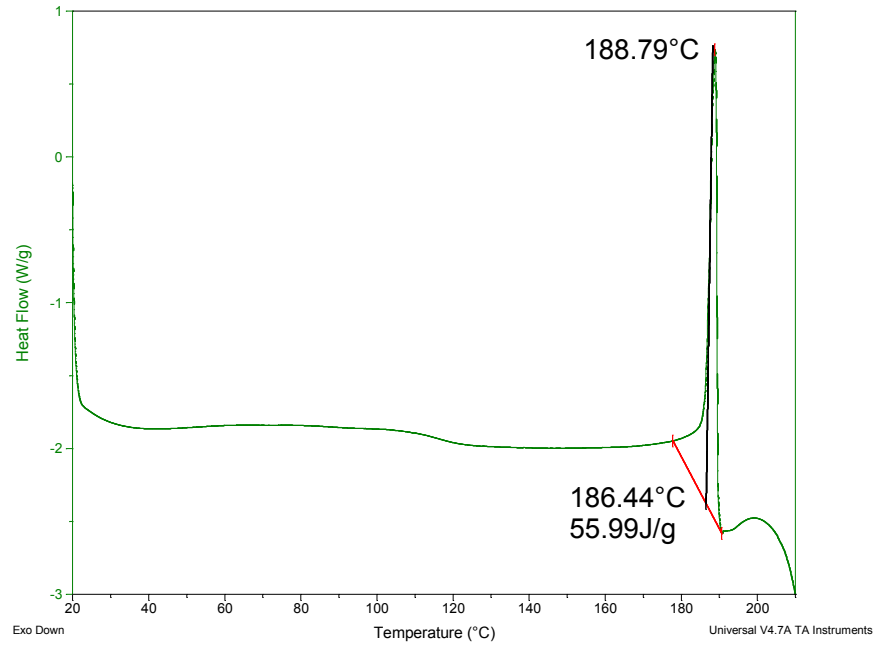

Figure A5.2 DSC Thermograph (10 °C min^{-1}) for β-RDX (sample mass 0.184 mg).

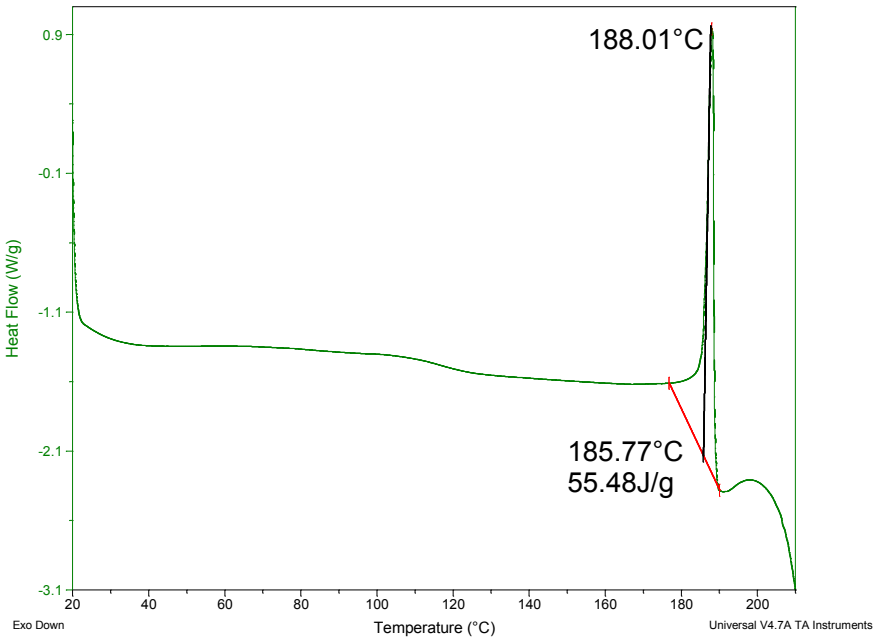

Figure A5.3 DSC Thermograph (10 °C min^{-1}) for β-RDX (sample mass 0.194 mg).

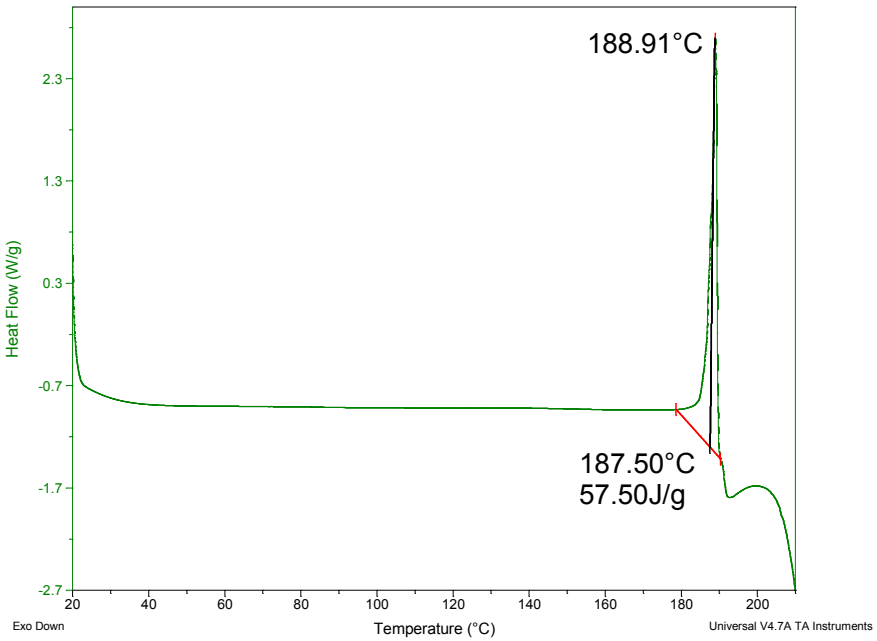

Figure A5.4 DSC Thermograph (10 °C min^{-1}) for β-RDX (sample mass 0.261 mg).

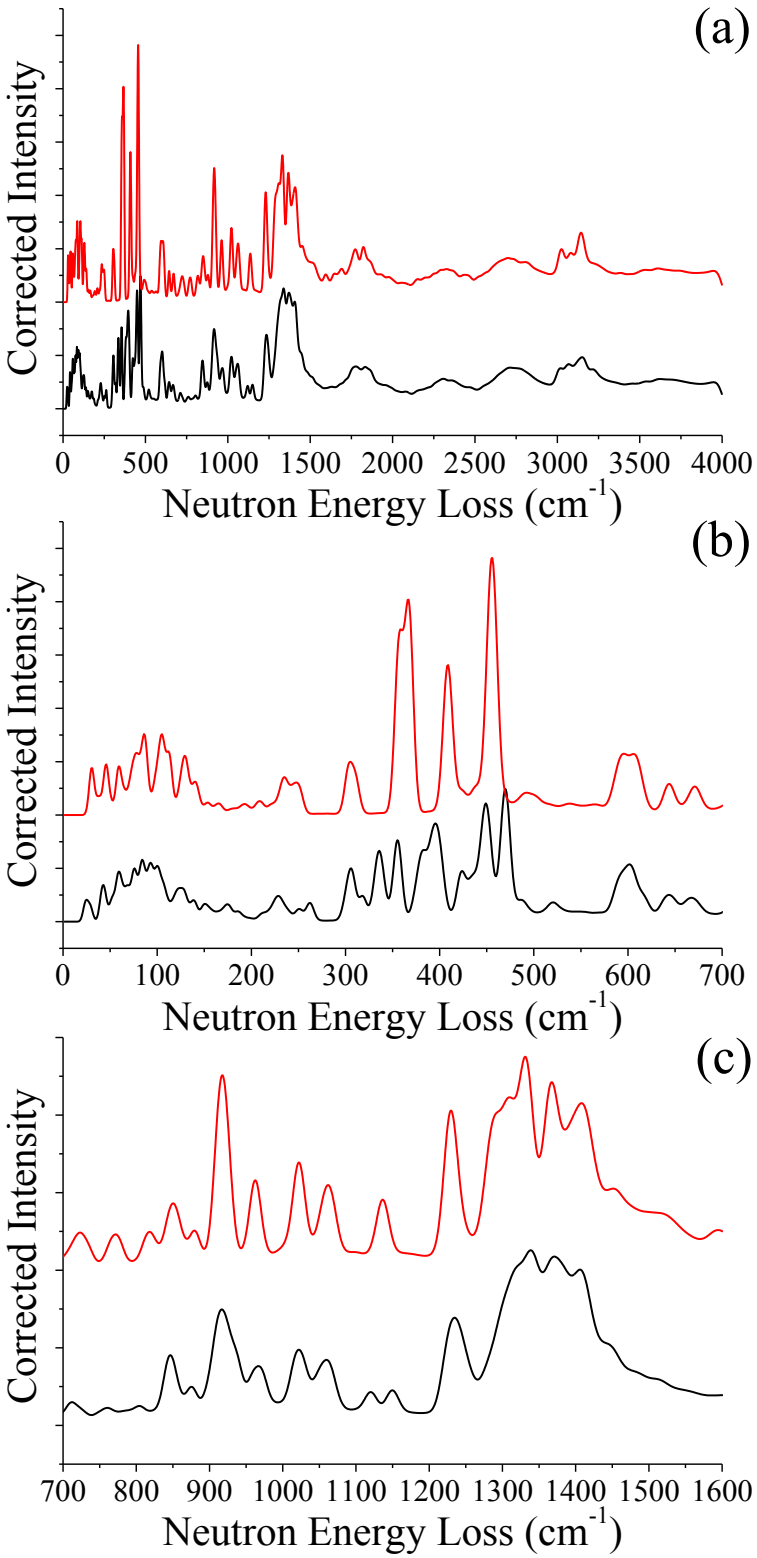

Figure A5.5 Comparison of computationally calculated INS spectra. γ-RDX at 3.90 GPa (black line) and α-RDX at 3.85 GPa (red line) in the regions (a) 0 – 4000 cm^{-1}, (b) 0 – 700 cm^{-1}, (c) 700 – 1600 cm^{-1}.

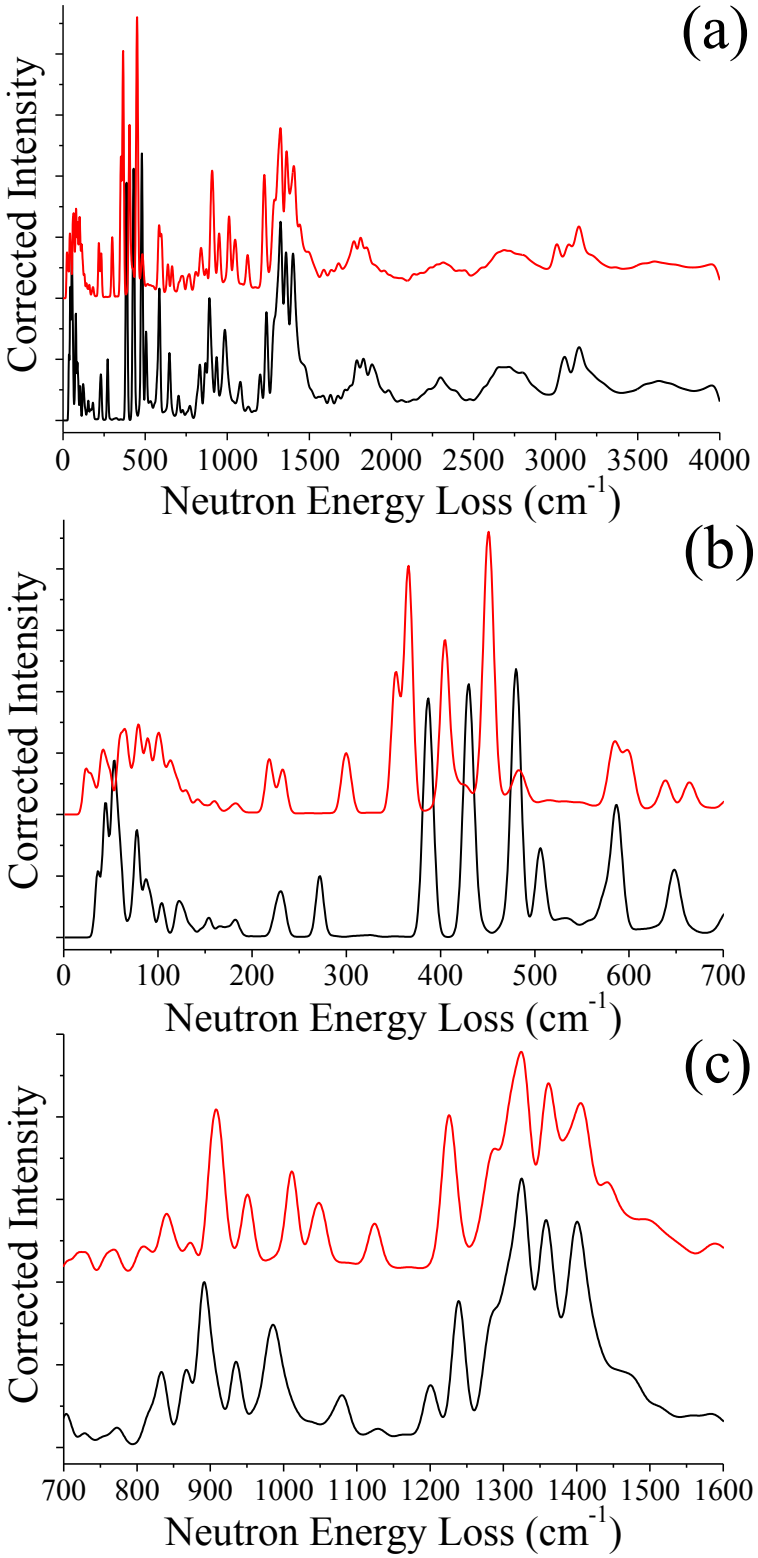

Figure A5.6 Comparison of computationally calculated INS spectra. ε-RDX at 1.32 GPa (black line) and α-RDX at 1.35 GPa (red line) in the regions (a) 0 – 4000 cm^{-1}, (b) 0 – 700 cm^{-1}, (c) 700 – 1600 cm^{-1}.

9.2 Chapter 6 Additional Information

Table A6.1 Comparison of experimental INS and calculated DFT-D combination and overtone vibrational modes for β-HMX. All frequencies, **ν**, are in units of cm^{-1}. * The respective experimental INS and computationally calculated modes are named in accordance with the annotated spectral comparisons given on the Supplementary Information CD.

*Mode**	*INS* **ν**	*Mode**	*Comp.* **ν**	*Mode**	*INS* **ν**	*Mode**	*Comp.* **ν**
m30	203	c1	209	m91	1782	c19	1827
m31	216			m92	1818		
m34	248	c2	261	m93	1854	c20	1877
m35	265			m94	1892	c21	1955
m37	288	c3	295	m95	1920		
m38	297			m96	1950		
m40	334	c4	327	m97	1978	c22	2034
m41	342			m98	2038	c23	2089
m47	451	c5	452	m99	2143	c24	2168
m48	460			m100	2175		
m49	469			m101	2231		
m50	478	c6	481	m102	2287		
m51	488			m103	2332	c25	2258
m52	507	c7	501	m104	2427	c26	2352
m53	515	c8	512	m105	2476	c27	2382
m54	523			m106	2526	c28	2458
m55	533	c9	538	m107	2577	c29	2535
m56	550			m108	2669	c30	2621
m57	561	c10	560	m109	2722	c31	2703
m62	681			m110	2791	c32	2800
m66	796	c11	779	m111	2876	c33	2887
m71	1005			m112	2920		
m72	1024			m115	3130	c34	3150
m73	1040	c12	1008	m116	3242	c35	3204
		c13	1050	m117	3290	c36	3258
m84	1542	c14	1509	m118	3390	c37	3443
m85	1573	c15	1534	m119	3441	c38	3509
m86	1597			m120	3599		
m87	1621	c16	1582	m121	3690	c39	3668
m88	1646	c17	1649	m122	3802	c40	3725
m89	1687			m123	3860	c41	3842
m90	1712	c18	1753				

Table A6.2 Comparison of experimental INS and calculated DFT-D combination and overtone vibrational modes for α-FOX-7. All frequencies, **ν**, are in units of cm^{-1}. * The respective experimental INS and computationally calculated modes are named in accordance with the annotated spectral comparisons given on the Supplementary Information CD.

*Mode**	*INS* **ν**	*Mode**	*Comp.* **ν**	*Mode**	*INS* **ν**	*Mode**	*Comp.* **ν**
29	186	c1	195	87	2105	c28	2029
30	192	c1	195	88	2147	c29	2085
31	204	c2	219	89	2180		
32	225	c3	242	90	2202	c30	2125
35	274	c4	288	91	2269	c31	2179
38	353	c5	356	92	2338	c32	2231
40	422	c6	423	93	2397	c33	2271
44	490			94	2445	c34	2348
45	511	c7	515	95	2519	c35	2413
57	853	c9	884	96	2583	c36	2453
58	888	c10	900			c37	2500
59	902			97	2609	c38	2583
60	921	c11	942	98	2661	c39	2638
63	1101	c12	1114			c40	2684
66	1174	c13	1167	99	2715	c41	2737
67	1213	c14	1232	100	2840	c42	2800
69	1311	c15	1297	101	2883	c43	2854
70	1343	c16	1340	102	3000	c44	2966
73	1420	c17	1394	103	3060	c45	3065
77	1616	c18	1628	104	3122	c46	3144
		c19	1672	105	3169	c47	3195
78	1707	c20	1722	106	3233	c48	3239
79	1812	c21	1796	107	3249	c49	3290
80	1840	c22	1848	110	3555	c50	3653
81	1876	c23	1899	111	3608	c51	3742
82	1905	c24	1899	112	3699	c52	3807
83	1944	c25	1950	113	3774	c53	3866
84	1973	c26	1964	114	3908		
85	2003			115	3967		
86	2064	c27	2001				

9.3 Chapter 7 Additional Information

Table A7.1 Comparison of experimental INS and calculated DFT-D combination and overtone vibrational modes for ε-CL-20. All frequencies, **ν**, are in units of cm^{-1}. * The respective experimental INS and computationally calculated modes are named in accordance with the annotated spectral comparisons given on the Supplementary Information CD.

*Mode**	*INS* **ν**	*Mode**	*Comp.* **ν**	*Mode**	*INS* **ν**	*Mode**	*Comp.* **ν**
m17	98			m113	2012	c14	1921
m18	100			m114	2074	c15	1989
m25	122			m115	2116	c16	2081
m44	238			m116	2147		
m48	276			m117	2213	c17	2160
m49	282			m118	2257	c18	2185
m50	286	c1	278			c19	2206
m51	290			m119	2326		
m52	295			m120	2350	c20	2299
m56	324			m121	2408	c21	2390
m57	332			m122	2494	c22	2451
m63	420			m123	2519		
m64	431	c2	416	m124	2570	c23	2494
m67	478			m125	2648	c24	2553
m68	488			m126	2715	c25	2638
m69	505			m127	2784	c26	2731
m70	513	c3	494	m128	2854		
m72	550			m129	2911	c27	2847
m102	1441	c4	1401	m131	3122		
m103	1477	c5	1442	m132	3170		
m104	1568	c6	1488	m133	3233	c28	3196
m105	1608	c7	1530	m134	3348	c29	3356
m106	1641			m135	3398	c30	3401
m107	1682	c8	1588	m136	3467	c31	3456
m108	1724	c9	1666	m137	3537	c32	3600
m109	1785	c10	1733	m138	3626	c33	3690
m110	1821	c11	1755	m139	3699	c34	3748
m111	1886	c12	1838	m140	3774	c35	3821
m112	1973	c13	1851	m141	3947		

9.4 Conferences and Lecture Courses Attended

9.1.1 Year 1

Poster Presentations

Steven Hunter, Colin R. Pulham, Carole A. Morrison, Peter J. Gould and David A. Hills, **Determination of the Effects of Extreme Conditions on the Properties of Energetic Materials,** *ScotCHEM Computational Chemistry Symposium*, Glasgow, UK, **April 2010**.

Courses Attended

Transkills: Getting Started with Your PhD – College of Science and Engineering, Edinburgh, UK, **September – December 2009**.

Introduction to Computational Chemistry – Graduate School Lectures, Edinburgh, UK, **October – December 2009**.

9.1.2 Year 2

Oral Presentations

Ian G. Cullis, Aaron Longbottom, David M. Williamson, Steven Hunter, Peter J. Gould and Colin R. Pulham, **Hazard Modelling & Simulation,** *UK-Energetics : Technical Review*, Kent, UK, **March 2011**. (My contribution delivered by Ian G. Cullis)

Steven Hunter, Colin R. Pulham, Carole A. Morrison and Peter J. Gould, **First Principles Hydrostatic Compression Study of Phase I Ammonium Perchlorate and α-, γ-, and ε-RDX,** *New Trends in Research of Energetic Materials*, Pardubice, Czech Republic, **April 2011**.

Steven Hunter, Colin R. Pulham, Carole A. Morrison and Peter J. Gould, **Determination of the Effects of Extreme Conditions on the Properties of α-, γ-, and ε-RDX,** *ScotCHEM SPIRIT Meeting*, St. Andrews, UK, **May 2011**.

Steven Hunter, Colin R. Pulham, Carole A. Morrison and Peter J. Gould, **Determination of the Effects of Extreme Conditions on the Properties of α-, γ-, and ε-RDX,** *UK-Singapore Energetics Workshop*, Edinburgh, UK, **June 2011**.

Poster Presentations

Steven Hunter, Colin R. Pulham, Carole A. Morrison and Peter J. Gould, **A computational hydrostatic compression study of the α- γ- and ε- polymorphs of RDX,** *ScotCHEM Computational Chemistry Symposium*, Edinburgh, UK, **June 2011**.

Steven Hunter, Colin R. Pulham, Carole A. Morrison and Peter J. Gould, **First Principles Hydrostatic Compression Study of Phase I Ammonium Perchlorate and α-, γ-, and ε-RDX,** *New Trends in Research of Energetic Materials*, Pardubice, Czech Republic, **April 2011**.

Courses Attended

Technology Commercialisation and Skills Workshop, Edinburgh UK, **July 2011**.

9.1.3 Year 3

Oral Presentations

Steven Hunter, **Experimental and DFT-D Studies of the Molecular Organic Energetic Material RDX,** *Final Year PhD Presentation*, Edinburgh UK, **July 2012**.

Poster Presentations

Steven Hunter, Tuuli Sutinen, Stewart F. Parker, Carole A. Morrison, David M. Williamson, and Colin R. Pulham, **Experimental and DFT-D Studies of RDX,** *Gordon Research Conference: Energetic Materials*, Mount Snow, VT, USA, **June 2012**.

9.5 Publications

Steven Hunter, Alistair J. Davidson, Carole A. Morrison, Colin R. Pulham, Patricia Richardson, Matthew J. Farrow, William G. Marshall, Alistair R. Lennie and Peter J. Gould, **Combined Experimental and Computational Hydrostatic Compression Study of Crystalline Ammonium Perchlorate,** *J. Phys. Chem. C*, **2011**, *115(38)*, 18782-18788.

Steven Hunter, Tuuli Sutinen, Stewart F. Parker, Carole A. Morrison, David M. Williamson, Stephen Thompson, Peter J. Gould and Colin R. Pulham, **Experimental and DFT-D Studies of the Molecular Organic Energetic Material RDX,** *J. Phys. Chem. C*, **2013**, *117(16)*, 8062-8071.

Petra Á. Szilágyi, Steven Hunter, Carole A. Morrison, David I. A. Millar, Alistair R. Lennie, Chiu C. Tang and Colin R. Pulham, **Pressure-Induced Structural Changes in $CH_3NH_2BH_3$ and $(CH_3)_2NHBH_3$,** *J. Phys. Chem. A*, **2013**, (submitted).